The Pennsylvania State University

The Graduate School

Department of Civil and Environmental Engineering

LOAD AND RESISTANCE FACTOR DESIGN

FOR INTEGRAL ABUTMENT BRIDGES

A Dissertation in

Civil Engineering

by

Woo Seok Kim

Submitted in Partial Fulfillment
of the Requirements
for the Degree of

Doctor of Philosophy

December 2008

The dissertation of Woo Seok Kim was reviewed and approved* by the following:

Jeffrey A. Laman
Associate Professor of Civil Engineering
Dissertation Advisor
Chair of Committee

Mian C. Wang
Professor of Civil Engineering

Angelica M. Palomino
Assistant Professor of Civil Engineering

Panagiotis Michaleris
Associate Professor of Mechanical Engineering

Peggy A. Johnson
Professor of Civil Engineering
Head of the Department of Civil and Environmental Engineering

*Signatures are on file in the Graduate School

ABSTRACT

A prestressed concrete girder integral abutment bridge (IAB) requires a new load combination due to inherent uncertainties in loads and resistances and the significant inelastic and hysteretic behavior over bridge life. The present study presents development of simplified numerical modeling methodologies, development of nominal IAB response prediction models through an extensive parametric study, and establishment of IAB response statistics using Monte Carlo simulation. Finally, new load combinations in a load and resistance factor design (LRFD) format have been developed using reliability analyses.

For a robust, long-term simulation and numerical probabilistic study, a simplified numerical modeling methodology has been developed based on field monitoring results of four IABs. The numerical model includes temperature variation, temperature gradient, time-dependent loads, soil-structure interaction, and plastic behavior of the backwall/abutment construction joint. The four field tested IABs were modeled to validate the methodology. The proposed numerical model provides accurate, long-term prediction of IAB behavior and response.

IAB response prediction models have been developed using a parametric study. Current design specifications and guides do not provide clearly defined analysis methods, therefore, there is a need for easily implemented preliminary analysis methods. Based on the calibrated, nonlinear, 2D numerical modeling methodology, a parametric study of 243 cases was performed to obtain 75-year bridge response. The parametric study considered five parameters: (1) thermal expansion coefficient; (2) bridge length; (3) backfill height;

(4) backfill stiffness; and (5) pile soil stiffness. The parametric study revealed that the thermal expansion coefficient, bridge length and pile soil stiffness significantly influence IAB response as measured by: (1) bridge axial force; (2) bridge bending moment at mid-span of the exterior span; (3) bridge bending moment at the abutment; (4) pile lateral force at pile head; (5) pile moment at pile head; (6) pile head/abutment displacement; and (7) abutment displacement at the centroid of a superstructure. The influence of backfill height and backfill stiffness are not significant relatively. The study results provide practical, preliminary estimates of bridge response and ranges for preliminary IAB design and analysis.

In order to establish IAB response statistics, Monte Carlo simulation has been performed based on the 2D numerical modeling methodology. Based on the established thermal load and resistance variable statistics, this study developed probabilistic numerical models and established IAB response statistics. Considered input variables to deal with uncertainties are resistance and load variables. IAB response statistics were established: (1) bridge axial force; (2) bridge bending moment; (3) pile lateral force; (4) pile moment; (5) pile head/abutment displacement; (6) compressive stress at the top fiber at the mid-span of the exterior span; and (7) tensile stress at the bottom fiber at the mid-span of the exterior span. IAB response statistics provide the basis for a reliability-based design. Reliability analyses were performed to develop new load combinations for IABs based on the developed IAB response prediction models and established statistics.

TABLE OF CONTENTS

LIST OF FIGURES....vii

LIST OF TABLES....xiii

NOTATIONS....xv

ACKNOWLEDGEMENTS....xviii

Chapter 1 INTRODUCTION....1

1.2 Problem Statement....4
1.3 Scope....5
1.4 Objectives....7
1.5 Organization....8

Chapter 2 LITERATURE REVIEW....10

2.1 Introduction....10
2.2 Current Design Specifications....11
2.3 Previous IAB Research....19
2.4 Numerical Analysis of IABs....24
2.4.1 Abutment Backfill Pressure....25
2.4.2 Laterally Displaced Piles....29
2.4.3 Time-dependent Effects....30
2.5 Reliability Analysis of IABs....33
2.6 Study Design....37

Chapter 3 DETERMINISTIC NUMERICAL MODEL CALIBRATION....43

3.1 Introduction....43
3.2 Field Data Description....45
3.3 Development of Model Component....46
3.3.1 Material Properties....47
3.3.2 Abutment-Backfill Interaction....51
3.3.3 Soil-Pile Interaction....52
3.3.4 Abutment-backwall Construction Joint....56
3.4 IAB Loads....60
3.4.1 Backfill Pressure....60
3.4.2 Time-dependent Effects....61
3.4.3 Superstructure Temperature Change....65
3.4.4 Temperature Gradient....66
3.5 Nominal Numerical Model Results....68
3.5.1 Bridge 109....69

3.5.2 Bridge 203 71
3.5.3 Bridge 211 74
3.5.4 Bridge 222 77
3.6 Summary 79

Chapter 4 DEVELOPMENT OF IAB REPONSE PREDICTION MODELS 83

4.1 Introduction 83
4.2 Deterministic Parameters 92
4.2.1 Bridge Construction Timeline 93
4.2.2 Thermal Expansion Coefficient 95
4.2.3 Bridge Length and Backfill Height 96
4.2.4 Girder Design 97
4.2.5 Soil Boundaries 98
4.2.5.1 Backfills stiffness 99
4.2.5.2 Soils stiffness around piles 101
4.2.6 Temperature Variation 104
4.2.7 Temperature Gradient 107
4.2.8 Time-dependent Loads 108
4.3 Parametric Study Result Discussion 109
4.3.1 Girder Axial Force 110
4.3.2 Girder Bending Moment at Mid-span of the Exterior Span 113
4.3.3 Girder Bending Moment at Abutment 116
4.3.4 Pile Lateral Force 120
4.3.5 Pile Bending Moment 123
4.3.6 Pile Head/Abutment Displacement 126
4.3.7 Abutment Displacement at Centroid of Superstructure 128
4.4 IAB Response Prediction 131
4.5 Summary 136

Chapter 5 PROBABILISTIC SIMULATION AND RESULTS 138

5.1 Introduction 138
5.2 Resistance Variables 141
5.2.1 Concrete Elastic Modulus 142
5.2.2 Backfill Stiffness 145
5.2.3 Pile Soil Stiffness 146
5.3 Load Variables 149
5.3.1 Superstructure Temperature 149
5.3.2 Concrete Thermal Expansion Coefficient 152
5.3.3 Temperature Gradient 153
5.3.4 Time-dependent Loads 155
5.3.5 Bridge Construction Timeline 156
5.4 Monte Carlo Simulation 158
5.5 Monte Carlo Simulation Results 161

5.5.1 Bridge Axial Force 165
5.5.2 Bridge Bending Moment 174
5.5.3 Pile Lateral Force 183
5.5.4 Pile Moment 187
5.5.5 Pile Head/Abutment Displacement 192
5.5.6 Compressive Stress at the Top Fiber of the Mid-span of the Exterior Span 196
5.5.7 Tensile Stress at the Bottom Fiber of the Mid-span of the Exterior Span 201
5.6 Summary 206

Chapter 6 DETERMINATION OF PARTIAL SAFETY FACTORS 208

6.1 Introduction 208
6.2 Statistics of Loads and Resistances 211
6.3 Reliability Analysis of AASHTO LRFD Limit State 214
6.3.1 Service I Limit State 218
6.3.2 Service III Limit State 221
6.3.3 Strength I Limit State 223
6.4 Calibration of Load and Resistance Factors 225
6.4.1 Simple Support Condition 229
6.4.2 Fixed End Support 231
6.5 Summary 234

Chapter 7 SUMMARY AND CONCLUSIONS 236

7.1 Summary 236
7.2 Conclusions 238
7.3 Recommendations for Future Research 242

Bibliography 243

LIST OF FIGURES

Figure 1.1: Typical Single Span Integral Abutment Bridge..2

Figure 1.2: Typical Cross Section...6

Figure 1.3: Organizations of the Present Study...9

Figure 2.1: Equivalent Cantilever...23

Figure 2.2: Lateral Earth Pressure Variation...25

Figure 2.3: Perfectly Elasto-Plastic Behavior...27

Figure 2.4: Force-Displacement Relationship for Abutment-Backfill Interaction............28

Figure 2.5: Concrete Strain under Variable Stress..31

Figure 2.6: Reliability Analysis Procedure using ASM..39

Figure 2.7: Nominal Load for AASHTO LRFD...41

Figure 3.1: Schematic 2D Numerical Model..46

Figure 3.2: Bridge 109 Soil Properties under Abutment 1...48

Figure 3.3: Bridge 109 Soil Properties under Abutment 2...49

Figure 3.4: Bridge 203 Soil Properties under Abutment 2...49

Figure 3.5: Bridge 211 Soil Properties under Abutment 1...50

Figure 3.6: Bridge 211 Soil Properties under Abutment 2...50

Figure 3.7: Bridge 222 Soil Properties under Abutment 1...50

Figure 3.8: Bridge 222 Soil Properties under Abutment 2...51

Figure 3.9: Abutment-Backfill Numerical Implementation Modification.........................51

Figure 3.10: Condensed Soil-Pile Interaction Model...53

Figure 3.11: Sample *p-y* Curves from Bridge 211..54

Figure 3.12: Pile Lateral Displacement Comparison..54

Figure 3.13: Pile Moment Comparison...55

Figure 3.14: Force vs. Displacement Comparison (Bridge 211).....................................55

Figure 3.15: Moment vs. Rotation Comparison (Bridge 211)...56

Figure 3.16: Rotational Stiffness of Construction Joints..58

Figure 3.17: Construction Joint Model..59

Figure 3.18: Creep Coefficient for Bridge 211...62

Figure 3.19: Aging Coefficient of Bridge 211..62

Figure 3.20: Age-Adjusted Effective Modulus...63

Figure 3.21: Shrinkage Strain of Bridge 211..63

Figure 3.22: Total Strain at Top Fiber of Bridge 211...64

Figure 3.23: Total Strain at Bottom Fiber of Bridge 211...64

Figure 3.24: Temperature Model for Deterministic Models...65

Figure 3.25: Temperature Gradient of Transformed Section..67

Figure 3.26: Temperature Variation with Temperature Gradient.....................................68

Figure 3.27: Measured and Predicted Bridge Response—Bridge 109.............................70

Figure 3.28: Measured and Predicted Bridge Response—Bridge 203.............................72

Figure 3.29: Measured and Predicted Bridge Response—Bridge 211.............................75

Figure 3.30: Measured and Predicted Bridge Response—Bridge 222.............................77

Figure 3.31: Comparison of Maximum Thermal Movements at Abutment Top...............80

Figure 3.32: Comparison of Maximum Thermal Movements at Abutment Bottom.........80

Figure 3.33: Comparison of Maximum Girder Bending Moment....................................81

Figure 3.34: Comparison of Maximum Girder Axial Force...82

Figure 4.1: Typical Bridge Construction Timeline....95

Figure 4.2: Typical Cross Section for Parametric Study....96

Figure 4.3: Backfill Height Parameter....97

Figure 4.4: Designed Girder Cross-section....98

Figure 4.5: Backfill Pressure versus Displacement of Abutment....100

Figure 4.6: Subgrade Modulus from Field Tests....101

Figure 4.7: Rotational and Lateral Pile Capacity....103

Figure 4.8: Construction Temperature Simulation Cases....105

Figure 4.9: Long-term Influence of Construction Temperature....105

Figure 4.10: Displacement Shifting due to Construction Temperature....106

Figure 4.11: Time-dependent Strain (L = 18.3 m)....108

Figure 4.12: Time-dependent Strain (L = 30.5 m)....109

Figure 4.13: Critical Responses....110

Figure 4.14: Girder Axial Force....112

Figure 4.15: Girder Bending Moment at the Mid-span of the Exterior Span....115

Figure 4.16: Girder Bending Moment at Abutment....118

Figure 4.17: Pile Lateral Force....122

Figure 4.18: Pile Bending Moment....125

Figure 4.19: Pile Head Displacement....127

Figure 4.20: Abutment Displacement at Centroid of Superstructure....129

Figure 4.21: Correlation of Abutment Displacement....130

Figure 4.22: Correlation between Prediction Models and Numerical Method....135

Figure 5.1: Probabilistic Analysis Procedure....139

Figure 5.2: Concrete Elastic Modulus vs. Concrete Compressive Strength I.................144

Figure 5.3: Soil-Pile Interaction Stiffness Definition..148

Figure 5.4: Temperature Variation in MCS..152

Figure 5.5: Temperature Gradient Distribution...154

Figure 5.6: Time-dependent Strain in MCS...156

Figure 5.7: Temperature Survey During Construction...157

Figure 5.8: Bridge Temperature and Backwall Placement Date Distribution................158

Figure 5.9: Monte Carlo Simulation Procedure...160

Figure 5.10: Determination of Required Number of Simulations Based on COV Testing...161

Figure 5.11: Probability Plots of Bridge Compressive Axial Force...............................166

Figure 5.12: CDFs of Bridge Compressive Axial Force...167

Figure 5.13: Histograms of Bridge Compressive Axial Force.......................................168

Figure 5.14: Probability Plots of Bridge Tensile Axial Force..170

Figure 5.15: CDFs of Bridge Tensile Axial Force...171

Figure 5.16: Histograms of Bridge Tensile Axial Force...172

Figure 5.17: Probability Plots of Maximum Positive Bridge Moment...........................175

Figure 5.18: CDFs of Maximum Positive Bridge Moment..176

Figure 5.19: Histograms of Maximum Positive Bridge Moment...................................177

Figure 5.20: Probability Plots of Maximum Negative Bridge Moment..........................179

Figure 5.21: CDFs of Maximum Negative Bridge Moment...180

Figure 5.22: Histograms of Maximum Negative Bridge Moment..................................181

Figure 5.23: Probability Plots of Maximum Pile Lateral Force......................................184

Figure 5.24: CDFs of Maximum Pile Lateral Force..185

Figure 5.25: Histograms of Maximum Pile Lateral Force...186

Figure 5.26: Probability Plots of Maximum Pile Moment..188

Figure 5.27: CDFs of Maximum Pile Moment..189

Figure 5.28: Histograms of Maximum Pile Moment...190

Figure 5.29: Probability Plots of Maximum Pile Head Displacements..........................193

Figure 5.30: CDFs of Maximum Pile Head Displacement..194

Figure 5.31: Histograms of Maximum Pile Head Displacement...................................195

Figure 5.32: Probability Plots of Maximum Compressive Stress at the Top Fiber.........197

Figure 5.33: CDFs of Maximum Compressive Stress at the Top Fiber..........................198

Figure 5.34: Histograms of Maximum Compressive Stress at the Top Fiber................199

Figure 5.35: Probability Plots of Maximum Tensile Stress at Girder Bottom Fiber.......202

Figure 5.36: CDFs of Maximum Tensile Stress at Girder Bottom Fiber........................203

Figure 5.37: Histograms of Maximum Tensile Stress at Girder Bottom Fiber..............204

Figure 6.1: Stress in Prestressed Concrete Girder...208

Figure 6.2: Load Combination Development Procedure...209

Figure 6.3: Relationship among Mean, Design and Factored Resistance or Load..........210

Figure 6.4: Vehicle Live Load...213

Figure 6.5: Reliability Analysis Procedure...217

Figure 6.6: Service I Limit State Reliability Indices for Permanent Loads....................220

Figure 6.7: Service I Limit State Reliability Indices for All Loads...............................220

Figure 6.8: Load Factors for Service III Limit State...223

Figure 6.9: Strength I Limit State Reliability Indices..225

Figure 6.10: Partial Safety Factor Calibration Procedure..226

Figure 6.11: Analysis Boundary Conditions..229

Figure 6.12: Load Factors for Thermal Loads (Simple Support)...................................229

Figure 6.13: Proposed Load and Resistance Factors (Simple Support)...........................230

Figure 6.14: Reliability Indices for Ratio of *IAB* to *DC*...231

Figure 6.15: Reliability Indices for IABs with respect to Boundary Condition..............232

Figure 6.16: Load Factors for Thermal Loads (Fix End Support)..................................233

Figure 6.17: Proposed Load and Resistance Factors (Fixed End Support).....................234

LIST OF TABLES

Table 2.1: Thermal Expansion Coefficients and Temperature Range....17

Table 2.2: Summary of Longest IAB Built and State Limit....18

Table 2.3: Influence of Foundation Type on Superstructure Stress....24

Table 2.4: Reliability Index (β) and Probability of Failure (P_f)....35

Table 2.5: Statistics of Bridge Resistances....40

Table 2.6: Statistics of Bridge Loads....41

Table 3.1: Field tested IABs....45

Table 3.2: Deterministic Properties of Bridge Materials....47

Table 3.3: Transformed Superstructure Section Properties....47

Table 3.4: Construction Joint Reinforcing Details....58

Table 3.5: Coefficients of Input Temperature Curve for Equation 3.1....69

Table 4.1: Parametric Study Cases....84

Table 4.2: Deck Slab Concrete Placement Date of Four Field Tested IABs....93

Table 4.3: Integral Backwall Placement Date of Field Tested IABs....94

Table 4.4: Backfill Properties and Range Determination....99

Table 4.5: Soil Layer Properties and Range Determination....102

Table 4.6: Temperature Gradient....107

Table 4.7: Maximum Combined Stresses of Axial Force and Bending Moment....119

Table 4.8: IAB Response Prediction Models....132

Table 4.9: IAB Stress Response Prediction models....134

Table 5.1: Published Concrete Elastic Modulus Statistics....144

Table 5.2: Statistics for Backfill Soils....146

Table 5.3: Soil Layer Properties and Range Determination....146

Table 5.4: Temperature Statistics....150

Table 5.5: Statistics for Concrete Thermal Expansion Coefficient....153

Table 5.6: Temperature Gradient Statistics....154

Table 5.7: Statistics for Creep and Shrinkage....155

Table 5.8: Statistics for Bridge Compressive Axial Forces....169

Table 5.9: Statistics for Bridge Tensile Axial Forces....173

Table 5.10: Statistics for Maximum Positive Bridge Moments....178

Table 5.11: Statistics for Maximum Negative Bridge Moments....183

Table 5.12: Statistics for Maximum Pile Lateral Forces....187

Table 5.13: Statistics for Maximum Pile Moments....191

Table 5.14: Statistics for Maximum Pile Head Displacements....196

Table 5.15: Statistics for Maximum Compressive Stresses at the Mid-span of the Exterior Span at the Top Fiber....200

Table 5.16: Statistics for Maximum Tensile Stresses at the Mid-span of the Exterior at the Bottom Fiber....205

Table 6.1: Dead Load Statistics....212

Table 6.2: Live Load Statistics....212

Table 6.3: Thermal load Statistics....214

Table 6.4: Statistics for Resistance....214

Table 6.5: Partial Safety Factors for β_T = 3.5 (HL-93 Load)....227

Table 6.6: Partial Safety Factors for β_T = 3.5 (HS-25 Truck + Lane Load)....227

NOTATIONS

B = backfill stiffness

CDF = cumulative density function

CI = confidence interval

COV = coefficient of variation

CR = concrete creep

E_c = elastic modulus of concrete

f_{DC} = stress due to dead load of bridge components

f_{DW} = stress due to dead load of wearing surface

f_{LL+IM} = stress due to vehicular live load including truck impact

f_{IAB} = stress due to thermal loading in an integral abutment bridge

f_c' = 28 day concrete compressive strength

f_r = modulus of rupture for concrete

F_y = yielding stress of steel material

$g(.)$ = limit state function

H = backfill height

IAB = integral abutment bridge

k_{cyclic} = soil modulus based on cyclic test

k_h = coefficient of lateral subgrade reaction modulus

k_{ref} = experimentally derived coefficient of lateral subgrade reaction modulus

L = bridge length

LHS = Latin hypercube sampling

LRFD = load and resistance factor design

MCS = Monte Carlo simulation

M_{DC} = moment due to dead load of bridge components

M_{DW} = moment due to dead load of wearing surface

M_{LL+IM} = moment due to vehicular live load including truck impact

M_{IAB} = moment due to thermal loading in an integral abutment bridge

M_t = moment due to thermal stresses

p = pile lateral force

PDF = probability density function

P_t = axial force due to thermal stresses

R_n = nominal design resistance

RGIV = randomly generated input variable

RGOV = randomly generated output variable

SE = settlement

SH = concrete shrinkage

T = temperature

TU = uniform temperature

TG = temperature gradient

WSD = working stress design

X = random variable

x^* = design point

y = pile lateral displacement

z = vertical soil depth

z_{ref} = vertical reference depth of soil layer

Δl = expanded length

ΔT = temperature changes

α = thermal expansion coefficient

β = reliability index

β_T = target reliability index

Φ = standard normal cumulative distribution function

ϕ or ϕ_f = friction angle of soil material

ϕ_R = resistance factor

γ or γ_{soil}= soil total weight or buoyancy weight when under ground water table

γ_i = load factor for load i

λ_i = bias factor (ratio of mean to nominal value) of i

μ_i = mean value of i

η = constant relating to load factor and reliability exceedance

σ_t = longitudinal thermal stress

ACKNOWLEDGEMENTS

First, I thank my dissertation advisor, Dr. Jeffrey A. Laman, for his insight, encouragement and constructive criticism throughout my course of this study. He showed me a role model that I pursue in all aspects. Invaluable help was also provided by my committee members. Dr. Peggy A. Johnson provided precious help in statistical analysis and modeling. Dr. Panagiotis Michaleris provided valuable insight and advice in numerical modeling. Dr. Mian C. Wang and Dr. Angelica M. Palomino provided helpful advice in soil mechanics.

This study was partially supported by the Pennsylvania Transportation Institute and the Pennsylvania Department of Transportation. I am thankful for their financial support.

Finally, my most sincere thanks goes to my wife, Jung Yeon Park. Without her patience, love and encouragement, this accomplishment would not have been possible. I am also thankful to my family and Jung Yeon's family for their love and support.

Chapter 1

INTRODUCTION

1.1 Background

Integral abutment bridges (IABs) have become a preferred design choice for bridge construction. An IAB is a type of bridge without a system of expansion joints and constructed as a rigid connection between superstructure and substructure. At least 30 states have constructed more than 10,000 IABs throughout the United States over the past 30 years. IABs have specific benefits: elimination of bearings, reduced deterioration due to deicing chemicals, impact loads and substructure costs, and improved riding quality, construction procedures and structural continuity to resist seismic excitation and overloads [11, 51].

Since bridge temperature variation influences bridge expansion and contraction related to soil-structure interaction and material nonlinearity, IABs are difficult to analyze and design. In the typical single span bridge, presented in Figure 1.1, the superstructure and substructure are integrally constructed, without expansion joints, as a rigid connection. This connection leads most loads from the superstructure to be transferred to abutments and pile foundations. To accommodate superstructure expansion and contraction due to thermally induced loads, backfill pressure, creep and shrinkage, IABs use relatively flexible pile foundations—such as a single row of pile foundation. IAB designs also incorporate weak-axis bending orientation of piles and very loose sand or gravel fill for pre-augered piles. However, the soil-structure interaction is one of the factors that creates difficulty for analysis and design of IABs, and therefore, solid design guidelines do not presently exist.

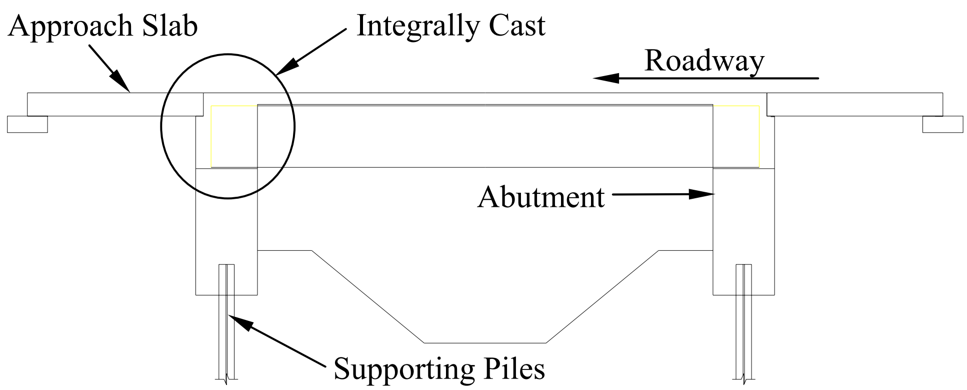

Figure 1.1: Typical Single Span Integral Abutment Bridge

Although *Load and Resistance Factor Bridge Design Specifications* by *the American Association of State Highway and Transportation Officials* (AASHTO LRFD) [4] merely provides design guidelines for IABs, those specifications are not solid design imperatives but only overall, general design concepts. Although boundary conditions and subjected loading scenarios of IABs are obviously different from conventional bridges, load combinations characteristic of IABs do not exist. Thorough research of IAB analysis and design has occurred over many years, but still design specifications for idealized IABs vary from state to state [10]. A large part of current design specifications and procedures for IABs are similar to conventional bridges, and some design procedures are inconsistent with current bridge design philosophy—not LRFD but working stress design (WSD). Therefore, load combinations and IAB design guidelines and specifications are essential to improve design and analysis of IAB structures.

Current AASHTO LRFD [4] bridge design code is a reliability-based design approach with which IAB design must be consistent. Based on the reliability analysis, the bridge code represents a widely-accepted requirement to attain minimum safety levels and to avoid structural and/or functional failures. levels are classified as [92]:

> **Level I**: Safety factors—ratio of design resistance to design load, or partial safety factors—load and resistance factors are used in deterministic design formulae.
>
> **Level II**: The actual reliability level is compared to the target reliability level or other safety-related parameters.
>
> **Level III**: A full reliability analysis is performed for a specific structure under various loading scenarios. The actual reliability is compared to the optimized reliability level.
>
> **Level IV**: The total cost of the design is compared to the optimized total design cost so that the final design maximizes the benefits and minimizes the costs.

Current AASHTO LRFD bridge design code uses deterministic design formulae incorporated with partial safety factors derived using reliability analysis. This design code, therefore, incorporates uncertainties in materials, professions and analyses.

As the first step to develop IAB LRFD load combinations, the present study develops a nominal numerical modeling method to predict IAB behavior. The results also compares with field collected data from four selected bridges. To understand IAB behavior during the expected bridge's 75-year life, the numerical model considers soil-structure interactions, material nonlinearity, and thermal gradient in the superstructure for loads and boundary conditions. However, 3D models considering all the above IAB characteristics require long computation time and huge data storage space because of bridge complexity. Therefore, this study develops a condensed nominal finite element model. A parametric study using the nominal numerical model establishes key parameters and their strengths. In addition, the parametric study results establish IAB response prediction models to accommodate a nominal design procedure and load models for reliability analysis. To account uncertainties in material properties, Monte Carlo simulation is performed and the results establish IAB response statistics. Finally, the present study performs the code calibration procedure by Nowak [91] to establish load combinations in LRFD format which is consistent with current AASHTO LRFD (2008) [3].

1.2 Problem Statement

IAB behavior and responses include many uncertainties. In addition, removing expansion joints in the bridges causes many difficulties in design and analysis due to complexity of soil-structure interactions and nonlinear material behavior. The additional loads on IABs include uncertainties of temperature variation, creep and shrinkage and backfill pressure on backwall and abutment which causes superstructure length and stress variations. Also, additional resistances are present in IABs: passive backfill pressure against bridge expansion and lateral resistance of supporting piles against bridge contraction. However, IAB behavior is concatenated to each bridge component behavior, and therefore, development of nominal IAB design in a closed-form solution requires extreme efforts. Therefore, a practical IAB design method is necessary.

Current IAB design practice requires to be consistent with sophisticated design practice AASHTO LRFD. While bridge designers must be allowed to consider inherent uncertainties of bridge structures to provide a minimum safety level, currently they use specific values for bridge design loads and resistances that are difficult to estimate accurately. However, IABs have uncertainties: (1) properties and lateral reactions of backfills and soil around supporting piles; (2) material properties of concrete members; (3) thermally induced superstructure and abutment displacement; and (4) creep and shrinkage of concrete members. Reliability-based design codes incorporate each bridge design with a consistent safety level without an additional detailed reliability analysis. Therefore, load combinations, specifically considered for IABs, must be established to provide a consistent safety level.

1.3 Scope

The present study focuses on short and medium length highway IABs. Bridges have cast-in-place deck on four prestressed concrete girders. A typical cross section appears in Figure 1.2. The bridge dimensions covered by this study ranges from 18 to 120 m (60 to 400 ft) of total bridge length, and 3 to 18 m (10 to 20 ft) of abutment height. The bridge configuration is symmetric to the bridge centerline and does not include skewed end supports. Typical maximum and minimum soil properties from published literatures [32, 33] were adopted with a single row of weak-axis oriented HP pile foundations and horizontally parallel soil layers under abutments. The soil property changes due to weathering and/or aging and ground water table variations were not considered in this study.

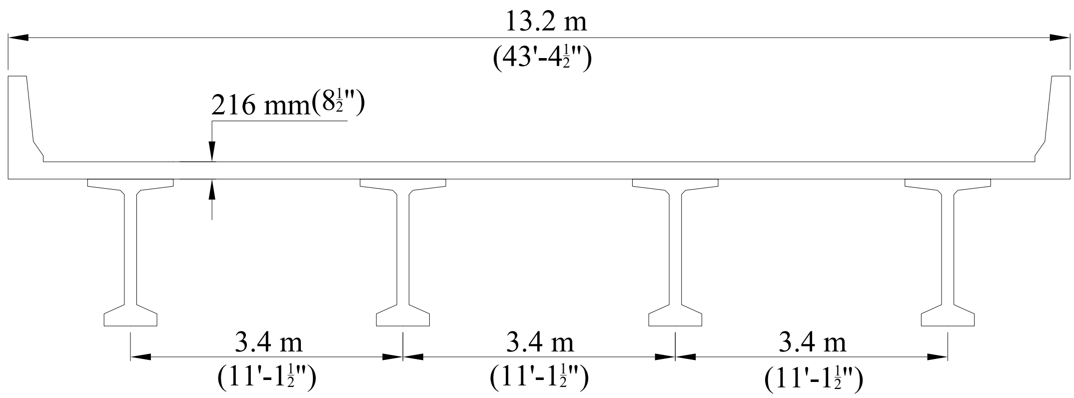

Figure 1.2: Typical Cross Section

The present study utilized 2D nominal numerical models by Kim [73], including soil-structure interactions, material nonlinearities, and concrete creep and shrinkage. Half of an IAB numerical model built. Condensed pile foundations were developed and utilized in the numerical simulation. Four actual IABs, in Port Matilda, PA, are used to calibrate the numerical modeling method.

For IAB response prediction models, the present study performed 243 sets of a parametric study using the nominal numerical model. Each of the parametric study was regarded as to representing nominal IAB behavior and responses. The numerical model considered superstructure temperature variation, temperature gradient of superstructure, and backfill pressure during an expected bridge life, 75 years. To form nominal response prediction model, the results of the parametric study were used based on regression analyses.

The present study utilized Monte Carlo simulation using Latin Hypercube sampling to form IAB response distributions and statistics. Each of the simulation considered bridge dimensions, span length and abutment height, to be deterministic parameters. Backfill soil properties, soil stiffness around piles, superstructure temperature variation, temperature gradient, superstructure concrete creep and shrinkage, superstructure material properties, thermal expansion coefficient, and bridge construction temperature and date were assumed random variables. IAB resistance model were considered the same as the conventional bridges.

The present study utilized code calibration procedure by Nowak [91] to develop new load combinations for IABs. The load combination considered only Service I and III for concrete compression and tension, and Strength I for ultimate strength condition. Reliability indices of the load combinations for various loading scenarios were derived using Rackwitz-Fiessler procedure and compared to the target reliability index (3.5), consistent with AASHTO LRFD [3].

1.4 Objectives

The objectives of the present study are to develop a condensed numerical modeling method for IABs and to establish a load combination based on reliability analysis. The main objectives of this study can be summarized as:

- Develop a condensed nominal numerical model for a 75-year bridge life simulation that includes soil-pile interaction, soil-abutment interaction, construction joint effects, soil material nonlinearity, creep and shrinkage of superstructure, thermal gradient of superstructure, and ambient temperature load.
- Identify sensitivities and influences of key parameters that significantly affect IAB superstructure stress changes and abutment displacement.

- Develop IAB response prediction models for: (1) girder axial force; (2) girder bending moment; (3) pile lateral force; (4) pile moment; and (5) pile head/abutment displacement.
- Develop a nominal IAB load and resistance model that can be used in practical design procedure.
- Establish statistical parameters and distribution types for IAB responses.
- Establish load combinations for IABs consistent with current AASHTO LRFD code.

1.5 Organization

This thesis consists of 7 chapters. Chapter 2 discusses current design practice, published standard analysis methods for IABs and IAB components, reliability methods. Chapter 3 presents the development of nominal numerical modeling methods and field data comparisons. Chapter 4 includes both a parametric study using the nominal numerical model and development of IAB response prediction models. Chapter 5 discusses development of probabilistic models for Monte Carlo simulation. Chapter 6 establishes statistics of thermal load models and presents code calibration procedure. Chapter 7 provides summary of this study, conclusions derived from each chapter. Graphic overview of the present study appears in Figure 1.3.

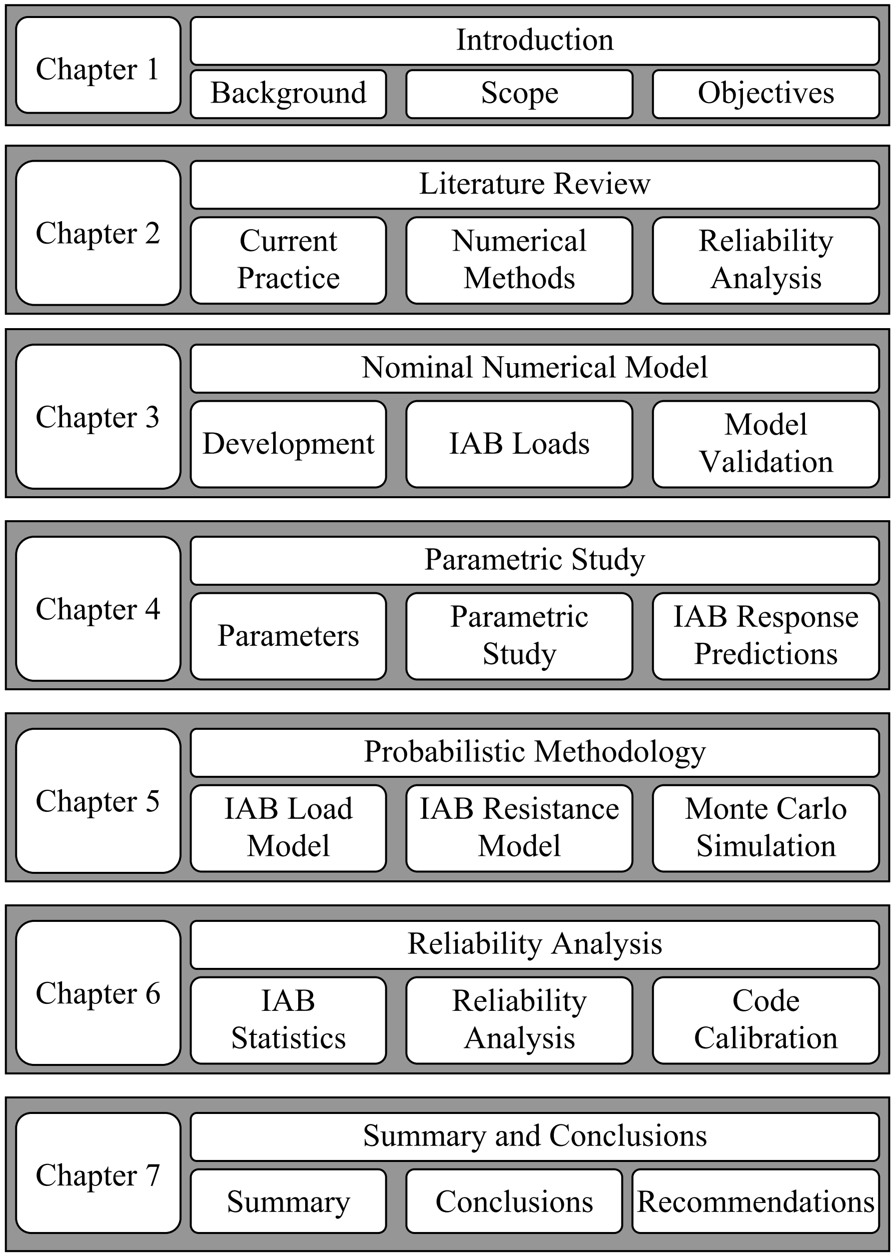

Figure 1.3: Organizations of the Present Study

Chapter 2

LITERATURE REVIEW

2.1 Introduction

This chapter discusses current IAB design practices and previous IAB research. Structural reliability methods and code calibration procedure to establish load combinations are also studied. This chapter provides the theoretical background of nominal numerical modeling methodologies and numerical reliability methods.

A discussion of current IAB design specifications establishes general IAB design concepts and practices. National standard IAB design specifications do not currently exist, and therefore, design and analysis of IABs vary from state to state. Thus, state agencies have developed their own design and analysis procedures based on past IAB construction experiences rather than theoretical and experimental studies [77]. A summary of design and construction guidelines by state agencies is discussed, including thermal movements, abutment height, pile orientations and pile driving details.

The following sections discuss numerical modeling methodologies to establish nominal numerical models, which include abutment-backfill interaction, soil-pile interaction and time-dependent effects of concrete. Also considered are analytical and numerical analysis methods, critical design and analysis parameters of IABs, including thermal movement, time-dependent effects, abutment-backfill interaction, and pile-soil interaction. This chapter also investigates published numerical methods to incorporate additional design considerations for numerical characterization of soil-pile interaction.

A discussion regarding reliability methodology and statistics derived from the previous research follows. Reliability analysis is essential for identifying bridge safety levels in accordance with a predetermined reliability index, thus, the rationale for reliability analysis methods discussion and code calibration procedures to establish specialized load combinations for IABs follow.

2.2 Current Design Specifications

This section discusses current design specifications of AASHTO and state agencies. Current IABs with capped-pile and stub abutments are the most popular design type and constitute more than 9,773 structures over 30 states, Canadian provinces and Europe [27, 77]. However, no standard analysis and design methods have yet been developed.

Superstructure Design

AASHTO LRFD (2008) [4] is the most commonly accepted bridge design code in the United States and provides performance criteria for a general IAB design. Section 11.6.1.3 of AASHTO LRFD states:

> Integral abutments shall be designed to resist and/or absorb creep, shrinkage, and thermal deformations of the superstructure.
>
> Movement calculations shall consider temperature, creep, and long-term prestress shortening in determining potential movements of abutments.

The AASHTO LRFD does not stipulate any detailed design or analysis methods. In addition, special load combinations for IABs are not given even though boundary conditions of IABs are different from conventional jointed bridges. However AASHTO LRFD considers force effects due to superimposed deformations (section 3.12) using load combinations as appearing in Table 1.2.7.6-1 of AASHTO LRFD, which considers uniform temperature (*TU*), temperature gradient (*TG*), shrinkage (*SH*), creep (*CR*), settlement (*SE*). In addition to these force effects, permanent loads of lateral earth pressures (*EH*) are of concern because backfill earth pressure translates into superstructure axial loads due to the absence of expansion joint systems.

The variation of uniform temperature or ambient temperature is the primary force inducing IABs' expansion and contraction. The thermally induced bridge movements change abutment and superstructure axial stresses. However, AASHTO LRFD load factors for uniform temperature change does not consider the axial loads in bridge superstructures and theoretical backgrounds including derivations of the load factor and sample regional information is less than complete.

Creep and shrinkage of IABs can be different from conventional bridges. Constraints at both ends of a superstructure may reduce creep and shrinkage but simultaneously permanent axial forces due to lateral earth pressure accelerate creep and shrinkage. AASHTO does not provide any methods to consider the creep and shrinkage influence on IABs. AASHTO Section 8.5.4 indicates only 0.0002 as the coefficient of shrinkage for concrete members while this coefficient must be separated from the conventional bridge.

Some state agencies developed their own guidelines: *Design Manual Part 4* of Pennsylvania Department of Transportation (PennDOT DM4) [110] includes IAB design specifications. Load Combination Table (Table 1.2.7.6-1) for IABs in PennDOT DM4 specifies that load combinations for IABs are the same as for AASHTO LRFD load combinations for conventional bridges. Regarding superstructure design of IABs, Penn DOT DM4 Section 1.3 of Appendix G states:

> The superstructure shall be designed similar to conventional superstructures with expansion joints. The fixity developed as a result of rigidly connecting the superstructure to the abutments and the piers shall not be considered in the design of the superstructure.

Section 11.6.1.6 in the New York State Department of Transportation (NYSDOT) *Bridge Manual* [97] suggests two design methods:

> Approximate design method: the superstructure support members are assumed to be simply supported at the abutment end for design purposes.
>
> Refined design method: the effects due to skew, curvature, thermal expansion of the superstructure, reveal, and grade are considered. It may be necessary to analyze the superstructure and abutment as a rigid frame system by using either a three dimensional finite element model or a two dimensional frame model.

Rigid connections of girders to abutments reduce girder bending moments at mid-span and induce negative moments at the connections. Thus, PennDOT guidelines as well as the NYSDOT approximate design method are conservative approaches at mid-span, but ignore the potential effects of negative moments at supports.

Backfill Pressure

Generally, the resistance of abutment backfills and supporting pile foundations determine the amount of IAB expansion and contraction, respectively [30]. Passive backfill pressure is the most commonly used for abutment and/or backwall design although most states have no special treatment to reduce backfill pressure described in AASHTO LRFD Section 11.6.1.3. However, some state agencies do consider backfill pressure based on abutment size or girder spacing, and other states exclude backfill pressure in their designs. Axial loads on superstructure and/or abutments due to backfill pressure are one of the critical differences between IABs and conventional jointed bridges. Thus, some state agencies consider this backfill pressure but most of them are only for passive pressure. California Department of Transportation (CALTRAN) [28] and Alaska Department of Transportation and Public Facilities (AKDOT) [2] assume passive resistance of 53 MPa (7.7 ksf) considering seismic loadings. North Dakota [95] assumes 6.9 MPa (1 ksf) on integral abutments. PennDOT DM4 Section 1.3 recommends considering the lateral earth pressure from backfills:

> Compressive axial load equal to the passive earth pressure on the abutment shall be considered in the design of the superstructure.

This provision limits the application only when compressive stress at the ends of prestressed girders in conjunction with deep depth (≥ 6'-0") and wide girder spacing (≥ 12'-0"). However, this provision does not consider a bridge length that determines the amount of IAB movements, which is equal to backfill passive level. In field collected data [63, 79, 80, 105], lateral backfill pressure exhibited fluctuating variation in accordance with bridge temperature changes and abutment displacements. Moreover, an IAB with a girder depth shallower than 6'-0" and spacing less than 12'-0" also produced lateral earth pressures close to the passive earth pressure. Therefore, the backfill pressure must be considered in the IAB design and analysis process.

Thermal Movement

Thermal movements due to temperature changes significantly influence bridge behavior and changes in superstructure stress. The amount of thermal movements is largely dependent on thermal expansion coefficient and total span length. Some states, therefore, specify the limits of total bridge length and have developed thermally induced expansion estimation as a design guideline for IABs. For precast concrete girder bridges, Tennessee has the longest length limit of 358m (1,175') with 51mm (2") of maximum allowable thermal movement, while AASHTO LRFD [4] specifies 38mm (1.5") horizontal movement for a typical foundation with driven piles. For steel girder and cast-in-place concrete bridges, Colorado [32] allows the longest length limit of 348m (1,044') and 290m (952') with 102mm (4") allowable movement.

The following paragraphs discuss limits of thermal movement of IABs and built information based on published literature [77, 79].

CALTRAN [28] recommends not using integral abutments when movement at the abutment joints is greater than 25 mm (1"). If movement at the abutment joint exceeds 13 mm (0.5"), an approach slab must be used. West Virginia Department of Transportation (WVDOT) [132] also limits 51 mm (2") allowable abutment movement rather than bridge length.

In Maine [83], the maximum length allowed is up to 90 m (295') for steel bridges, 150 m (490') for cast-in-place concrete. An approximat calculation for thermal movement is assumed to be 1.04 mm/m span length for steel bridges and 0.625 mm/m span length for concrete bridges.

North Dakota [95] has separate length limitations for skewed and non-skewed IABs. For skewed bridges, the maximum limit length is 122.0 m (400') multiplied by the cosine of the skew angle. For straight bridges, the maximum length is 122.0 m (400'). Virginia also specifies different total bridge length as per skew angle: steel girder — 91.5 m (300') for 0° skew and 46.8 m (150') for 30° skew; precast concrete — 152.5 m (500') for 0° skew and 79.3 m (260') for 30° skew. The total thermal movement allowed is limited to 1.5% of the total bridge length. In addition, girders, regardless of the material, are designed with the assumption that the ends are free to rotate.

Arizona Department of Transportation (ADOT) discontinued using integral abutments and Maryland (MDOT) typically uses integral abutments only for very short bridges that are less than 18.3 m (60').

AASHTO Specifications 10.2.2 provides the thermally induced expansion estimation Eq. 2.1 for one abutment of the bridge:

$$\Delta l = \frac{\alpha \cdot \Delta T \cdot L}{2} \tag{2.1}$$

where, Δl is the expanded length;
α is thermal expansion coefficient in Table 2.1 (AASHTO 3.16);
ΔT is temperature changes in Table 2.1 (AASHTO 3.16), and
L is span length.

Table 2.1 provides the application range of Eq. 2.1. However, Eq. 2.1 represents free expansion of a prismatic and homogeneous structure and the specified temperature changes are typically conservative for steel and not conservative for concrete members [105].

Table 2.1: Thermal Expansion Coefficients and Temperature Range

Parameter		Steel Girder	Concrete Girder
Thermal Expansion Coefficients (α)		11.7e-6/°C (6.5e-6/F°)	10.8 e-6/°C (6.0e-6/F°)
ΔT	Moderate Climate	-17.8 to 48.9 °C (range 0 to 120 F°)	rise 16.7 °C and fall 22.2 °C (rise 30 F° and fall 40 F°)
	Cold Climate	-34.4 to 48.9 °C (range -30 to 120 F°)	rise 19.4 °C and fall 25.0 °C (rise 35 F° and fall 45 F°)

For the state design guidelines, Table 2.2 presents the total bridge length limitations by American state agencies and Canadian provinces and IAB build information based on the surveys by Kunin and Alampalli [77] and Laman *et al.* [79]. As aforementioned, the IAB length limit varies state to state. The longest steel girder IAB of each state varies from 24.4 m (80 ft) to 318.4 m (1,045 ft) while the state thermal movement limit varies from 24.4 m (80 ft) to no-limit. The longest precast concrete girder IAB of each state varies from 15.9 m (52 ft) to 358.4 m (1,176 ft) while the state thermal movement limit varies 18.3 m (60 ft) to 224.0 m (735 ft).

Table 2.2: Summary of Longest IAB Built and State Limit

State	Thermal Movement (mm)	Steel Girder		Precast Concrete Girder		Cast-in-place Concrete Girder	
		Built (m)	Limit (m)	Built (m)	Limit (m)	Built (m)	Limit (m)
AK	-	-	-	41.2	61.0	-	-
AZ	-	-	-	-	-	-	-
AR	-	90.9	91.5	-	91.5	-	-
CA	13	-	31.1	-	50.9	122.0	50.9
CO	102	318.4	91.5	339.2	183.0	290.4	152.5
GA	NL*	91.5	NL	-	NL	125.1	NL
IL	NL	61.0	83.9	91.5	114.4	36.6	114.4
IA	LBL**	82.4	-	152.5	152.5	41.2	152.5
IN	-	-	76.2	-	91.4	-	61.0
KS	51	136.8	91.5	126.4	152.5	177.6	152.5
KY	NL	89.1	91.5	122.0	122.0	31.7	122.0
ME	95	57.3	90.0	45.8	150.0	29.3	150.0
MD	25	-	-	15.9	18.3	-	-
MA	-	106.8	99.1	84.8	99.1	43.9	99.1
MI	NL	-	NL	147.9	NL	-	NL
MN	NL	53.4	61.0	53.4	61.0	30.5	61.0
NV	25	77.8	76.3	33.6	122.0	84.2	122.0
NH	38	45.8	45.8	24.4	24.4	-	-
NY	LBL	93.3	140.0	68.3	140.0	-	140.0
ND	LBL	122.0	122.0	122.0	122.0	48.8	48.8
NS	-	-	-	38.0	-	-	-
OK	-	-	91.5	91.5	122.0	-	-
ON	-	-	100	-	100	-	100
OR	NL	-	NL	335.5	NL	-	NL
PA	51	122.0	120	183.0	180.0	-	-
QC	NL	-	-	78.1	78.1	-	-
SD	LBL	112.9	106.8	209.2	213.5	106.8	231.5
TN	51	175.4	130.8	358.4	244.0	189.1	244.0
VT	LBL	24.4	24.4	-	-	-	-
VA	38	97.6	91.5	235.5	152.5	-	-
WA	NL	-	-	183.0	106.8	61.0	61.0
WV	51	97.6	-	137.3	-	33.6	-
WY	50	100.0	100.0	127.0	130.0	99.0	100.0
Max.	NL	318.4	NL	358.4	NL	290.4	
Min.	13	24.4	24.4	15.9	18.3	29.3	

NS: Nova Scotia, ON:Ontario, QC: Quebec
* No Limit; ** Limited by length

Pile Design

In IABs, the pile cap is integral with the superstructure and the supporting piles causes the bridge to behave as a frame rather than the conventional beam. While typical IAB pile details are fixed-head connections to abutments, the connection type may cause high pile moments [46]. Most states use steel H- or HP- piles with weak axis orientations. Some states combine predrilled oversized holes to relieve pile bending stresses. In addition, half of states specify pile design guidelines purely for axial loads. For instance, CALTRAN [28] and South Dakota (SDDOT) [118] use vertical loads to determine the number of piles. California assumes the lateral load for steel piles is 66.7 kN (15 kips) per a pile.

The design practices discussed above are largely based on past IAB construction experience; however, the assumptions and design details need validation through experiments and analysis to achieve efficient and reliable design.

2.3 Previous IAB Research

IAB designs are a very complex because bridge act like a frame rather than a beam. In addition, the frame actions of IABs are partially restrained by backfill and supporting piles. Hence, the secondary loads, such as creep, shrinkage, thermal movement, temperature gradient and earth pressure, are more prevalent effects on IABs [125]. Despite the many additioanal influences, reliability studies of IABs have not been conducted.

Following is a discussion regarding previous research of IABs.

Time-dependent Behavior

Many researchers monitored actual IABs to understand the IAB behavior [30, 34, 52, 96, 126]. The results of the research demonstrated the significant influence of thermal movements on abutment displacements and superstructure stress variations. An abutment displacement comparison between the free thermal expansion prediction (Eq. 2.1) and field measurements revealed that restraints from backfill and supporting piles are influencial and the bridge response is time-dependent and irreversible.

The time-dependent effects of creep, shrinkage and temperature on composite superstructures as well as soil-structure interactions are the main issues in IABs. Creep of concrete in IABs helps reduce bending stress in superstructures while shrinkage induces tension stress [125]. Both AASHTO LRFD [4] and ACI209 [6] provide different equations for creep and shrinkage estimation. Arockiasamy [12] developed IAB numerical models with restraint at abutments using AASHTO LRFD and ACI creep and shrinkage models. The age-adjusted effective modulus (AAEM) [58] was used to account for variations in concrete properties. The results proved that the influence of creep and shrinkage is significant on superstructure stress variation.

In Huang's research [63], time-dependent movement using 150 instruments closely monitored an IAB for 7 years. Stress variation of the superstructure was numerically and experimentally demonstrated as the result of thermal movement, creep and shrinkage of composite girders. Laman *et al.* [79, 80] and Pugasap [112] collected long-term behavior of four IABs, simulated and predicted using complex 3D hysteresis-based numerical models. The research revealed that long-term abutment displacements and stress variations of superstructures and backfills accumulate during 30 years of bridge life. In addition, observations showed that thermal movements of IABs affect superstructure stresses and backfill pressures [37]. Thus, as discussed in the previous section, some states limit the total amount of thermal movement ranging from 13 to 102 mm (0.5 to 4"), and other states limit the total bridge length to control superstructure stresses and backfill pressures. However, the limits and prediction of thermal movements still need more careful scrutiny because IAB behavior has significant uncertainty parameters such as ambient temperature variation, temperature gradient, and soil properties.

Backfill Pressure

Stresses in IABs induced by backfill pressure are not initially significant [125]. However, the backfill pressure should be considered in long-term behavior because the backfill causes abutment-ratcheting behavior. The research by Civjan [30] demonstrated that backfill conditions predominantly affect IAB expansion and pile restraint conditions influence IAB contraction. Earth pressures acting against the abutments correlate with thermal movement of the superstructure and generally are proportional to depth [37]. Thermal movements over a long period causing abutment displacement accumulate and therefore, backfill pressures on IABs increase. A stub type abutment, therefore, is the recommendation to reduce backfill pressure and to provide relative flexibility of the substructure [12].

Backfill pressure variation strongly correlates with soil stiffness supporting piles. Denser backfill properties result in greater abutment rotation and larger backfill pressures, while pile moments with denser backfill are smaller than those with looser backfill.

Due to thermal expansion and contraction of the superstructure, an abutment is continuously subjected to cyclic lateral displacements toward backfill and away from backfill, respectively. When an IAB expands, passive pressure provides lateral restraint. When an IAB contracts, active pressure exerts additional driving pressure on abutments. Active earth pressure (σ'_a) is easily induced by a very small abutment displacement (Δ_a) away from backfill soil [13, 38, 43]. However, movement of the abutment back toward the backfill during the bridge expansion is difficult because the backfill soil behind the abutment resists the expansion. The lateral earth pressure is, therefore, dependent on the amount of displacement toward backfill and passive pressure may occur. Therefore, an IAB analysis and design must consider this backfill pressure variation.

Laterally Displaced Piles

Soil-structure interactions greatly influence IAB behavior because thermal movements of the superstructure displace supporting piles. Pile restraints significantly influence IAB contraction behavior. Piles driven in stiff soils experience higher moments than the moments of piles in soft soils. Thus, less axial load capacity of piles in soft soils would be larger than piles in stiff soils. Field tests and numerical analysis by University of Tennessee demonstrated that the piles in soft soils were capable of supporting a larger axial load than those in stiff soils [68]. All numerical models with high soil stiffness exceeded pile yielding moments. Other numerical models with low soil stiffness buckled, although the considered soil stiffness was not practical. Another research [12, 13] also reported that denser backfills and lower pile restraints reduce pile moments below a pile yielding, regardless of pile types. However, neglecting soil boundaries around piles is inappropriate. Supporting piles, designed according to AASHTO LRFD [4] or American Institute of Steel Construction (AISC) beam-column equations, neglect lateral supports of surrounding soils, and therefore, the design of the piles are extremely conservative [68]. The pile analysis method adopted by Dicleli [38] and Huang [63] is an equivalent cantilever method, as in Figure 2.1, to simplify pile analysis. However, this method does not consider the soil boundaries around piles. Experimental study by Arsoy [13] for steel, reinforced concrete and prestressed concrete piles were conducted to simulate pile behavior in an IAB, while this particular research also neglected soil restraints around pile. However, this research recommended consideration of soil-structure interactions between piles and soils and abutments and backfills during design procedures. To achieve an efficient and accurate design, pile analysis must consider soil-structure interaction.

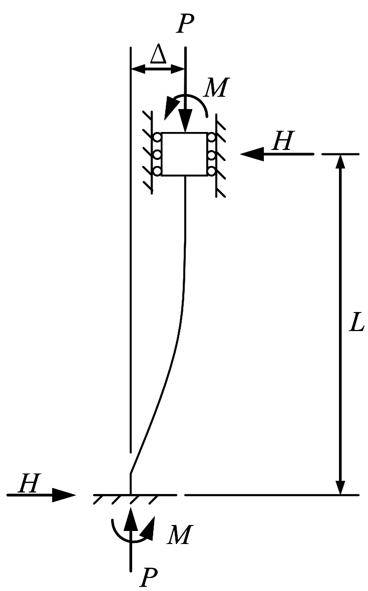

M(Pile moment) = $E_p I_p \phi_p = \dfrac{6 E_p I_p \Delta}{L^2}$

E_p = pile stiffness

ϕ_p = pile head curvature

Δ = Abutment displacement

L (equivalent cantilever length) $= \sqrt{\dfrac{6\Delta}{\phi_p}}$

Figure 2.1: Equivalent Cantilever

Foundation type is influencial on bridge responses [125]. Weak axis oriented piles reduce stresses at the superstructure and make an IAB behave like a simply supported structure. A spread footing with fixed boundaries, therefore, should be avoided. Table 2.3 summarizes the influence of foundation types on superstructure stresses.

Table 2.3: Influence of Foundation Type on Superstructure Stress

Location		Spread Footing	Pile Foundation
Integral connection between backwall and superstructure	Top	• High stresses by DL and LL • CR reduces tensile stress • TG has a significant influence • EP influence is negligible	• DL and LL induce negligible stress • TG has a significant influence
	Bottom	• Highest stresses by DL and LL • CR increases compressive stress • EP influence is negligible	• DL and LL induce negligible stress • TG induces tensile stress
Mid-span	Top	• High stresses by DL and LL • CR reduces compressive stress • EP influence is negligible	• TG induces high tensile stress
	Bottom	• Highest stresses by DL and LL • CR increases compressive stress • EP influence is negligible	• DL and LL induce high stress • TG induces significant tensile stress
Over pier support	Top	• DL and LL induce significant compressive stress • CR reduces tensile stress • Stress by TG relatively smaller • EP influence is negligible	• DL and TG induce significant tensile stress • EP influence is negligible
	Bottom	• Highest stresses by DL and LL • CR increases compressive stress • EP influence is negligible	• DL and LL induce high stress • TG induces significant tensile stress • EP influence is negligible

*DL=dead load; LL=live load; CR=creep; TG=temperature gradient; EP=earth pressure

2.4 Numerical Analysis of IABs

This section investigates and reviews most recent numerical analysis methodologies to simulate IABs. Unlike conventional jointed bridges, IABs encounter additional loads and resistances mostly related to soil-structure interactions. Abutment backfills resist IAB expansion, which results in compression stress in superstructures [52]. To the contrary, supporting piles resist IAB contraction, which causes tension stress in superstructures [38]. Therefore, accurate numerical models need to consider the soil-structure interactions including time-dependent. The following sections discuss numerical modeling techniques to achieve favorable numerical models.

2.4.1 Abutment Backfill Pressure

Abutment-backfill interaction considerably influences IAB behavior [13, 38, 51, 80]. Thermal movement of IABs that pushes the abutment toward backfills and pulls them away from backfills induces lateral backfill pressure changes. Clough and Duncan [31] derived the lateral backfill pressure coefficient as a function of the abutment displacement from experiments and numerical analyses. Typical lateral earth pressure as per the abutment movement appears in Figure 2.2.

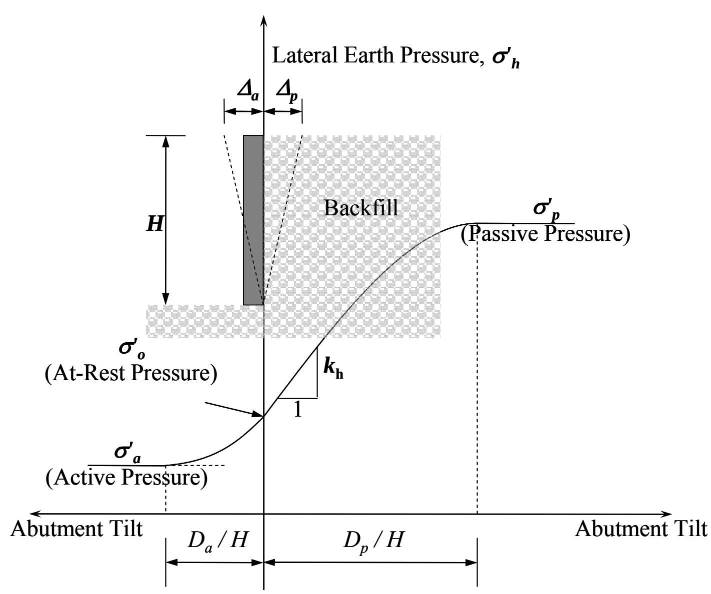

Figure 2.2: Lateral Earth Pressure Variation

When an IAB expands due to temperature increase, resistances of backfills behind abutments may increase to passive pressure that induces significant compressive axial forces on the superstructure. Thus, IAB superstructure design must consider the compressive loads by passive pressure of backfill [45]. To the contrary, the bridge contraction during nocturnal and/or winter may cause the active failure of backfills. However, some state agencies do not consider earth pressure at all in their design specifications and others suggest no special procedures to reduce earth pressure [77].

There are many theories to model the lateral earth pressure variation between active and passive pressure. Faraji *et al.* [51] and Oesterle *et al.* [105] reported Rankine's theory produces good results for abutment-backfill interaction of IABs. The present study adopts Rankine's theory with a linear variation between active and passive pressure.

Horvath [62] argued an inherent problem of IABs as the "ratcheting" effect of abutment displacement. The ratcheting effect maintains that earth pressures of a succeeding year exceed those of a preceding year and accumulates for decades. IABs inevitably experience daily and seasonal temperature changes causing cyclic thermal expansion and contraction of the superstructure. The thermal contraction plus creep and shrinkage of the superstructure is sufficient to cause active pressure in backfill soil [43]. Thus, the backfill tends to slip toward the abutment along the active wedge failure line when the backfill pressure reaches the active pressure. During the succeeding summer season, the significant superstructure expansion causes the backfill earth pressure to approach the theoretical passive pressure. Seasonal effects of these expansions and contractions continue through the design life of IABs and the abutment moves inward. The ratcheting behavior of integral abutments—the unrecoverable displacement—should be considered to predict the abutment displacement. However, most previous IAB research considered unidirectional behavior—non-cyclic loads applied—and prediction and/or numerical methods to incorporate the behavior of accumulated abutment displacements were not investigated for the bridge life.

Behavior of soil material has nonlinearity: force or stress applied to the material is not proportional to displacement or strain of the material. This nonlinear characteristic of soils causes difficulty in analyzing IABs that interact with soils. The thermally induced expansion and contraction of IABs is fully related to the lateral resistance of abutment backfills and surrounding soil around piles. The abutment mass, compared to pile foundation, is dominant so that the ratcheting behavior of IABs or lateral resistance is mainly determined by the characteristics of backfill soils.

A method using nonlinear force-displacement relationship is one of well-known methods for analyzing and predicting the behavior of abutments and supporting piles. An elasto-plastic force-displacement curve can represent the unrecoverable plastic behavior of abutment displacements induced by backfill, presented in Figure 2.3.

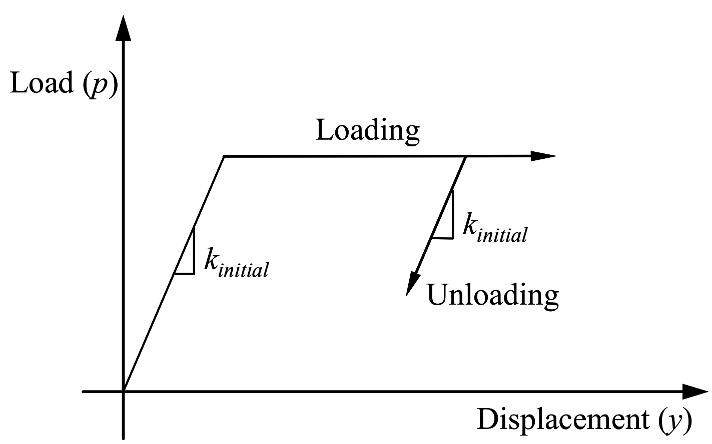

Figure 2.3: Perfectly Elasto-Plastic Behavior

The accuracy of soil-abutment interaction mainly relies on the determination of the coefficient of lateral subgrade reaction (k_h) that is proportional to the square root of confinement of gravel backfill soils [25]. When a pressure measurement at a depth (z_{ref}) is utilized, k_h with respect to depth (z) can be represented as in Eq. 2.2.

$$k_h(z) = k_{ref}\left(\frac{z}{z_{ref}}\right)^{0.5} \tag{2.2}$$

where, k_{ref} = experimentally derived subgrade reaction modulus at depth z.

Numerical analysis models of abutment-backfill interaction using Winkler springs can be found in many research studies [38, 51, 52, 75, 107]. The Winkler spring model, under cyclic loadings, was based on a force-displacement relationship. The conventional lateral earth pressure theory with elasto-plastic behavior appears in Figure 2.4.

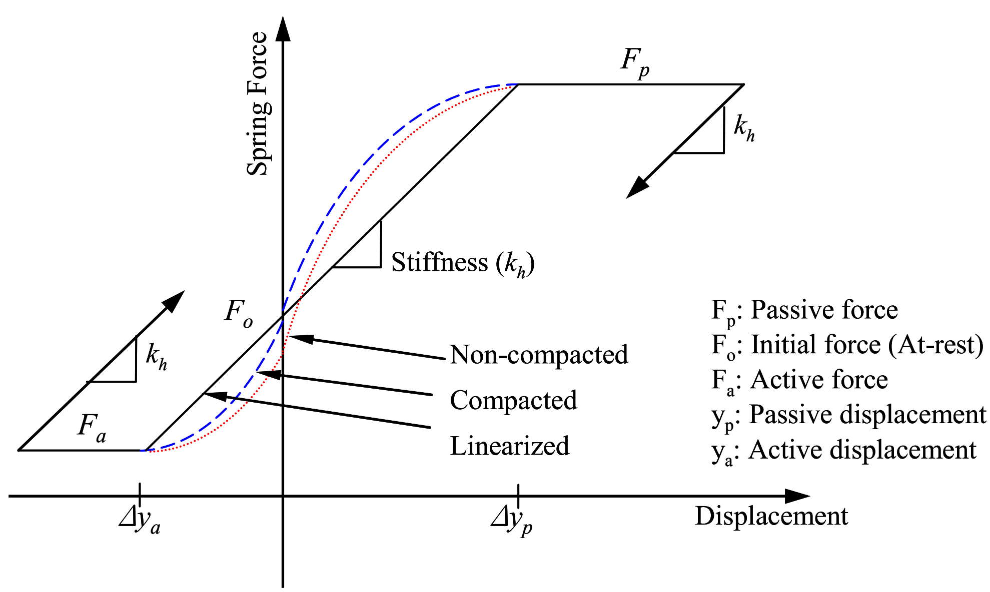

Figure 2.4: Force-Displacement Relationship for Abutment-Backfill Interaction

Design curves for abutment-backfill interaction can be found in Clough and Duncan [31] and NCHRP report [90]. In bridge construction, backfills are compacted to a required degree and the dash-line curve in Figure 2.4 represents the more acceptable level for a typical bridge abutment case.

2.4.2 Laterally Displaced Piles

Many research studies used to simplify modeling of soil-pile interactions in IABs with Winkler spring models [38, 39, 40, 42, 51, 60, 80, 113] that are not expensive in terms of numerical modeling time and storage, but simulate actual pile behavior well. The discrete nonlinear springs, based on relationship between lateral forces versus lateral displacements (*p*-*y* curves), are modeled for soil-pile interactions. The equivalent cantilever method in Figure 2.1 can further simplify the pile model. The bottom end of the pile in the method is restrained in all translations and rotations, while the top end has free lateral translation and other translations and rotations are restrained. In addition, the lateral displacement of the pile is regarded as equivalent to the abutment movement. Thus, the moment in the pile head can be written as:

$$M_{Pile\,Head} = E_p I_p \phi_p = \frac{6 E_p I_p \Delta_{abut}}{L^2_e} \leftrightarrow \frac{L_e^2}{6} = \frac{\Delta_{abut}}{\phi_p} \tag{2.3}$$

where, E_p is the modulus of elasticity of the pile; I_p is the moment inertia of the pile; L_e is the equivalent pile length; ϕ_p is the curvature in the pile head, and Δ_{abut} is the abutment longitudinal displacement. However, the actual abutment displacements simultaneously occur with abutment rotations, and therefore, the abutment displacement along backfill depth is not constant. The top elevation of the abutment has greater expansion and contraction during summer and winter, respectively. However, the equivalent cantilever method requires numbers of equally spaced, nonlinear, Winkler springs to model the laterally displaced piles, and therefore, may result in consuming significant running time and difficulties in conversion for IAB numerical models or probabilistic simulations.

2.4.3 Time-dependent Effects

Time-dependent effects in IABs include creep and shrinkage of concrete members and prestressing steel relaxation. Time-dependent effects induce a secondary effect in addition to thermal loading responses, and the magnitude in concrete members is considerable [70, 125]. Several methods, ACI Committee 209 [6], CEB-FIP MC 90 [33], and Model B3 [23] provide valuable solutions for time-dependent effects. The age-adjusted effective modulus method [58, 70, 109, 125] based on ACI Committee 209 is one of simplest methods to simulate time-dependent effects as a time-varying concrete modulus. As a force method, equivalent temperature loadings by means of strains from time-dependent effects can be determined and applied on the bridge superstructure [58]. For intrinsic prestressing steel relaxation, the AASHTO LRFD method [4] is widely used. Therefore, total strain in a concrete member can be expressed as:

$$\varepsilon(t) = \varepsilon_{\sigma} + \varepsilon_{cr} + \varepsilon_{sh} = \frac{\sigma(t_o)}{E(t_o)}\left[1 + \varphi(t, t_o)\right] + \varepsilon_{sh} \tag{2.4}$$

where, $\varepsilon(t)$: total concrete strain at analysis time t due to constant stress at analysis time t due to constant stress;

ε_{σ}: the immediate strain due to applied stress, σ;

ε_{cr}: the time-dependent creep strain;
ε_{sh}: free shrinkage strain;
$\sigma(t_o)$: the initial stress at the initial loading time t_o;
$E(t_o)$: modulus of elasticity at t_o, and
$\varphi(t,t_o)$: creep coefficient at time t corresponding to the age at loading t_o.

However, Eq. 2.4 cannot be used directly because the applied stress, σ, is variable over time. Figure 2.5 illustrates the strain variation under variable stress.

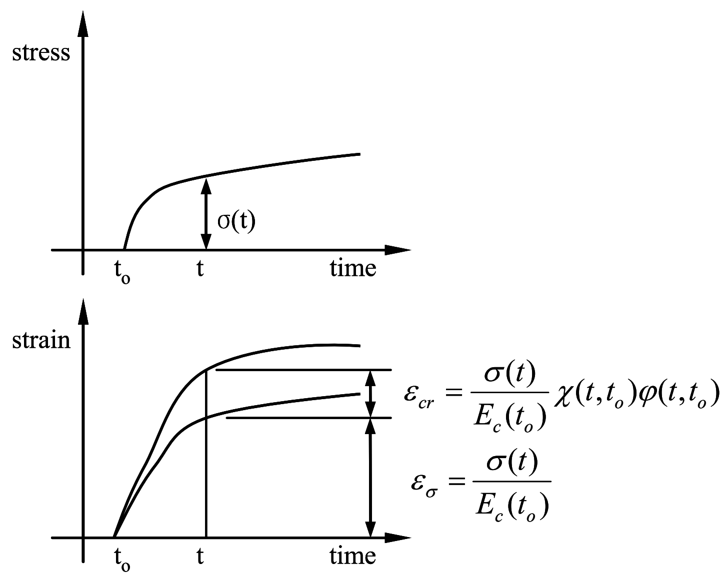

Figure 2.5: Concrete Strain under Variable Stress

To consider the strain variation, the effects of a series of applied stresses are determined individually and then, all strains are combined based on the superposition principle. For stress variation, Jirásek and Bažant [70] used the aging coefficient, χ, to adjust the creep coefficient. The PCI bridge manual [109] summarizes the concept of χ accounts for:

- The concrete member experiences the maximum force only at the end of the time interval (t_o,t).
- The modulus is increasing with time because the concrete is gaining strength.
- The total creep is larger for a given environment when the concrete is young.

Eq. 2.5 should be used when the applied stress is variable.

$$\varepsilon = \frac{\sigma(t)}{E_c(t_o)}\left[1 + \chi(t,t_o)\varphi(t,t_o)\right] + \varepsilon_{sh} \tag{2.5}$$

For time-dependent elastic modulus variation, the effective modulus (E_c^*) method simplifies creep analysis because the method allows a pseudo-elastic analysis within a given time interval. E_c^* relates the immediate strain and time-dependant strain and defined as:

$$E_c^*(t,t_o) = \frac{E_c(t_o)}{1 + \chi(t,t_o)\varphi(t,t_o)} \tag{2.6}$$

The aging coefficient can be precisely computed [70] and tabulated in ACI 209 [6], but $\chi = 0.7$ for a relatively young concrete age and $\chi = 0.8$ for all other uncertainties generally produces sufficiently accurate results [109].

ACI 209 [6] provides concrete shrinkage prediction as:

$$\varepsilon_{sh}(t) = \frac{t - t_o}{55 + (t - t_o)}\alpha\gamma_{sh} \tag{2.7}$$

where, α is a constant, 0.00078, and γ_{sh} is values determined by ambient relative humidity and size, shape effect, concrete slump test, fine aggregate percentage and air content in concrete.

Most prestressing materials exhibit relaxation similar to creep by means of the loss of stress. In Eq. 2.8, AASHTO LRFD (2008) [4] provides intrinsic relaxation of prestressing steel for a low-relaxation strand:

$$\Delta f_{RE} = \frac{\left[\log(24t) - \log(24t_o)\right]}{40}\left[\frac{f_{pj}}{f_{py}} - 0.55\right]f_{pj} \tag{2.8}$$

where, f_{pj} is prestressing jacking stress (ksi), and f_{py} is yield strength of prestressing steel (ksi). However, Eq. 2.8 describes the intrinsic relaxation while the relaxation of prestressing steel is relieved due to the effects of elastic shortening, creep and shrinkage. To compensate the stress relieve, Ghali [58] derived an approximate, reduced relaxation coefficient, χ_r. The reduced relaxation, Δf_R, is expressed as:

$$\Delta f_R = \chi_r \Delta f_{RE} \tag{2.9}$$

where, $\chi_r = \exp[(-6.7 + 5.3\lambda)\Omega]$;

$\lambda = \dfrac{\text{steel stress immediately after transfer}}{\text{characteristic tensile stress}}$, and

$\Omega = \dfrac{\text{total prestress change - intrinsic relaxation}}{\text{steel stress immediately after transfer}}$.

However, for the low-relaxation prestressing steel, the relaxation effects are very small compared to creep and shrinkage. Thus, in most practical situations, a factor of 0.8 is appropriate for the relaxation portion for reducing strain [109]. Therefore, the total strain due to time-dependent effects is expressed as:

$$\varepsilon(t) = \frac{\sigma(t_o)}{E_c(t_o)}[1 + \varphi(t, t_o)] + \frac{(\sigma(t) - \sigma(t_o))}{E_c^*(t, t_o)} + \varepsilon_{sh}(t, t_{sh,o}) \tag{2.10}$$

2.5 Reliability Analysis of IABs

A correct distribution of load and resistance models for IABs is essential to design IABs with satisfying safety level. To construct the distributions, statistics are minimum requirements. Currently IABs are designed and analyzed based on deterministic parameters from field tests and experiences [11]. However, the inherent uncertainties in

IABs, such as bridge temperature variations, bridge components and soil properties, create difficulties which must be thoroughly considered. To account for the uncertainties in IAB design procedure, reliability analysis is required to determine if the design procedure can provide a predetermined minimum safety level. Thus, the absence of reliability analysis may cause catastrophes due to structural failure or unsatisfactory performance of the structures. Reliability analysis provides valuable information even though the calculation does not enhance the accuracy of analysis or design [44]. Hence, IAB load and resistance statistics are essential for providing minimum safety in IAB designs.

Reliability of a structure (R_e) is the probability that the structural resistance (R) exceeds the applied loads (Q). Thus, R_e can be written as:

$$\begin{aligned} &R_e = Probability(R > L) \\ &\leftrightarrow Probability(g = R - L\,) > 0 \\ &\leftrightarrow g(X_1, X_2, \ldots X_n) > 0 \end{aligned} \tag{2.11}$$

where, g = limit state function that describes resistance versus load effect, $X_1, X_2, \ldots, X_n$ = random variables that consist of the limit state function $g(.)$. To the contrary, the probability of failure (P_f) is the probability that Q is greater than R. The probability of failure (P_f) is expressed as:

$$P_f = P(Z < 0) = P(R < Q) = 1 - R_e \tag{2.12}$$

Reliability index (β), the inverse of the coefficient of variation of the function (Z), is useful to represent the probability of failure (P_f) and Table 2.4 indicates β variations with respect to P_f.

Table 2.4: Reliability Index (β) and Probability of Failure (P_f)

P_f	10^{-1}	10^{-2}	10^{-3}	10^{-4}	10^{-5}	10^{-6}	10^{-7}	10^{-8}	10^{-9}
β	1.282	2.326	3.090	3.719	4.265	4.753	5.199	5.612	5.998

For normal random variables, R and Q, the relationship between β and P_f can be written using the standard normal cumulative distribution function (Φ):

$$\beta = -\Phi^{-1}(P_f) \quad or \quad P_f = \Phi(-\beta) \tag{2.13}$$

Therefore, the probability of failure can be derived from integrating:

$$P_f = \iint_{over\ Z \leq 0} f_{X_1, X_1, \ldots, X_n}(x_1, x_2, \ldots, x_n) dx_1 dx_2 \ldots dx_n \tag{2.14}$$

where f_{X_i} is the joint probability density function for the basic random variables (X_i). However, the integration in Eq. 2.14 is difficult because the joint probability density function is generally unknown [16]. Thus, an approximation, using a Taylor series expansion that truncates the series at the first order term, is used to avoid computational difficulties of the integration.

The Taylor series method, also referred to as First Order Reliability Method (FORM), is one of several well-known methods to assess the reliability and compute best values for key parameters. A summary of the procedure presented by Duncan [44] is:

1. Compute the result (R_μ) using the most likely values (μ) of the parameters.
2. Estimate standard deviations (σ) of the parameters that involved uncertainties.
3. Compute the result with one parameter increased as $\mu + \sigma$ and the others remain as μ.
4. Compute the result with one parameter increased as $\mu - \sigma$ and the others remain as μ.

5. Compute the difference (Δ) from (*Procedure 3*) – (*Procedure 4*) for each parameter.
6. Compute σ and the coefficient of variation (V) for the results
7. Determine the probability of failure (P_f) from R_μ and V

FORM analysis is a useful and simple procedure only when the performance function is known. In addition, FORM includes inevitable truncation errors compared to other refined methods.

Direct Monte Carlo simulation can be used to assess the reliability of IABs [16], and is the most common method for probabilistic analyses. The behavior of IABs is extremely complicated, and therefore, the adoption of an analytical model for a performance function to describe the correct behavior is very difficult or unfeasible. A numerical solution for the behavior of IABs is the most appropriate method. Monte Carlo simulation randomly draws random input variables with respect to the assumed probability distribution and then feeds into the predetermined performance function. Thus, the number of simulation is important to obtain appropriate results because a complex model can be run for numerous simulations. The number of failure simulations (N_f) for the total number of simulations (N) expresses directly the probability of failure. P_f can be estimated as:

$$P_f = \frac{N_f}{N} \tag{2.15}$$

P_f approaches to the actual probability of failure when N goes to infinity.

Eq. 2.15 presents another method to derive the required number of simulations (N). If P_f is an estimated probability ($\overline{P}$) and $\overline{P}$ =P_{ture} is set, the variance ($\sigma^2_{\overline{P}}$) and coefficient of variation ($V_{\overline{P}}$) can be:

$$\sigma_{\bar{P}}^2 = \frac{P_{true}(1-P_{true})}{N} \; ; \; V_{\bar{P}} = \sqrt{\frac{1-P_{true}}{N \cdot P_{true}}} \tag{2.16}$$

From the above equation, the required number of simulations (N) can be estimated as:

$$N = \frac{1-P_{true}}{V_{\bar{P}}^2 \cdot P_{true}} \tag{2.17}$$

P_{ture} is substituted for the target probability and then, the required number of simulations can be obtained. However, the above calculations for the required number of simulations are sometimes unrealistic for complex numerical models that require long running time and large storage space.

Direct Monte Carlo simulation can be incorporated with the numerical method. Since the resultant response of an IAB is difficult to formulate into the performance function, response of IABs based on the randomly drawn input variables can be numerically computed with a large number of simulation cycles. One simulation loop of thousands simulation cycles represents an IAB structure that is subjected to a particular set of material properties and loads and boundary conditions.

2.6 Study Design

AASHTO *Load and Resistance Factor Design Specifications* (AASHTO LRFD) [4] specifies requirements intended to achieve a minimum safety level and is based on a limit states philosophy. In each prescribed limit state, partial safety factors for loads and resistances are derived using a reliability analysis to provide a minimum safety level.

Also, different load and resistance factors are used for each load and resistance component to design bridges more economically and efficiently. Load factors account for uncertainties related to dead load, live load, environmental loads and special loads. Resistance factors are derived from the product of three sets of statistical data: (1) material (*M*); (2) fabrication (*F*); and (3) professional/analysis (*P*) [100]. The general format of a load combination is:

$$\sum \gamma_i Q_i \leq \phi_R R_n \tag{2.18}$$

where, γ_i is load factor; Q_i is load; ϕ_R is resistance factor, and R_n is nominal resistance. Both load and resistance factors are treated as random variables. To maintain a consistent probability of failure, a reliability index (β) was used. For a target reliability index (β_T), load and resistance factors can be computed using various reliability methods. Based on the advanced second-moment (ASM) method, a procedure of code calibration that determines load and resistance factors, appears in Figure 2.6 [101]. During the AASHTO LRFD code calibration, the initial design point of R^* is determined using statistical parameters of the mean of *R* (m_R), coefficient of variation (V_R) and a constant, *k*, as:

$$R^* = m_R(1 - kV_R) \tag{2.19}$$

The constant *k* ranges from 1.5 and 2.5 according to Nowak [101]. Preliminary load factors are determined using both a ratio of mean to nominal (bias factor, λ) and coefficient of variation (COV) to achieve the target reliability. Eq. 2.20 presents the initial load factor of i^{th} load component:

$$y_i = \lambda(1 + kV) \tag{2.20}$$

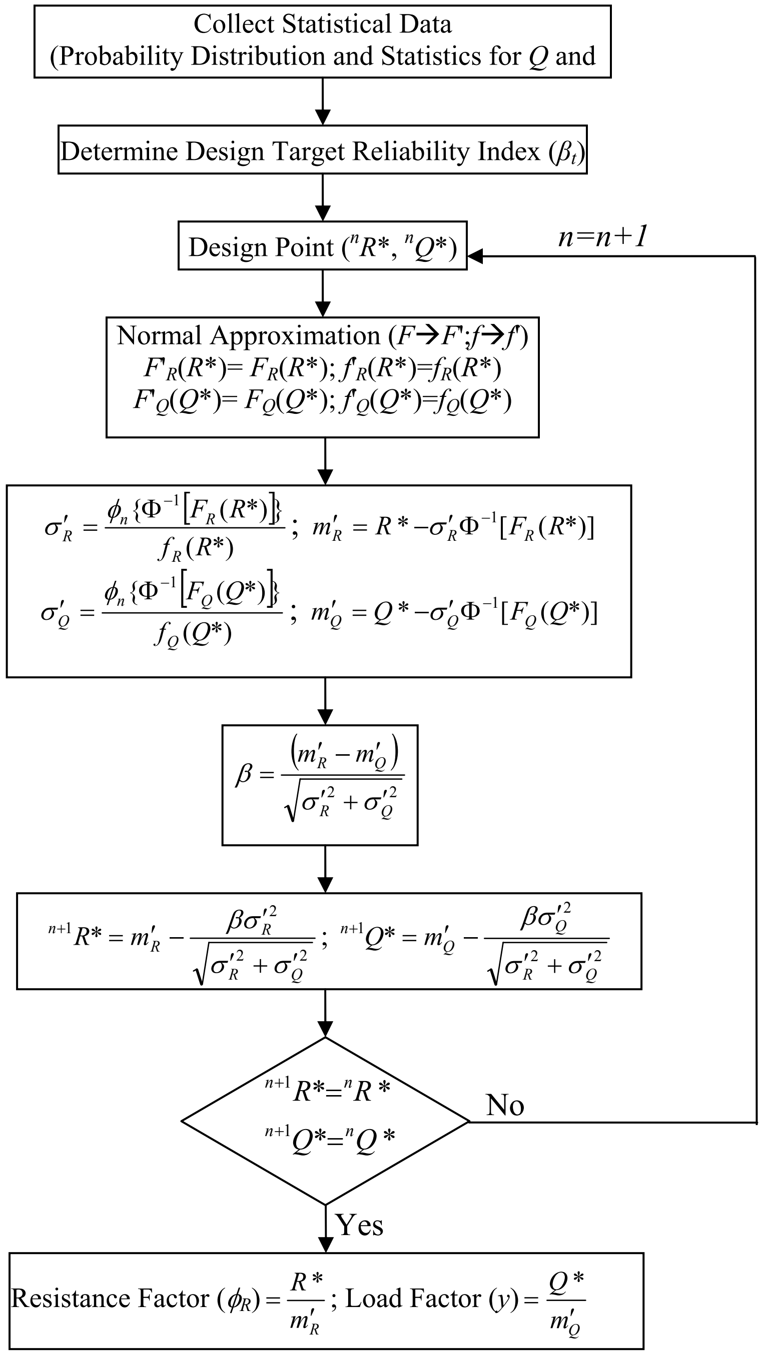

F = Cumulative distribution function (CDF); f = Probability density function (PDF);
Φ^{-1} = Inverse standard normal CDF; ϕ = Standard normal PDF;
F_R' = normal approximated distribution of F_R; f_R' = normal approximated distribution of f_R;
F_Q' = normal approximated distribution of F_Q; f_Q' = normal approximated distribution of f_Q;
m_R' = mean of R'; σ_R' = standard deviation of R'; m_Q' = mean of Q'; σ_Q' = standard deviation of Q'

Figure 2.6: Reliability Analysis Procedure using ASM

The probability of 0.02 is exceeded for $k = 2$. Once the target reliability index is determined, resistance factors are determined using the procedure in Figure 2.6.

Resistance factors are based on (1) material (M); (2) fabrication (F); and (3) professional/analysis. The resistance (R) can, therefore, be derived as:

$$R = R_n \cdot M \cdot F \cdot P \tag{2.21}$$

where, R_n is nominal resistance of the material. Generally, cumulative distribution function (CDF) of resistance is assumed to be lognormal because R is a product of M, F and P. Based on test data and numerical simulations, Nowak *et al.* [100] derived statistics for concrete bridges as presented in Table 2.5.

Table 2.5: Statistics of Bridge Resistances [100]

Girder Type			Bias Factor	COV
Steel	Noncomposite	Moment	1.11	0.115
		Shear	1.14	0.12
	Composite	Moment	1.11	0.12
		Shear	1.14	0.12
Reinforced concrete T-beams		Moment	1.14	1.14
		Shear	1.165	1.165
Prestressed concrete		Moment	1.05	1.05
		Shear	1.165	1.165

Considered loads in AASHTO LRFD code calibration include dead load (DC), wearing surface dead load (DW), vehicular live load (LL) and vehicular dynamic load allowance (I) and the limit state can be expressed as:

$$\phi R > 1.25DC + 1.5DW + 1.6(1+I)LL \tag{2.22}$$

Load factors for each load component were pre-determined based on Eq. 2.20 and statistics from Table 2.6.

Table 2.6: Statistics of Bridge Loads [100]

Load	Bias Factor (λ)	COV (V)
Dead Load (Factory-made component)	1.03	0.08
Dead Load (Cast-in-place component)	1.05	0.10
Asphalt Wearing Surface (3.5" assumed)	1.00	0.25
Live Load and Dynamic Load	1.1-1.2	0.18

For the nominal live load model for AASHTO LRFD code [99], a superposition of (a) HS-20 truck and a uniform lane load of 9.34 kN/m (0.64 k/ft) and (b) tandem and lane load are used and appear in Figure 2.7.

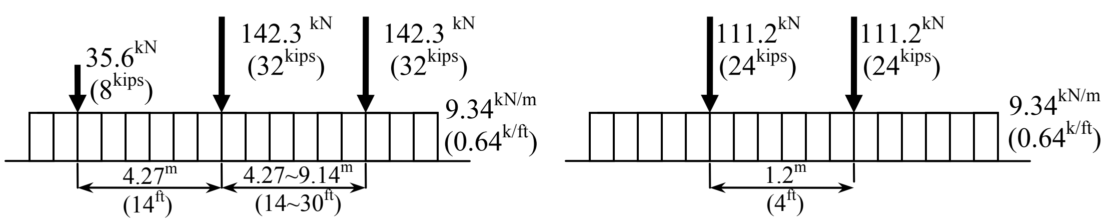

(a) Truck and uniform load (b) Tandem and uniform load

Figure 2.7: Nominal Load for AASHTO LRFD

The current AASHTO LRFD code [4] has been developed based on a reliability analysis. The simple reliability analysis for the development of the LRFD code was possible because statistical databases for various ranges of bridges were constructed and the boundary conditions of conventional bridges were simply supported. However, IABs have too complex to from a closed-form solution for the performance function.

Chapter 3

DETERMINISTIC NUMERICAL MODEL CALIBRATION

3.1 Introduction

This chapter presents the deterministic, nominal numerical, modeling methodologies for bridge components and the calibrated results based on field monitored response. IAB numerical modeling methods must be established to form the basis for practical long-term numerical analysis and probabilistic simulations. The modeling process includes material property representation, environmental and time-dependent load modeling, and boundary condition modeling for critical bridge components. For these purposes, measured bridge material and dimensions of four field tested IABs by Laman *et al.* [79, 80] are used. The modeling of IAB loads and boundary conditions, based on recommendations of AASHTO [4], ACI [6] and PCI [109] achieves developed numerical modeling methodologies according to Kim [73].

The numerical model, built in 2D, considers superstructure transverse and longitudinal center line symmetry. A 2D numerical model rather than a 3D model is preferred due to efficiency demands with respect to engineering resources, computing capacity and storage space. Many previous studies [38, 39, 40 41, 52, 59, 80, 112, 113, 125] demonstrated that 2D models accurately simulate IAB behavior and responses. While reducing the model size to accommodate long-term simulations, a 2D nominal numerical model is capable of incorporating behavior of IABs' key components. A comparison between 2D and 3D numerical models appears in Laman *et al.* [79, 80]. The developed, nominal numerical models were evaluated and calibrated according to field collected responses. The calibrated, nominal numerical model provides an accurate basis for subsequent probabilistic simulations.

Two key behaviors of IABs are: (1) soil-structure interaction; and (2) nonlinear behavior of construction joints between abutments and backwalls. Soil-structure interaction consists of two parts: (1) abutment backfill interaction; and (2) soil-pile interaction. In the present study, the Winkler Spring Model, adopted for abutment-backfill interaction, is based on classical Rankine active and passive pressure theory [35]. Soil-pile interaction modeling uses nonlinear force-displacement (*p-y*) curves derived from American Petroleum Institute [10] recommendations. Modeling construction joints between the backwall and abutments, below girder seats, is based on moment-rotation characteristics of the joints [80, 107].

Loads applied to the numerical models are: (1) backfill pressure on abutments; (2) time-dependent effects of concrete superstructure; (3) ambient temperature change; and (4) temperature gradient along the superstructure depth. Backfill pressure modeling applied to abutments is according to the linearly varying distribution with depth [35]. Consideration of time-dependant effects due to prestressing steel relaxation, and concrete creep and shrinkage used both the equivalent temperature method [58] and the age-adjusted elastic modulus method (AAEM) [58, 109]. Temperature gradient modeling of the superstructure is an equivalent linear variation along the depth due to modeling limitations for representing the complex variations recommended by AASHTO LRFD [4].

3.2 Field Data Description

Field instrumentation and monitoring measure actual IAB responses. Data collection occurred at four selected IABs and one weather station on I-99 near Port Matilda, PA. Brief descriptions of the four IABs appear in Table 3.1. The instrumented IABs have four prestressed concrete girders with a cast-in-place deck, and no skew ends on either abutment. The abutments are supported by a single row of weak-axis oriented, HP310×110 (HP12×74), steel piles. For each of the bridges, 64, 60, 64 and 48 vibrating wire instruments, were installed for bridges 109, 203, 211 and 222, respectively. These instruments are: pressure cells for backfill pressure, extensometers for abutment displacement, strain gages for girder axial force and moment, girder tiltmeters, abutment tiltmeters, pile strain gages, and sisterbar gages in approach slabs. The weather station data has been initiated since August 2002. Data for bridges 203, 222, 211 and 109 has been initiated from November 2002, November 2003, September 2004 and July 2006, respectively. A detailed monitoring plan and bridge description appears in Laman *et al.* [79, 80].

Table 3.1: Field tested IABs

Structure No.	Girder Type	No.of Spans	Integral Abutment	Spans m (ft)	Total Length m (ft)
109	P/S I	4	Both	26.8-37.2-37.2-26.8 (88-122-122-88)	128.0 (420)
203	P/S I	3	North Only	14.3-26.8-11.3 (47-88-37)	52.4 (172)
211	P/S I	1	Both	34.7 (114)	34.7 (114)
222	P/S I	1	Both	18.9 (62)	18.9 (62)

Note: All bridges have no skew at supports.

3.3 Development of Model Component

This section presents numerical modeling methodologies used to simulate IAB behavior. A schematic, 2D numerical model developed for use in the present study appears in Figure 3.1.

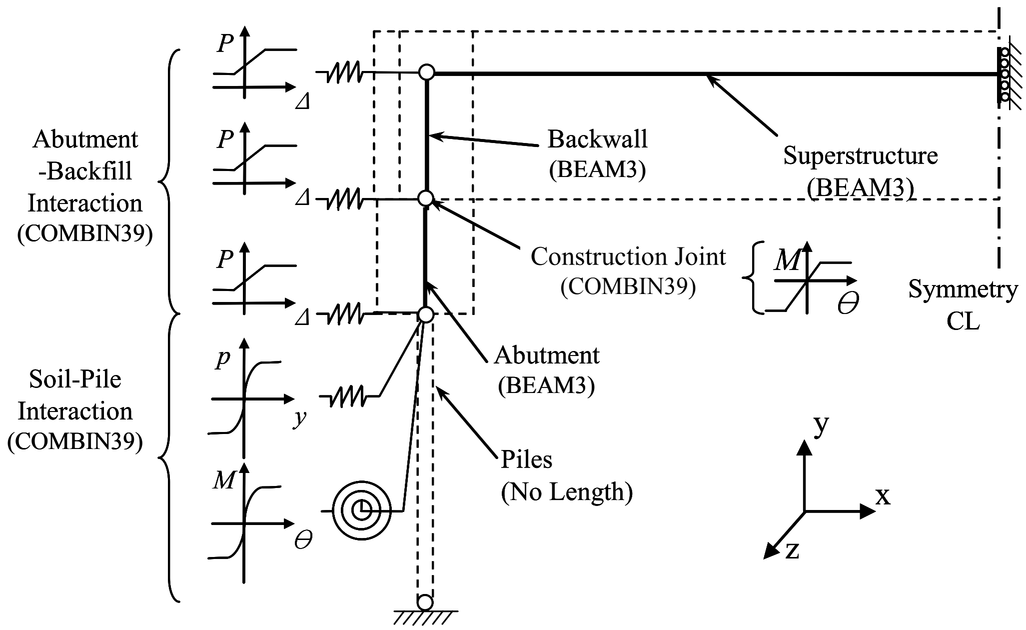

Figure 3.1: Schematic 2D Numerical Model

Half of the bridge structure's model is due to symmetry. The end node at the bridge superstructure centerline is restrained in x-axis translation and z-axis rotation. The single row of weak axis oriented steel H-piles are assumed to be rigidly connected to the abutment. The degree of freedom in the y-axis pile displacement was eliminated at the pile tip and was restraint at the pile-head. Supporting piles were modeled as equivalent lateral and rotational nonlinear springs. The nonlinear properties of the construction joint between the backwall and abutment were modeled according to moment-curvature properties.

3.3.1 Material Properties

The present study adopted the material properties for structural members and soils from the concrete mix design, design calculations, and geotechnical reports [79, 80]. All material properties of the instrumented four bridges appear in Table 3.2.

Table 3.2: Deterministic Properties of Bridge Materials

Material	Strength (f_c' or F_y) MPa (ksi)	Elasticity MPa (ksi)	Thermal Expansion Coefficient (mm/mm/°C) (in/in/°F)
Concrete (Precast Girder)	55.2 (8.0)	35,536 (5,154)	9.0E-6 (5.0 E-6)
Concrete (Deck and Backwall)	27.6 (4.0)	25,124 (3,644)	9.0E-6 (5.0 E-6)
Concrete (Parapet and Diaphragm)	24.2 (3.5)	23,504 (3,409)	9.0E-6 (5.0 E-6)
Concrete (Pier and Abutment)	20.7 (3.0)	21,760 (3,156)	9.0E-6 (5.0 E-6)
Steel (HP Piles)	345 (50)	200,000 (29,000)	13E-6 (7E-6)

Section properties were calculated based on the actual size. Then, the transformed superstructure section properties, as Table 3.3 were computed and used as inputs.

Table 3.3: Transformed Superstructure Section Properties

Bridge	Area m^2 (in^2)	Moment of Inertia m^4 (in^4)	Elastic neutral axis from bottom of section (y_b) m (in)
109	5.34 (8,282)	3.548 (8,525,124)	1.557 (60.60)
203	5.03 (7,802)	2.378 (5,713,283)	1.308 (51.51)
211	5.34 (8,282)	3.548 (8,525,124)	1.557 (60.60)
222	4.37 (6,775)	1.432 (3,440,291)	1.098 (43.22)

Engineering soil properties are critical factors in determining IAB behavior because soil character determines the soil-structure interaction behavior. Soil models are required to simulate the hysteretic, nonlinear, soil-structure interaction against cyclic loading and unloading. Derived engineering properties of soil strata around supporting piles appear in Figures 3.2 through 3.8. Figures 3.2 and 3.3 illustrate soil properties under both abutments of bridge 109, and Figure 3.4 describes abutment 2 of bridge 203, which has one integral abutment and a spread footing on bedrock for the other abutment. Figures 3.5, 3.6, 3.7 and 3.8 are soil layer properties under each abutment of bridges 211 and 222. The first stratum of bridge 203, 211 and 222 is a stiff clay layer while bridge 109 stands on a sand layer.

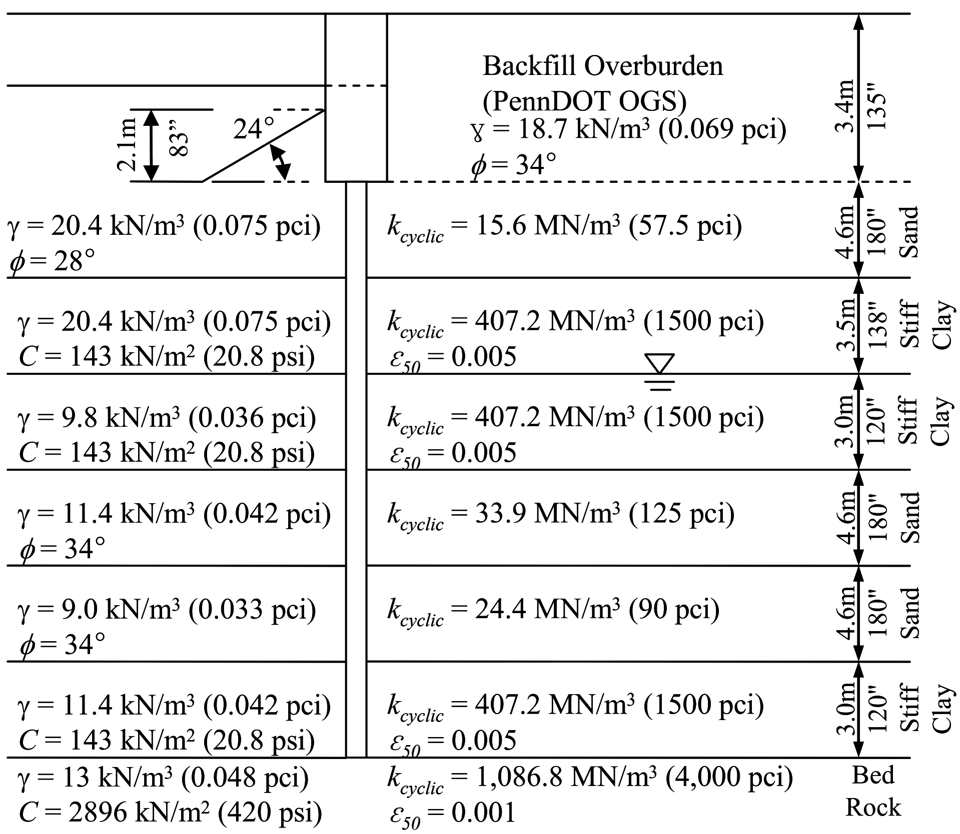

Figure 3.2: Bridge 109 Soil Properties under Abutment 1

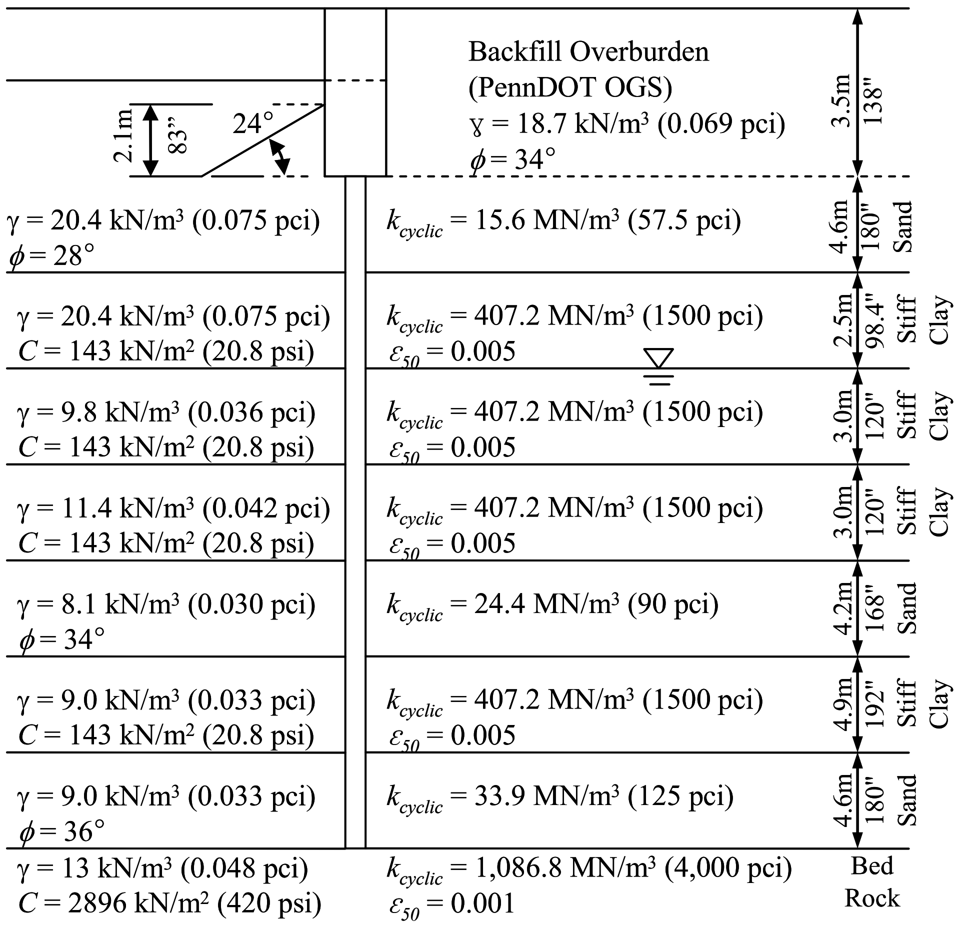

Figure 3.3: Bridge 109 Soil Properties under Abutment 2

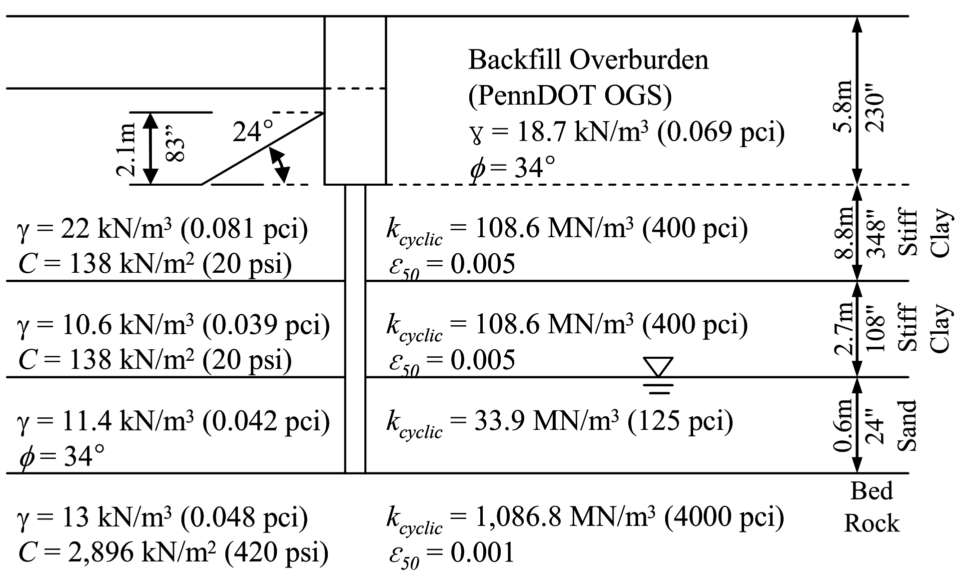

Figure 3.4: Bridge 203 Soil Properties under Abutment 2*
(* Bridge 203 has only one integral abutment)

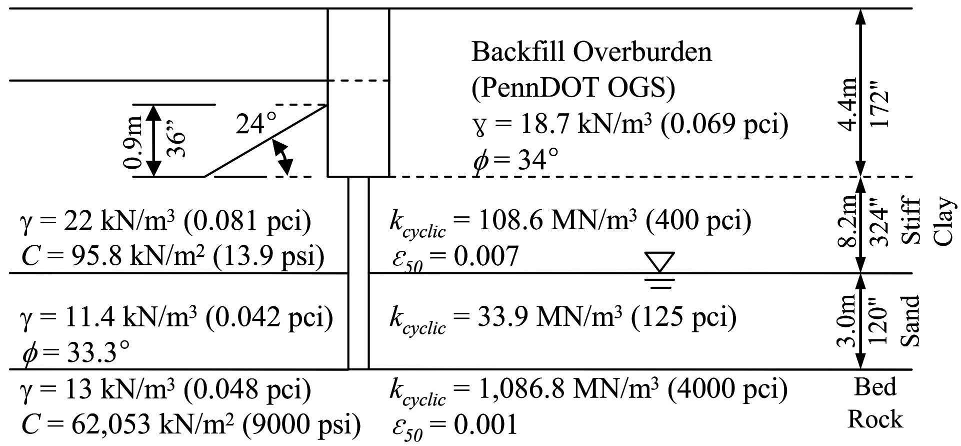

Figure 3.5: Bridge 211 Soil Properties under Abutment 1

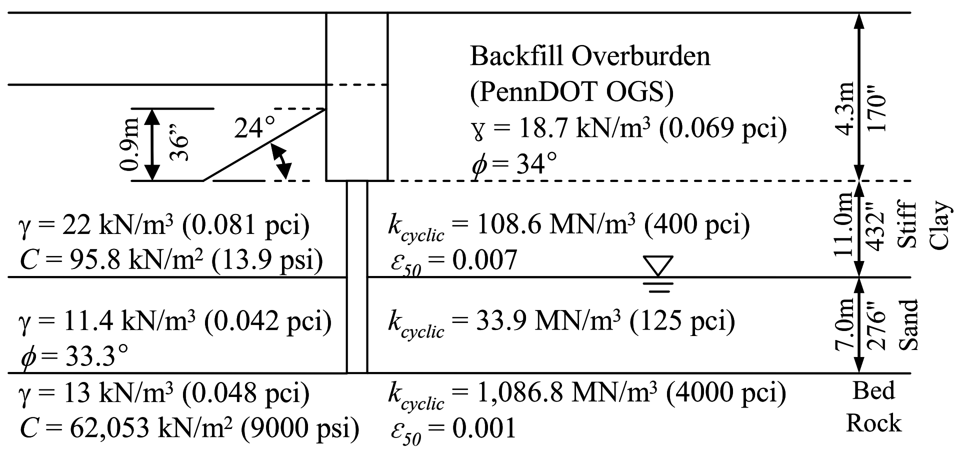

Figure 3.6: Bridge 211 Soil Properties under Abutment 2

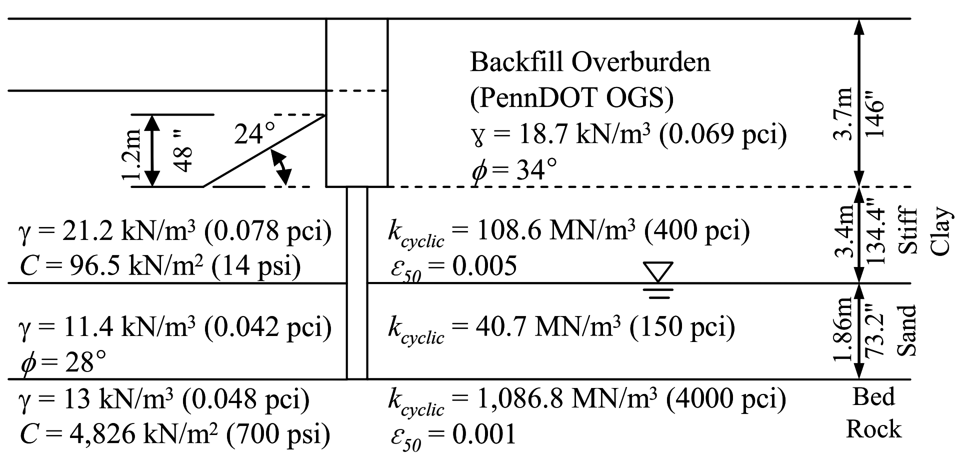

Figure 3.7: Bridge 222 Soil Properties under Abutment 1

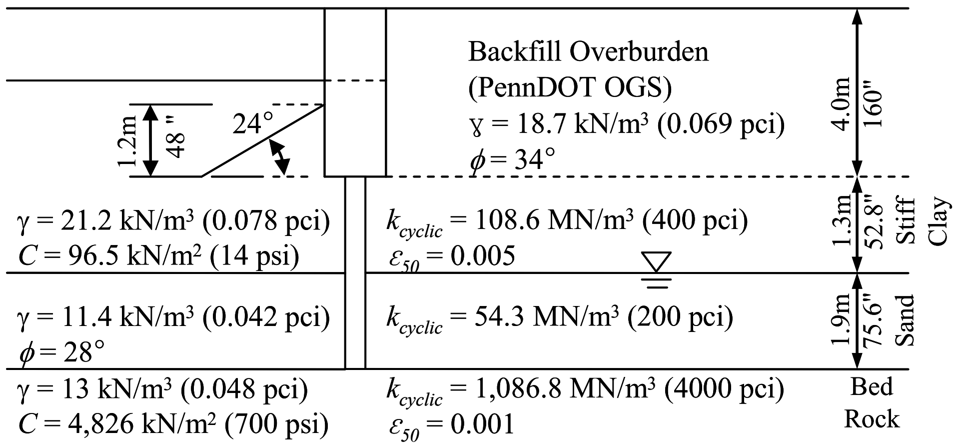

Figure 3.8: Bridge 222 Soil Properties under Abutment 2

3.3.2 Abutment-Backfill Interaction

Modeling the interaction between the abutment and the backfill used a backfill pressure (P)-displacement (Δ) curve. The relationship between backfill pressure and abutment displacement is assumed to be a linear variation between active and passive pressure as presented Figure 3.9.

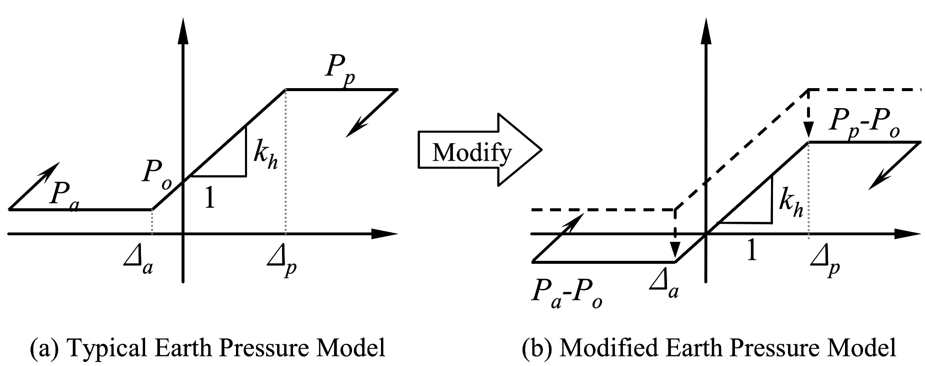

Figure 3.9: Abutment-Backfill Numerical Implementation Modification

Once active or passive pressure is reached, the model adopts perfectly plastic behavior. The unloading branch is a slope parallel to the initial slope. The lateral earth pressure theory by Rankine provided active and passive coefficients (K_a and K_p). The initial slope of the curve, subgrade reaction (k_h) in Figure 3.9 originates from the slope of backfill pressures and abutment displacements based on the field observations [80]. ANSYS COMBIN39 element, a nonlinear user definable spring, represents the expected hysteretic behavior.

Figure 3.9(b) shows a modification allowing application of the derived P-Δ curve [80, 112]. Backfill, regardless of abutment movement, exerts lateral pressure toward the abutment with an intensity varying between active (P_a) and passive pressure (P_p). Thus, at-rest pressure (P_o) was applied as an external force and the element was defined as reduced active pressure, P_a-P_o, and reduced passive pressure, P_p-P_o. In the preliminary step, the abutment-backfill interaction members are subject to pressure, P_o. When running the model, the displacement of each interaction element from the preliminary step was applied as an initial displacement.

3.3.3 Soil-Pile Interaction

The numerical model incorporates a condensed soil-pile interaction model. A nonlinear load (p)-displacement (y) curve at each depth simulates soil-pile interaction using Winkler Springs along the pile depth [42, 51, 80, 107]. Condensing this soil-pile interaction reduces the model size in anticipation of significant computing demand for 75 years of bridge life simulations. Figure 3.10 illustrates the condensed soil-pile interaction model.

The full pile model in Figure 3.10(a) was condensed into two elements in Figure 3.10(b): (1) one lateral nonlinear spring; and (2) one rotational nonlinear spring. The full pile model for bridge 211 consists of 65 nonlinear springs with 196 degrees of freedom. Selected *p-y* curves for bridge 211 were computed with respect to the pile depth and appear in Figure 3.11. To validate the condensed soil-pile interaction model, first, a comparison was made first between COM624P results and the full pile model in Figure 3.10(a). A single pile in abutment 1 of Bridge 211, Figure 3.5, was selected and 22.2kN (5kips) applied to test lateral load for bridge contraction and expansion. Lateral displacement and pile bending moment about its weak-axis were compared and appear in Figures 3.12 and 3.13.

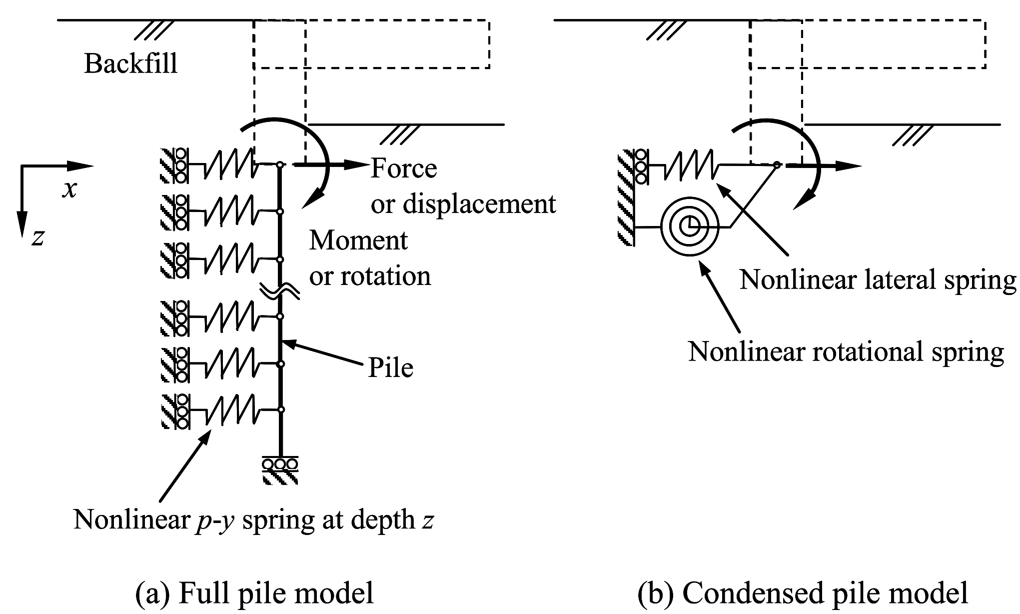

Figure 3.10: Condensed Soil-Pile Interaction Model

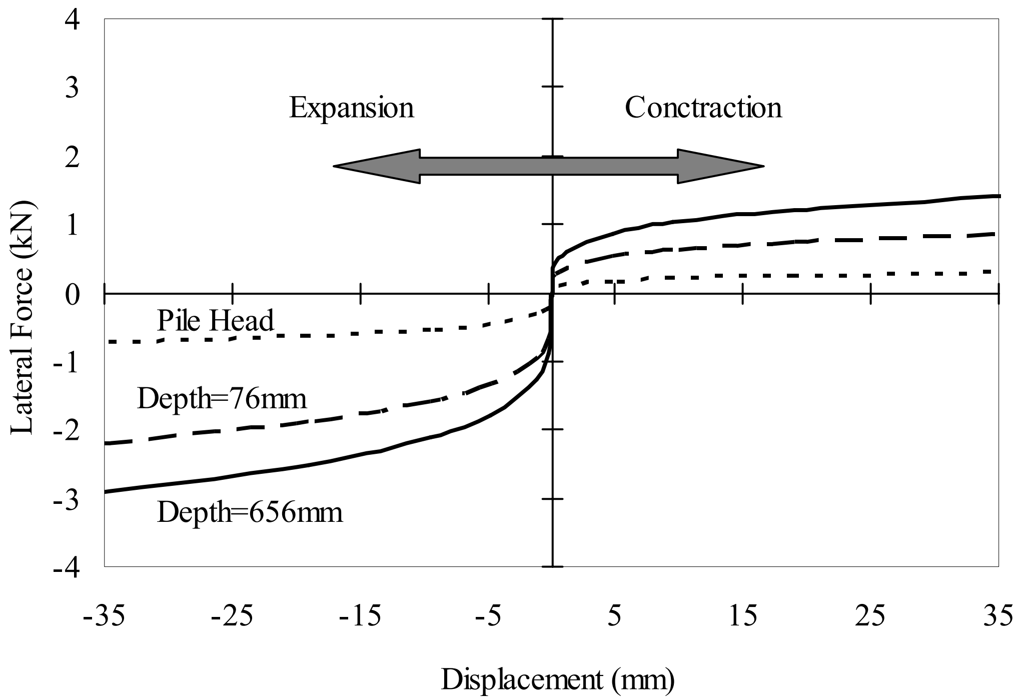

Figure 3.11: Sample *p*-*y* Curves from Bridge 211

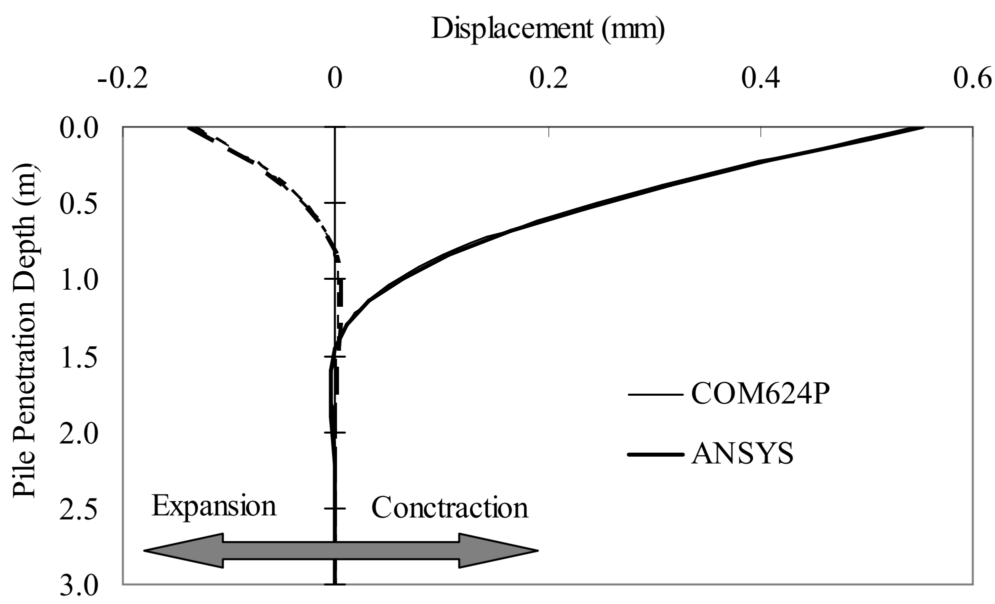

Figure 3.12: Pile Lateral Displacement Comparison

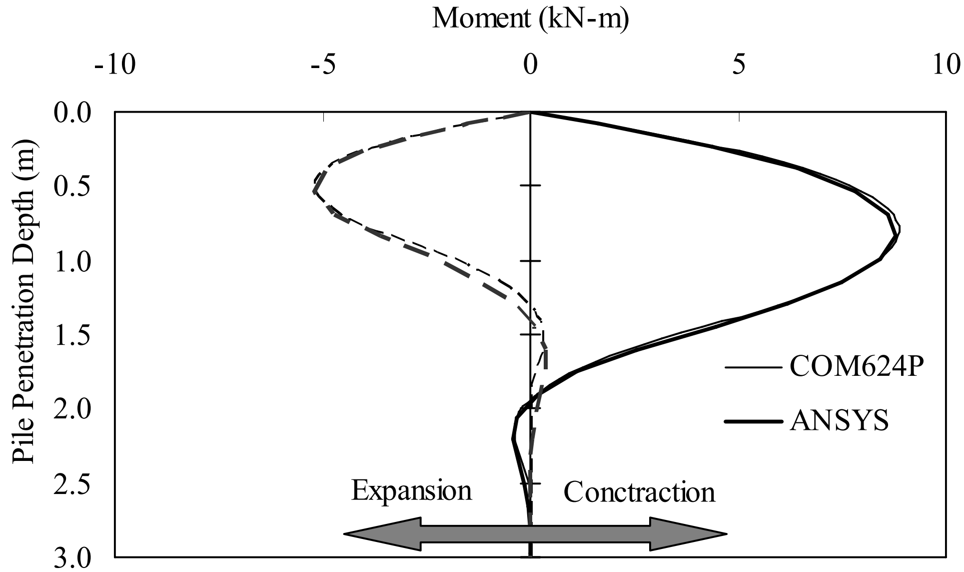

Figure 3.13: Pile Moment Comparison

The pile displacements and moments occur within 3m (10') from the pile head, which agrees with previous research [38, 51]. Comparisons of the full pile model and condensed pile model for bridge 211 were made and appear in Figures 3.14 and 3.15, respectively. In the numerical simulation, the unloading branch of *p-y* curves was defined as a line parallel to slope at the origin of loading curve.

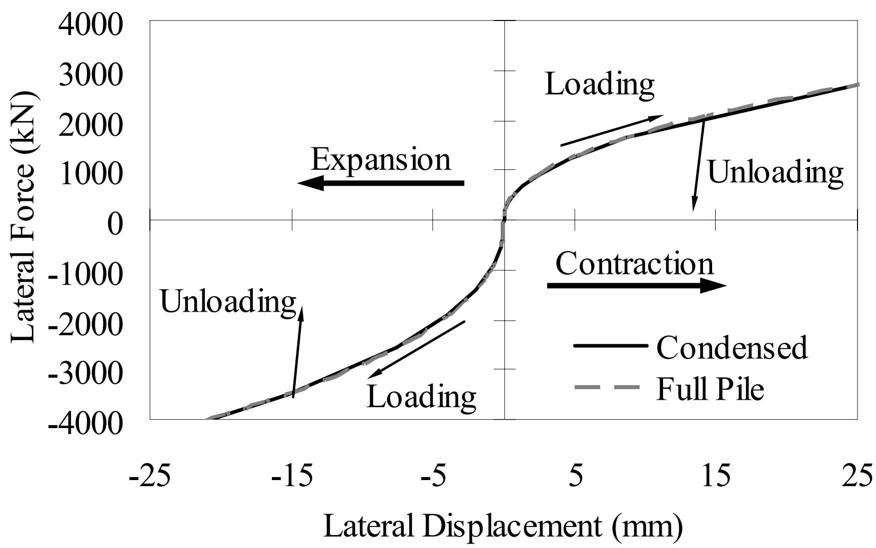

Figure 3.14: Force vs. Displacement Comparison (Bridge 211)

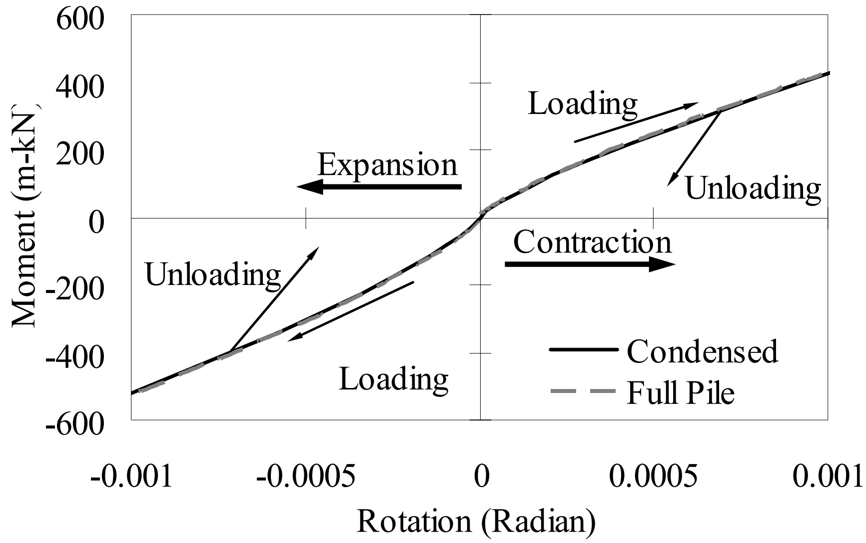

Figure 3.15: Moment vs. Rotation Comparison (Bridge 211)

3.3.4 Abutment-backwall Construction Joint

The construction joint between abutment and backwall has a significant influence on abutment response and has been considered in the numerical model. Reinforcement crossing the joint in the standard detail adopted by several states' bridge design manuals is very low. Pennsylvania Department of Transportation (PennDOT) [110] uses ϕ16mm at 250mm U-shaped reinforcing bars, resulting in joint reinforcement ratios for the field tested bridges generally less than 25% of the recommended AASHTO minimum reinforcement ratio. Thus, the joint permits significant rotation in response to superstructure expansion and contraction [106, 107, 112]. However, this joint is often assumed to be rigidly connected in IAB analyses. Field monitoring by Laman *et al.* [80] observed differential rotations of the backwall and abutment due to the lack of rotational stiffness in the construction joint. Because of the significance of the construction joint in the IAB behavior, this joint has been considered in the present study.

In practice, reinforcement details of construction joints in practice vary from state to state and some state agencies such as Virginia Department of Transportation (VDOT) adopted various semi-integral connections [13, 130]. Most states use U-shape steel rebars. Table 3.4 presents a survey summary of construction joint reinforcing details from state agencies. Based on the survey results, the U-shape rebar with ϕ16mm at 250mm (#5 at 10″) can be a representative construction joint reinforcement and is adopted into the nominal numerical model.

Table 3.4: Construction Joint Reinforcing Details

State Agency	U-shape Rebar (Concrete Girder)	Anchor Rod (Steel Girder)	Remarks
IL	ϕ16mm at 300mm (#5 at 12″)	N/A	
PA	ϕ16mm at 250mm (#5 at 10″)	ϕ16mm at 250mm (#5 at 10″)	use the same rebar details for concrete and steel girder
MA	ϕ16mm at 150mm (#5 at 6″)	ϕ40mm (ϕ1½″)	up to 30.5 m (100') span, otherwise design
NJ	ϕ16mm at 300mm (#5 at 12″)	use but not specified	
NY	ϕ16mm at 300mm (#5 at 12″)	use but not specified	
VA	N/A	ϕ22 mm at 300 mm (ϕ⅞″ at 12")	Sometimes shearkey is used

To inspect the actual IABs, rotational properties for each of the four field tested bridges were developed as presented in Figure 3.16.

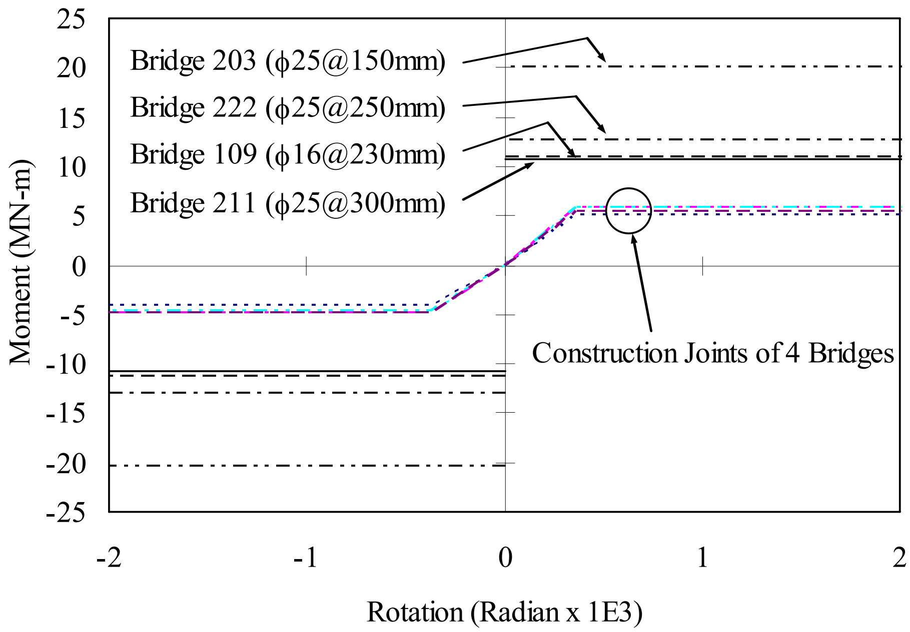

Figure 3.16: Rotational Stiffness of Construction Joints

Because reinforcement details of all bridges adopted ϕ16mm at 250mm (#5 at 10″) U-shaped rebar, the rotational properties are very similar among all of them. From the abutment capacities of the four bridges presented in Figure 3.16, it can be observed that the abutment capacities appear to be approximately two to four times larger than construction joint strength.

In the numerical model, bi-linear elasto-plastic properties were developed and used for the z-axis rotation based on moment vs. curvature property of the construction joint. Figure 3.17 (a) presents a schematic plot of reinforcement detail and Figure 3.17(b) illustrates the derivation of rotational properties used by Paul [160, 107].

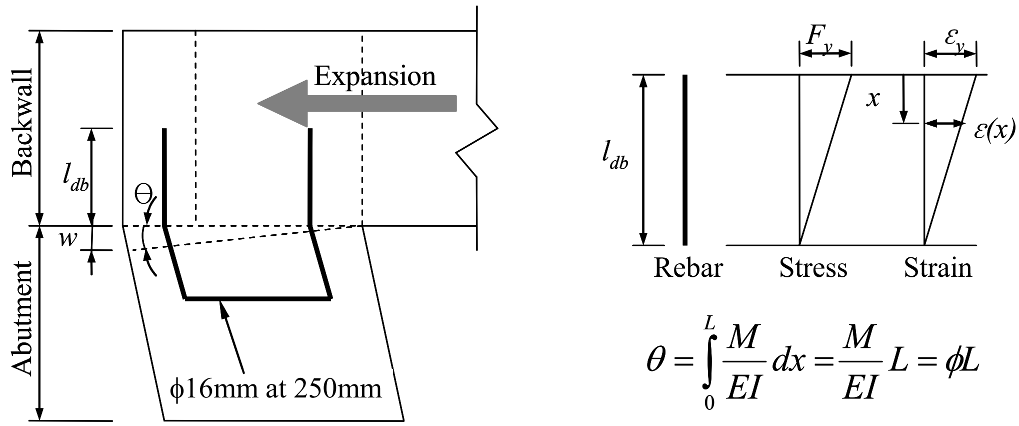

(a) Rebar Detail (Not to Scale)

(b) Rotation Derivation

Figure 3.17: Construction Joint Model

The construction joint of abutment to backwall joint was restrained for all translations except z-axis rotation, which was modeled using the ANSYS COMBIN39 nonlinear rotational spring. The moment-curvature relationship was computed based on reinforcement crossing the backwall/abutment joint. The derived moment-curvature (M-ϕ) relationship was converted to moment-rotation (M-θ) based on the assumption of small deformation and constant stress over a joint length, which was assumed to be half of the AASHTO LRFD (2008) minimum development length, l_{db} in Figure 3.17(b), of 200mm (8").

For the unloading path of the rotational stiffness diagram, conservative unloading from ANSYS [9] was adopted because hysteretic behavior is inappropriate. In reality, the construction joint can not have a residual rotational angle during rotational cycles. The conservative option, however, allows unloading along the same loading curve.

3.4 IAB Loads

This study considers four major loads: (1) backfill pressure; (2) time-dependent effect; (3) ambient temperature change; and (4) temperature gradient in superstructure. Dead loads are a consideration in the numerical model because the analysis begins after the abutment/backwall connection has cured [113]. Also, the stress due to the secondary load effect of dead load is negligible compared to the yield stress of the pile. The abutment displacement is very small, so the secondary load effect is insignificant, compared to the pile moment capacity. For bridge 211, the secondary load effect is approximately 0.8% of the pile moment capacity. Therefore, backfill pressure on abutments and backwalls, time-dependent effect, temperature change and temperature gradient loads in the superstructure have consideration in the numerical model.

3.4.1 Backfill Pressure

Pressure behind the abutment, considered in the numerical model, is a triangular distribution along the abutment depth with a unit weight of 18.7kN/m^3 (119pcf). Backfilling generally begins after the abutment and backwall cures so that the superstructure-backwall abutment behaves integrally. Thus, construction sequence is a consideration in the numerical model. The bridge begins to interact with the superstructure movement after backfilling. Initially applied backfill pressure is based on at-rest lateral earth pressure coefficient of K_o = 1.0, and assumes a compacted condition, as indicated by Barker *et al.* [18]. During the simulation, the lateral earth pressure varies between active and passive pressures as presented earlier in Figure 3.9. The bridge was subject to the backfill pressure with time-dependent and temperature loads.

3.4.2 Time-dependent Effects

Time-dependent effects, concrete creep and shrinkage, and prestressing steel relaxation have consideration in the numerical models. As discussed in Section 2.9.3, the AAEM [58, 70, 109, 125] method is utilized to compute time-dependent effects as a time-varying concrete modulus. The analysis, using AAEM, considers girder and deck section properties, pre-tensioning forces, elastic and time-dependent loss through time, dead load of girder and deck, and actual age of girders and deck at placement. Total strains (Eq. 2.4) from time-dependent effects are represented as equivalent temperature loadings based on the superstructure thermal expansion coefficient [58, 113].

The present study primarily used ACI 209 [6] to compute the creep coefficient, $\varphi(t,t_o)$ and aging coefficients, $\chi(t,t_o)$. Calculations of $\varphi(t,t_o)$ and $\chi(t,t_o)$ for bridge 211 with t_o = 3 and 264 days appear in Figures 3.18 and 3.19, respectively. In addition, the computed AAEM (E_c*) is presented in Figure 3.20.

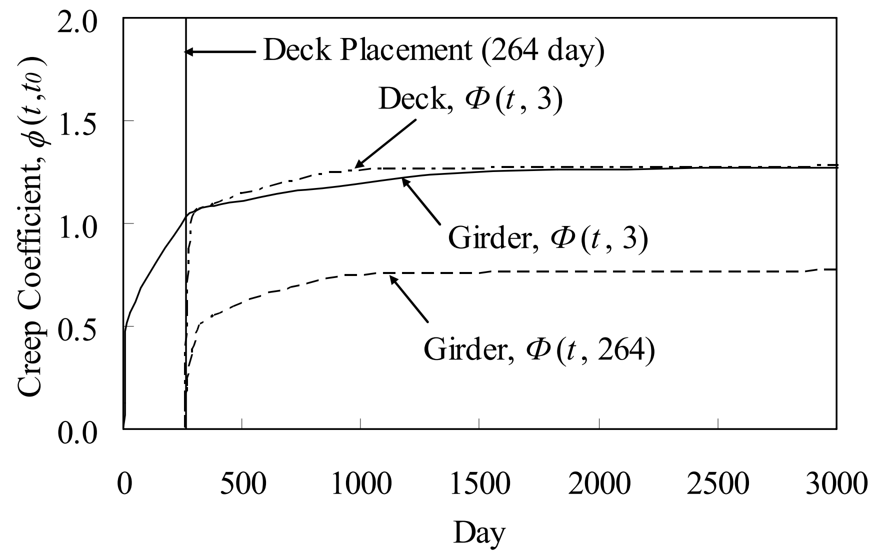

Figure 3.18: Creep Coefficient for Bridge 211

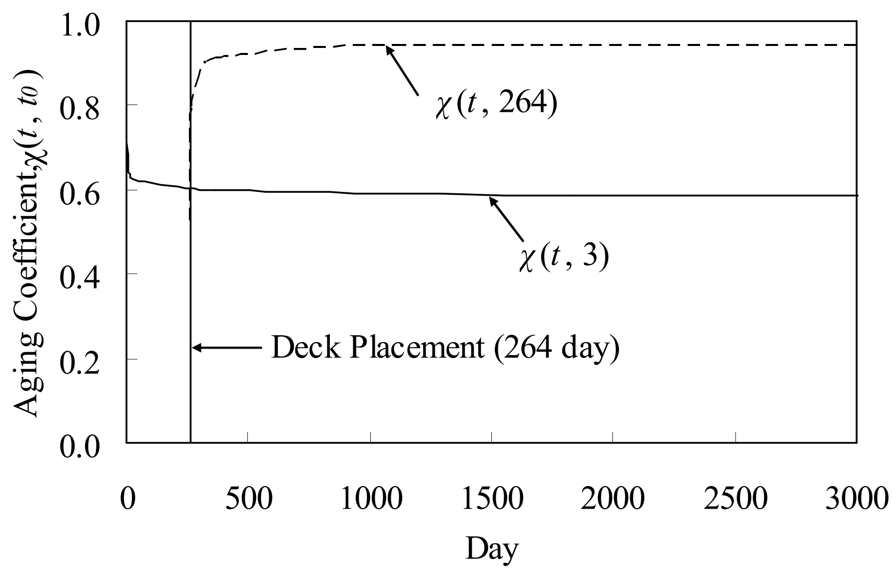

Figure 3.19: Aging Coefficient of Bridge 211

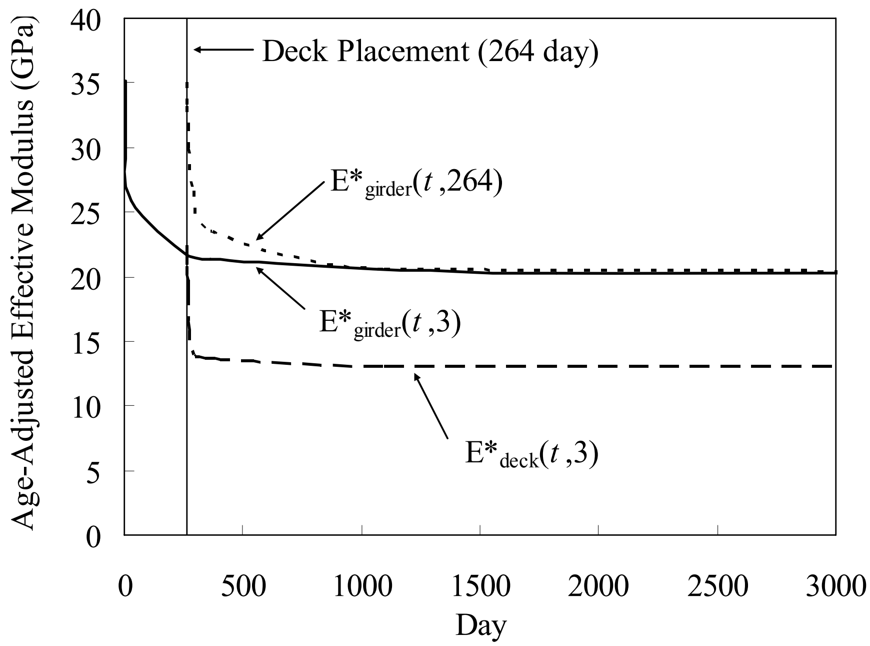

Figure 3.20: Age-Adjusted Effective Modulus

Shrinkage strain in concrete members was computed from ACI 209 [6] as represented in Eq. 2.7. Computed shrinkage strains for bridge 211 appear in Figure 3.21.

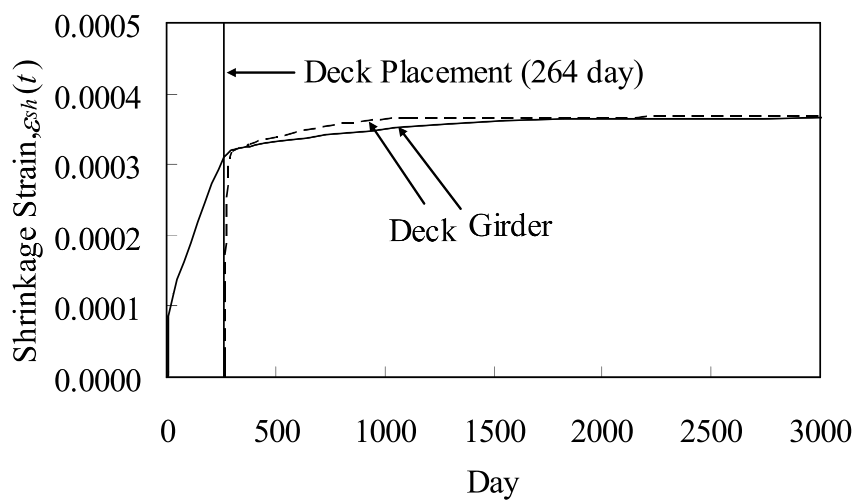

Figure 3.21: Shrinkage Strain of Bridge 211

Total strains due to concrete creep and shrinkage and prestressing relaxation at the top (Figure 3.22) and bottom (Figure 3.23) fibers of a girder of bridge 211 are computed for 3 days (267 days), 100 days (1 year) and 75 years from the deck concrete placement (264 days).

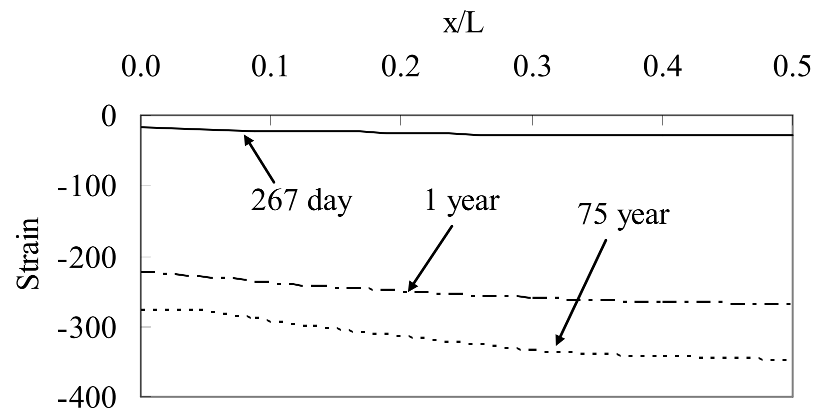

Figure 3.22: Total Strain at Top Fiber of Bridge 211

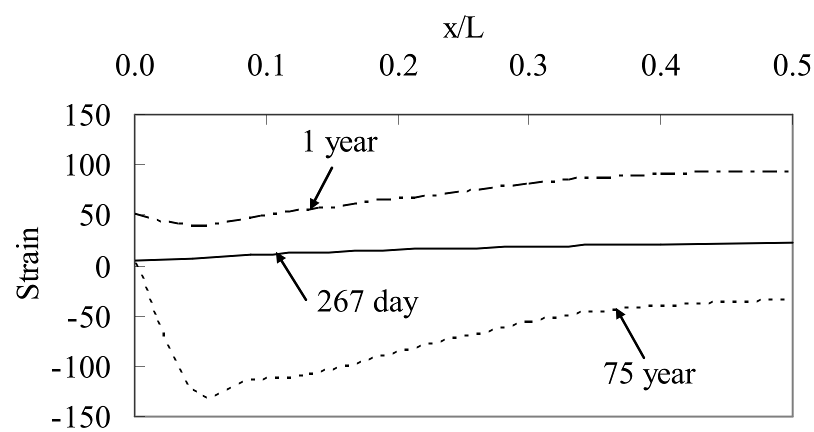

Figure 3.23: Total Strain at Bottom Fiber of Bridge 211

3.4.3 Superstructure Temperature Change

Superstructure thermal loading is one of the most significant influences affecting bridge behavior. The primary component of thermal loading is ambient air temperature [13]. Actual ambient temperature data, collected from a nearby weather station, was applied in the numerical model. Ambient temperature data, collected from September 2002 to September 2007, appears in Figure 3.24.

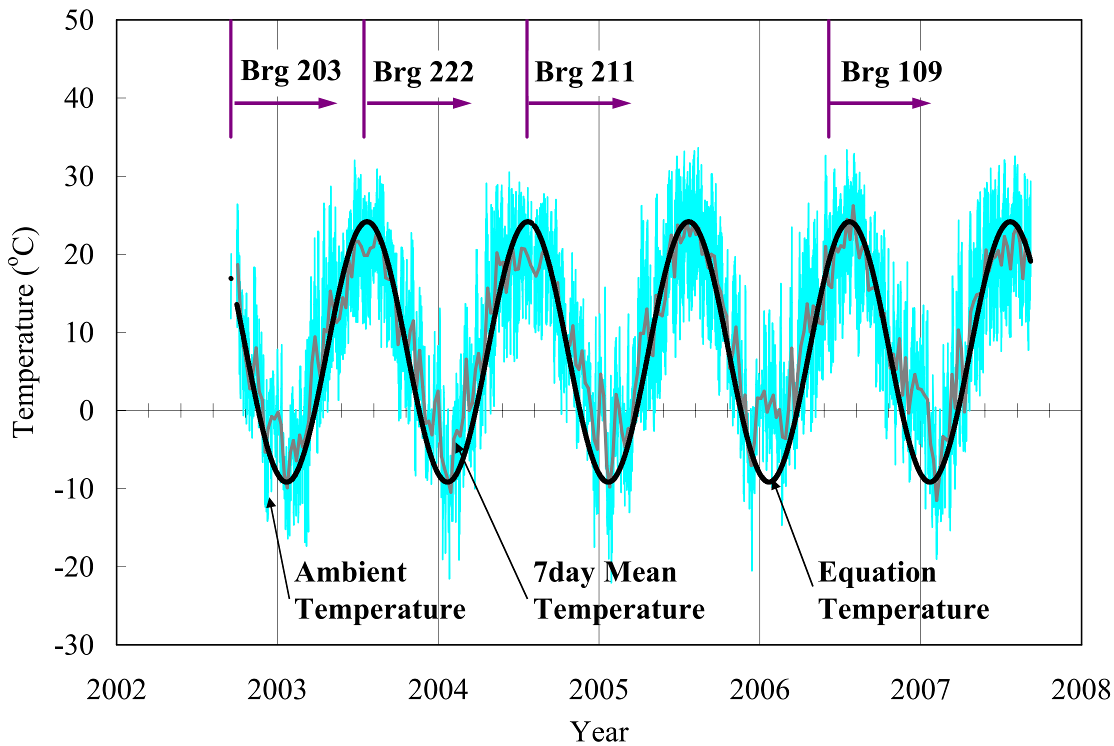

Figure 3.24: Temperature Model for Deterministic Models

As discussed in Section 2.2, the temperature loads specified in AASHTO LRFD [4] are considered conservative for steel and not conservative for concrete members and can be used only for one-way action of expansion or contraction. However, applying actual ambient temperature due to too many load steps (4 temperature loads per day × 365 days

= 1460 loading steps for one year). In addition, structure temperature is not the same as ambient temperature due to thermal mass. Hence, the 7 day mean temperature, the thick gray line in Figure 3.24 is the basis for the nominal superstructure temperature load model, since the girder temperature is close to ambient temperature on average. To represent temperature loading mathematically, temperature loading was assumed to be a sinusoidal variation over a year and is represented as:

$$T(t) = T_m + A\sin\left(\omega t + \phi\right) \tag{3.1}$$

where, T_m = mean temperature; A = amplitude of temperature fluctuation; ω = frequency; t = analysis time (day), and ϕ = phase lag (radian). The thick black line in Figure 3.24 represents the mathematical prediction.

3.4.4 Temperature Gradient

The numerical model includes a superstructure temperature gradient that exerts significant stresses [125]. A concrete deck and/or girder has relatively low thermal conductivity; therefore, the distribution of temperature along a girder depth is nonlinear. Because the AASHTO LRFD [3] multi-linear temperature gradient can not be modeled without significant complications, the study develops an equivalent temperature gradient based on the axial and bending strains obtained from the AASHTO gradient profile. The thermal stress (Eq. 3.2) induced by temperature gradient along a girder depth can be represented as:

$$\sigma_t(y) = E \cdot \alpha \cdot T(y) \tag{3.2}$$

where $\sigma_t(y)$ = longitudinal thermal stress at a fiber located a distance y; E = elastic modulus; α = thermal expansion coefficient, and $T(y)$ = temperature at a depth y. Thus, the axial force (P_t) and moment (M_t) due to thermal stresses (Eq. 3.3) are respectively:

$$P_t = \int E\alpha T(y)b(y)dY \text{ , and} \\ M_t = \int E\alpha T(y)b(y)YdY \tag{3.3}$$

The solid line in Figure 3.25 illustrates the equivalent temperature gradient for bridge 211 that produces the same axial force and bending moment as the AASHTO gradient load. This equivalent temperature gradient load was applied throughout the numerical model of the superstructure. In the numerical implementation, Figure 3.26 represents the individually applied temperature gradient loads at the top of the deck and the bottom of girder during 1 year.

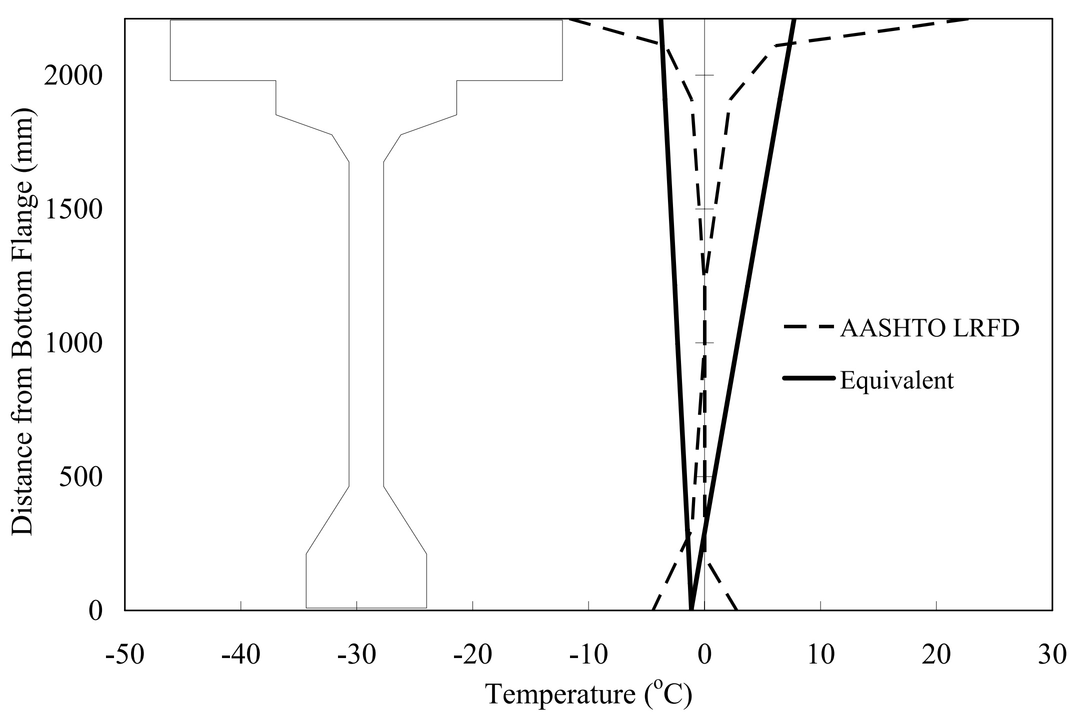

Figure 3.25: Temperature Gradient of Transformed Section

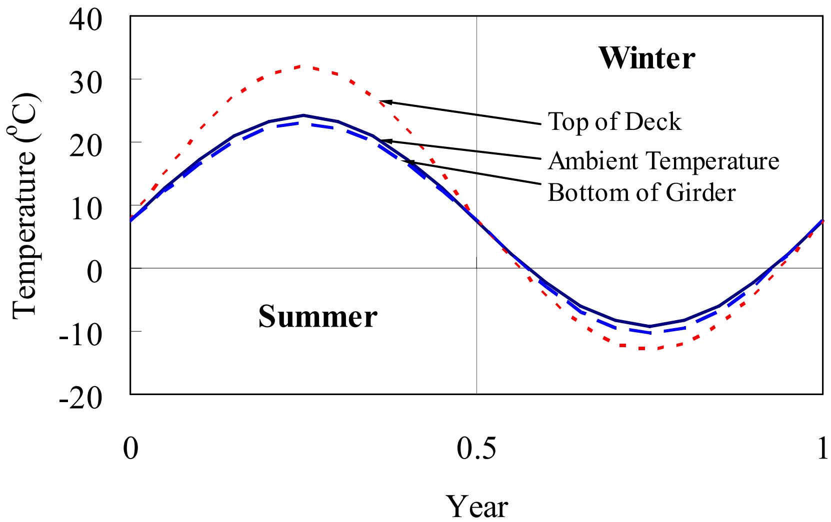

Figure 3.26: Temperature Variation with Temperature Gradient

3.5 Nominal Numerical Model Results

Predicted responses from the developed nominal numerical models were compared to measured responses from the field tested four IABs in Table 3.2. Field measurements included daily variations, establishing a response envelope, while the numerical model reflects average or weekly responses. The present study utilized Eq. 3.1 as the temperature model, and the temperature model for each bridge appears in Table 3.5. Vehicular loads are not included because the bridges were not open to traffic until December 2007. The comparisons include longitudinal displacements at top and bottom locations of abutments, girder bending moments near abutments, and girder axial forces. To permit direct comparison, numerical predictions included at-rest backfill pressures.

Table 3.5: Coefficients of Input Temperature Curve for Equation 3.1

Bridge	Mean Temperature (T_m) °C (F°)	Amplitude (A) °C (F°)	Phase lag (radian) (ϕ)
109	7.5 (45.5)	16.7 (30)	0.751
203	7.5 (45.5)	16.7 (30)	2.54
211	7.5 (45.5)	16.7 (30)	1.53
222	7.5 (45.5)	16.7 (30)	1.45

3.5.1 Bridge 109

Monitoring bridge 109 began in July 2006 (see Figure 3.24). Deck slab concrete was poured 487 days later than the date of girder manufacture, which was June 6, 2006. Measured and predicted responses of bridge 109 are presented in Figure 3.27. Measured and predicted longitudinal abutment displacements at top and bottom locations of the abutment appear in Figure 3.27(a) and (b). Measured and predicted girder bending moment appears in Figure 3.27(c). Measured and predicted girder axial force appears in Figure 3.27(d).

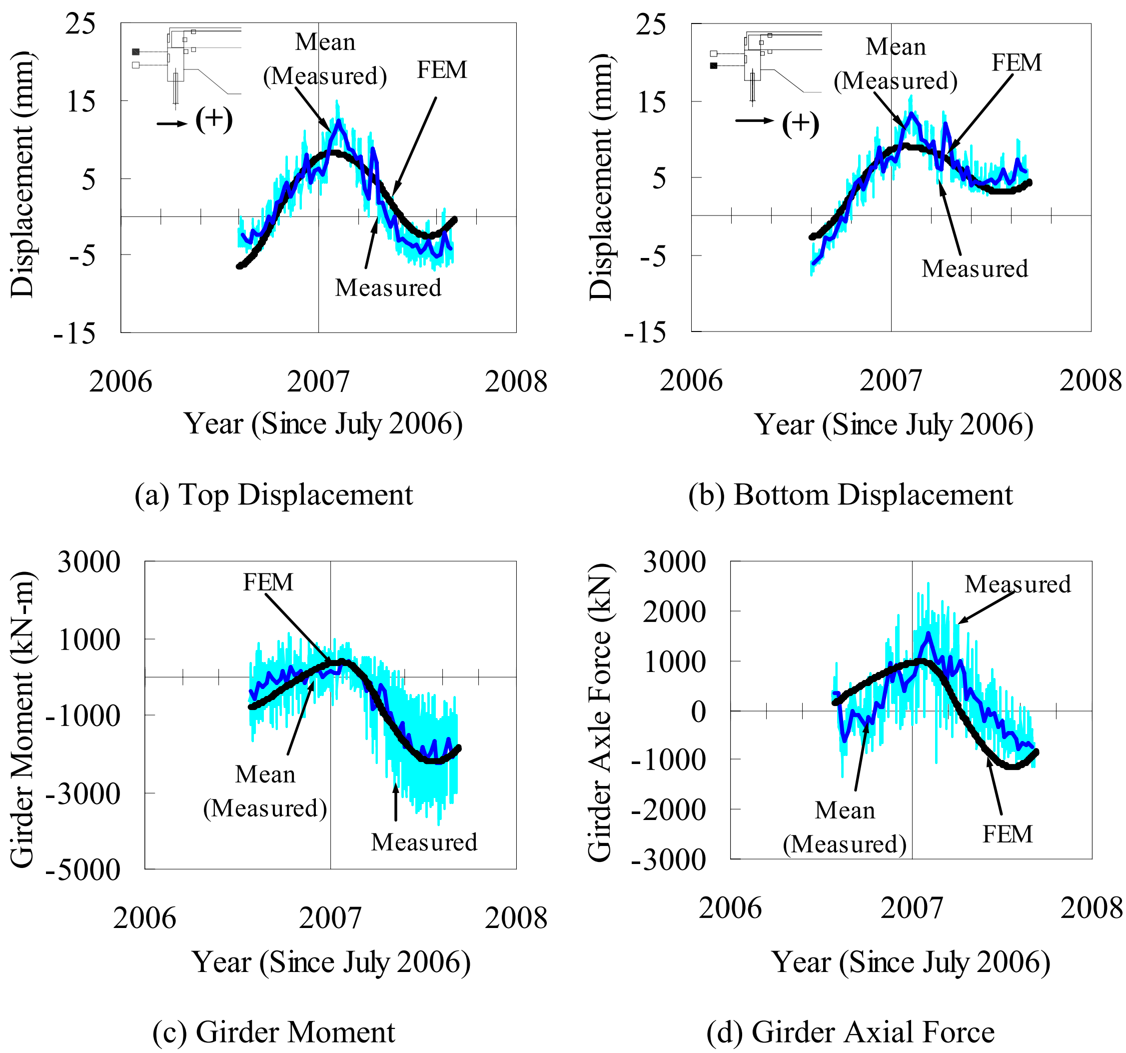

Figure 3.27: Measured and Predicted Bridge Response—Bridge 109

Displacements at the top location of the abutment accurately represent superstructure contraction and expansion movements due to superstructure temperature changes. Field measurements represent the abutment tendency to move fully back and forth while the nominal numerical model predictions are slightly accumulated. Both displacements at the abutment bottom location from field measurement and the nominal model prediction have a trend that displacements obviously accumulate. Compared to the preceding year, the lower bounds (minimum displacement) of the bottom location displacements increased, from -11.4 to 2.8 mm (-0.45 to 0.11 in) for field measurement and from -3.5 to 3.1 mm (-0.14 to 0.12 in) for the nominal model prediction. Maximum contraction displacements from field measurement at the top and bottom locations are 15.0 and 15.6 mm (0.59 and 0.61 in), respectively. Maximum contraction displacements of the nominal model prediction at the top and bottom locations are 8.2 and 9.0 mm (0.32 and 0.35 in), respectively.

Due to the superstructure thermal movement, girder bending moments fluctuate. During winter, negative girder moments decreased while negative girder moments increased during summer. However, girder moments have an apparent decreasing trend as the year goes on, which corresponds to abutment displacements. Compared to the preceding year, for both field measurements and nominal model predictions, the lower bounds (maximum negative bending moment) increased from -1665 to -3879 kN-m (-1228 to 2861 kip-ft) and from -979 to -3098 kN-m (-722 to -2285 kip-ft), respectively. The maximum positive bending moments from field measurements and nominal model predictions are 1143 and 798 kN-m (843 and 589 kip-ft), respectively.

3.5.2 Bridge 203

Monitoring of bridge 203 began in November 2002 (see Figure 3.24). Deck slab concrete was poured 121 days later than the date of girder manufacture, which was September 17, 2002. Measured and predicted bridge responses of bridge 203 appear in Figure 3.28.

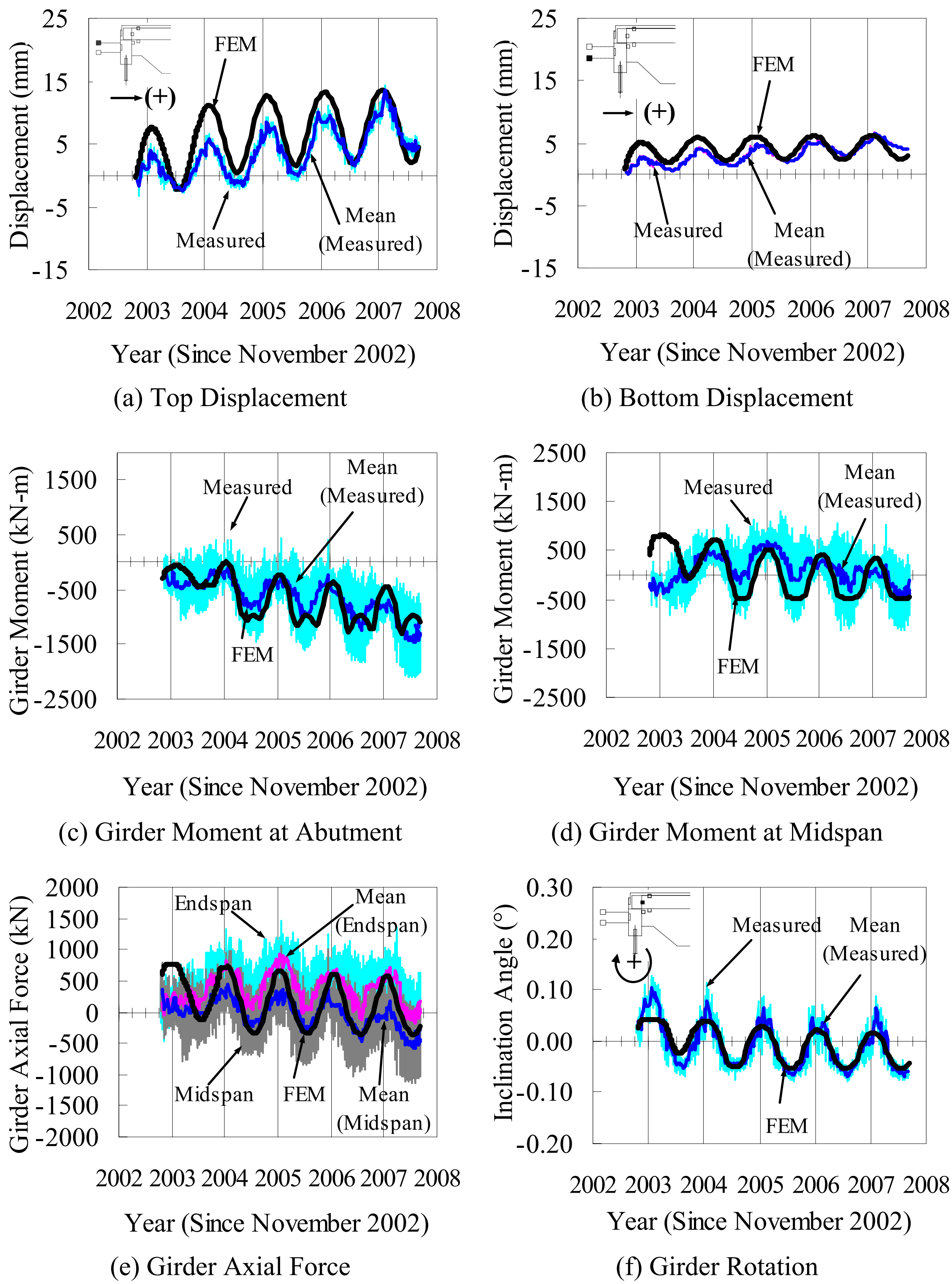

(a) Top Displacement

(b) Bottom Displacement

(c) Girder Moment at Abutment

(d) Girder Moment at Midspan

(e) Girder Axial Force

(f) Girder Rotation

Figure 3.28: Measured and Predicted Bridge Response—Bridge 203

Measured and predicted longitudinal abutment displacements at the top and bottom locations of the abutment are in Figures 3.28(a) and (b). Both top and bottom displacements from field measurement and nominal model prediction obviously accumulate. Compared to the preceding year, from field measurement, the lower bounds (minimum displacement) of bottom location displacements increased from 0.1 to 0.9 to 1.3 to 2.3 to 3.2 to 4.0 mm (0.004 to 0.035 to 0.051 to 0.091 to 0.13 to 0.16 in). Compared to the preceding year, from the nominal model prediction, the lower bounds of the bottom location displacements increased from 1.0 to 1.9 to 2.1 to 2.3 to 2.3 to 2.4 mm (0.039 to 0.075 to 0.083 to 0.091 to 0.091 to 0.094 in). Maximum contraction displacements from field measurement at the top and bottom locations are 14.0 and 6.4 mm (0.55 and 0.25 in), respectively. Maximum contraction displacements of nominal model prediction at top and bottom location are 13.5 and 6.1 mm (0.53 and 0.24 in), respectively. Abutment height of bridge 203 is relatively higher than other bridges, and thus the bottom location displacements fluctuate less and accumulate more.

Measured and predicted girder bending moments at endspan and midspan near the integral abutment (abutment 2) are presented in Figures 3.28(c) and (d), respectively. Compared to the preceding year, from both field measurement and nominal model, the lower bounds (maximum negative bending moment) increase. Both moments fluctuate according to the temperature variation.

Figure 3.28(e) presents a comparison between measured and predicted girder axial force. The field measurements derive from two locations—endspan and midspan. The girder axial forces from the numerical results are constant throughout the bridge span. Overall trends of both measured and predicted girder axial forces tend to slightly decrease over time. Similar to the trend to bridge 109, but at a lower magnitude, predicted axial force varies between -390 and 900kN (-88 and 202 kips), which covers both ranges of mean girder axial forces at midspan and endspan. Mean girder axial force at midspan varies between -590 and 390kN (-133 and 88 kips) and girder axial force at endspan varies between -170 and 900kN (-38 and 202 kips).

Measured and predicted girder rotations appear in Figure 3.28(f). The measured and predicted girder rotations gradually decrease during the entire year. The measured girder rotations oscillate between -0.06 and 1.2 degrees and the predicted girder rotations oscillate between -0.05 and 0.03 degrees. These girder rotation results correspond to abutment displacements. The field measurements during the first winter produced relatively larger positive rotation of 1.23 degrees, while the nominal model prediction was 0.04 degrees. However, the nominal model prediction closely follows the average field measurements during the remainder of the monitoring period.

3.5.3 Bridge 211

Monitoring bridge 211 began in September 2004 (see Figure 3.29). Deck slab concrete was poured 264 days later than the date of girder manufacture, which was July 20, 2004. Measured and predicted bridge responses of bridge 211 are presented in Figure 3.29.

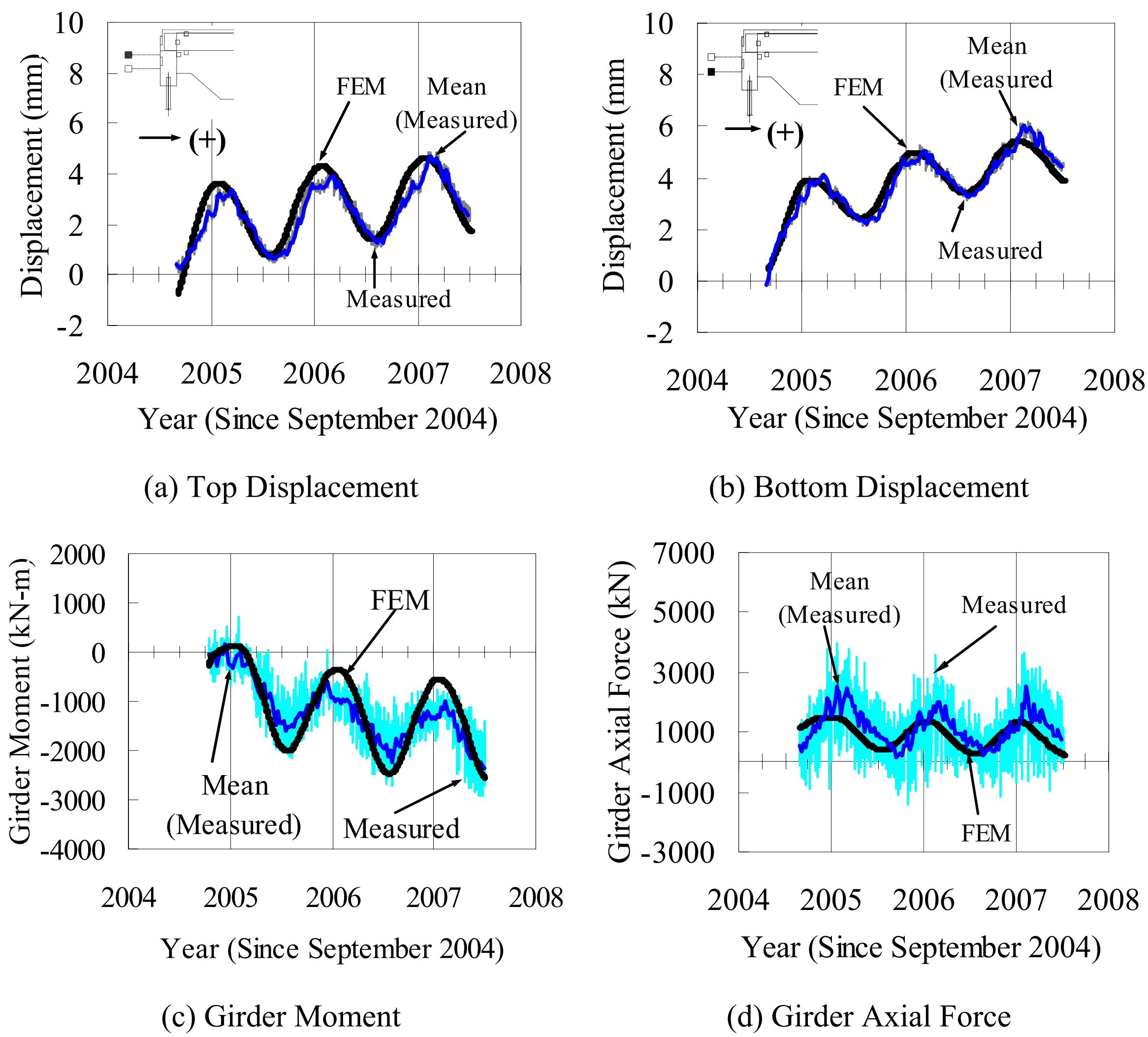

Figure 3.29: Measured and Predicted Bridge Response—Bridge 211

Measured and predicted longitudinal abutment displacements at the top and bottom appear in Figures 3.29(a) and (b). Both the measured top and bottom displacements and numerical model prediction displacements have an observable accumulative trend. Compared to the preceding year, the lower bound (minimum displacement) of the measured abutment bottom displacement increased from -0.3 to 2.1 to 3.1 to 4.3 mm (-0.012 to 0.083 to 0.12 to 0.17 in). Compared to the preceding year, the lower bound of predicted abutment bottom displacement increased from -1.16 to 2.2 to 3.2 to 3.6 mm (0.046 to 0.087 to 0.13 to 0.14 in). Maximum measured contraction displacements at the top and bottom locations are 5.5 and 6.1 mm (0.22 and 0.24 in), respectively. Maximum predicted contraction displacements at top and bottom location are 4.9 and 5.2 mm (0.19 and 0.20 in), respectively.

Measured and predicted girder bending moments appear in Figure 3.29(c). Compared to preceding year, for both measured and predicted, the lower bound (maximum negative bending moment) clearly increase. The lower bound of measured girder bending moment varies from -265 to -1594 to -2237 to -2359 kN-m (-195 to -1176 to 1650 to 1740 kip-ft) over a 4 year period. The lower bound of predicted girder bending moment varies from -292 to -2016 to -2469 to -2570 kN-m (215 to 1487 to 1821 to 1895 kip-ft) over a 4 year period. Maximum positive measured and predicted bending moments are 721 and 130 kN-m (532 and 96 kip-ft), respectively. The increasing tendency for negative bending moment matches with the tendency for contraction of the abutment displacement.

Measured and predicted girder axial forces appear in Figure 3.29(d). Overall trends of both measured and predicted girder axial forces tend to fluctuate from year-to-year. Compression axial force increases during summer and decreases during winter. The upper bound of measured girder bending moment varies from 2354 to 1796 to 1779 kN (529 to 404 to 400 kips). The upper bound of predicted girder bending moment varies from 1097 to 1082 to 1081 kN (247 to 243 to 243 kips).

3.5.4 Bridge 222

Monitoring bridge 222 began in October 2003 (see Figure 3.30). Deck slab concrete was poured 168 days after the date of girder manufacture, which was July 16, 2003. Measured and predicted bridge responses of bridge 222 appear in Figure 3.30.

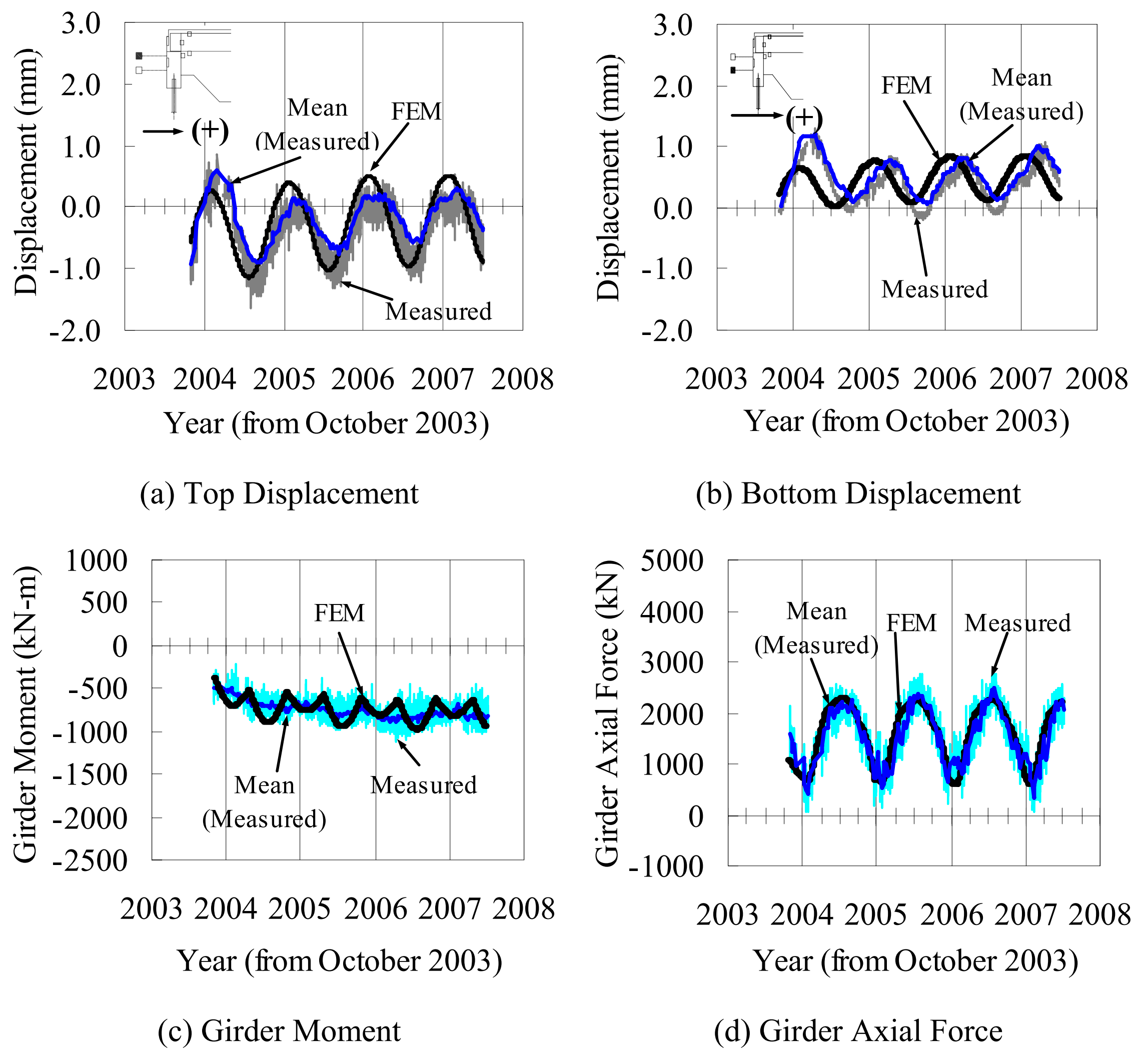

Figure 3.30: Measured and Predicted Bridge Response—Bridge 222

Measured and predicted longitudinal abutment displacements at the top and bottom locations of the abutment are in Figures 3.30(a) and (b). Both the top and bottom displacements of field measurement and nominal model prediction have a slight accumulation due to a relatively short bridge length. Compared to the preceding year, the measured lower bounds (minimum displacement) of bottom displacements increased from -1.1 to -1.1 to -1.0 to -0.8 mm (-0.044 to -0.042in to -0.039 to -0.031 in). The predicted lower bounds of bottom displacements increased from -0.7 to -1.1 to -1.0 to -1.0 to -0.9 mm (-0.027 to -0.043 to -0.039 to -0.038 to -0.035 in). Maximum contraction displacements of field measurement at the top and bottom locations are 1.1 and 1.3 mm (0.043 and 0.051 in), respectively. Maximum contraction displacements of the nominal model prediction at the top and bottom locations are 0.5 and 0.8 mm (0.02 and 0.031 in), respectively. During the first winter, field measurements experienced significant contraction differentiation due to sever temperature changes.

Measured and predicted girder bending moments appear in Figure 3.30(c). Girder bending moment variation of bridge 222 produced a gradually decreasing trend and did not fluctuate according to a temperature variation. Soil-pile interaction and abutment-backfill interaction produced severe influence on girder bending moment variation. For both field measurement and nominal model prediction, the lower bounds (maximum negative bending moment) clearly decreased for the given years, when compared to the preceding year. The lower bound of a mean measured girder bending moment varies -516 to -768 to -854 to -899 to -866 kN-m (-380 to -566 to -630 to -663 to -639 kip-ft) over 5 years. The lower bound of nominal numerical model varies -643 to -897 to -947 to -973 to -945kN-m (-474 to -661 to -698 to -718 to -697 kip-ft)over 5 years. Bridge 222 produced the smallest moment variation and magnitude of girder bending moments.

Measured and predicted girder axial force appears in Figure 3.30(d). Overall trends of both measured and predicted girder axial forces tend to oscillate within the given range rather than decrease or increase over the years. Compression axial force increases during summer and decreases during winter. Compared to the preceding winter, the increase of compression axial force increase 1535 to 1572 to 1624 to 1617 kN (345 to 353 to 365 to 363 kips) according to the nominal model prediction, and 1280 to 1952 to 1971 to 1456 kN (288 to 439 to 443 to 327 kips) according to 7 day mean measurements.

3.6 Summary

The present study developed numerical modeling methodologies to accommodate long-term simulations and probabilistic simulations. To validate the numerical modeling methodology, four numerical models of field tested IABs have been built and compared to field monitored responses. The key components of the numerical model include abutment-backfill interaction, soil-pile interaction and construction joints. IAB loads include backfill pressure, time-dependent effects, temperature change and temperature gradient. The developed numerical model requires relatively low computer resources and run times. Also, the numerical model effectively simulates the measured IAB responses.

Maximum abutment displacements at the tops and bottoms of four IABs appear in Figures 3.31 and 3.32. The numerical model predictions were compared to 6-hour extreme measurements, 7-day mean measurements and free expansions. The free expansion predictions by Eq. 2.1 were calculated to demonstrate current AASHTO design estimation of IAB thermal movements. For bridge 203, two times of the bridge length was considered because one spread footing abutment stands on bedrock. Coefficients for Eq. 2.1 were selected from Table 2.1 and both displacements corresponding to the rise and fall of temperature were considered. The nominal numerical model simulates the mean measurements with an average -3% difference. The extreme measurements and free expansion prediction average 23% and 106% larger than mean measurements.

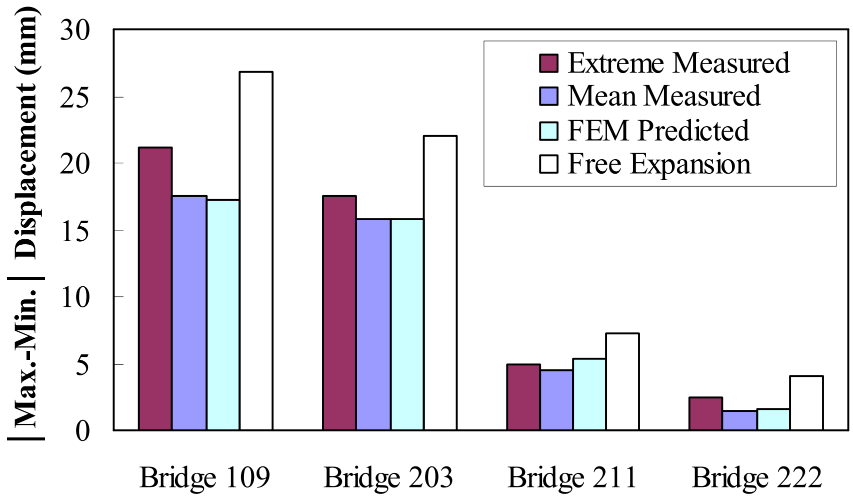

Figure 3.31: Comparison of Maximum Thermal Movements at Abutment Top

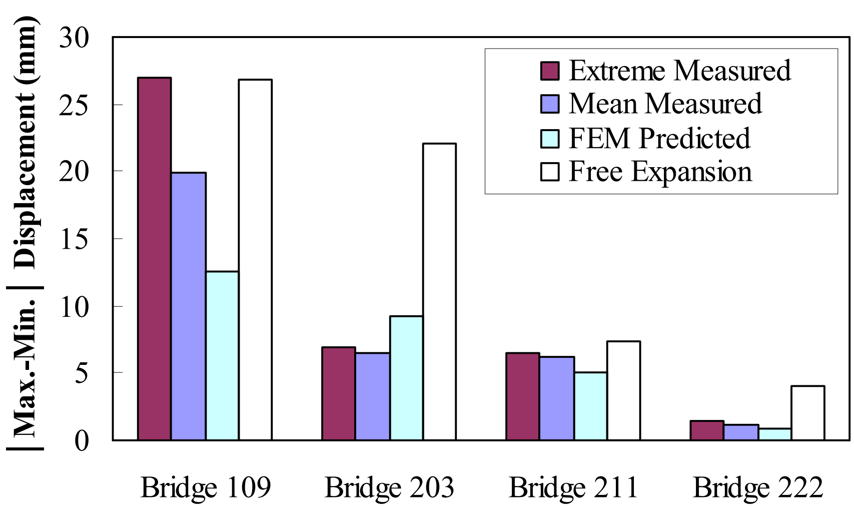

Figure 3.32: Comparison of Maximum Thermal Movements at Abutment Bottom

Girder bending moments of all four IABs at each endspan were compared and results appear in Figure 3.33. Obviously, the bridge lengths significantly influenced bridge moments. The nominal numerical model closely simulated the mean measurement with differences of 14%. The extreme responses average 96% larger than mean measurements.

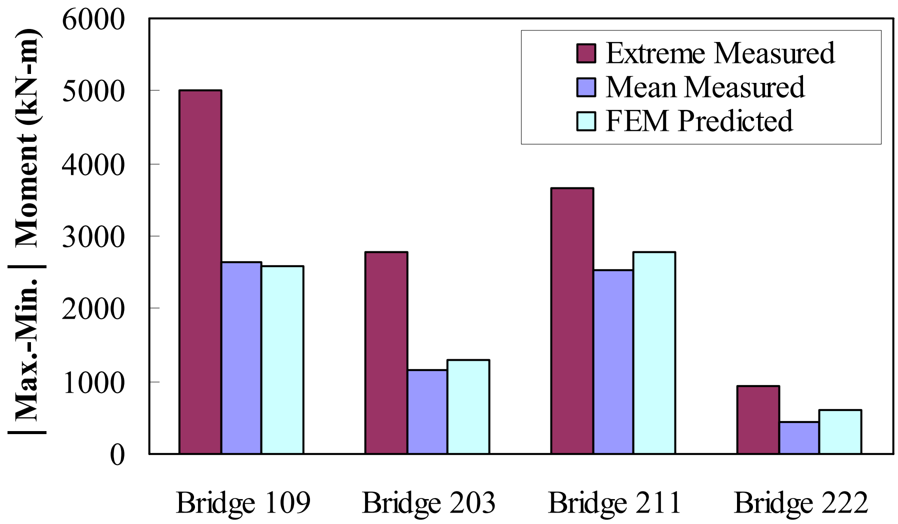

Figure 3.33: Comparison of Maximum Girder Bending Moment

Girder axial forces of all four IABs were compared and results appear in Figure 3.34. The nominal numerical model predicted the mean measurements with differences of -17%. The extreme measurements average 87% larger than the mean measurements.

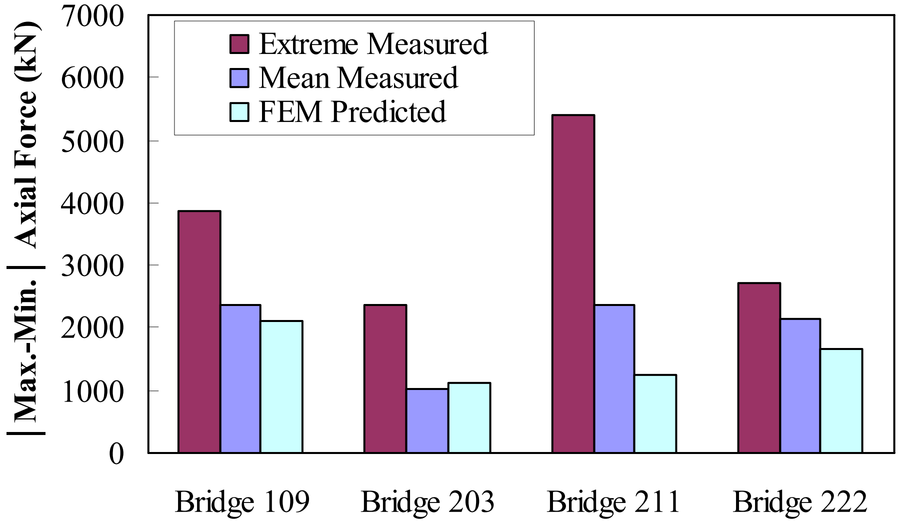

Figure 3.34: Comparison of Maximum Girder Axial Force

Chapter 4

DEVELOPMENT OF IAB REPONSE PREDICTION MODELS

4.1 Introduction

For the present study, a parametric study established influential key parameters of IAB behavior and a prediction model for IAB responses. The parametric study, based on the calibrated nominal numerical models in Chapter 3, also investigated key parameters and the strength of key parameters for IAB responses. Previous studies [30, 42, 51, 125] with a limited number of parameters have been performed, but are insufficient to allow expansion to various other bridge types, such as longer span length and pile supports in clay or sand. Based on a preliminary analysis, five selected key parameters cover commonly encountered IABs.

The parametric study considers five parameters: (1) thermal expansion coefficient; (2) bridge length; (3) backfill height; (4) backfill stiffness; and (5) soil stiffness around piles. Three variables from each parameter result in 243 parametric study cases (see Table 4.1). The present study investigates maximum or minimum long-term critical responses during the expected 75-year bridge life: (1) bridge axial force; (2) bridge bending moment; (3) pile lateral force; (4) pile moment; and (5) pile head/abutment displacement. The parametric study results of the critical responses form the basis for nominal prediction models for a probabilistic study.

Table 4.1: Parametric Study Cases

Case ID	Thermal Expansion Coefficient (α) $\times 10^{-6}$ /°C ($\times 10^{-6}$ /F°)	Total Bridge Length (L) *m (ft)*	Backfill Height (H) *m (ft)*	Backfill Stiffness (B) (Table 4.4)	Soil Stiffness around Piles (P) (Table 4.5)
1					*High*
2				*High*	*Intermediate*
3					*Low*
4					*High*
5			3.0 (10)	*Intermediate*	*Intermediate*
6					*Low*
7					*High*
8				*Low*	*Intermediate*
9					*Low*
10					*High*
11				*High*	*Intermediate*
12					*Low*
13					*High*
14	5.4 (3.0)	18.3 (60)	4.6 (15)	*Intermediate*	*Intermediate*
15					*Low*
16					*High*
17				*Low*	*Intermediate*
18					*Low*
19					*High*
20				*High*	*Intermediate*
21					*Low*
22					*High*
23			6.1 (20)	*Intermediate*	*Intermediate*
24					*Low*
25					*High*
26				*Low*	*Intermediate*
27					*Low*

Table 4.1 Parametric Study Cases (Cont.)

Case ID	Thermal Expansion Coefficient (α) $\times 10^{-6}$ /°C ($\times 10^{-6}$ /F°)	Total Bridge Length (L) *m (ft)*	Backfill Height (H) *m (ft)*	Backfill Stiffness (B) (Table 4.4)	Soil Stiffness around Piles (P) (Table 4.5)
55	5.4 (3.0)	121.9 (400)	3.0 (10)	*High*	*High*
56					*Intermediate*
57					*Low*
58				*Intermediate*	*High*
59					*Intermediate*
60					*Low*
61				*Low*	*High*
62					*Intermediate*
63					*Low*
64			4.6 (15)	*High*	*High*
65					*Intermediate*
66					*Low*
67				*Intermediate*	*High*
68					*Intermediate*
69					*Low*
70				*Low*	*High*
71					*Intermediate*
72					*Low*
73			6.1 (20)	*High*	*High*
74					*Intermediate*
75					*Low*
76				*Intermediate*	*High*
77					*Intermediate*
78					*Low*
79				*Low*	*High*
80					*Intermediate*
81					*Low*

Table 4.1: Parametric Study Cases (Cont.)

Case ID	Thermal Expansion Coefficient (α) $\times 10^{-6}$ /°C ($\times 10^{-6}$ /F°)	Total Bridge Length (L) *m (ft)*	Backfill Height (H) *m (ft)*	Backfill Stiffness (B) (Table 4.4)	Soil Stiffness around Piles (P) (Table 4.5)
82	9.9 (5.5)	18.3 (60)	3.0 (10)	*High*	*High*
83					*Intermediate*
84					*Low*
85				*Intermediate*	*High*
86					*Intermediate*
87					*Low*
88				*Low*	*High*
89					*Intermediate*
90					*Low*
91			4.6 (15)	*High*	*High*
92					*Intermediate*
93					*Low*
94				*Intermediate*	*High*
95					*Intermediate*
96					*Low*
97				*Low*	*High*
98					*Intermediate*
99					*Low*
100			6.1 (20)	*High*	*High*
101					*Intermediate*
102					*Low*
103				*Intermediate*	*High*
104					*Intermediate*
105					*Low*
106				*Low*	*High*
107					*Intermediate*
108					*Low*

Table 4.1: Parametric Study Cases (Cont.)

Case ID	Thermal Expansion Coefficient (α) $\times 10^{-6}$ /°C ($\times 10^{-6}$ /F°)	Total Bridge Length (L) *m (ft)*	Backfill Height (H) *m (ft)*	Backfill Stiffness (B) (Table 4.4)	Soil Stiffness around Piles (P) (Table 4.5)
109	9.9 (5.5)	61.0 (200)	3.0 (10)	*High*	*High*
110					*Intermediate*
111					*Low*
112				*Intermediate*	*High*
113					*Intermediate*
114					*Low*
115				*Low*	*High*
116					*Intermediate*
117					*Low*
118			4.6 (15)	*High*	*High*
119					*Intermediate*
120					*Low*
121				*Intermediate*	*High*
122					*Intermediate*
123					*Low*
124				*Low*	*High*
125					*Intermediate*
126					*Low*
127			6.1 (20)	*High*	*High*
128					*Intermediate*
129					*Low*
130				*Intermediate*	*High*
131					*Intermediate*
132					*Low*
133				*Low*	*High*
134					*Intermediate*
135					*Low*

Table 4.1: Parametric Study Cases (Cont.)

Case ID	Thermal Expansion Coefficient (α) $\times 10^{-6}$ /°C ($\times 10^{-6}$ /F°)	Total Bridge Length (L) *m (ft)*	Backfill Height (H) *m (ft)*	Backfill Stiffness (B) (Table 4.4)	Soil Stiffness around Piles (P) (Table 4.5)
136	9.9 (5.5)	121.9 (400)	3.0 (10)	*High*	*High*
137					*Intermediate*
138					*Low*
139				*Intermediate*	*High*
140					*Intermediate*
141					*Low*
142				*Low*	*High*
143					*Intermediate*
144					*Low*
145			4.6 (15)	*High*	*High*
146					*Intermediate*
147					*Low*
148				*Intermediate*	*High*
149					*Intermediate*
150					*Low*
151				*Low*	*High*
152					*Intermediate*
153					*Low*
154			6.1 (20)	*High*	*High*
155					*Intermediate*
156					*Low*
157				*Intermediate*	*High*
158					*Intermediate*
159					*Low*
160				*Low*	*High*
161					*Intermediate*
162					*Low*

Table 4.1: Parametric Study Cases (Cont.)

Case ID	Thermal Expansion Coefficient (α) $\times 10^{-6}$ /°C ($\times 10^{-6}$ /F°)	Total Bridge Length (L) *m (ft)*	Backfill Height (H) *m (ft)*	Backfill Stiffness (B) (Table 4.4)	Soil Stiffness around Piles (P) (Table 4.5)
163	14.4 (8.0)	18.3 (60)	3.0 (10)	*High*	*High*
164					*Intermediate*
165					*Low*
166				*Intermediate*	*High*
167					*Intermediate*
168					*Low*
169				*Low*	*High*
170					*Intermediate*
171					*Low*
172			4.6 (15)	*High*	*High*
173					*Intermediate*
174					*Low*
175				*Intermediate*	*High*
176					*Intermediate*
177					*Low*
178				*Low*	*High*
179					*Intermediate*
180					*Low*
181			6.1 (20)	*High*	*High*
182					*Intermediate*
183					*Low*
184				*Intermediate*	*High*
185					*Intermediate*
186					*Low*
187				*Low*	*High*
188					*Intermediate*
189					*Low*

Table 4.1: Parametric Study Cases (Cont.)

Case ID	Thermal Expansion Coefficient (α) $\times 10^{-6}$ /°C ($\times 10^{-6}$ /F°)	Total Bridge Length (L) *m (ft)*	Backfill Height (H) *m (ft)*	Backfill Stiffness (B) (Table 4.4)	Soil Stiffness around Piles (P) (Table 4.5)
190	14.4 (8.0)	61.0 (200)	3.0 (10)	*High*	*High*
191					*Intermediate*
192					*Low*
193				*Intermediate*	*High*
194					*Intermediate*
195					*Low*
196				*Low*	*High*
197					*Intermediate*
198					*Low*
199			4.6 (15)	*High*	*High*
200					*Intermediate*
201					*Low*
202				*Intermediate*	*High*
203					*Intermediate*
204					*Low*
205				*Low*	*High*
206					*Intermediate*
207					*Low*
208			6.1 (20)	*High*	*High*
209					*Intermediate*
210					*Low*
211				*Intermediate*	*High*
212					*Intermediate*
213					*Low*
214				*Low*	*High*
215					*Intermediate*
216					*Low*

Table 4.1: Parametric Study Cases (Cont.)

Case ID	Thermal Expansion Coefficient (α) $\times 10^{-6}$ /°C ($\times 10^{-6}$ /F°)	Total Bridge Length (L) *m (ft)*	Backfill Height (H) *m (ft)*	Backfill Stiffness (B) (Table 4.4)	Soil Stiffness around Piles (P) (Table 4.5)
217	14.4 (8.0)	121.9 (400)	3.0 (10)	*High*	*High*
218					*Intermediate*
219					*Low*
220				*Intermediate*	*High*
221					*Intermediate*
222					*Low*
223				*Low*	*High*
224					*Intermediate*
225					*Low*
226			4.6 (15)	*High*	*High*
227					*Intermediate*
228					*Low*
229				*Intermediate*	*High*
230					*Intermediate*
231					*Low*
232				*Low*	*High*
233					*Intermediate*
234					*Low*
235			6.1 (20)	*High*	*High*
236					*Intermediate*
237					*Low*
238				*Intermediate*	*High*
239					*Intermediate*
240					*Low*
241				*Low*	*High*
242					*Intermediate*
243					*Low*

4.2 Deterministic Parameters

This section discusses the determination and range of five key parameters. The construction sequence and environmental condition is also an influential factor for IAB response. This study determined a representative bridge construction timeline that is applicable for the entire parametric study cases. Girder section designs are also designed for selected bridge dimensions.

The selected five parameters arise from widely-accepted bridge design codes, previous research and IAB monitoring experience [79, 80]. Thermal expansion coefficient and total bridge length are the essential parameters to determine thermally induced bridge movements in accordance with AASHTO LRFD [4] and AASHTO Guide Specifications [5]. Thus, thermal expansion coefficient and total bridge length parameters are considered in the parametric study. Also, the pile performance and behavior is considerably significant for determining IAB behavior [40]. Other studies [30, 41, 51] found that the stiffness of the soils around supporting piles and backfill height have significant effects on IAB behavior. Thus, backfill stiffness and soil stiffness around piles must be included in the parametric study. However backfill stiffness and soil stiffness around piles are dependent on many parameters, such as soil unit weight, internal friction angle and undrained shear strength. To consider various range of backfill stiffness and soil stiffness around piles, the present study determined maximum and minimum stiffness properties within the practical ranges. The following soil boundary section provides a more detailed explanation of the stiffness property derivation process.

4.2.1 Bridge Construction Timeline

The bridge construction timeline influences IAB behavior due to time dependent effects inherent in the concrete deck, backwall, and superstructure. Prior to completion of construction, all structural elements are substantially free to undergo creep and shrinkage with no significant effect on the substructure. After the concrete backwall, girders and deck slabs become structurally integrated, the bridge superstructure and substructure become a unit, developing complex frame action resisting vertical loads as well as horizontal loads.

The present study investigated the actual construction sequence and concrete cast date of field tested IABs. The bridges 109 experienced an exceptional long delay to place concrete because of pyrite contamination problem in the construction site. Deck slab concrete placement dates for four filed tested bridges appear in Table 4.2 and backwall concrete placement dates appear in Table 4.3.

Table 4.2: Deck Slab Concrete Placement Date of Four Field Tested IABs

Bridge No.	Deck Placement Date	Starting Date (Date of Girder Manufacture)
109	Span 1: 6/6/2006 (487 days) Span 2: 6/6/2006 (238 days) Span 3: 6/20/2006 (252 days) Span 4: 6/20/2006 (501 days)	Span 1&4: approx. 02/05/2005 Span 2&3: approx. 10/12/2005
203	Span 1, 2, 3: 9/17/02 (121 days)	5/20/2002
211	7/20/04 (266 days)	10/29/2003
222	7/16/03 (169 days)	1/29/2003

Note: Average deck placement = 253 days from girder manufacture date

Table 4.3: Integral Backwall Placement Date of Field Tested IABs

Bridge No.	Abutment 1	Abutment 2	Starting Date (from Girder Manufacture)
109	6/29/2006 (510 days)	6/29/2006 (510 days)	Span 1&4: 02/05/2005
203	–	9/19/2002 (123 days)	5/20/2002
211	7/23/2004 (269 days)	8/9/2004 (286 days)	10/29/2003
222	7/24/2003 (177 days)	7/28/2003 (181 days)	1/29/2003

Note 1: Average backwall placement = 273 days from girder manufacture date
Note 2: Average delay between abutment 1 and 2 = 5 days

Cast-in-place concrete deck slabs and backwalls on abutments of four IABs averaged 253 and 273 days after girder manufacture, respectively. For bridge 109, more time elapsed before placement of deck slab concrete. However, once the construction started, backwall concrete was poured only 20 days after placing deck slab concrete. Therefore, it is reasonable that the average deck concrete placement date is between 60 to 180 days after girder manufacture. Backwall concrete placement date is between 10 to 30 days after deck concrete placement. Based on these assumptions, a representative bridge construction timeline is assumed and presented in Figure 4.1. The parametric study assumes that deck concrete is placed 100 days after girder manufacture and the backwall is placed 20 days after the deck placement.

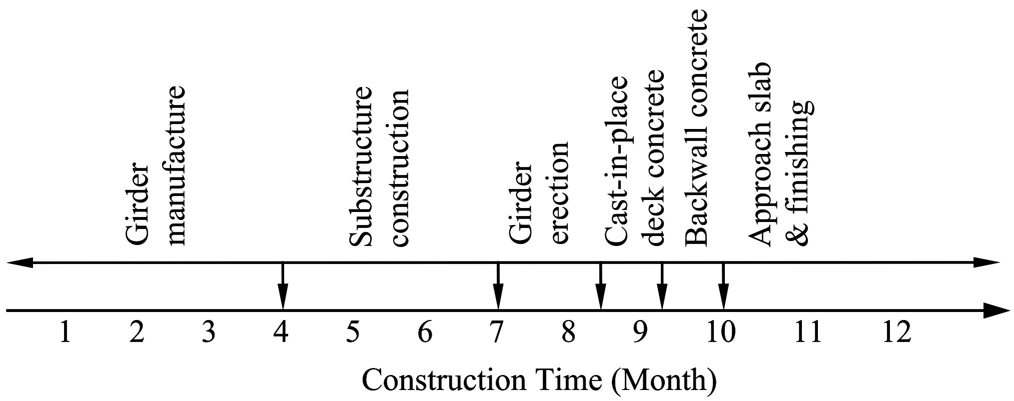

Figure 4.1: Typical Bridge Construction Timeline

4.2.2 Thermal Expansion Coefficient

The thermal expansion coefficient, α, determines superstructure strain in response to concrete temperature changes. Estimates of the concrete thermal expansion coefficient vary significantly due to variations in concrete mix properties, aggregate properties and proportions, water to cement ratio, relative humidity, age of concrete, and other factors. When test data is not available, AASHTO LRFD [4] recommends α equal to 10.8×10^{-6}/°C (6.0×10^{-6}/°F) with a range of (3 to 8×10^{-6}/°F). Nilson [94] reported that α generally varies from 7.2 to 12.6×10^{-6}/°C (4 to 7×10^{-6}/°F). Oesterle et al. [105] reported a mean of 8.77×10^{-6}/°C (4.87×10^{-6}/°F) and a range of 4.1 to 14.6×10^{-6}/°C (2.3 to 8.1×10^{-6}/°F). As presented in Table 4.1, the present study considers low, intermediate and high values for α as 5.4, 9.9, 14.4×10^{-6}/°C (3.0, 5.5, 8.0×10^{-6}/°F), as representatives of expected concrete thermal expansion coefficients.

4.2.3 Bridge Length and Backfill Height

The present study adopted a common bridge superstructure cross-section that consists of four precast, prestressed concrete girders with concrete compressive strength, f_c' = 55.2 MPa (8 ksi) and a cast-in-place concrete deck with f_c' = 27.6 MPa (4 ksi) (see Figure 4.2). An adopted common IAB foundation configuration consists of a single row of eleven steel H-piles [40] supporting a cast-in-place wall-type abutment with f_c' = 20.7 MPa (3 ksi) supporting girders and a backwall with f_c' = 27.6 MPa (3.5 ksi).

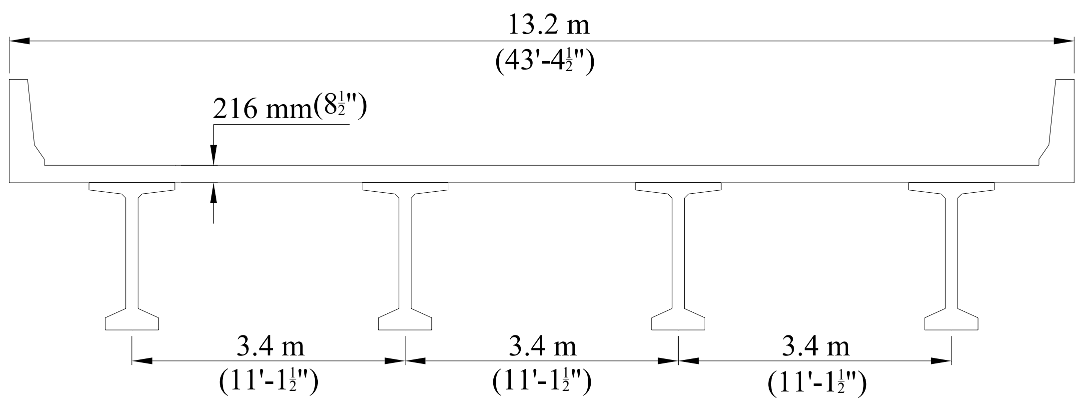

Figure 4.2: Typical Cross Section for Parametric Study

The two bridge dimensional parameters considered in the parametric study are bridge length (L) and backfill height (H). Bridge lengths were selected to represent short- to medium-long bridges. Backfill heights were selected to represent stub type to medium-high abutments. The bridge lengths considered are 18.3, 61.0, 121.9 m (60, 200, 400 ft). H represents the total backfill height from the bottom of the abutment/pile cap to the bottom of the approach slab. The roadway elevation was maintained for each IAB while the abutment below the girder seat height (h_2 in Figure 4.3) was varied due to different girder heights (h_1 in Figure 4.3) for different bridge lengths. As a result of this convention, the construction joint between backwall and abutment have different elevations as the bridge length changed. Each girder for a different bridge length was designed in accordance with the AASHTO LRFD [4] and PCI Bridge manual [109].

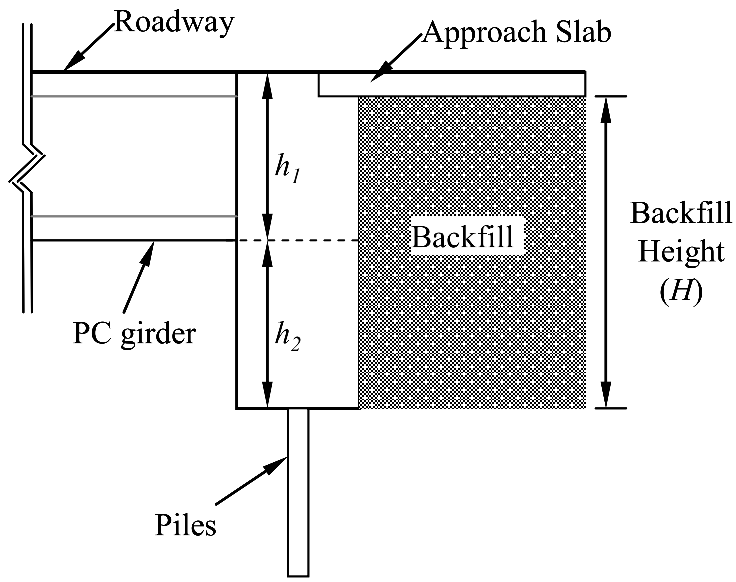

Figure 4.3: Backfill Height Parameter

4.2.4 Girder Design

Three total bridge lengths were considered and designed: 4-span continuous for 121.9 m (400 ft) total bridge span length; 2-span continuous for 61.0 m (200 ft), and a single span of 18.3 m (60 ft). The present study adopted a common bridge superstructure cross-section that consists of four precast, prestressed concrete girders with concrete compressive strength, f_c' = 55.2 MPa (8 ksi) and a cast-in-place concrete deck with f_c' = 27.6 MPa (4 ksi). Girder sections were designed in accordance with AASHTO LRFD [4] and PCI Bridge manual [109]. For the single span bridge of 18.3 m (60 ft), AASHTO

Type III girder was selected. AASHTO-PCI BT72 girders were used for the 61.0 m (200 ft) and 121.9 m (400 ft) span length. Detailed girder cross-section and prestressing tendon profiles appear in Figure 4.4.

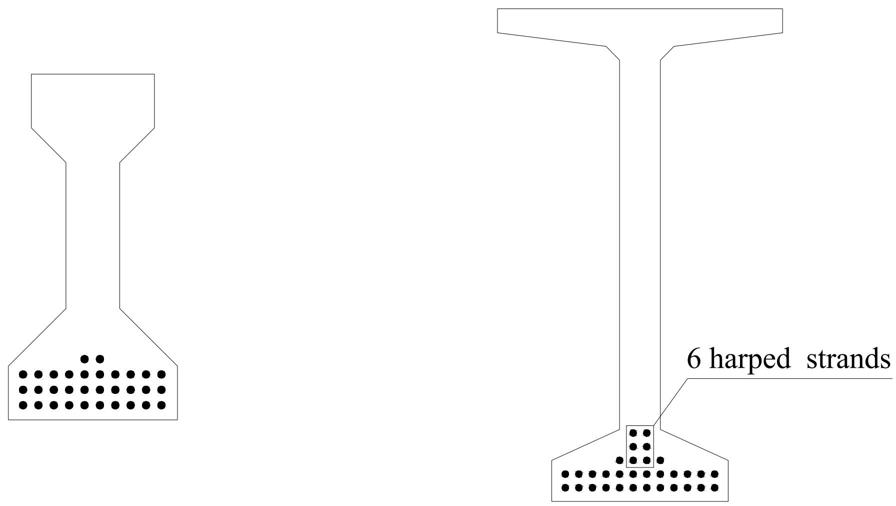

AASHTO Type III

(a) 60 ft span girder (Typ.)

AASHTO-PCI BT-72

(b) 200 and 400 ft girder (Typ.)

Figure 4.4: Designed Girder Cross-section

4.2.5 Soil Boundaries

Soil properties of backfills and soils around supporting piles were considered in the parametric study. Soil-structure interaction, dependent on soil properties, is a crucial factor that determines IAB global behavior. The soil-structure interaction characteristics, however, are difficult to consider in a parametric study because soil strength is dependent on many parameters such as soil density, friction angle, undrained shear strength, etc. Backfills behind abutments, due to soil density, exert lateral loads during bridge contraction while backfills also exert resistances during bridge expansion. Thus, the abutment backfill parameter was established based on soil density and friction angle which correspond to load and resistance of backfill, respectively. On the other hand, soil layers around supporting piles only resist bridge loads and movement. Thus, the present study only considers the resistance of supporting piles. In the present study, the variation of soil-structure interaction is represented as the resistance of abutment backfill and resistance of supporting pile. The resistances were developed to cover typical soil properties based on field tested data and extensive literature review.

4.2.5.1 Backfills stiffness

The parametric study also considers backfill property variation. Characteristics and variations of typical backfill soil properties were investigated from literature [24, 36, 44, 80, 123] and appear in Table 4.4.

Table 4.4: Backfill Properties and Range Determination

Property	Intermediate	Standard Deviation	High	Low
Density (ρ) kN/m^3 (pcf)	18.7 (119)	0.6 (3.6)	19.3 (123)	18.2 (116)
Angle of friction (ϕ_f) (Degree)	34	3.4	37.4	30.6
Subgrade Modulus (K_h) MN/m^3 (pci)	12 (43.8)	6 (21.2)	18 (65)	6 (22.5)

Density and friction angle of backfill soils of field tested bridges were all the same [79, 80], and these parameters were assumed as mean values. For the subgrade modulus, field measurements were analyzed using backfill pressure and abutment displacement (see Figure 4.5).

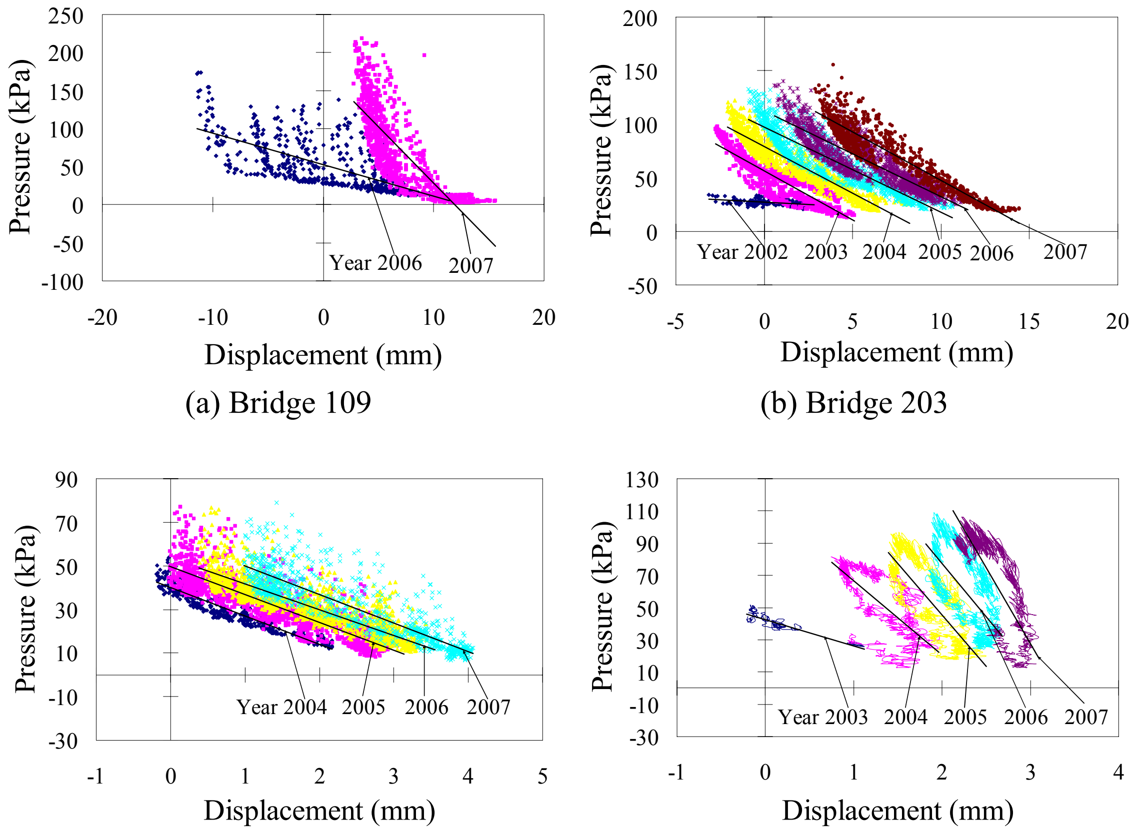

(a) Bridge 109 (b) Bridge 203

(c) Bridge 211 (d) Bridge 222

Figure 4.5: Backfill Pressure versus Displacement of Abutment

Each of field tested bridge responses was plotted and the response variation of each year was fitted using a linear line. The slope representing each year tends to be constant value because all backfill materials and backfill compaction condition were the same. Subsequently, the obtained slopes (subgrade modulus) of each bridge were averaged to obtain a representative subgrade modulus for each bridge. The results appear in Figure 4.6.

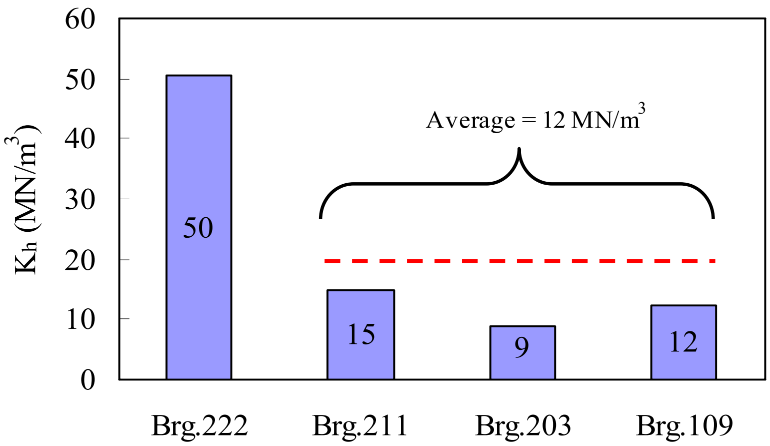

Figure 4.6: Subgrade Modulus from Field Tests

The subgrade modulus of bridge 222 was significantly larger than that of other bridges while all backfill materials are the same. This abnormality may be caused because the bridge length that influences the magnitude of the thermal movement is short. Thus, the subgrade modulus of bridge 222 was excluded in the calculation of the representative subgrade modulus. The representative subgrade modulus from field test results produced the same subgrade modulus from literature (see Table 4.4). Therefore, the present study adopted three different backfill properties to consider the influence of backfill stiffness: low, intermediate and high.

4.2.5.2 Soils stiffness around piles

The present study assumes soil properties for determining soil-pile interaction properties in the parametric study. Eleven HP310×110 (HP12×74) piles with yield strength of 345 MPa (50 ksi) were used for the parametric study. Two uniform soil layers with depth of 6.1 m (20 ft) for clay or sand layer and 1.5 m (5 ft) were assumed, because previous field and analytical studies [12, 26, 51, 125] showed that, generally, pile fixity points are between 3.0 to 4.6 m (10 to 15 ft) from the surface or 10 times the pile diameter. In the present study, piles were assumed to be driven up to 7.6 m (25 ft) below the surface. Soil-pile interaction properties also considered various overburden pressures and soil properties.

Three different high and low values for soil-pile interaction have been developed with respect to the different overburden pressures (backfill heights: 3.1, 4.6 and 6.1 m (10, 15, 20 ft)). To cover a practical range of soil properties, consideration of previous researches [24, 35, 36, 44, 55, 60] allowed determining representative values. The assumed high and low soil stiffness properties for clay and sand are tabulated in Table 4.5. Intermediate values were established from the average of high and low values.

Table 4.5: Soil Layer Properties and Range Determination

Property	Intermediate	High	Low
Sand Density kN/m^3 (pcf)	19 (121)	22 (142)	16 (100)
Clay Density kN/m^3 (pcf)	19 (121)	22 (142)	16 (100)
Angle of Friction (Sand) (Degree)	35	42	28
Undrained Shear Strength (clay) kN/m^2 (psi)	121 (17.5)	193 (28)	48 (7)
Elastic Modulus (K) MN/m^3 (pci)	271 (1000)	353 (1,300)	190 (700)
ε_{50} mm (in)	0.20 (0.008)	0.13 (0.005)	0.25 (0.01)

Developed moment-rotation curves and force-displacement curves of clay and sand for three different backfill heights model soil-pile interaction behavior appear in Figure 4.7.

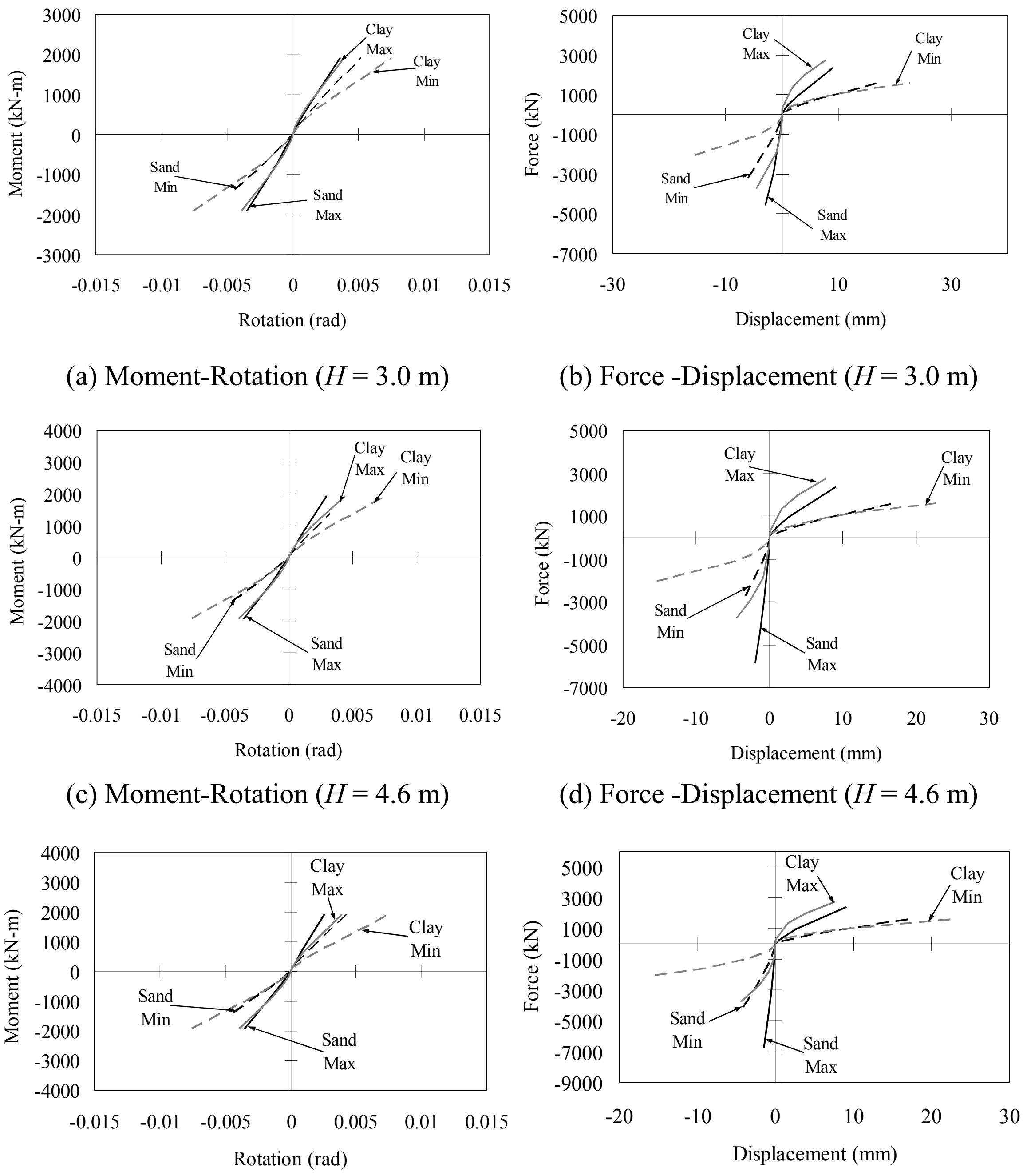

(a) Moment-Rotation ($H = 3.0$ m) (b) Force -Displacement ($H = 3.0$ m)

(c) Moment-Rotation ($H = 4.6$ m) (d) Force -Displacement ($H = 4.6$ m)

(e) Moment-Rotation ($H = 6.1$ m) (f) Force-Displacement (H= 6.1 m)

Figure 4.7: Rotational and Lateral Pile Capacity

The strength of soils tends to increase as overburden pressure increases, i.e. backfill height increases. However, due to the yield of soil strength, the strength converges at the maximum soil-pile interaction strength. The moment-rotation curves and force-displacement curves for backfill height 4.6 m (15 ft) and 6.1 m (20 ft) produce the very similar curves. The parametric study adopted three different cases for three assumed backfill heights: (1) high and (2) low of the soil-pile interaction of each case and (3) average of high and low.

4.2.6 Temperature Variation

The present study modeled bridge superstructure temperature, *T(t)*, at year *t*, over a 75-year bridge life. The established superstructure temperature model was used with Table 3.5 and a phase lag of $-\pi$. This study also investigated the initial temperature influence on IAB responses. The initial temperature is when the backwall is placed and integral behavior initiates. Thus, the bridge contraction is more significant if the backwall is placed during summer. The bridge expansion is more significant if the backwall is placed during winter.

Three cases were compared for the 75-year simulation: (1) case 1 - during spring = 7.5°C (45.5°F); (2) case 2 - during summer = 24.2°C (75.5°F); and (3) case 3 - during fall = 7.5°C (45.5°F). An initial temperature during winter was not considered because bridge specifications require concrete to cure at a minimum concrete temperature of 10 °C (50 °F) and completion of bridge construction in January or February is unusual. The three simulation cases appear in Figure 4.8.

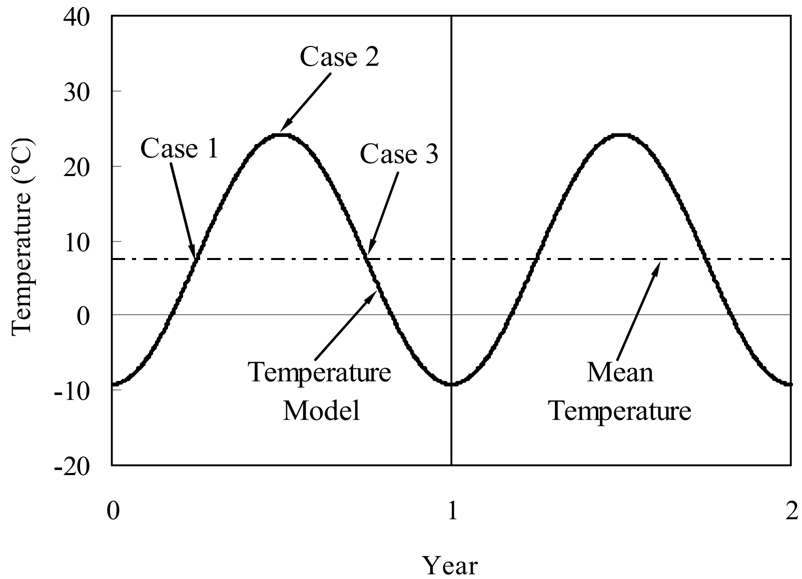

Figure 4.8: Construction Temperature Simulation Cases

The initial temperature significantly influences both the initial and long-term responses. Figure 4.9 represents 75-year simulation results and obvious influences in abutment displacement due to construction temperature are apparent.

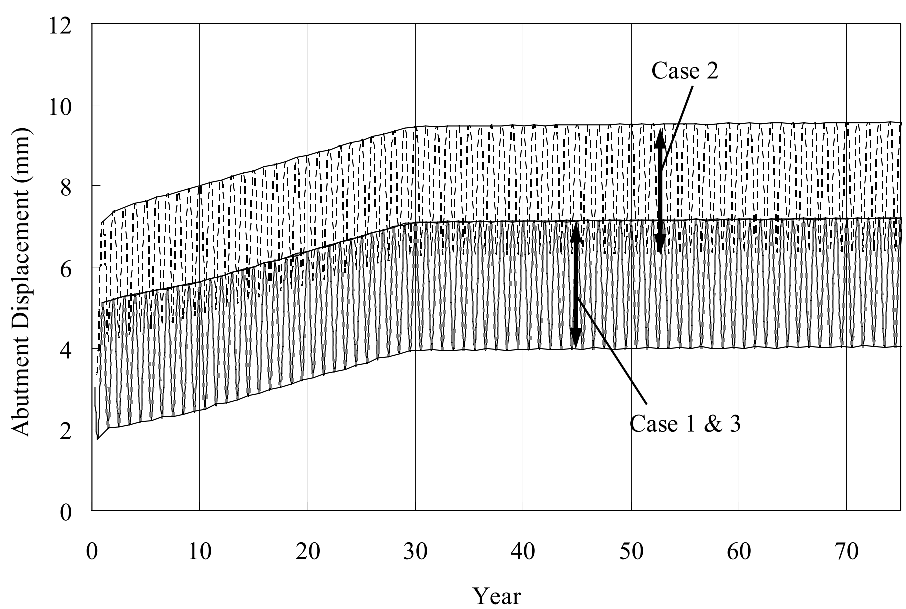

Figure 4.9: Long-term Influence of Construction Temperature

More detailed comparison results are presented in Figure 4.10.

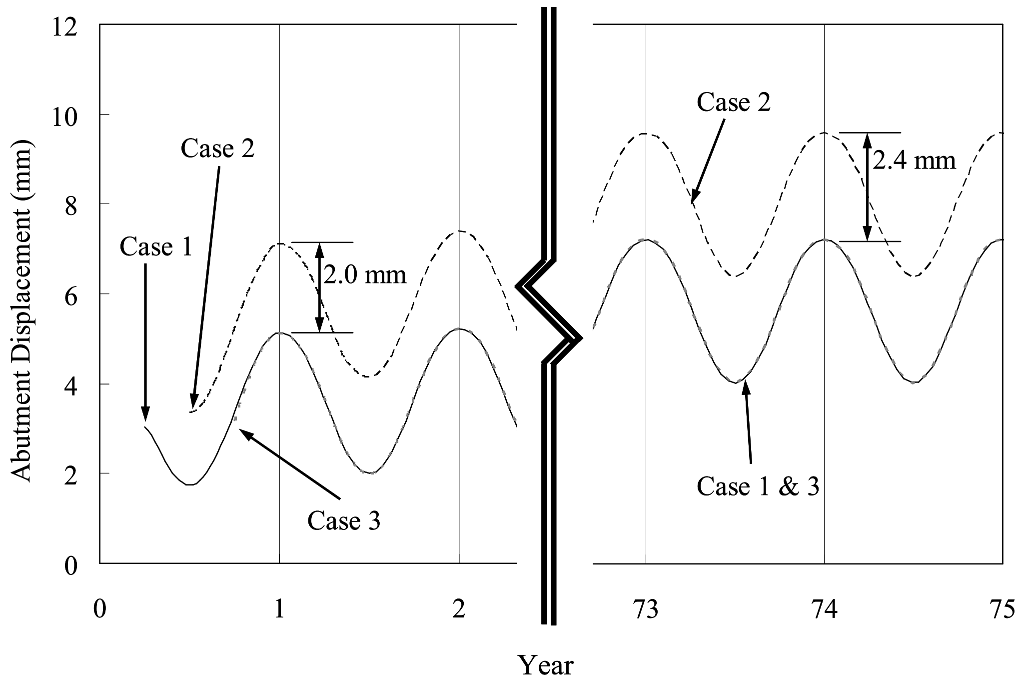

Figure 4.10: Displacement Shifting due to Construction Temperature

The initial abutment displacement differences between Cases 1 and 2 or Cases 3 and 2 due to construction temperature difference are 2.0 mm (0.08 in), while the 75-year abutment displacement differences are 2.4 mm (0.09 in). The 75-year abutment displacement differences between Cases 1 and 2 or Cases 3 and 2 are similar to the initial abutment displacement difference. Based on the numerical simulation, the higher the initial temperature, the larger abutment contraction displacement the bridge experiences during its bridge life.

4.2.7 Temperature Gradient

The parametric study numerical model included a superstructure temperature gradient, recognizing that the temperature in the superstructure is not uniform. The deck and girder are irregularly shaped; therefore, the thermal transfer and resulting temperature profile is both non-uniform and nonlinear. Based on AASHTO LRFD [4] multi-linear temperature profile, an equivalent linear temperature gradient was created to develop equivalent axial and bending strains in the superstructure. The temperature gradient, A_{TG}, at the top and bottom fibers was calculated for different girder sections (in Table 4.6). The temperature gradient at t year, $T_{TG}(t)$, was superimposed on the superstructure temperature and was applied throughout for the 75-year bridge life.

Table 4.6: Temperature Gradient

Girder Type	Temperature Gradient	Equivalent Temperature °C (°F)	
		Top Fiber	Bottom Fiber
AASHTO III	Positive (A_{TG_P})	13.1 (23.6)	1.8 (3.3)
	Negative (A_{TG_N})	-5.9 (-10.6)	-1.2 (-2.1)
BT-72	Positive (A_{TG_P})	8.3 (14.9)	-1.1 (-1.9)
	Negative (A_{TG_N})	-4.0 (-7.3)	-1.1 (-2.0)

Note: $T_{TG}(t) = 0.5 A_{TG} \sin(\omega t + \phi)$, if $0.25 \leq$ fraction of $t \leq 0.75$, then $A_{TG} = A_{TG\_P}$, else $A_{TG} = A_{TG\_N}$.

4.2.8 Time-dependent Loads

Time-dependent loads include concrete creep, concrete shrinkage, and prestressing steel relaxation. AAEM [58, 109] was utilized to compute time-dependent effects as a time-varying concrete elastic modulus based on ACI 209 [6] creep coefficient and aging coefficient. Girder and deck section properties, pre-tensioning forces, elastic and time-dependent loss over time, dead load of girder and deck, and age of girders and deck at placement were considered in the concrete creep stress analysis. Computation of stress loss due to prestressing steel relaxation used the AASHTO LRFD [4] intrinsic relaxation with a reduced relaxation coefficient suggested by Ghali *et al.* [58].

Total strains from time-dependent effects, represented in the 2D numerical model, are equivalent temperature loads based on the superstructure thermal expansion coefficient. Total strains at the top and bottom fibers of each girder section and thermal expansion coefficient were computed from an assumed deck concrete placement date of 100 days after girder manufacture date. Figures 4.11 and 4.12 present the total strain at the top and bottom fibers of girder cross-sections.

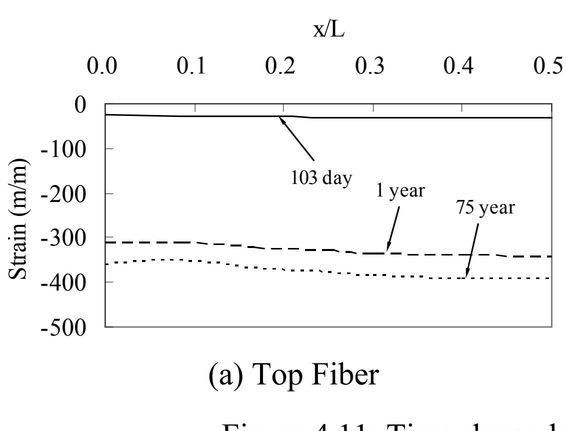

(a) Top Fiber

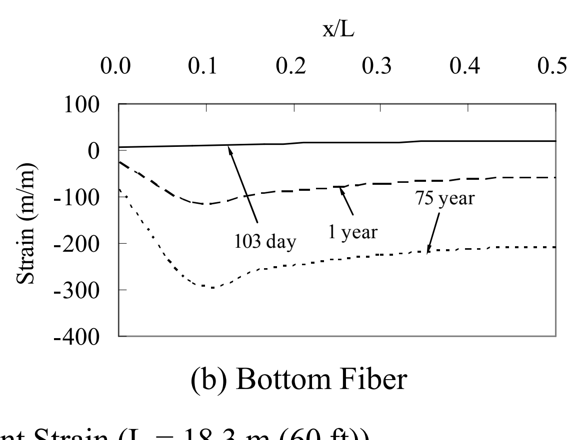

(b) Bottom Fiber

Figure 4.11: Time-dependent Strain (L = 18.3 m (60 ft))

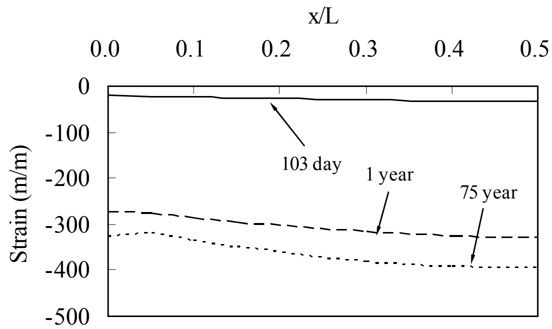

(a) Top Fiber

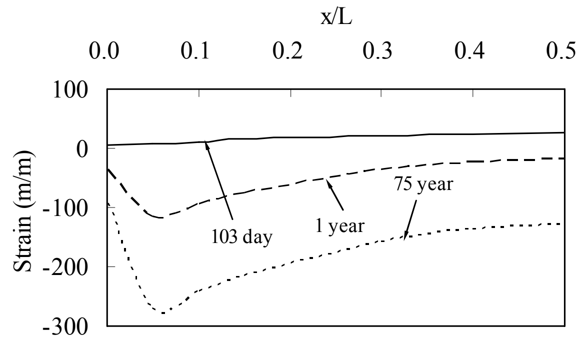

(b) Bottom Fiber

Figure 4.12: Time-dependent Strain (L = 30.5 m (100 ft))

4.3 Parametric Study Result Discussion

The present study performed 243 sets of parametric investigation of IABs using a 2D numerical model. The considered parameters include: (1) thermal expansion coefficient; (2) bridge length; (3) backfill height; (4) backfill stiffness; and (5) soil stiffness around piles. Critical responses of: (1) bridge axial force; (2) bridge bending moment; (3) pile lateral force; (4) pile moment; and (5) pile head/abutment displacement were determined. The specific locations of critical responses appear in Figure 4.13. For each response, the present study derived averages and envelops representing the range between upper and lower responses. Both positive and negative responses were investigated for girder axial force and moment. Envelopes of each response provide the bridge response ranges.

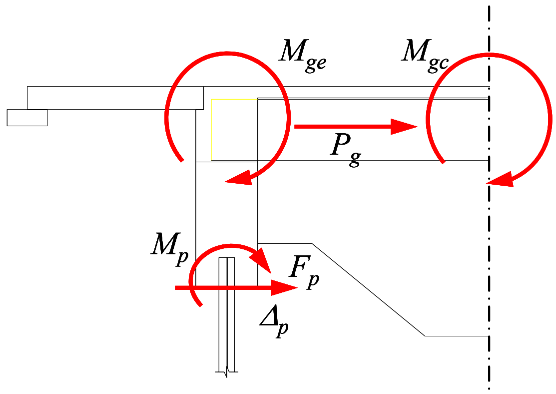

P_g: Girder Axial Force
M_{gc}: Girder Moment at Girder Center of Endspan
M_{ge}: Girder Moment at Girder End of Endspan
M_p: Pile Head Moment
F_p: Pile Head Lateral Force
Δ_p: Pile Head Displacement

Figure 4.13: Critical Responses

4.3.1 Girder Axial Force

Thermal expansion coefficient, bridge length, backfill height and soil stiffness around piles significantly influence girder axial force, while backfill stiffness is not influential (Figure 4.14). The study case with $\alpha = 14.4 \times 10^{-6}$/°C ($8.0 \times 10^{-6}$/°F); L = 121.9 m (400 ft); H = 3.0 m (10 ft); B = high value, and P = high value produced both the maximum tension (positive) and compression (negative) girder axial force of 883 kN (199 kips) and 2,189 kN (492 kips), respectively. These forces translate to tensile and compressive stress of 862 kPa (0.125 ksi) and 2136 kPa (0.31 ksi) or 23.3% and 8.6% of the AASHTO LRFD (2008) service stress limits, respectively.

Thermal expansion coefficient does not significantly influence tensile axial force, but does significantly influence compressive girder axial force. An increase in thermal expansion coefficient increases elongation of the bridge and therefore, the compressive axial force increases. The maximum average compressive axial force increase between the studied cases with $\alpha = 5.4 \times 10^{-6}$/°C ($3.0 \times 10^{-6}$/°F) and $\alpha = 14.4 \times 10^{-6}$/°C ($8.0 \times 10^{-6}$/°F) was 494 kN (111 kips). The average tensile force increase was 65 kN (15.5 kips).

As bridge length increases, both tensile and compressive girder axial forces significantly increase. The maximum average tensile and compressive girder axial force increase between the studied cases with L = 18.3 m (60 ft) and L = 121.9 m (400 ft) was 436 kN (98 kips) and 865kN (194 kips), respectively.

Increase of backfill height significantly decreases tensile axial force while backfill height does not significantly influence compressive axial force. The maximum average tensile girder axial force reduction between H = 3.0 m (10 ft) and H = 6.1 m (20 ft) was -374 kN (-84 kips). The average compressive girder axial force reduction was -58kN (13 kips).

Backfill stiffness significantly influences compressive axial force. The maximum average compressive girder axial force increase between B = low and B = high was 249 kN (56 kips). The average tensile girder axial force increase was 16 kN (3.6 kips).

Soil stiffness around pile significantly influences tensile axial force. The maximum average tensile girder axial force increase between P = low and P= high was 226kN (51kip). The average compressive axial force reduction was 20kN (4.5kip).

A low thermal expansion coefficient, short bridge length, high backfill height and low soil stiffness around piles minimizes tensile axial force. A low thermal expansion coefficient, short span length and low backfill stiffness minimizes compressive axial force.

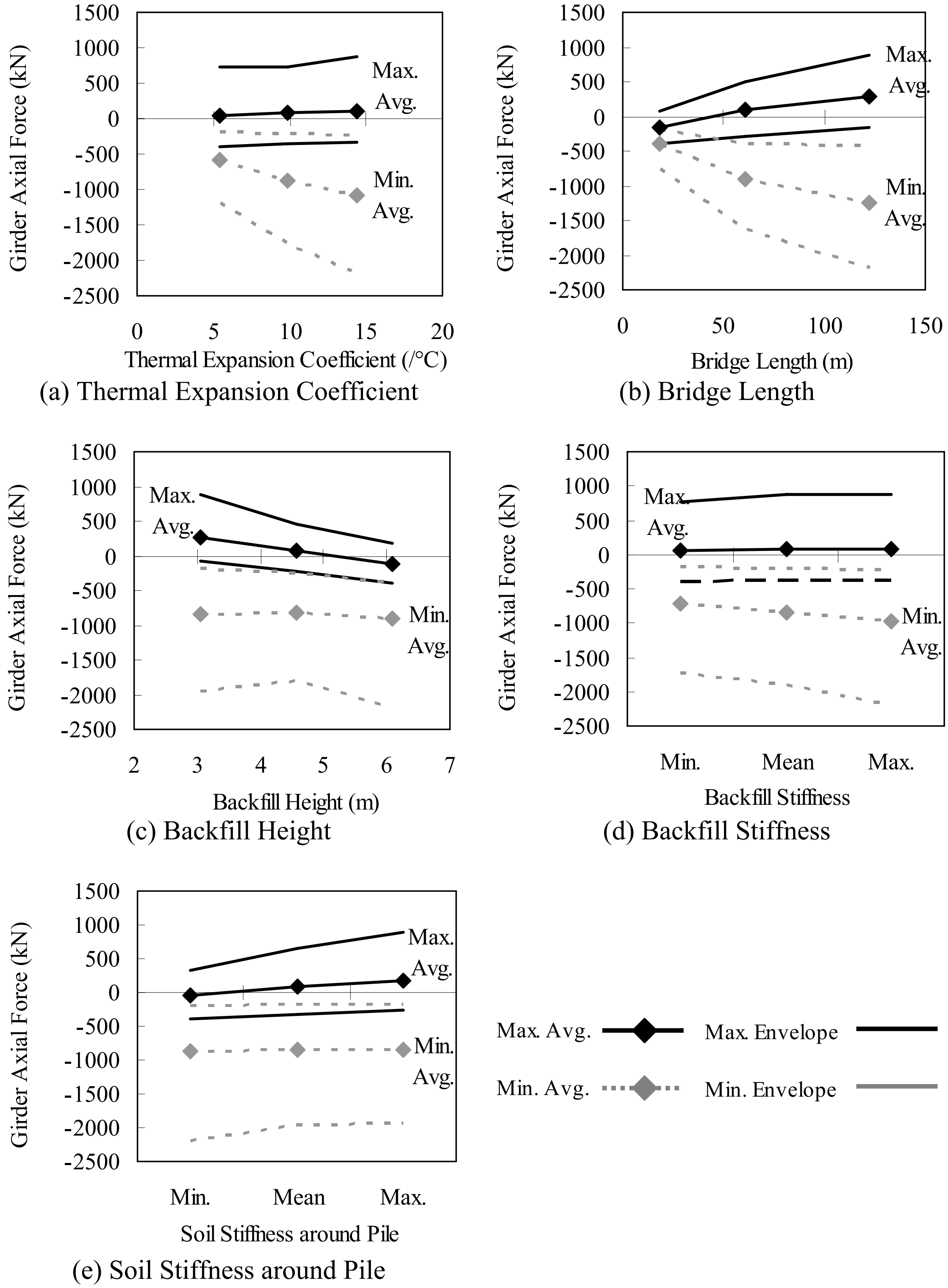

Figure 4.14: Girder Axial Force

4.3.2 Girder Bending Moment at Mid-span of the Exterior Span

Thermal expansion coefficient, bridge length, backfill height and soil stiffness around piles significantly influence girder bending moment at the mid-span of the exterior span (Figure 4.16**)**. Backfill stiffness was relatively uninfluential. The superstructure forms a convex curve during bridge expansion while it forms a concave curve during bridge contraction. This shape formation is more obvious in single span bridges. The study case with $\alpha = 14.4 \times 10^{-6}/°C$ ($8.0 \times 10^{-6}/°F$); L = 18.3 m (60 ft); H = 3.0m (10 ft); B = high value, and P = high value produced maximum positive moment of 184 kN-m (136 kip-ft). This moment translates to 45 kPa (0.007 ksi) tensile stress at the bottom fiber and 36 kPa (0.005 ksi) compressive stress at the top fiber, or 1.2% and 0.14% of the AASHTO LRFD [**4**] service stress limits, respectively. The study case with $\alpha = 14.4 \times 10^{-6}/°C$ ($8.0 \times 10^{-6}/°F$), L = 121.9 m (400 ft), H = 3.0 m (10 ft), B = high value, and P = high value produced maximum negative moment of 2213 kN-m (1632 kip-ft), which translates to 347 kPa (0.050 ksi) compressive (1.4% AASHTO limit) at the bottom fiber and 242kPa (0.035ksi) tensile stress (6.5% AASHTO limit) at the top fiber.

Thermal expansion coefficient significantly influences girder bending moment. The average maximum moment increase between the studied cases with $\alpha = 5.4 \times 10^{-6}/°C$ ($3.0 \times 10^{-6}/°F$) and $\alpha = 14.4 \times 10^{-6}/°C$ ($8.0 \times 10^{-6}/°F$) was 241 kN-m (177 kip-ft). The average negative moment increase was 294 kN (217 kip-ft).

As bridge length increases, negative girder bending moment significantly increases. The average maximum moment decrease between the studied cases with L =

18.3m and L = 121.9 m (400 ft)was 67 kN-m (50 kip-ft). The average maximum negative moment increase was 616kN-m (454 kip-ft).

Increase of backfill height decreases girder bending moment. The average maximum moment decrease between H = 3.0 m (10 ft) and H = 6.1 m (20 ft) was 188 kN-m (138 kip-ft). The average negative moment increase was 194 kN-m (143 kip-ft).

The backfill stiffness is relatively uninfluential on girder bending moment. The average maximum girder moment decrease between B = low and B = high was 23 kN-m (17 kip-ft). The average maximum negative girder moment increase was 19 kN-m (14 kip-ft).

Soil stiffness around piles significantly influences girder bending moment. The average maximum girder moment increase between P = low and P = high was 377 kN-m (278 kip-ft). The maximum average negative moment decrease was 154 kN-m (114 kip-ft).

Low thermal expansion coefficient and low soil stiffness around piles minimizes positive girder moment at the mid-span of the exterior span in an IAB. Low thermal expansion coefficient, short span length and low soil stiffness around piles minimizes negative girder moment at the mid-span of the exterior span.

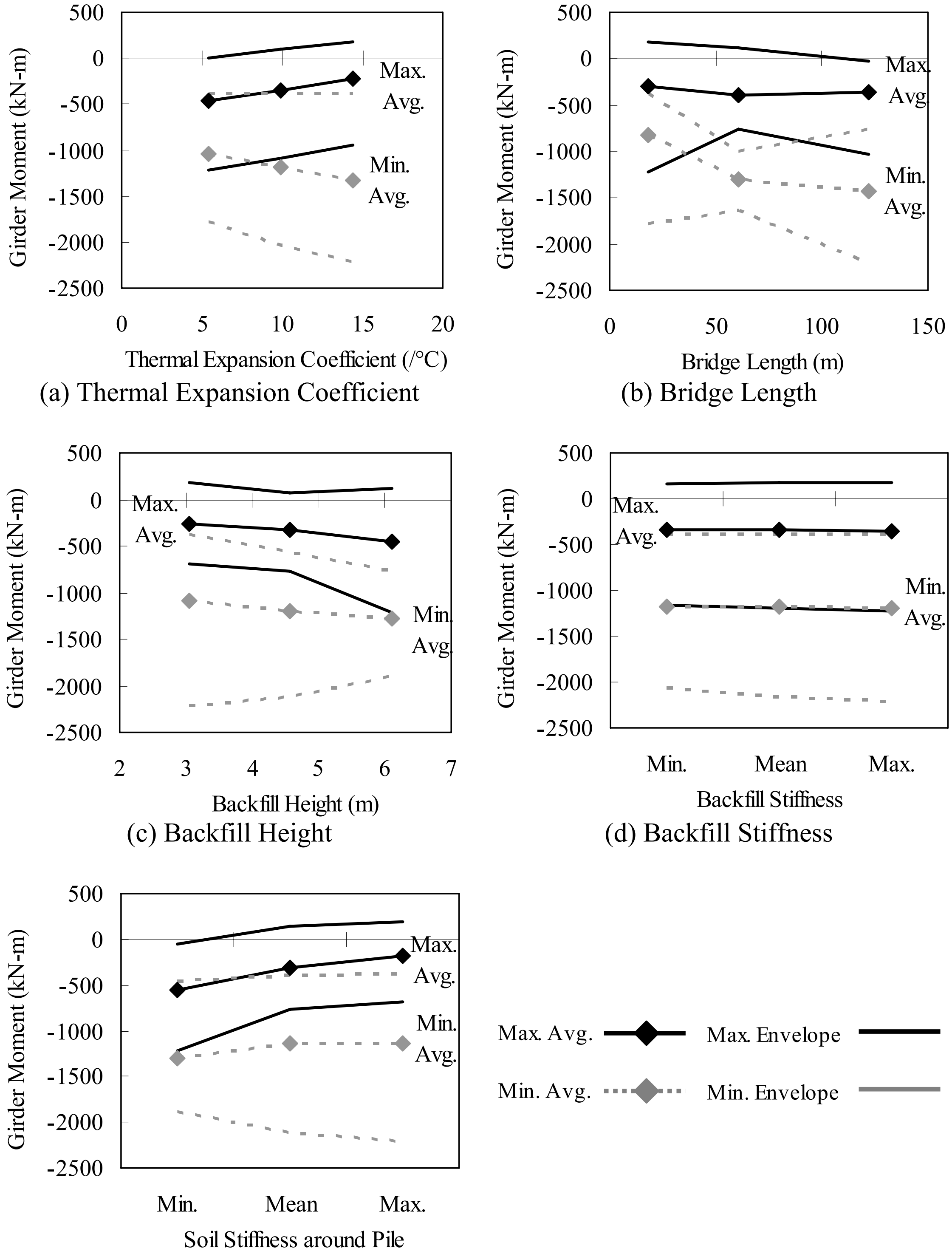

(a) Thermal Expansion Coefficient

(b) Bridge Length

(c) Backfill Height

(d) Backfill Stiffness

(e) Soil Stiffness around Pile

Figure 4.15: Girder Bending Moment at the Mid-span of the Exterior Span

4.3.3 Girder Bending Moment at Abutment

Thermal expansion coefficient, bridge length, backfill height and soil stiffness around piles significantly influence girder bending moment at the abutment (Figure 4.16). Backfill stiffness was relatively uninfluential. Girder moments at the abutment were higher than girder moment at the mid-span of the exterior span, and experienced higher positive and negative moments except three parametric study cases (case ID in Table 4.1: 136, 145 and 154) with (α = 9.9 × 10^{-6}/°C (5.5 × 10^{-6}/°F), L = 121.9 m (400 ft), B = high value, and P = high value). The study case with α = 14.4 × 10^{-6}/°C (8.0 × 10^{-6}/°F), L = 121.9 m (400 ft), H = 3.0 m(10 ft), B = high value, and P = high value produced maximum positive moment of 2189 kN-m (1615 kip-ft), which translates to 343 kPa (0.050 ksi) tensile stress (9.3% AASHTO limit) at the bottom fiber and 239 kPa (0.035 ksi) compressive stress (1.0% of the AASHTO limit) at the top fiber. The study case with α = 14.4 × 10^{-6}/°C (8.0 × 10^{-6}/°F), L = 121.9 m (400 ft), H = 6.1 m(20 ft), B = high value, and P = low value produced maximum negative moment of 4387kN-m (3235kip-ft), which translates to 687 kPa (0.100 ksi) compressive stress (2.8% AASHTO limit) at the bottom fiber and 479kPa (0.069 ksi) tensile stress (12.9% AASHTO limit) at the top fiber.

Thermal expansion coefficient significantly influences girder bending moment at the abutment. The average maximum positive moment increase between the studied cases with α = 5.4 × 10^{-6}/°C (3.0 × 10^{-6}/°F) and α = 14.4×10^{-6}/°C (8.0 × 10^{-6}/°F) was 263 kN-m (194 kip-ft). The average maximum negative moment increase was 1132 kN (835 kip-ft).

As bridge length increases, both positive and negative girder bending moment at the abutment significantly increases. The maximum average positive moment increase between the studied cases with L = 18.3 m (60 ft) and L = 121.9 m (400 ft) was 1482 kN-m (1093 kip-ft). The average maximum negative moment increase was 1548 kN-m (1142 kip-ft).

Increase of backfill height significantly decreases positive girder bending moment at the abutment. The maximum average positive moment decrease between H = 3.0 m (10 ft) and H = 6.1 m (20 ft) was 575 kN-m (425 kip-ft). The average negative girder moment decrease was 174 kN-m (128 kip-ft).

The backfill stiffness is relatively uninfluential on girder bending moment at the abutment. The average maximum positive girder moment change between B = low and B = high was 3 kN-m (2 kip-ft). The average maximum negative girder moment increase was 108 kN-m (79 kip-ft).

Soil stiffness around piles significantly influences positive girder bending moment at the abutment and decreases negative girder bending moment at the abutment. The average maximum girder moment increase between P = low and P= high was 826 kN-m (610 kip-ft). The average maximum negative moment decrease was 356 kN-m (263 kip-ft).

Low thermal expansion coefficient, shorter bridge length, higher backfill height and low soil stiffness around piles minimizes both positive and negative girder bending moment at the abutment in an IAB.

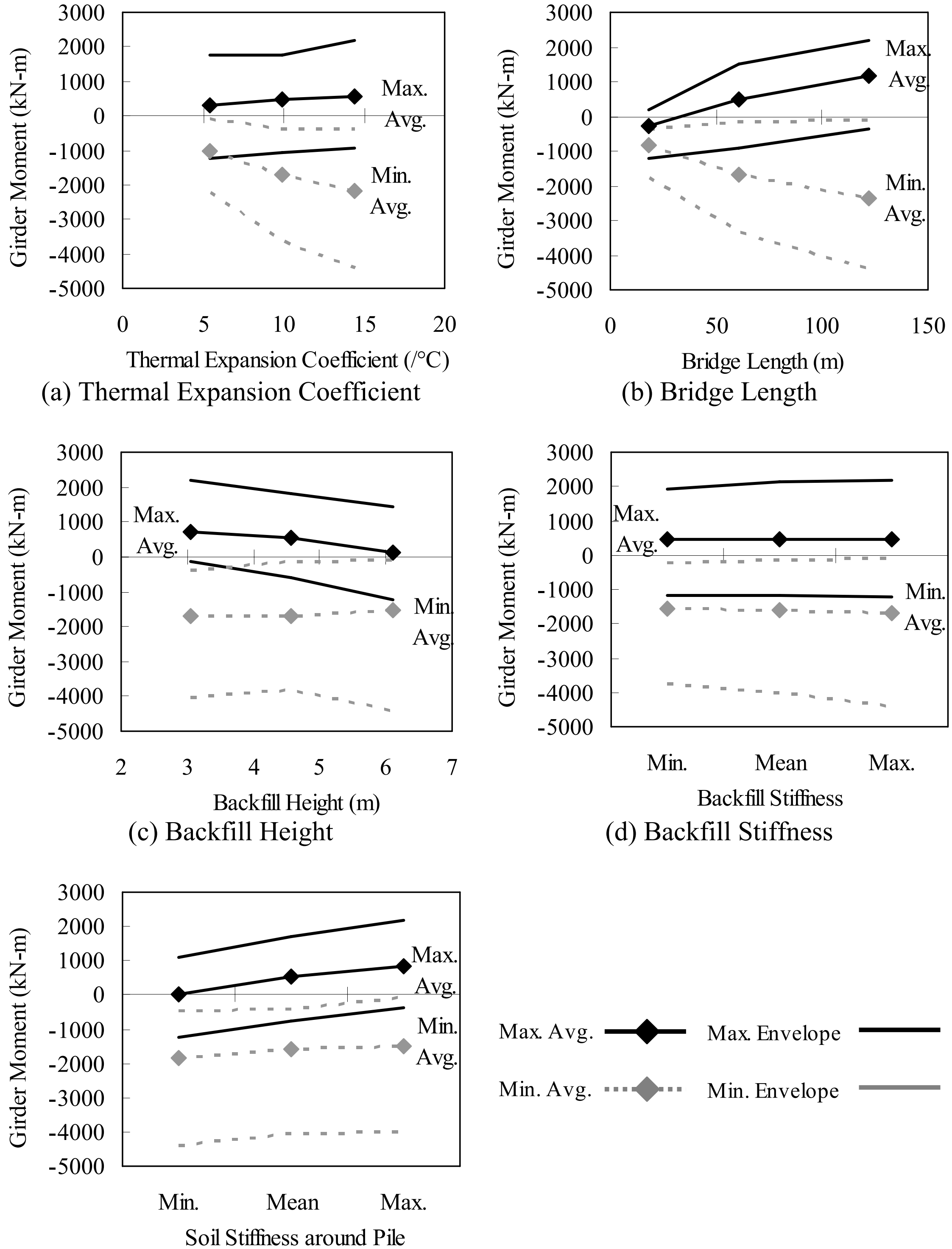

(a) Thermal Expansion Coefficient

(b) Bridge Length

(c) Backfill Height

(d) Backfill Stiffness

(e) Soil Stiffness around Pile

Figure 4.16: Girder Bending Moment at Abutment

The maximum combined stresses of girder axial forces and girder moments are presented in Table 4.7. The study case with α = 14.4 × 10-6/°C (α = 8.0 × 10-6/°F), L = 121.9 m (400 ft), H = 3.0 m (10 ft), B = high value, and P = high value produced maximum tensile stresses: (1) at the top fiber of the mid-span: 861 kPa (0.125 ksi) (23.2% AASHTO limit); and (2) at the bottom fiber of the abutment: 1,205 kPa (0.175 ksi) (32.5% AASHTO limit). The study case with α = 14.4 × 10-6/°C (α = 8.0 × 10-6/°F), L = 121.9 m (400 ft), H = 6.1 m (20 ft), B = high value, and P = low value produced maximum compressive stresses: (1) at the top fiber of the mid-span: 2,226 kPa (0.323 ksi) (9.0% AASHTO limit); and (2) at the bottom fiber of the abutment: 2,823 kPa (0.409 ksi) (11.4% AASHTO limit).

Table 4.7: Maximum Combined Stresses of Axial Force and Bending Moment

Location	Fiber	Compressive Stress kPa (ksi)		Tensile Stress kPa (ksi)	
		Stress	AASHTO limit	Stress	AASHTO limit
Girder Center	Top	2.23 (0.323)[1]	9.0%	0.86 (0.125)[2]	23.2%
	Bottom	2.43 (0.353)[1]	9.8%	0.86 (0.124)[2]	23.1%
Girder End	Top	1.95 (0.283)[1]	7.9%	0.62 (0.090)[2]	16.7%
	Bottom	2.82 (0.409)[1]	11.4%	1.21 (0.175)[2]	32.5%

[1]: case ID in Table 4.1: 237
[2]: case ID in Table 4.1: 217

4.3.4 Pile Lateral Force

Thermal expansion coefficient, bridge length and soil stiffness around piles significantly influence pile lateral force at pile head (Figure 4.17). Backfill height and backfill stiffness have relatively low influences. However, stub type abutments produce higher pile lateral force than higher abutments do when soil stiffness around piles is high enough. The study case with $\alpha = 14.4 \times 10^{-6}$/°C ($8.0 \times 10^{-6}$/°F); L = 121.9 m (400 ft); H = 3.0 m (10 ft); B = low value, and P = high value produced maximum shear force of 425 kN (96 kips). This shear force translates to shear stress of 30 MPa (4.4 ksi) or 15% of shear capacity, ϕV_n, respectively. The average shear stress of all studied cases was 5.1% of ϕV_n.

Thermal expansion coefficient significantly influences pile lateral force. The maximum average positive moment increase between the studied cases with $\alpha = 5.4 \times 10^{-6}$/°C ($3.0 \times 10^{-6}$/°F) and $\alpha = 14.4 \times 10^{-6}$/°C ($8.0 \times 10^{-6}$/°F) was 34 kN (7.6 kips).

Bridge length significantly influences pile lateral force. The maximum average positive moment increase between the studied cases with L = 18.3 m and L = 121.9 m was 79 kN-m (18 kips). Influences of bridge length significantly increase when backfill height is lower. For L = 18.3, 61.0 and 121.9 m (60, 200 and 400 ft), IABs with H = 3.0 m (10 ft) produced 12, 38 and 58 kN (2.7, 8.5 and 13 kips) average pile lateral force, respectively. However, IABs with H = 4.6 m (15 ft) produced 22, 25 and 35 kN (4.9, 5.6 and 7.9 kips) average pile lateral force. IABs with H = 6.1 m (20 ft) produced 42, 35 and 36 kN (9.4, 7.9 and 8.1 kips) average pile lateral force.

Backfill height does not significantly influence pile lateral force. The maximum average pile lateral force between H = 3.0 m (10 ft) and H = 6.1m (20 ft) was 7.1 kN (1.6 kips). The maximum envelopes between H = 3.0 m (10 ft) and H = 6.1m (20 ft) decreased from 425 to 228 to 249 kN (from 96 to 51 to 56 kips).

The backfill stiffness is relatively uninfluential on pile lateral force. The maximum average positive girder moment change between B = low and B = high was -12kN (-2.8).

Soil stiffness around piles significantly influences pile lateral force. The maximum average pile lateral force increased between P = low and P= high was 110 kN (25 kips).

Low thermal expansion coefficient, short bridge length, and low soil stiffness around piles minimizes pile lateral force at pile head in an IAB.

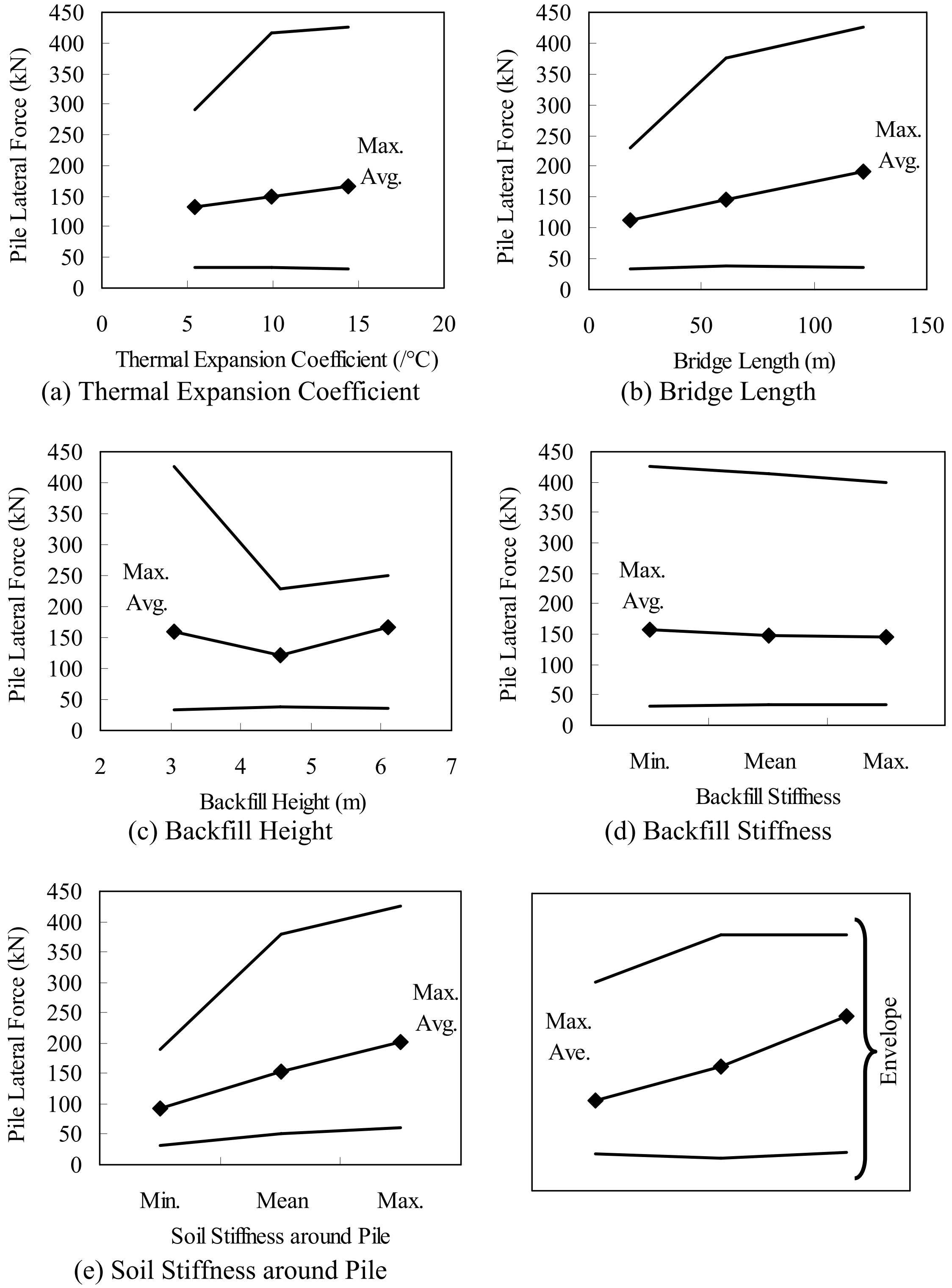

Figure 4.17: Pile Lateral Force

4.3.5 Pile Bending Moment

Thermal expansion coefficient, bridge length and soil stiffness around piles significantly influences pile bending moment at pile head (Figure 4.18). Some parametric study cases with high thermal expansion coefficients and long bridge lengths experienced pile yielding moments due to large abutment rotations while pile head displacement did not cause pile yielding. Soil stiffness around piles is the most important factor in this pile yielding. The study cases with $\alpha = 14.4 \times 10^{-6}$/°C ($8.0 \times 10^{-6}$/°F); L = 121.9 m (400 ft) and P = high value produced maximum moment of 172 kN-m (127 kip-ft). This moment translates to bending stress of 345kPa (50ksi) or 100% of the weak-axis oriented HP310×110 (HP12×74) pile section capacity, ϕM_y.

Thermal expansion coefficient significantly influences pile bending moment. The maximum average positive moment increase between the studied cases with $\alpha = 5.4 \times 10^{-6}$/°C ($3.0 \times 10^{-6}$/°F) and $\alpha = 14.4 \times 10^{-6}$/°C ($8.0 \times 10^{-6}$/°F) was 42 kN-m (31 kip-ft). Most of pile yielding cases were IABs with $\alpha = 14.4 \times 10^{-6}$/°C ($8.0 \times 10^{-6}$/°F), but some cases with $\alpha = 9.9 \times 10^{-6}$/°C ($5.5 \times 10^{-6}$/°F); L = 121.9 m (400 ft), and P = high value (case ID in Table 4.1: 139, 136, 142, 145, 148, 151, 157, 154, 160) produced pile yielding moments.

As bridge length increases, pile bending moment significantly increases. The maximum average positive moment increase between the studied cases with L = 18.3 m (60 ft) and L = 121.9 m (400 ft) was 74 kN-m (54 kip-ft). Most of pile yielding cases were IABs with L = 121.9 m (400 ft), but some cases with $\alpha = 14.4 \times 10^{-6}$/°C (8.0 × 10⁻

^{6}/°F), L = 61.0 m (200 ft), and P = high value (case ID in Table 4.1: 190, 193, 196, 199, 202, 204, 214) produced pile yielding moments.

Backfill height does not influence pile bending moment. The maximum average pile moment change between H = 3.0 m (10 ft) and H = 6.1 m (20 ft) was -5.4 kN-m (-4.0 kip-ft).

The backfill stiffness does not influence pile bending moment. The maximum average pile moment change between B = low and B = high was -0.2 kN-m (-0.1 kip-ft).

Soil stiffness around piles most significantly influences pile bending moment. The maximum average pile moment increase between P = low and P= high was 57 kN-m (42 kip-ft). Most of pile yielding cases were IABs with P = high value, but some cases with $\alpha = 14.4\times10^{-6}$/°C, L = 121.9m, and P = intermediate value (case ID in Table 4.1: 218, 221, 224, 227, 230, 233) produced pile yielding moments.

Low thermal expansion coefficient, short bridge length and low soil stiffness around piles minimizes pile bending moment.

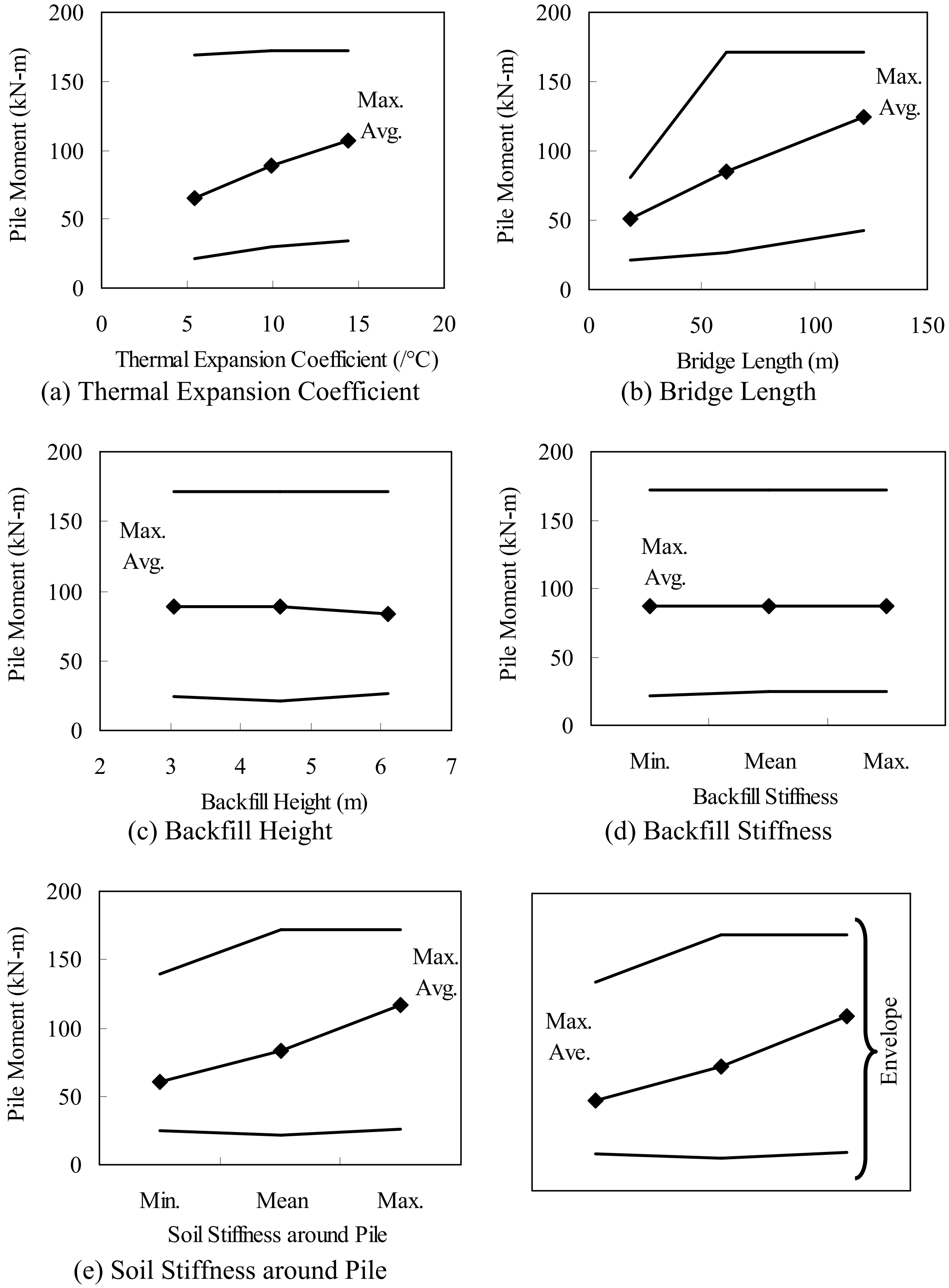

Figure 4.18: Pile Bending Moment

4.3.6 Pile Head/Abutment Displacement

Thermal expansion coefficient, bridge length and soil stiffness around piles significantly influences pile head/abutment displacement (Figure 4.19). Backfill height and backfill stiffness were not notably influential. However, higher backfill height led to larger displacement when soil stiffness around pile was low. The study cases with α = 14.4 × 10^{-6}/°C (8.0 × 10^{-6}/°F); L = 121.9 m (400 ft); H = 6.1 m (20 ft); B = low value and P = low value produced maximum displacement of 37mm (1.45in). This maximum displacement is close to the pile foundation allowable displacement of 38mm (1.5in) according to AASHTO LRFD [4].

Thermal expansion coefficient significantly influences pile head/abutment displacement. The average displacement increase between the studied cases with α = 5.4 × 10^{-6}/°C (3.0 × 10^{-6}/°F) and α = 14.4 × 10^{-6}/°C (8.0 × 10^{-6}/°F) was 5.3 mm (0.21 in).

As bridge length increases, pile head displacement significantly increases. The maximum average pile head displacement increase between the studied cases with L = 18.3 m (60 ft) and L = 121.9 m (400 ft) was 14.7 mm (0.58 in).

Backfill height and backfill stiffness do not influence pile head/abutment displacement. The average displacement changes were close to zero displacement.

Increase of soil stiffness around piles significantly reduces pile head displacement. The average pile head displacement decrease between P = low and P= high was 6.2 mm (0.24 in).

Low thermal expansion coefficient, short bridge length and high soil stiffness around piles minimizes pile head/abutment displacement.

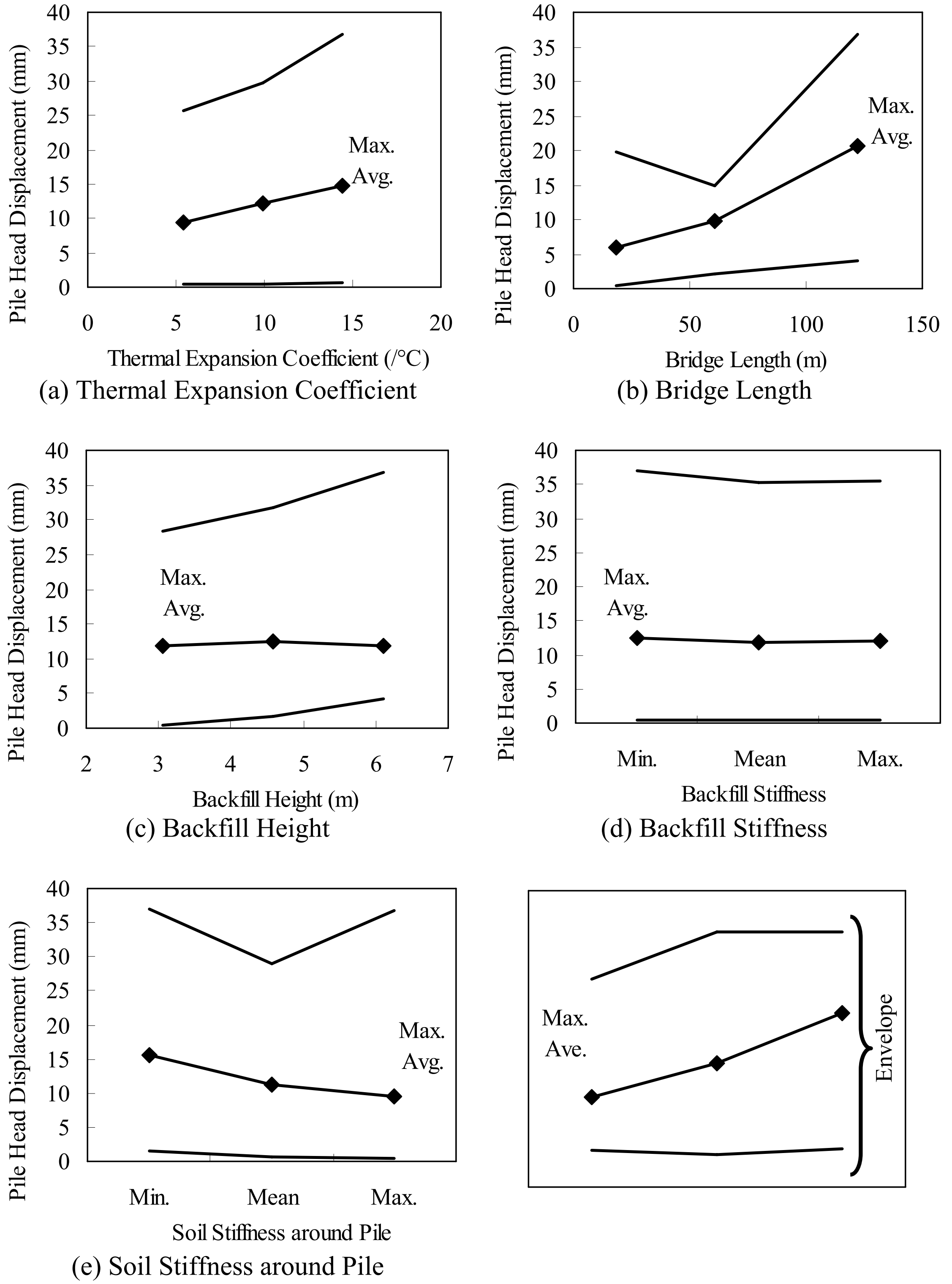

Figure 4.19: Pile Head Displacement

4.3.7 Abutment Displacement at Centroid of Superstructure

Thermal expansion coefficient and bridge length significantly influences abutment displacement at the centroid of a superstructure (Figure 4.20). Backfill height, backfill stiffness and soil stiffness around piles are not influential. The study cases with $\alpha = 14.4 \times 10^{-6}$/°C ($8.0 \times 10^{-6}$/°F); L = 121.9 m (400 ft); H = 6.1 m (20 ft); B = low value and P = low value produced maximum displacement of 33.7 mm (1.33 in). This maximum displacement is less than the allowable displacement of 38mm (1.5in) according to AASHTO LRFD [4].

Thermal expansion coefficient significantly influences abutment displacement. The average displacement increase between the studied cases with $\alpha = 5.4 \times 10^{-6}$/°C ($3.0 \times 10^{-6}$/°F)and $\alpha = 14.4 \times 10^{-6}$/°C ($8.0 \times 10^{-6}$/°F) was 4.8 mm (0.19 in).

As bridge length increases, abutment displacement significantly increases. The average abutment displacement increase between the studied cases with L = 18.3 m (60 ft) and L = 121.9 m (400 ft) was 23.1 mm (0.91 in).

Backfill height, backfill stiffness and soil stiffness around piles do not influence abutment displacement. The maximum displacement change was close to zero displacement.

Low thermal expansion coefficient and short bridge length minimizes abutment displacement at the centroid of a superstructure.

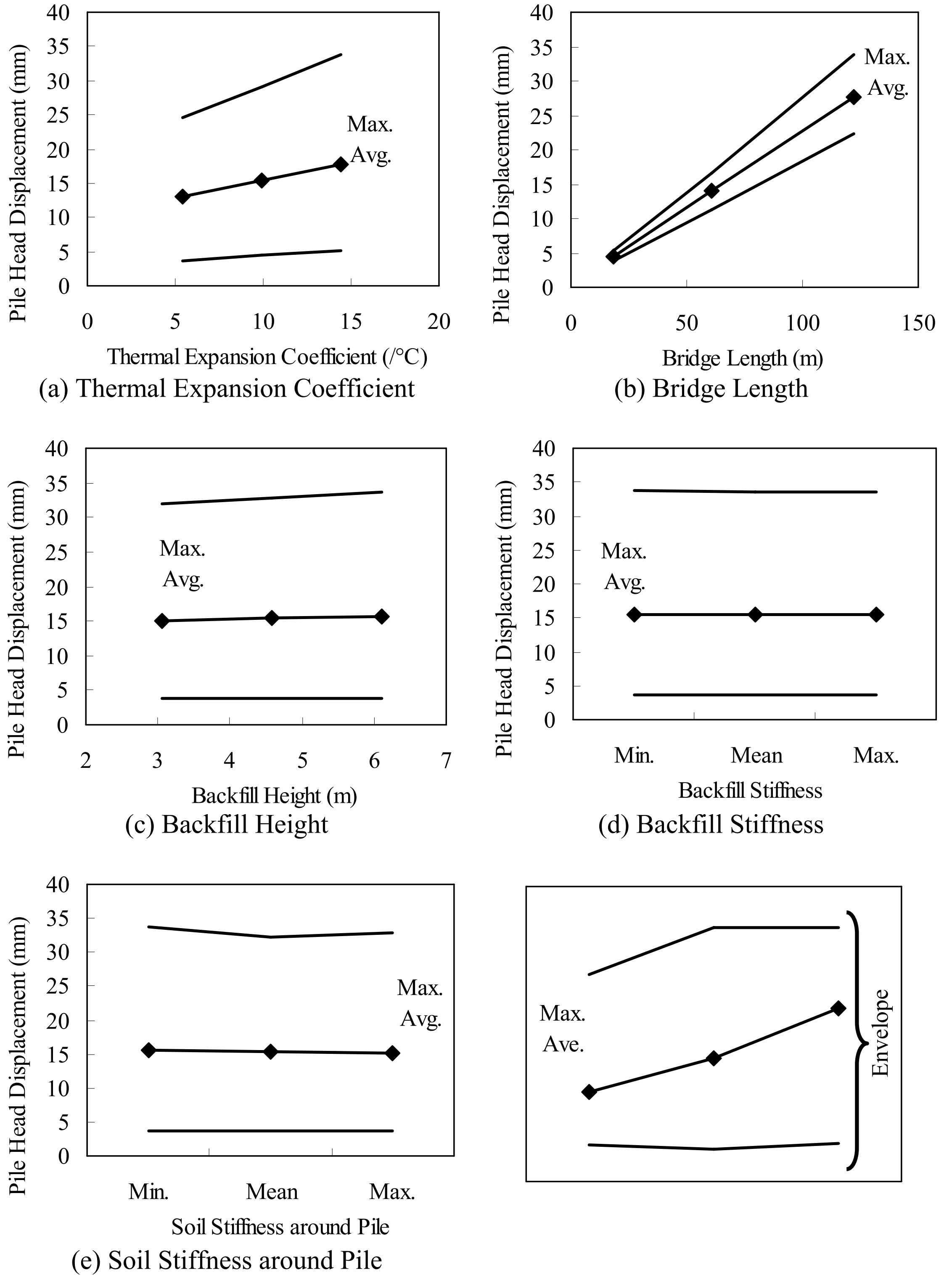

(a) Thermal Expansion Coefficient

(b) Bridge Length

(c) Backfill Height

(d) Backfill Stiffness

(e) Soil Stiffness around Pile

Figure 4.20: Abutment Displacement at Centroid of Superstructure

Figure 4.21 shows the comparison of the parametric study results with the free expansion of a superstructure.

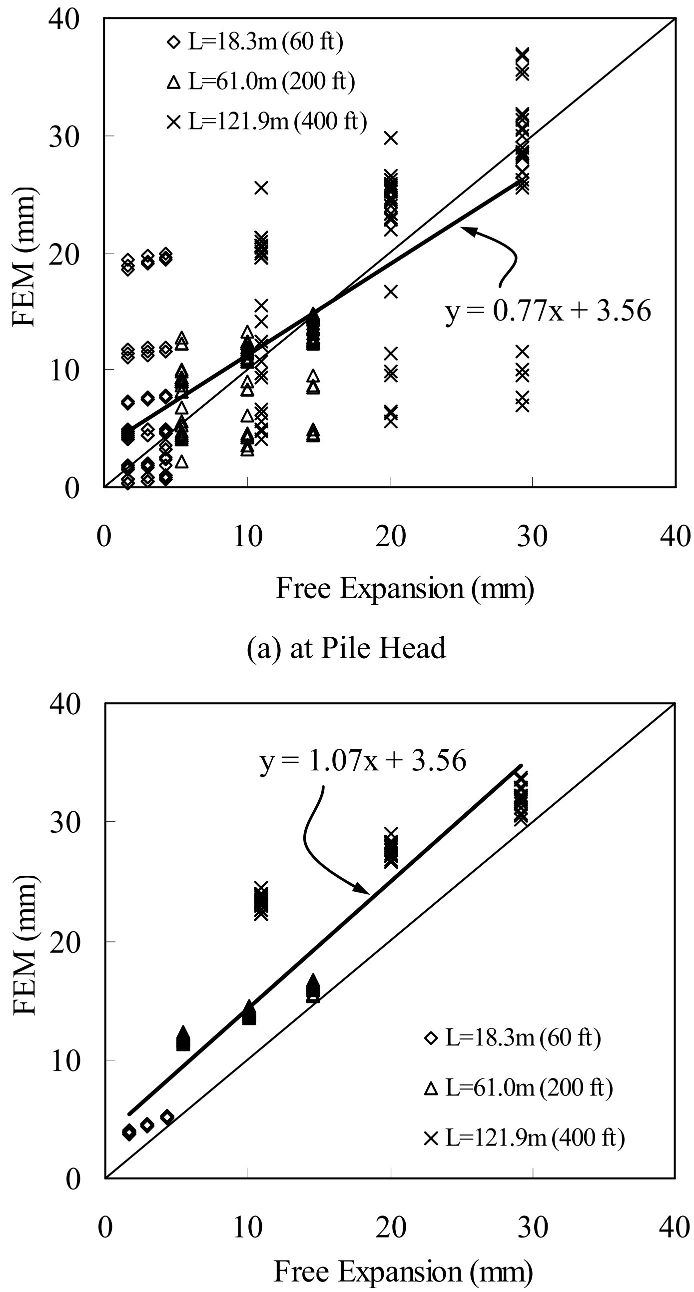

(a) at Pile Head

(b) at Centroid of Superstructure

Figure 4.21: Correlation of Abutment Displacement

The bridge length and thermal expansion coefficient effects were clearly observed. The pile head displacement in Figure 4.21(a) is highly dependent on bridge length, thermal expansion coefficient and soil stiffness around piles as described earlier. However, the displacement at the centroid of the superstructure in Figure 4.21(b) is dependent on bridge length and thermal expansion coefficient. Also, the time-dependent effects that are not considered in the free expansion significantly influence the displacements at the centroid so that all parametric study cases were larger than those for the free expansion displacements.

4.4 IAB Response Prediction

Based on the parametric study results, IAB response prediction models: (1) bridge axial force; (2) bridge bending moment at the mid-span of the exterior span; (3) bridge bending moment at the abutment; (4) pile lateral force at pile head; (5) pile moment at pile head; (6) pile head/abutment displacement; and (7) abutment displacement at the centroid of a superstructure have been developed using regression analyses (Tables 4.8 and 4.9). The present study utilized the coefficient of determination, R^2 to determine a model from various equations, regardless of linear or nonlinear forms. In the development process, *p*-value test, based on 95% acceptance, has been performed to reduce the number of parameters and to identify insignificant parameters. Each of the prediction models exhibits a high R^2 compared to the numerical model results. Based on the IAB response prediction models, a single member response can be computed using the total response models divided by the expected number of members (number of girders or number of piles). Correlations between the prediction models and the parametric study appear in Figure 4.22.

Table 4.8: IAB Response Prediction Models (SI Unit)

Response		Prediction Model	Range	R^2
Bridge Axial Force (kN)	(+)	$31\alpha + 16L - 491H + 453P + 165 \geq 0$		0.90
	(-)	$-29\alpha^{0.65}L^{0.75}B^{0.15}P^{0.25}$ $-39\alpha^{0.75}L^{0.60}B^{0.30}P^{-0.05}$ $-149\alpha^{0.60}L^{0.45}B^{0.35}P^{-0.20}$	for $H \leq 3.8$m for $3.8 \leq H \leq 5.4$m for $H \geq 5.4$m	0.94 0.92 0.95
Bridge Bending Moment at Girder Center (kN-m)	(+)	$93\alpha - 850H + 940P - 19 \geq 0$ $180\alpha + 160H + 330P - 4700 \geq 0$ $45\alpha + 1000P - 3500 \geq 0$	for $L \leq 39.7$ m for $39.7 \leq L \leq 91.5$m for $L \geq 91.5$m	0.90 0.74 0.75
	(-)	$-162\alpha^{0.35}L^{0.60}P^{0.20}$ $-460\alpha^{0.40}L^{0.35}$ $-4950\alpha^{0.1}P^{-0.40}$	for $H \leq 3.8$m for $3.8 \leq H \leq 5.4$m for $H \geq 5.4$m	0.87 0.80 0.56
Bridge Bending Moment at Girder End (kN-m)	(+)	$100\alpha + 50L + 1400P - 4500 \geq 0$ $89\alpha + 58L + 1500P - 5400 \geq 0$ $160\alpha + 61L + 2100P - 9200 \geq 0$	for $H \leq 3.8$m for $3.8 \leq H \leq 5.4$m for $H \geq 5.4$m	0.91
	(-)	$-38\alpha^{0.70}L^{0.80}B^{0.10}P^{0.20}$ $-43\alpha^{1.00}L^{0.65}B^{0.10}P^{-0.08}$ $-900\alpha^{0.55}L^{0.25}B^{0.04}P^{-0.70}$	for $H \leq 3.8$m for $3.8 \leq H \leq 5.4$m for $H \geq 5.4$m	0.84 0.73 0.64
Total Pile Lateral Force (kN)		$15\alpha^{0.5}L^{0.7}B^{-0.1}P^{0.9} \leq N_p F_{y\_pile}$ $216\alpha^{0.2}L^{0.3}B^{-0.1}P^{0.7} \leq N_p F_{y\_pile}$ $1720L^{-0.1}B^{-0.1}P^{0.6} \leq N_p F_{y\_pile}$	for $H \leq 3.8$m for $3.8 \leq H \leq 5.4$m for $H \geq 5.4$m	0.96 0.89 0.85
Total Pile Head Moment (kN-m)		$33\alpha^{0.5}L^{0.5}H^{-0.1}P^{0.6} \leq N_p M_{y\_pile}$		0.83
Pile Head Displacement (mm)		$0.04\alpha^{0.3}L^{1.2}P^{-0.05}$ $0.03\alpha^{0.7}L^{1.0}P^{-0.15}$ $5.3\alpha^{0.3}L^{0.1}P^{-1.0}$	for $H \leq 3.8$m for $3.8 \leq H \leq 5.4$m for $H \geq 5.4$m	0.99 0.89 0.56
Abutment Displacement at Centroid		$0.12\alpha^{0.3}L^{1.0}H^{0.04}P^{-0.03}$		0.99

Note 1: (+): maximum axial force or positive moment.
(-): minimum axial force or negative moment.

Note 2: α: (thermal expansion coefficient) $\times 10^6$/°C; L and H: meter; B and P: low = 1, intermediate = 2, high = 3 in Table 4.4 and Table 4.5.
F_{y_pile}: pile shear capacity; M_{y_pile}: pile moment capacity; N_p: number of piles.

Note 3: Single member response = (total response)/(number of members).

Table 4.8: IAB Response Prediction Models (U.S. Customary Unit)

Response		Prediction Model	Range	R^2
Bridge Axial Force (kip)	(+)	$17\alpha + L - 35H + 120P \geq 0$		0.90
	(-)	$-3\alpha^{0.7}L^{0.8}B^{0.2}P^{0.3}$ $-5.5\alpha^{0.8}L^{0.65}B^{0.2}P^{0.02}$ $-29\alpha^{0.55}L^{0.45}B^{0.40}P^{-0.20}$	for $H \leq 3.8$m for $3.8 \leq H \leq 5.4$m for $H \geq 5.4$m	0.94 0.92 0.95
Bridge Bending Moment at Girder Center (kip-ft)	(+)	$120\alpha - 190H + 690P - 14 \geq 0$ $210\alpha + 53H + 170P - 3400 \geq 0$ $59\alpha + 740P - 2600 \geq 0$	for $L \leq 39.7$ m for $39.7 \leq L \leq 91.5$m for $L \geq 91.5$m	0.90 0.74 0.75
	(-)	$-74\alpha^{0.35}L^{0.60}P^{0.20}$ $-280\alpha^{0.40}L^{0.35}$ $-4000\alpha^{0.1}P^{-0.40}$	for $H \leq 3.8$m for $3.8 \leq H \leq 5.4$m for $H \geq 5.4$m	0.87 0.80 0.56
Bridge Bending Moment at Girder End (kip-ft)	(+)	$134\alpha + 11L + 1040P - 3300 \geq 0$ $118\alpha + 13L + 1100P - 4000 \geq 0$ $213\alpha + 14L + 1500P - 6700 \geq 0$	for $H \leq 3.8$m for $3.8 \leq H \leq 5.4$m for $H \geq 5.4$m	0.91
	(-)	$-17\alpha^{0.70}L^{0.80}B^{0.10}P^{0.30}$ $-26\alpha^{1.00}L^{0.65}B^{0.10}P^{-0.08}$ $-700\alpha^{0.55}L^{0.25}B^{0.04}P^{-0.70}$	for $H \leq 3.8$m for $3.8 \leq H \leq 5.4$m for $H \geq 5.4$m	0.84 0.73 0.64
Total Pile Lateral Force (kip)		$2\alpha^{0.5}L^{0.7}B^{-0.1}P^{0.9} \leq N_p F_{y\_pile}$ $19\alpha^{0.2}L^{0.3}B^{-0.1}P^{0.7} \leq N_p F_{y\_pile}$ $418L^{-0.1}B^{-0.1}P^{0.6} \leq N_p F_{y\_pile}$	for $H \leq 3.8$m for $3.8 \leq H \leq 5.4$m for $H \geq 5.4$m	0.96 0.89 0.85
Total Pile Head Moment (kip-ft)		$21\alpha^{0.5}L^{0.5}H^{-0.1}P^{0.6} \leq N_p M_{y\_pile}$		0.83
Pile Head Displacement (in)		$0.0004\alpha^{0.3}L^{1.2}P^{-0.06}$ $0.0006\alpha^{0.7}L^{1.0}P^{-0.15}$ $0.21\alpha^{0.35}L^{0.15}P^{-1.0}$	for $H \leq 3.8$m for $3.8 \leq H \leq 5.4$m for $H \geq 5.4$m	0.99 0.89 0.56
Abutment Displacement at Centroid (in)		$0.0017\alpha^{0.35}L^{1.0}H^{0.05}P^{-0.05}$		0.99

Note 1: (+): maximum axial force or positive moment.
(-): minimum axial force or negative moment.

Note 2: α: (thermal expansion coefficient) $\times 10^6$/°F; L and H: foot; B and P: low = 1, intermediate = 2, high = 3 in Table 4.4 and Table 4.5.
F_{y_pile}: pile shear capacity; M_{y_pile}: pile moment capacity; N_p: number of piles.

Note 3: Single member response = (total response)/(number of members).

Table 4.9: IAB Stress Response Prediction models (SI Unit)

Response	Location	Fiber	Prediction Model	R2
Maximum Stress (kPa)	Girder Center	Top	$-183+13\alpha-0.2\alpha^2+9L-0.03L^2-152H+2H^2+22B-4B^2+222P-24P^2$	0.96
		Bottom**	$-332+16\alpha-0.2\alpha^2+10L-0.04L^2-149H+0.7H^2+23B-4B^2+275P-31P^2$	0.96
	Girder End	Bottom*	$-623+21\alpha-0.4\alpha^2+14L-0.05L^2-89H-8H^2+33B-7B^2+352P-42P^2$	0.96
Minimum Stress (kPa)	Girder Center	Top	$-23\alpha^{0.6}L^{0.5}B^{0.2}$	0.84
		Bottom**	$-42\alpha^{0.6}L^{0.45}H^{0.04}B^{0.2}P^{-0.02}$	0.78
	Girder End	Bottom*	$-31\alpha^{0.7}L^{0.5}B^{0.2}$	0.79

* maximum or minimum stress throughout the girder.
** maximum or minim stress at the mid-span of the exterior span.
Note 1: (+): maximum or tensile stress; (-): minimum or compressive stress.
Note 2: α: (thermal expansion coefficient) $\times 10^6$/°C; L and H: m; B and P: *low* = 1, *intermediate* = 2, *high* = 3 in Table 4.4 and Table 4.5.

Table 4.9: IAB Stress Response Prediction models (U.S. Customary Unit)

Response	Location	Fiber	Prediction Model	R2
Maximum Stress (psi)	Girder Center	Top	$-27+3.5\alpha-0.1\alpha^2+0.4L-0.0005L^2-6.7H+0.033H^2+3B-0.55B^2+32P-3.6P^2$	0.96
		Bottom**	$-48+4\alpha-0.08\alpha^2+0.4L-0.0005L^2-6H+0.01H^2+3B-0.6B^2+40P-4P^2$	0.96
	Girder End	Bottom*	$-90+5.6\alpha-0.2\alpha^2+0.63L-0.0007L^2-3.9H-0.11H^2+4.8B-0.96B^2+51P-6P^2$	0.96
Minimum Stress (psi)	Girder Center	Top	$-3\alpha^{0.6}L^{0.5}B^{0.25}$	0.84
		Bottom**	$-4.9\alpha^{0.6}L^{0.45}H^{0.04}B^{0.2}P^{-0.02}$	0.78
	Girder End	Bottom*	$-4\alpha^{0.7}L^{0.5}B^{0.2}$	0.79

* maximum or minimum stress throughout the girder.
** maximum or minim stress at the mid-span of the exterior span.
Note 1: (+): maximum or tensile stress; (-): minimum or compressive stress.
Note 2: α: (thermal expansion coefficient) $\times 10^6$/°F; L and H: foot; B and P: *low* = 1, *intermediate* = 2, *high* = 3 in Table 4.4 and Table 4.5.

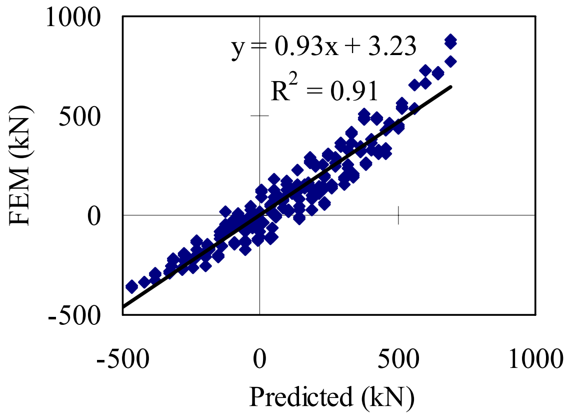

(a) Maximum Girder Axial Force

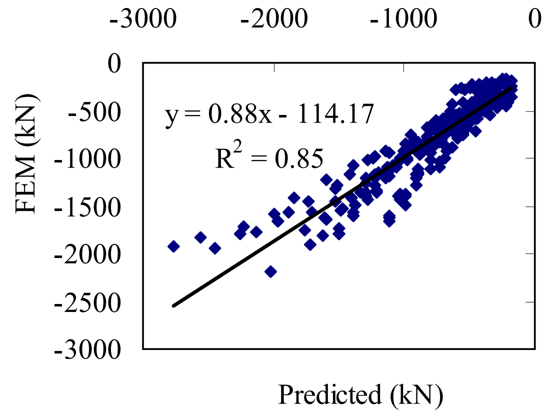

(b) Minimum Girder Axial Force

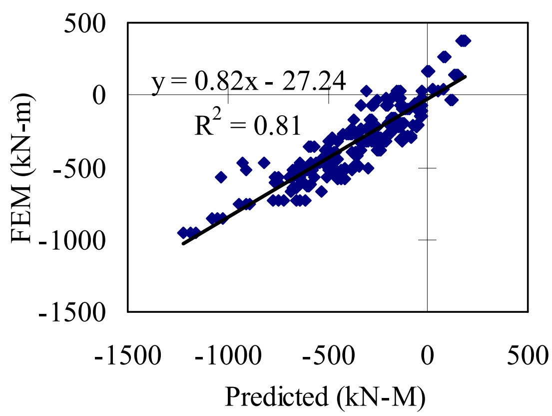

(c) Maximum Girder Bending Moment

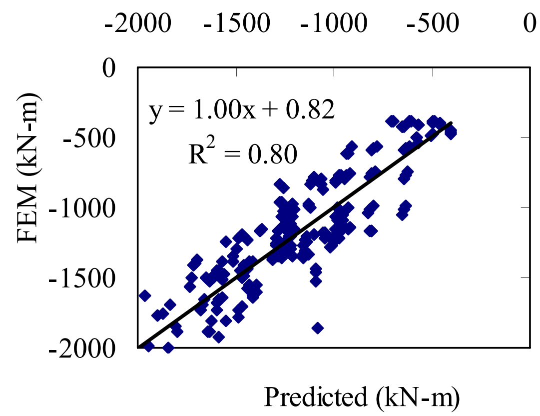

(d) Minimum Girder Bending Moment

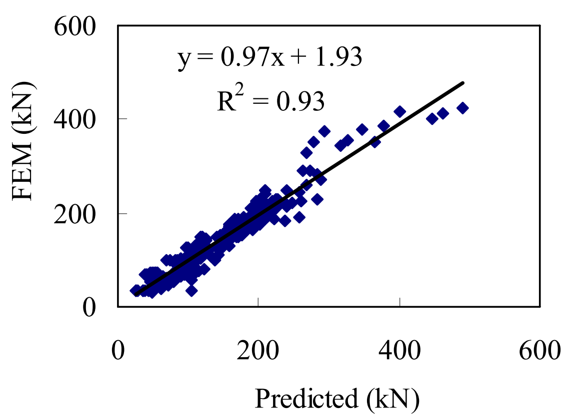

(e) Pile Lateral Force

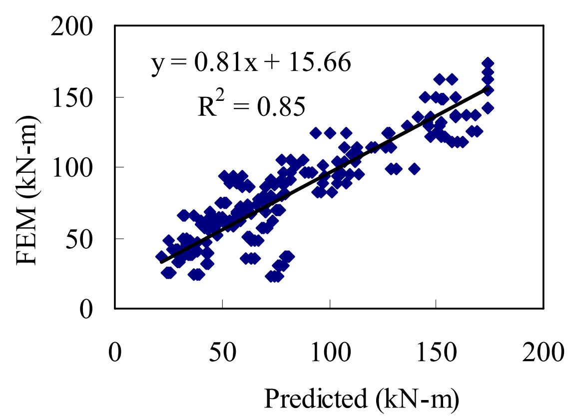

(f) Pile Moment

Figure 4.22: Correlation between Prediction Models and Numerical Method

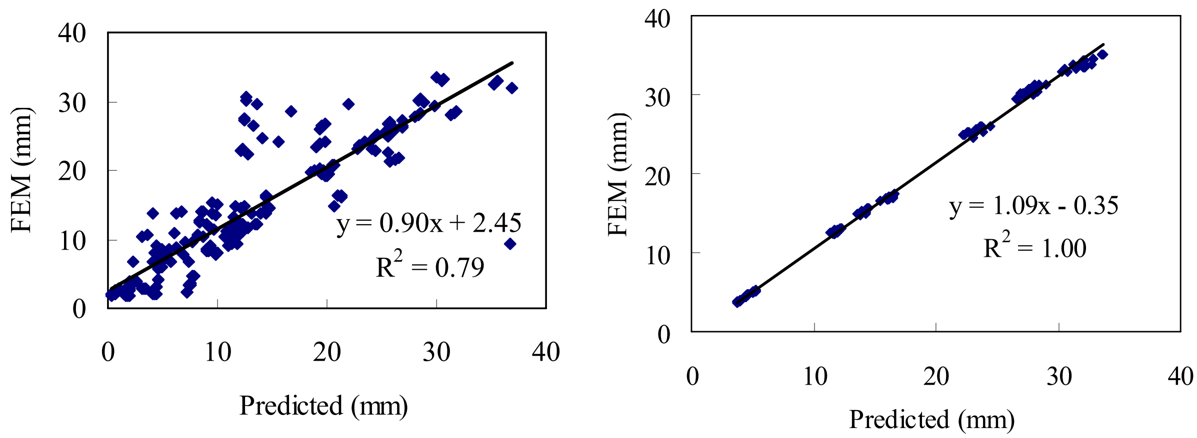

(g) Pile Head Displacement

(h) Abutment Displacement at Centroid of Superstructure

Figure 4.22: Correlation between Prediction Models and Numerical Method (Cont.)

4.5 Summary

The present study developed and demonstrated characterization methods for the key parameters. The numerical model included key features of IABs—backfill-abutment interaction, pile-soil interaction, construction joint, temperature variation, temperature gradient, and time-dependent effects. Based on the numerical method, 243 sets of a parametric study with five parameters was performed. The key parameters considered are: (1) thermal expansion coefficient; (2) bridge length; (3) backfill height; (4) backfill stiffness; and (5) soil stiffness around piles. Based on the results, regression analysis provides accurate IAB response predictions of: (1) bridge axial force; (2) bridge bending moment at the mid-span of the exterior span; (3) bridge bending moment at the abutment; (4) pile lateral force at pile head; (5) pile moment at pile head; (6) pile head/abutment displacement; and (7) abutment displacement at the centroid of a superstructure. The parametric study revealed that the thermal expansion coefficient, bridge length and pile soil stiffness significantly influence IAB response. The influences of backfill height and backfill stiffness are not relatively significant. The study results provide practical, preliminary estimates of bridge response and ranges for preliminary IAB design and analysis.

Chapter 5

PROBABILISTIC SIMULATION AND RESULTS

5.1 Introduction

In order to evaluate the uncertainties of prestressed concrete stress levels in IABs, a Monte Carlo simulation (MCS) has been performed. A MCS requires the establishment of IAB load and resistance statistics, and development of probabilistic numerical models, in order to establish IAB response statistics. IAB response statistics provide the basis for a reliability-based design format, allowing the determination of appropriate load factors. Load and resistance input variable statistics are defined for MCS in terms of distribution type, mean and standard deviation. The numerical models for MCS utilize previously developed, simplified, numerical models to streamline the simulation process. MCS iteratively computes the IAB response variables until the required number of cycles are reached. Based on the IAB response statistics, a reliability analysis of IABs develops new load and resistance factors for IABs.

Generally, MCS is applied to solving problems with complex uncertainty. Prediction of IAB behavior has inherent uncertainties due to concrete creep and shrinkage, soil nonlinearity and superstructure temperature variation. A deterministic analysis, as presented in Chapters 3 and 4 is able to determine nominal IAB responses. However, uncertainties in input variables can not be avoided due to variability, vagueness and randomness in loads and resistances. Therefore, a probabilistic simulation is required to examine the response uncertainties.

A schematic of probabilistic analysis is presented in Figure 5.1. In MCS, input variables related to uncertainties are regarded as random variables (RVs). The MCS

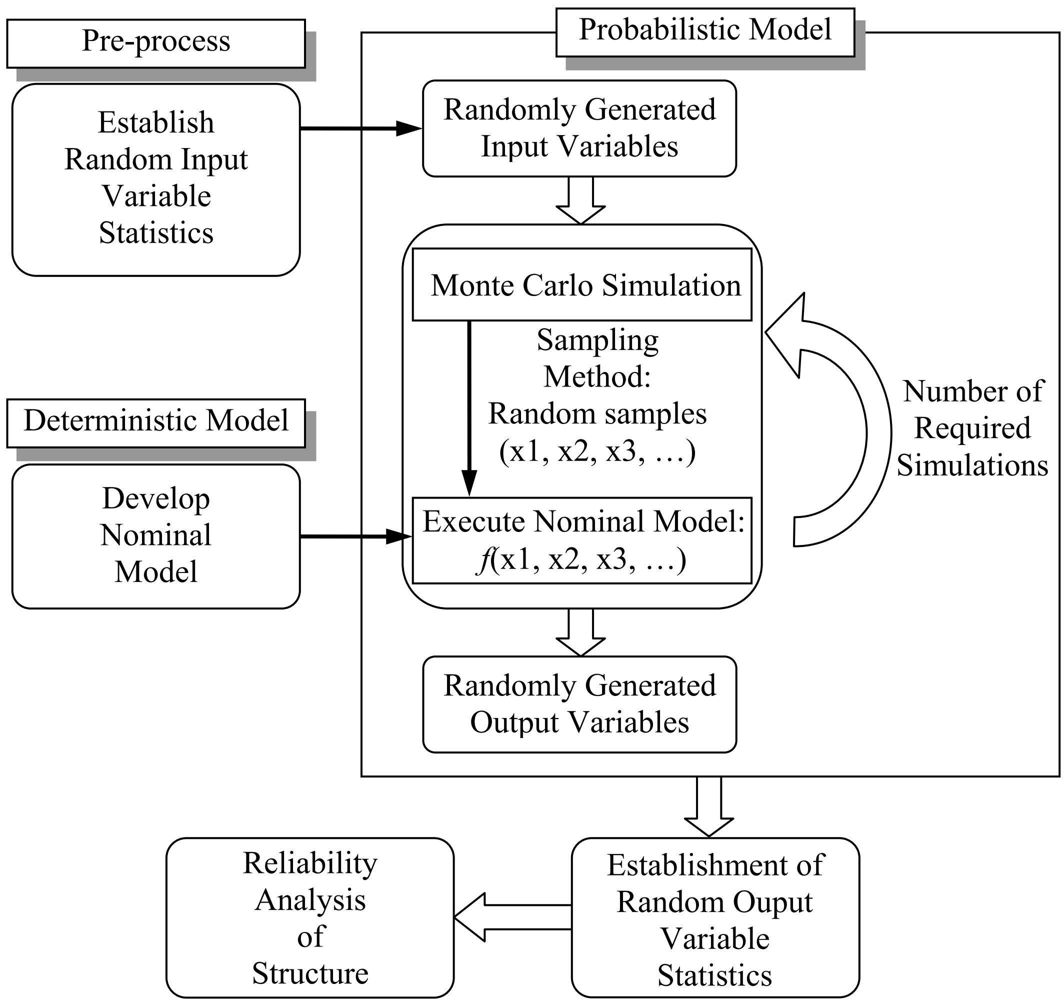

Figure 5.1: Probabilistic Analysis Procedure

method produces randomly generated input variables (RGIVs) that are accepted by the numerical model to compute randomly generated output variables (RGOVs). The RGIVs and RGOVs are characterized by distribution type, mean and standard deviation. MCS requires a significant number of cycles to obtain valid results. Thus, MCS may be unfeasible in situations of extremely complex and large numerical models due to prohibitively extensive computing time.

MCS determines the distribution and statistics of the IAB responses, utilizing the previously developed nominal numerical model that provides both prediction accuracy and reduction of model complexity. However, IAB nominal numerical models are still complex nonlinear models and require a long loading step—each 7-day average temperature loading is applied to the numerical model for a 75-year bridge life. To overcome this problem, this study used high performance computing machines (Sun SunFire v40z 3U Rackmount Boxes, Quad 2.6 GHz AMD Opteron processors, 32 GB of ECC RAM, 584 GB of local scratch disk). In addition, adopting the Latin hypercube sampling (LHS) method allowed reducing the number of simulations. LHS partitions the range of input variables into a desired number of strata with an equal probability and then randomly draws an RGIV within each stratum.

RGIVs are categorized into resistance variables and load. Bridge resistances and loads are regarded as RVs because bridge resistances and loads have uncertainties due to variability and randomness. Resistance variables are: (1) concrete elastic modulus; (2) backfill stiffness; and (3) lateral pile soil stiffness. Load variables are: (1) superstructure temperature variation; (2) superstructure concrete thermal expansion coefficient; (3) superstructure temperature gradient; (4) concrete creep and shrinkage; (5) bridge construction sequence/time; and (6) backfill pressure on backwall and abutment. The probabilistic simulation considered three deterministic bridge lengths: 18.3 m (60 ft), 61.0 m (200 ft) and 122.0 m (400 ft).

RGOVs are IAB responses in MCS and consist of: (1) bridge axial force; (2) bridge bending moment; (3) pile lateral force; (4) pile moment; (5) pile head/abutment displacement; (6) compressive stress at the top fiber at the mid-span of the exterior span; and (7) tensile stress at the bottom fiber at the mid-span of the exterior span. The following sections first establish statistics of input variables and then MCS is implemented to establish statistics of output variables.

5.2 Resistance Variables

Bridge components resist loads; however, the bridge resistance inherently includes uncertainty due to randomness and variability. The present study focuses on uncertainties in resistance material properties. Recent technical progress and manufacturing improvements have greatly reduced the uncertainties in prestressed member fabrication and dimension error variations. Uncertainties are small compared to material property variation [100]. Therefore, the present study regarded the material properties as the only source of resistance uncertainty and treated dimensional parameters as deterministic.

Resistance variables are: (1) concrete elastic modulus; (2) backfill stiffness; and (3) lateral pile soil stiffness. Each resistance variable relates directly to IAB resistance: the concrete superstructure provides resistance against vertical and horizontal loads; backfill provides lateral restraint during bridge expansion; and soil layers under abutments provide resistance against both bridge expansion and contraction. Therefore, based on the published literature and published experimental data, each resistance variable is described in terms of distribution type, mean and standard deviation.

5.2.1 Concrete Elastic Modulus

Because usage of high strength concrete ($f_c' \geq 55.2$ MPa (8 ksi)) in recent bridge construction has greatly increased [7, 91, 116], a 28-day concrete compressive strength, f_c' = 55.2MPa (8 ksi) is the adopted measure for prestressed concrete girder material. Previous research [56, 85, 100, 119] determined the statistics for normal strength concrete (20.7 MPa (3 ksi) $\leq f_c' \leq$ 34.5 MPa (5 ksi)): bias factor (λ) = 0.95 to 1.08, and coefficient of variation (COV) = 0.15 to 0.18. However, the statistics for high strength concrete have not been established. Because published E_c data are not as extensive as f_c' data, empirical equations to represent the relationship between f_c' and E_c are utilized.

Three empirical equations relating f_c' to E_c are compared to available testing data. AASHTO LRFD [4] provides an empirical equation for normal concrete:

$$\begin{aligned} E_c &= 0.043 w_c^{1.5} \sqrt{f_c'} \qquad &(\text{kg/m}^3 \text{ and MPa}) \\ E_c &= 33{,}000 w^{1.5} \sqrt{f_c'} \qquad &(\text{kcf and ksi}) \end{aligned} \tag{5.1}$$

where f_c' = 28-day concrete compressive strength (MPa or ksi), and w_c = concrete density (kg/m^3 or kcf). ACI 363 [7] suggests an empirical equation for high strength concrete:

$$\begin{aligned} E_c &= \left(\frac{w_c}{86} \right)^{1.5} \left(6900 + 3320 \sqrt{f_c'} \right) \qquad &(\text{kg/m}^3 \text{ and MPa}) \\ E_c &= \left(\frac{w_c}{0.145} \right)^{1.5} \left(1000 + 1265 \sqrt{f_c'} \right) \qquad &(\text{kcf and ksi}) \end{aligned} \tag{5.2}$$

NCHRP18-07 [91] proposes an empirical equation to relate f_c' to E_c for high strength concrete:

$$E_c = 33{,}000 K_1 K_2 \left(0.140 + \frac{f_c'}{1000}\right)^{1.5} \sqrt{f_c'} \qquad \text{(ksi)} \qquad (5.3)$$

where f_c' = 28-day concrete compressive strength (ksi); and K_1 and K_2 are correction factors. K_1 = 1.0 corresponds to an average compressive strength. K_2 is based on the 90th percentile upper bound and the 10th percentile lower bound. A comparison of these three equations to 245 data from published experiments [80, 91, 116] appears in Figure 5.2. In the experimental data, the f_c' ranges between 55.8 and 70.3 MPa (8.1 and 10.2 ksi), which is between -11% and 12% of the mean strength ($\mu_{fc'}$). E_c varies more severely between 23.8 and 74.4 GPa (3450 and 10785 ksi), which is between -39% and 90% of the mean elastic modulus (μ_{Ec}).

For f_c' = 55.2 MPa (8000 psi), Eq. 5.1 and 5.3 predicted -4.6% and -6.5% lower E_c than the mean of experimental data at the specified strength, f_c' = 55.2 MPa (8000 psi). The accuracy of Eq. 5.2 is relatively lower than others (-19.5%). At the mean compressive strength ($\mu_{fc'}$ = 62.7 MPa (9.10 ksi)), Eq. 5.1 and 5.3 predicts 1.8% and 0.8% smaller E_c than the mean of the experimental data. Therefore, both Eq. 5.1 and 5.3 are appropriate predictions for f_c' = 55.2 MPa (8 ksi).

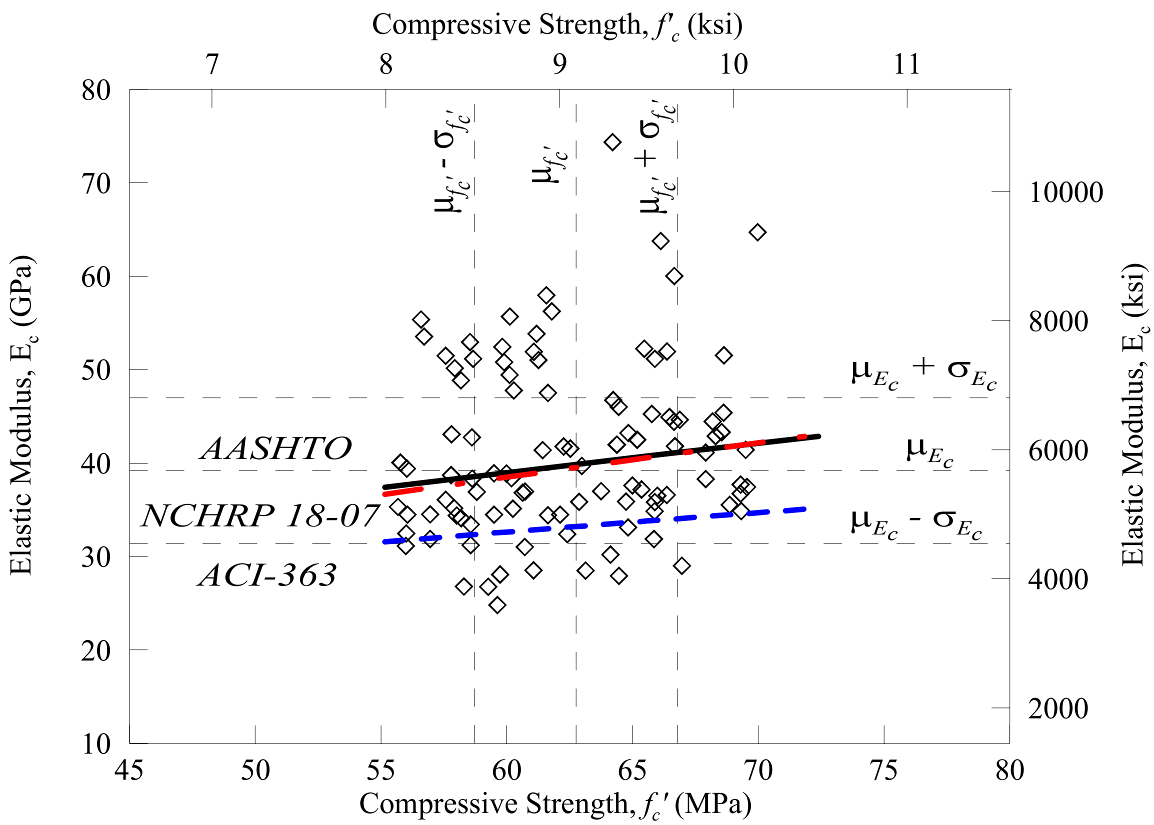

$\mu_{fc'}$ and μ_{Ec} = mean of f_c' and E_c; σ_{Ec} and $\sigma_{fc'}$ = standard deviation of f_c' and E_c

Figure 5.2: Concrete Elastic Modulus (E_c) vs. Concrete Compressive Strength (f_c')

Table 5.1: Published Concrete Elastic Modulus, E_c Statistics

Source	Concrete Elastic Modulus (E_c), f_c' = 55.2MPa (8 ksi) GPa (ksi)			
	Lower Limit	Mean	Upper Limit	Standard Deviation
Laman *et al.* [80] (Based on Eq. 5.1)	36.1 (5242)	38.3 (5553)	39.9 (5789)	0.9 (124)
NCHRP18-07 [91]	23.8 (3450)	**39.2 (5684)**	74.4 (10785)	**7.8 (1130)**
Nowak and Szerszen [103] (Based on Eq. 5.1)	-	37.1 (5386)	-	11.1 (1615)
Russell *et al.* [116]	36.9 (5350)	40.2 (5830)	43.5 (6310)	-

As presented in Figure 5.2, 77% of E_c and 80% of f_c' are located within two standard deviations ($\mu_{Ec} + \sigma_{Ec} \leq E_c \leq \mu_{Ec} - \sigma_{Ec}$, and $\mu_{fc'} + \sigma_{fc'} \leq f_c' \leq \mu_{fc'} - \sigma_{fc'}$). This is close to the standard normal distribution (69.2%). Thus, experimental data in Figure 5.2 represent an actual concrete elastic modulus variation. Other sources also considered and Table 5.1 summarizes the collected data of E_c for f_c' = 55.2MPa (8 ksi). Therefore, mean = 39.2 GPa (5,684 ksi) and standard deviation = 7.8 GPa (1,130 ksi) for E_c based on extensive test data from NCHRP18-07 [91] are adopted in MCS.

5.2.2 Backfill Stiffness

Backfill resists bridge expansion while resulting backfill pressure is a permanent load on abutments. The lateral earth pressure is determined by the unit weight and friction angle of backfill soils because backfill soils are cohesionless materials. In the construction of four field monitored IABs, PennDOT OGS coarse aggregate was the backfill material. The design value of the PennDOT OGS coarse aggregate backfill was adopted: mean unit weight, (γ_{soil}) = 5.7 kPa (119 pcf), and an internal friction angle, (ϕ_f) = 34º. Harr [61], Kullhawy [76], Lacasse [78] and Duncan [44] investigated COVs as in Table 5.2. Oesterle *et al.* [105] also surveyed U.S., and reported COV = 33% for granular soils, assuming the granular soils are uncompacted and undisturbed conditions. In practice, backfill is compacted aggregate rather than granular soils but has very similar properties in every bridge construction site. Based on the published literature, many research report that means for γ_{soil} and ϕ_f are 5.7 kPa (119 pcf) and 34º and COVs for γ_{soil} and ϕ_f are 3% and 10%, respectively. Therefore, these values are utilized in MCS. For subgrade modulus (K_h), few researches report its variation. Field measurements in Figure 4.6 are utilized to determine mean = 12 MN/m^3 (43.8 pci). COV for K_h is adopted from available published value of 50%.

Table 5.2: Statistics for Backfill Soils

Source	Soil Property	COV (%)
Baecher [24], Harr [61], Kulhawy [76]	Unit Weight (γ_{soil})	3 – 7
Baecher [24], Harr [61], Kulhawy [76]	Friction Angle (ϕ_f)	2 – 13
Baecher [24]	Subgrade Modulus (K_h)	50

5.2.3 Pile Soil Stiffness

Pile soil stiffness significantly influences IAB response and the soil material stiffness definition contains uncertainties. Based on published literature [24, 35, 36, 44, 55, 60], an upper, mean and lower limit for each soil property is established to allow consideration of uncertainties in soil materials (Table 5.3).

Table 5.3: Soil Layer Properties and Range Determination [24, 35, 36, 44, 55, 60]

Property	Upper Limit	Mean	Lower Limit
Sand Density, kN/m^3 (pcf)	22 (142)	19 (121)	16 (100)
Clay Density, kN/m^3 (pcf)	22 (142)	19 (121)	16 (100)
Angle of Friction (Sand), Degree	42	35	28
Undrained Shear Strength (clay), kN/m^2 (psi)	193 (28)	121 (17.5)	48 (7)
Elastic Modulus (K), MN/m^3 (pci)	353 (1,300)	271 (1000)	190 (700)
ε_{50}, mm (in)	0.13 (0.005)	0.20 (0.008)	0.25 (0.01)

Pile models in an IAB use the previously developed condensed pile model with a lateral translation spring and rotational spring. To determine pile soil stiffness, maximum and minimum pile soil stiffness is first established based on the determined maximum and minimum soil property. Then upper and lower limit for pile soil stiffness is established based on maximum and minimum pile soil stiffness without regard to cohesive or cohesionless soils. The mean pile soil stiffness is based on the average of upper and lower pile soil stiffness.

The COV of pile soil stiffness is adopted from the available literature [105]. The condensed pile models in this study represent only the pile head stiffness for lateral translation and rotation. Thus, COV for pile soil stiffness is more convenient to represent pile soil stiffness than COVs of soil properties. The research [105] surveyed numerous soil types (called “General type”) at the bridge construction sites and reports 26% of COV that was adopted by this study.

Normal distributions for both force-displacement and moment-rotation relationships were constructed and are presented in Figure 5.3. Means of the distributions were determined based on the mean properties in Table 5.3. Also, the previously determined 26% COV was utilized to construct normal distributions for force-displacement and moment-rotation relationships. In MCS, these distributions were truncated by the upper and lower limit in Table 5.3.

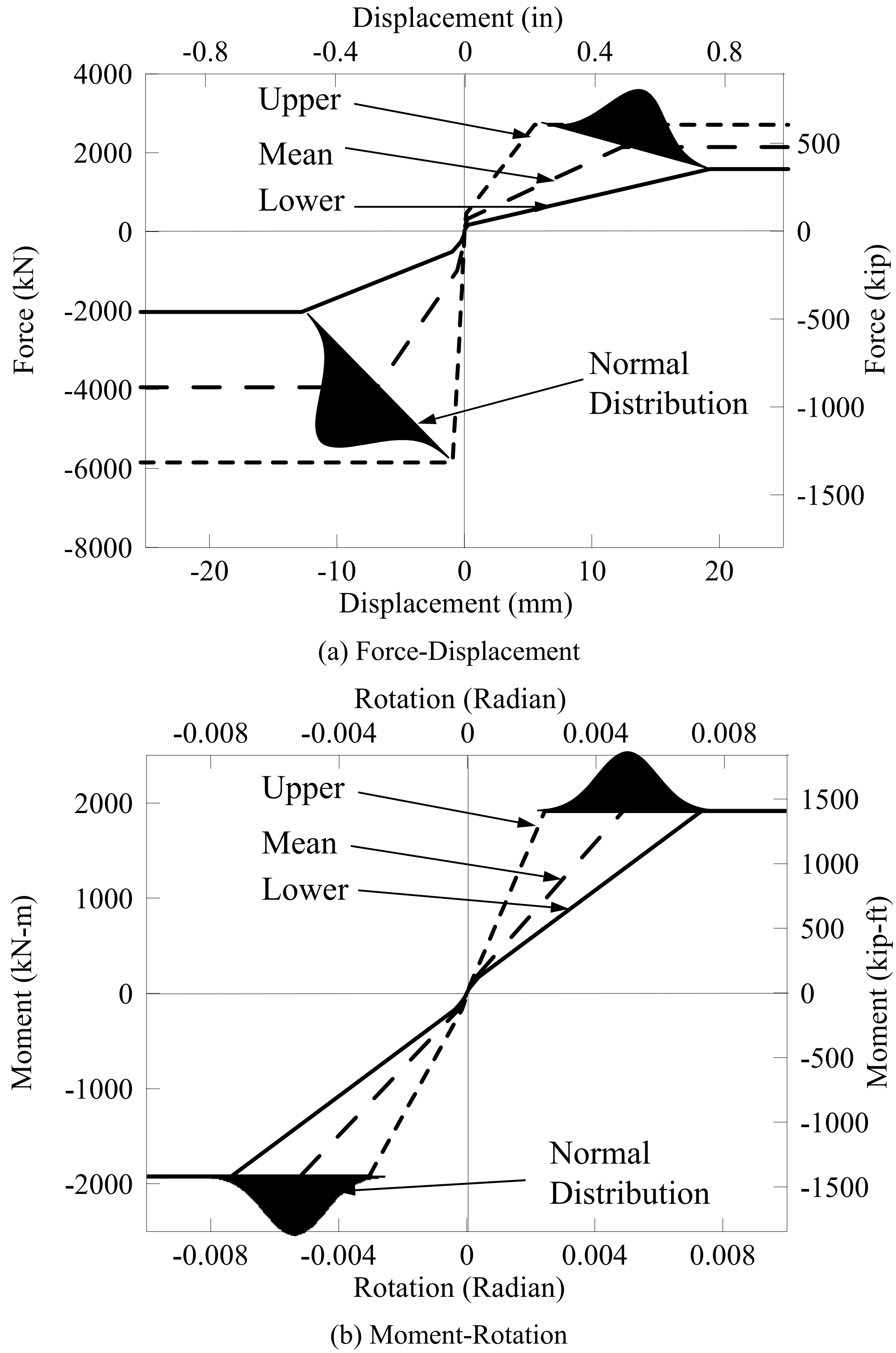

Figure 5.3: Soil-Pile Interaction Stiffness Definition

5.3 Load Variables

Bridge loads have uncertainties due to randomness and variability. Bridge load uncertainties must be considered in a MCS to obtain valid simulation results. Load variables for IABs are superstructure temperature, concrete thermal expansion coefficient variation, thermal gradient, and time-dependent effects with construction timeline. Dead load and live load are not considered herein because analyses for dead load, traffic loads, etc. are well established elsewhere.

Load variables are assumed to be normally distributed because the true distributions of these loads are unknown. Central Limit Theorem [104] provides mathematical and theoretical justification for the sampling distribution approximating the normal distribution. Each load variable is randomly generated within its distribution and statistics and applied to bridges to obtain RGOVs.

5.3.1 Superstructure Temperature

The superstructure temperature variation is a primary loading in IABs and induces bridge movements, although temperature variation in concrete structures is difficult to predict. Although solar radiation, precipitation and wind speed may be influencial to bridge temperature, the ambient temperature has the most significant influence on bridge temperature changes in regions similar to Pennsylvania. However, local temperature varies significantly and is difficult to represent as a single temperature variation model. Therefore, the temperature model in this study is limited to the Mid-Atlantic area. Climate conditions for the other regions in the U.S. can be found in other sources [15, 89, 105]. Three sources of temperature measurement have been used to determine mean annual temperature, annual mean temperature variation and standard deviation of daily temperature variation: a local weather station [79, 80], the Pennsylvania State Climatologist (PSC) [111], and the National Climate Data Center (NCDC) [89]. The local weather station in the vicinity of the bridges collected climate data from August 2002 to present. PSC collected weather information since 1888 and NCDC since 1971.

Annual mean temperature, annual mean temperature variation and daily temperature variation standard deviation were established and tabulated for Table 5.4. For comparison purposes, local weather station data from the Port Matilda area, PSC for Pennsylvania, NCDC for Mid-Atlantic states and NCDC data for U.S. 50 states were collected. Except U.S. 50 states temperature statistics, local weather station data, PSC data and NCDC data produced similar temperature statistics. Based on the collected data, annual mean temperature (μ_T) is 9.4ºC (49ºF) and the standard deviation of daily temperature variation (σ_T) for the present study is 6.5ºC (11.7ºF).

Table 5.4: Temperature Statistics

	Port Matilda, PA ºC (ºF)	PA (PSC) ºC (ºF)	Mid-Atlantic (NCDC) ºC (ºF)	U.S 50 states (NCDC) ºC (ºF)
Annual Mean	7.5 (45.5)	9.7 (49.5)	**9.4 (49)**	12.8 (55)
Annual Variation (× 0.5)	**16.7 (30)**	13.9 (25)	12.8 (23)	11.6 (20.8)
Daily Standard Deviation	5.6 (11.2)	5.8 (10.5)	**6.5 (11.7)**	13.3 (24)

However, annual mean temperature variation = 16.7ºC (30ºF) is adopted to cover 7-day average temperature because solar radiation is high during summer and low during winter.

For a MCS, the nominal temperature model in Eq. 3.1 is a mean temperature at time t. To consider uncertainties in the variation of temperature, the mean temperature is multiplied the standard deviation of daily temperature variation (σ_T). Therefore, RGIV temperature (T_{MCS}) at time t is defined as:

$$T_{MCS}(t) = \left[\mu_T + A\sin\left(\omega t + \phi\right)\right]\left(\sigma_T\right) \tag{5.4}$$

where, μ_T = mean temperature (9.4ºC (49ºF));

A = amplitude of temperature variation (16.7ºC (30ºF));

ω = frequency (2π);

t = analysis time (year);

ϕ = phase lag, $\left(\dfrac{Backwall\ Placement\ Date}{365\ Days} - 0.09\right)$(radian), and

σ_T = standard deviation of daily temperature (6.5ºC (11.7ºF)).

An example RGIV temperature for 5 years appears in Figure 5.4. The mean bridge temperature follows a sinusoidal curve and all bridge temperature variation is bounded by μ_T - 3σ_T and μ_T + 3σ_T. In a deterministic model, temperature at time t follows the mean temperature (Eq. 3.1) in Figure 5.4. However, in a MCS, bridge temperature at time, t, follows the RGIV temperature in Figure 5.4 to account for uncertainties in temperature variation. At every 7-day, a RGIV temperature from a normal distribution with mean =

mean temperature in Eq. 3.1 and standard deviation = 6.5ºC (11.7ºF) is derived and applied to the bridge as a thermal loading.

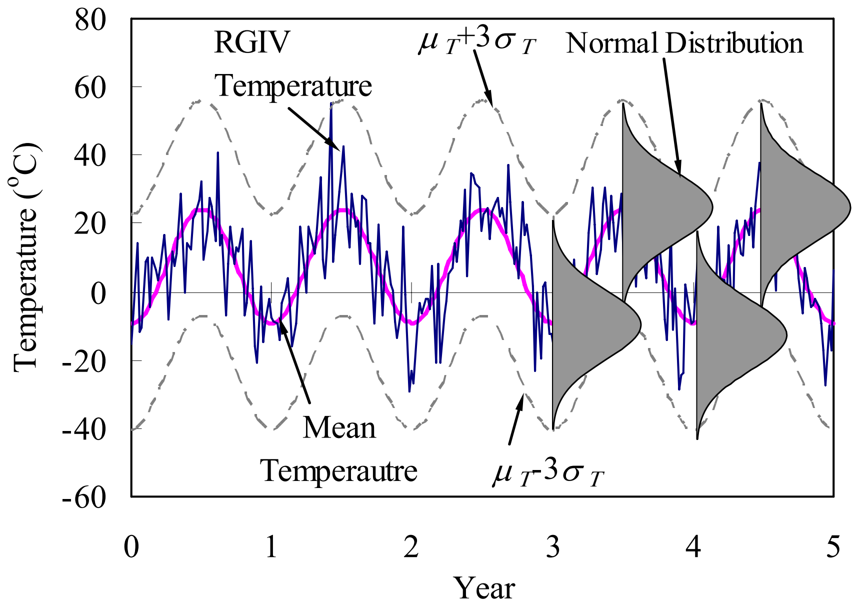

Figure 5.4: Temperature Variation in MCS

5.3.2 Concrete Thermal Expansion Coefficient

The MCS considers uncertainty in the thermal expansion coefficient. The thermal expansion coefficient determines thermal expansion and contraction of IABs. Concrete thermal expansion coefficient varies significantly due to variations in mix design: properties and proportions of aggregate, water to cement ratio, relative humidity, age of concrete, concrete temperature, and concrete temperature alternations. A summary of a survey of published thermal expansion coefficients appears in Table 5.5. Because the study by Oesterle *et al.* [105] considered most extensive test data, the present study adopted 4.07×10^{-6}/°C (2.26×10^{-6}/°F) for mean, 4.07×10^{-6}/°C (2.26×10^{-6}/°F) for lower limit and 14.4 × 10^{-6}/°C (8.0 × 10^{-6}/°F) for upper limit with a standard deviation of 2.36 × 10^{-6}/°C (1.31 × 10^{-6}/°F).

Table 5.5: Statistics for Concrete Thermal Expansion Coefficient

Source	Thermal Expansion Coefficient × 10^{-6}/°C (× 10^{-6}/°F)			
	Lower Bound	Mean	Upper Bound	Standard Deviation
AASHTO LRFD [4]	5.4 (3.0)	10.8 (6.0)	14.4 (8.0)	-
Emanuel and Hulsey* [50]	-	1.00	-	0.11
Kada *et al.* [72]	6.5 (3.6)	-	7.6 (4.2)	-
Oesterle *et al.* [105]	**4.07 (2.26)**	**8.77 (4.87)**	**13.5 (7.49)**	**2.36 (1.31)**
Nison [94]	7.2 (4.0)	-	12.6 (7.0)	-
Russell *et al.* [116]	8.14 (4.52)	11.38 (6.32)	15.77 (8.76)	-
Tanesi *et al.* [122]	8.47 (4.71)	9.97 (5.54)	11.70 (6.50)	0.77 (0.43)
Present Study	4.07 (2.26)	8.77 (4.87)	14.4 (8.00)	2.36 (1.31)

* Normalized to the mean

5.3.3 Temperature Gradient

The MCS considers uncertainty in the superstructure temperature gradient (TG). Statistical data are not available and, therefore, this study adopted the temperature gradient model by AASHTO LRFD [4, 5]. By Empirical Rule [104], AASHTO temperature gradient is divided into four standard deviations, and mean and standard deviation is established. At each girder depth, it is assumed to be proportional to the AASHTO temperature gradient. The assumed temperature gradient distribution appears in Figure 5.5. In a MCS, the equivalent temperature gradient model (T_{TG}) in Section 3.4.8 for the mean AASHTO temperature gradient (μ_{TG}) is computed and corresponding standard deviation (σ_{TG}) is established. Determined temperature gradients (T_{MCS_TG}) for a MCS corresponding to Table 4.6 are presented in Table 5.6. At every 7-day, a RGIV temperature gradient from a normal distribution with mean = μ_{TG} in Table 5.6 and standard deviation = σ_{TG} in Table 5.6 is derived and applied to the bridge.

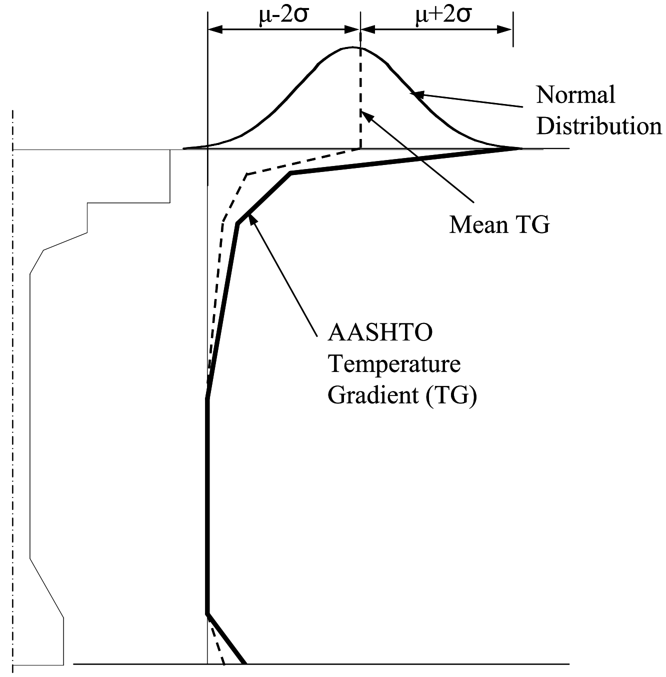

Figure 5.5: Temperature Gradient Distribution

Table 5.6: Temperature Gradient Statistics

Bridge Length m (ft)	Gradient	Mean (μ_{TG}) °C (°F)		Standard Deviation (σ_{TG}) °C (°F)	
		Top	Bottom	Top	Bottom
18.3m (60ft)	Positive (A_{TG_P})	6.5 (11.8)	0.9 (1.7)	3.3 (5.9)	0.5 (0.9)
	Negative (A_{TG_N})	-2.9 (-5.3)	-0.6 (-1.1)	1.5 (2.7)	-0.3 (-0.6)
61.0 & 121.9m (200 & 400ft)	Positive (A_{TG_P})	4.2 (7.5)	-0.6 (-1.0)	1.0 (1..9)	-0.3 (-0.5)
	Negative (A_{TG_N})	-2.0 (-3.7)	-0.6 (-1.0)	0.5 (0.9)	-0.3 (-0.5)

5.3.4 Time-dependent Loads

The MCS considers uncertainties in concrete creep and shrinkage. Statistics for both concrete creep and shrinkage determined by previous research [6, 22, 33, 134] are presented in Table 5.7. The average of the previous research recommendations is adopted as mean = 1.0 and standard deviation = 0.5.

Table 5.7: Creep and Shrinkage Statistics

Source	Creep		Shrinkage	
	Mean	Standard Deviation	Mean	Standard Deviation
ACI 209 [6]	1.00	0.32	1.00	0.55
Bazănt and Baweja [22]	1.00	0.528	1.00	0.553
CEB-FIP [33]	1.00	0.339	1.00	0.451
Yang [134]	1.00	0.517	1.00	0.542

The present study utilizes a modification factor. In MCS, computed creep and shrinkage effect assumed to be a mean is multiplied by this modification factor to account uncertainty. A modification factor is drawn from a normal distribution with mean = 1.0 and standard deviation = 0.5. To obtain valid results, a normal distribution of a modification factor was truncated at 0.1 to prevent creep and shrinkage effect inducing a large tensile stress. Figure 5.6 presents an example of time-dependent strain at the top and bottom fibers at the mid-span of the exterior span. At every beginning of simulation cycles, a RGIV modification factor is drawn and multiplied to the time-dependent strain.

As presented in Figure 5.6, strain at the top and bottom fibers varies with respect to normal distribution.

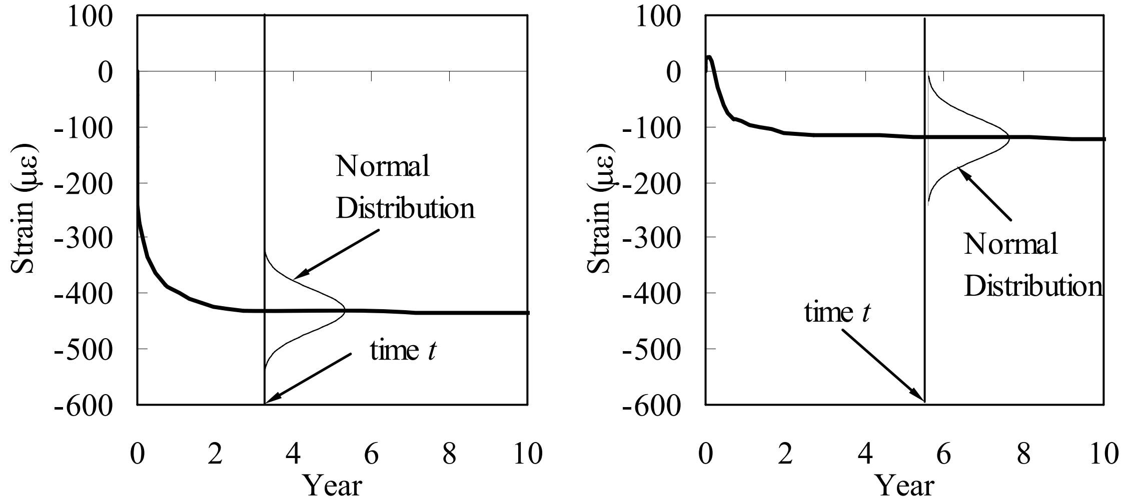

(a) Top Fiber at the Mid-span (b) Bottom Fiber at the Mid-span

Figure 5.6: Time-dependent Strain in Concrete Girder

5.3.5 Bridge Construction Timeline

MCS considers uncertainties in the bridge construction timeline. The deck slab concrete placement date influences the time-dependent effects. Also, frame action in an IAB due to the integral backwall begins just after backwall concrete placement date. Therefore, the days are counted from girder manufacture to the deck concrete placement date because time-dependent effects start from girder manufacture. For the backwall concrete placement date, Julian date (JD) is used because the backwall concrete placement date relates to the initial bridge temperature. In MCS, the bridge construction timeline in Figure 4.1 is the assumed mean construction timeline.

Standard deviation of deck placement and backwall placement date is determined from published literature. Oesterle *et al.* [105] surveyed 9 bridges in the U.S. and collected construction temperature and dates (Figure 5.7).

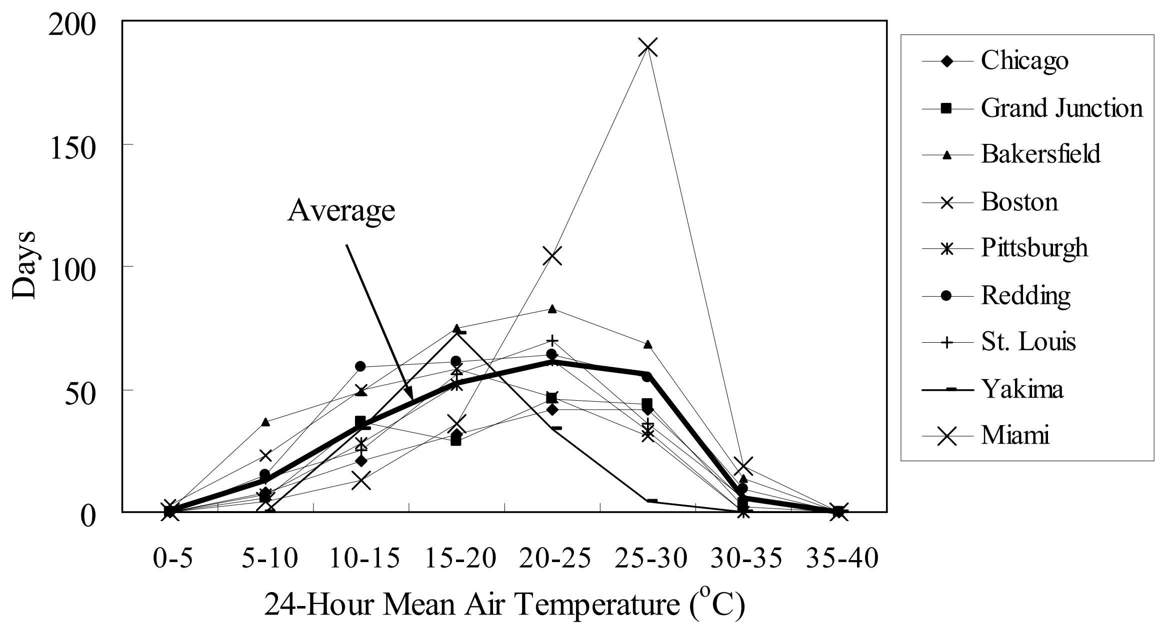

Figure 5.7: Temperature Survey During Construction [105]

Bridge construction surveyed began in April and ceased in November, which corresponds to the representative construction timeline (Figure 4.1). The construction temperature ranges from 5°C to 35°C (41°F to 95°F). Generally, bridge construction begins in early spring and ceases in late fall or early winter. Based on Figures 4.1 and 5.7, the temperature on deck slab concrete placement date and backwall concrete placement date may range from 5°C to 15°C (41°F to 59 °F), which are temperatures typical of the fall season.

Based on the field tested bridges construction timelines in Tables 4.2 and 4.3 and survey results in Figure 5.7, the deck concrete placement date mean is assumed to be 100 days from girder manufacture. The standard deviation is 30 days, the lower limit is 30 days from girder manufacture, and the upper limit is 200 days from girder manufacture. The backwall concrete placement date ranges from July to November. Therefore, the backwall placement date mean is 242 JD (September), standard deviation is 81 days, the lower limit is 60 JD, and the upper limit is 300 JD. The backwall placement date distribution with the assumed bridge temperature variation during a year is presented in Figure 5.8. Based on a RIGV backwall placement date, the initial bridge temperature in the MCS is determined and the established sinusoidal temperature load starts.

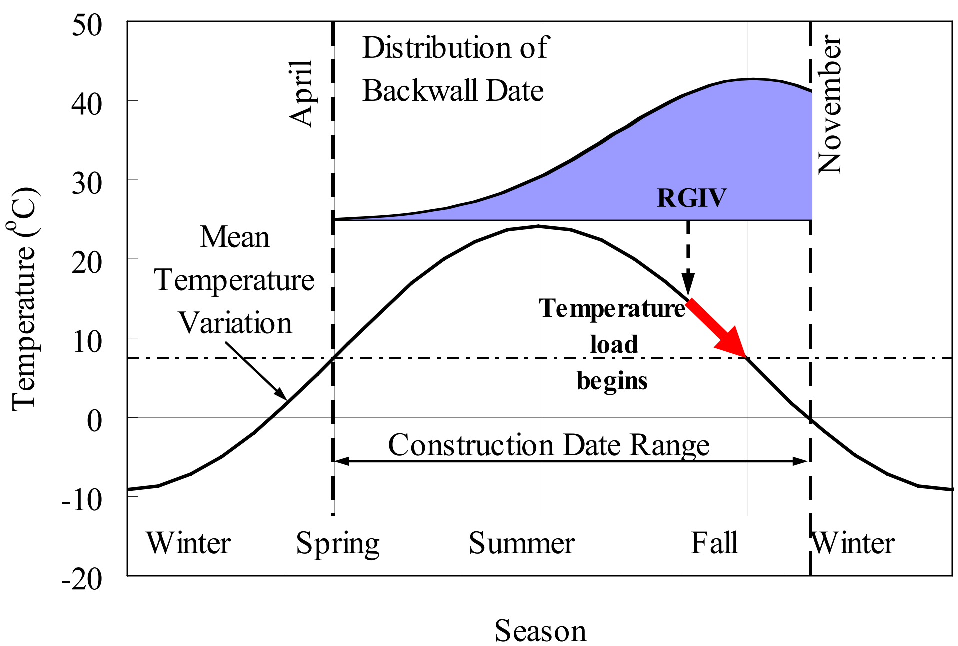

Figure 5.8: Bridge Temperature and Backwall Placement Date Distribution

5.4 Monte Carlo Simulation

Performing a MCS establishes the required IAB response statistics. Because bridge loads and resistance are uncertain due to variability and randomness, prediction of bridge response is uncertain. The MCS is used to simulate a bridge subjected to randomly generated loads and possessing uncertain resistance to obtain randomly generated bridge response. Each trial simulation in the MCS is independent from other trial simulations. This independent simulation allows the MCS to investigate numerous bridges. Therefore, the present study develops MCS models based on the previously developed nominal model. To determine the required number of simulations and valid results, the simulation is iterated until COVs of IAB responses are stable.

A schematic of the developed MCS model appears in Figure 5.9. Based on the previously established resistance and load variables statistics, input variables are randomly generated and are accepted by the developed nominal numerical model from Chapter 3. The resistance variables include: (1) elastic modulus of superstructure; (2) backfill stiffness; and (3) pile soil stiffness. The load variables include: (1) temperature variation; (2) thermal expansion coefficient; (3) temperature gradient; (4) time-dependent load; (5) deck concrete placement date; (6) backwall concrete placement date; and (7) backfill pressure. For each trial, the nominal model is solved based on a set of RGIVs. Then, each trial simulation produces RGOVs, IAB critical responses: (1) bridge axial force; (2) bridge bending moment; (3) pile lateral force; (4) pile moment; (5) pile head/abutment displacement; (6) compressive stress at the top fiber at the mid-span of the exterior span; and (7) tensile stress at the bottom fiber at the mid-span of the exterior span. Finally, the accumulated data of each trial simulation derives the response statistics. MCS iterates this computation for a required number of simulations; the LHS method, a sampling technique, dramatically reduces the required number of simulations.

LHS divides each input variable range into intervals with an equal probability. Randomly selected input variables from each interval are combined, which prevents each randomly selected value from being selected more than twice. For a seed value to generate random numbers, the present study used the continuous updating seed values for a random number generator to calculate the next random number [9].

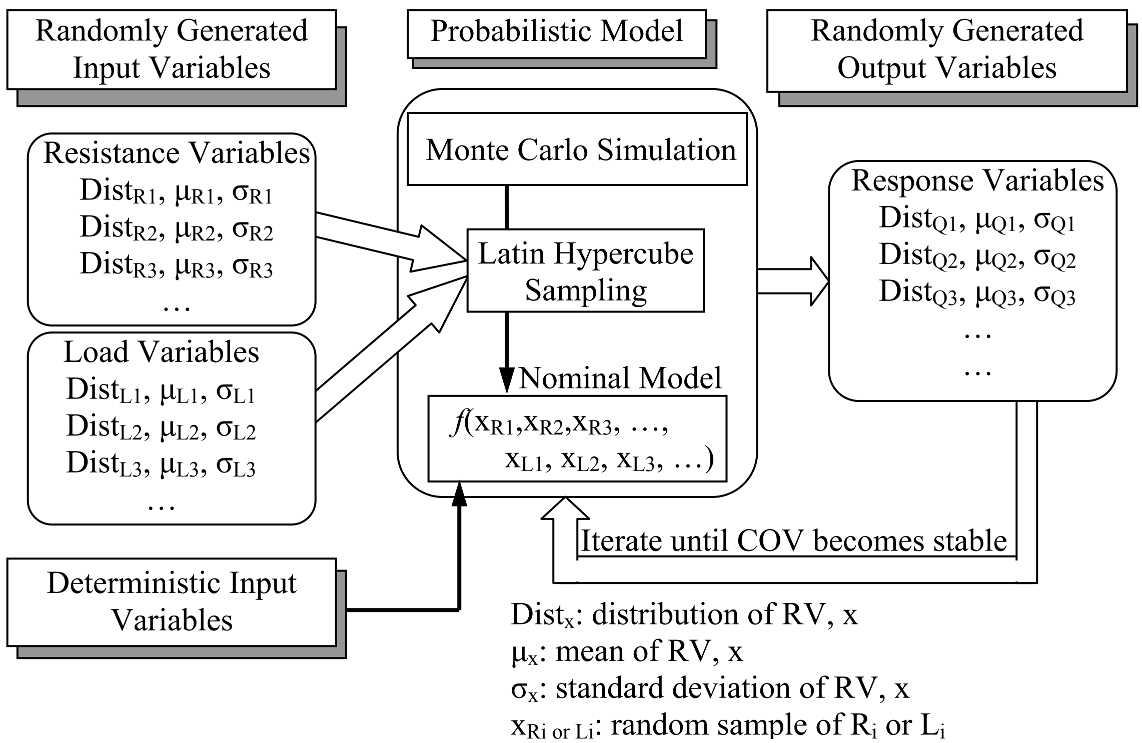

Figure 5.9: Monte Carlo Simulation Procedure

A preliminary simulation estimates the ultimate number of required simulations. The required number of simulations, by Eq. 2.17, with target reliability = 3.5 and coefficient of variation of the probability failure = 0.5, is 17164 simulation loops, which is time-consuming for complex numerical models. The present study adopted COVs to estimate the required number of simulations [16]. A 61.0 m (200 ft) long bridge was tested to investigate the number of simulations making COVs of IAB critical responses stable as presented in Figure 5.10. Bridge moment, pile lateral force, pile moment and pile displacement start to converge from 100 trial simulations, while bridge axial force starts to converge from 400 trial simulations. Therefore, the required number of simulations for this study is 500.

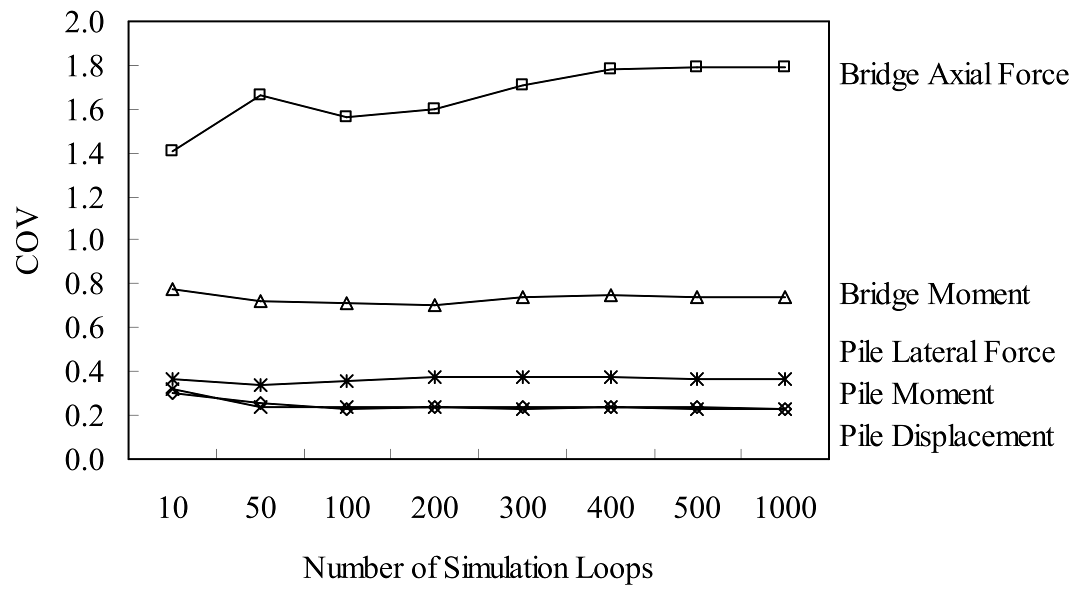

Figure 5.10: Determination of Required Number of Simulations Based on COV Testing

5.5 Monte Carlo Simulation Results

MCS results established IAB response statistics. Previously determined statistics for load and resistance variables were used as RGIVs in the simulation. Critical responses (RGOVs) of (1) bridge axial force; (2) bridge bending moment; (3) pile lateral force; (4) pile moment; (5) pile head/abutment displacement; (6) compressive stress at the top fiber at the mid-span of the exterior span; and (7) tensile stress at the bottom fiber at the mid-span of the exterior span during a 75-year bridge life have been evaluated and statistics have been established. For bridge axial force, compressive and maximum positive bridge moments are discussed. For bridge bending moment, both positive and negative moments are evaluated. For pile lateral force and pile moment, maximum shear forces and weak-axis bending moments at the pile head are investigated. Pile head/abutment displacements are also investigated at the pile head for maximum displacement during a 75-year bridge life.

Three graphical tools are utilized to determine a best-fit distribution model for each response: probability distribution, empirical cumulative distribution function (CDF), and histogram. Confidence interval (CI) of 95% and P-value were also included in the probability distribution. CI represents the intervals covering the estimation. P-value represents the probability of obtaining an observed result and its significance level. The smaller the P-value, the more significant the results are. First, a commercial program was used to determine goodness-of-fit test statistics and a best-fit distribution, considering various distribution types. However, a determined distribution for a RGOV response by a commercial program, especially distributions for L = 121.9m (400 ft), could not fully describe its peak frequency and maximum responses. For a RGOV response, a distribution type and statistics, therefore, was determined maximum responses from MCS results to be located within 95% CI, be close to a proposed distribution CDF, and well-represent peak frequency of probability density function (PDF).

Considering various distribution types, a best-fit distribution for each IAB response was determined. All IAB responses, however, were fit using three distribution types: normal, lognormal, and Weibull distributions. A normal distribution is represented by mean (μ) and standard deviation (σ) to describe the distribution shape. PDF and CDF for the normal distribution is:

$$\begin{aligned} &\text{PDF: } f_X(x) = \frac{1}{\sigma\sqrt{2}} \exp\left(-\frac{1}{2}\left[\frac{x-\mu}{\sigma}\right]^2 \right) \quad (-\infty < x < \infty) \\ &\text{CDF: } F_X(x) = \int_{-\infty}^{x} \frac{1}{\sigma\sqrt{2\pi}} \exp\left(-\frac{1}{2}\left[\frac{x-\mu}{\sigma}\right]^2 \right) dx \end{aligned} \tag{5.5}$$

PDF and CDF for the lognormal distribution is:

$$\begin{aligned} &\text{PDF: } f_X(x) = \frac{1}{x\sigma_Y\sqrt{2}} \exp\left(-\frac{1}{2}\left[\frac{\ln x-\mu_Y}{\sigma_Y}\right]^2 \right) \quad (0 < x < \infty) \\ &\text{CDF: } F_X(x) = \int_{-\infty}^{x} \frac{1}{x\sigma_Y\sqrt{2\pi}} \exp\left(-\frac{1}{2}\left[\frac{\ln x-\mu_Y}{\sigma_Y}\right]^2 \right) dx \end{aligned} \tag{5.6}$$

where, $\sigma_Y^2 = \ln\left[1 + \left(\frac{\sigma_X}{\mu_X}\right)^2\right]$, and $\mu_Y = \ln(\mu_X) - \frac{1}{2}\sigma_Y^2$.

It is convenient to describe location (*Loc*) and scale (*Scale*) parameters for lognormal distribution. Loc and Scale have a relationship with mean and standard deviation:

$$\begin{aligned} &Loc = 2\ln(\mu) - \frac{\ln(\mu^2 + \sigma^2)}{2} \\ &Scale = \sqrt{\ln(\mu^2 + \sigma^2) - 2\ln(\mu)} \end{aligned} \tag{5.7}$$

where, $\mu =$ the desired mean of the lognormal data, and $\sigma =$ the desired standard deviation of the lognormal data. From Eq. 5.7, μ and σ can be derived from location (*Loc*) and scale (*Scale*) parameters as:

$$\mu = \exp\left(Loc + \frac{Scale^2}{2}\right)$$
$$\sigma = \exp\left[2\left(Loc + Scale^2\right)\right] - \mu^2 \tag{5.8}$$

The basic characteristics of Weibull distribution appear in Eq. 5.9 and Eq. 5.10. This distribution type is commonly used to model extreme RGOVs.

$$\text{PDF: } f_X = \frac{k}{u}\left(\frac{x}{u}\right)^{k-1} \exp\left[-\left(\frac{x}{u}\right)^k\right]$$
$$\text{CDF: } F_X = \exp\left[-\left(\frac{x}{u}\right)^k\right] \tag{5.9}$$

where, u = the scale parameter, and k = the shape parameter.

$$\mu_X = (u)\Gamma\left(1 + \frac{1}{k}\right)$$
$$\sigma_X^2 = (u)^2\left[\Gamma\left(1 + \frac{1}{k}\right) - \Gamma^2\left(1 + \frac{1}{k}\right)\right] \tag{5.10}$$

where, gamma function, $\Gamma(t) = \int_0^\infty r^{t-1} \exp(-r)dr$ = (t-1) Γ(t-1).

In response the evaluation summary, the RGOVs are described using distribution type, biased factor (λ) and COV. Biased factor represents a ratio of mean to nominal. Mean values are determined from the above equations. The nominal responses are calculated based on the IAB response prediction models (Table 4.8) with α. = 10.8×10^{-6} /°C (6.0×10^{-6} /°F) (AASHTO LRFD [4]), and $B = P = 2$.

5.5.1 Bridge Axial Force

MCS results established statistics of both bridge compressive and tensile axial forces. A best-fit statistical distribution for bridge compressive axial force was determined using a commercial program, and bridge compressive (negative) axial force is assumed to be normally distributed. Figures 5.11, 5.12 and 5.13 present probability distributions, CDFs, and histograms for bridge compressive axial force with respect to L = 18.3, 61.0 and 121.9 m (60, 200 and 400 ft). The RGOVs of compressive axial forces encompass a wide range: for L = 18.3 m (60 ft), the compressive axial force ranges between 1920 and 4140 kN (432 and 931 kips); for L = 61.0 m (200 ft), the compressive axial force ranges between 2730 and 7600 kN (614 and 1708 kips); and for L = 121.9 m (400 ft), the compressive axial force ranges between 1800 and 8120 kN (405 and 1825 kips).

From probability distributions, bridge compressive axial forces for L = 18.3 and 61.0 (60 and 200 ft) locate within 95% CI, but bridge compressive axial forces for L = 121.9 m (400 ft) did not fully locate within 95% of CI. P-values for all lengths were less than 0.5%. CDFs of L = 18.3 and 61.0 (60 and 200 ft) match the proposed normal distribution CDFs. Histograms of L = 18.3 and 61.0 (60 and 200 ft) represent all frequency bars within the proposed density function. For L = 121.9 m (400 ft), a best-fit distribution determined by a commercial program, however, did not represent well maximum responses and peak frequency. Thus, a normal distribution was determined maximum responses to be located within 95% CI, be close to a proposed distribution CDF, and well-represent maximum peak frequency of MCS results.

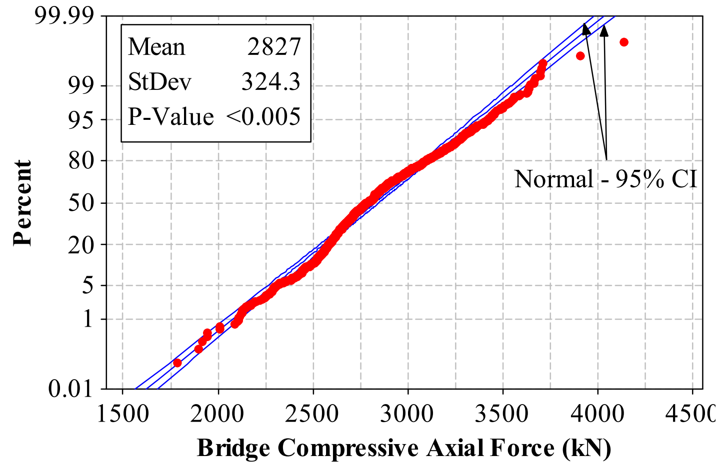

(a) L = 18.3 m (60 ft)

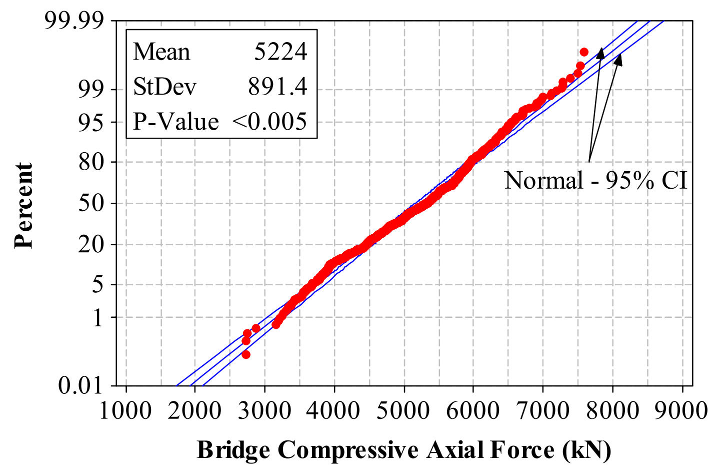

(b) L = 61.0 m (200 ft)

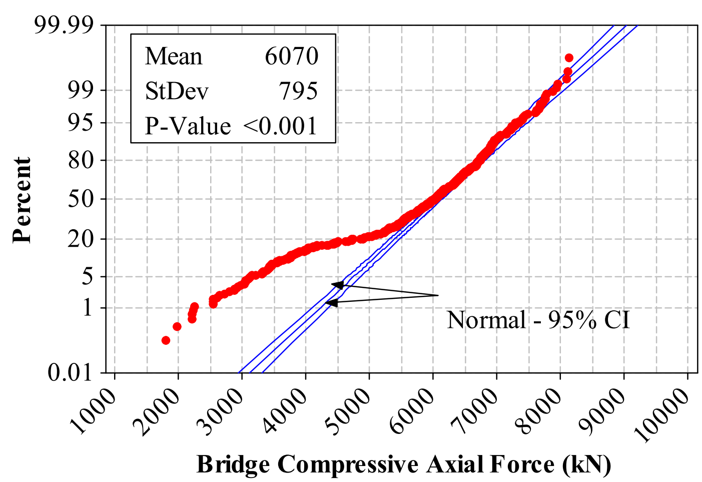

(c) L = 121.9 m (400 ft)

Figure 5.11: Probability Plots of Bridge Compressive Axial Force

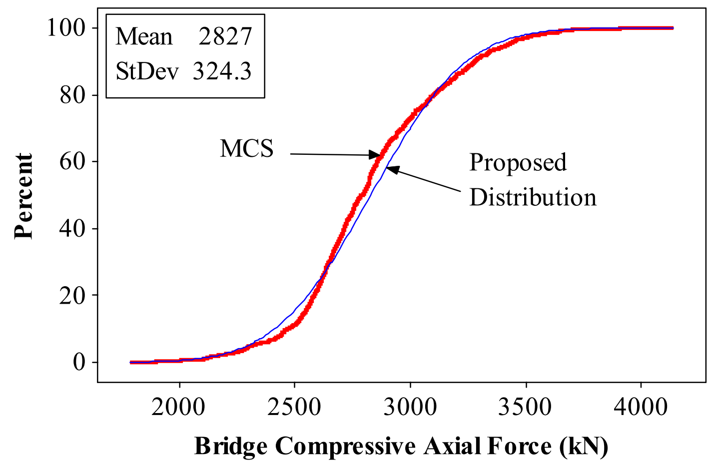

(a) L = 18.3 m (60 ft)

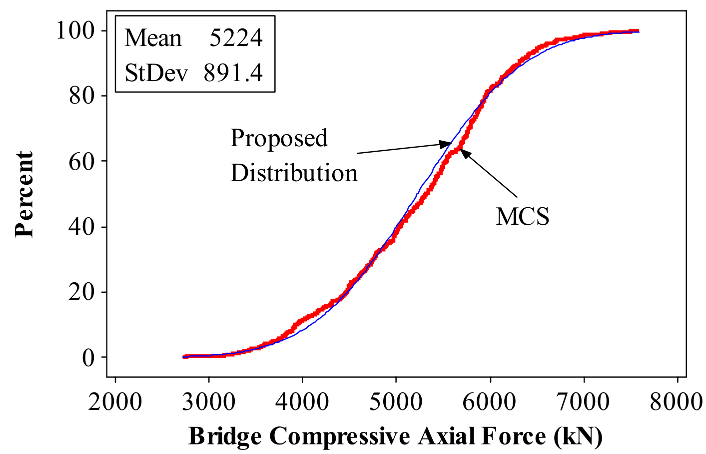

(b) L = 61.0 m (200 ft)

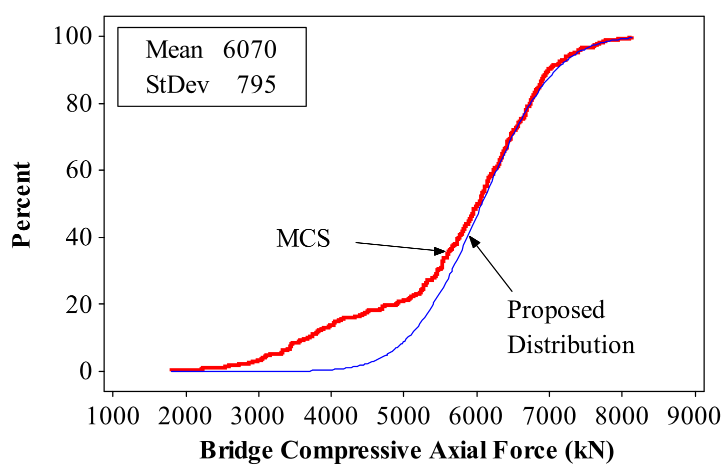

(c) L = 121.9 m (400 ft)

Figure 5.12: CDFs of Bridge Compressive Axial Force

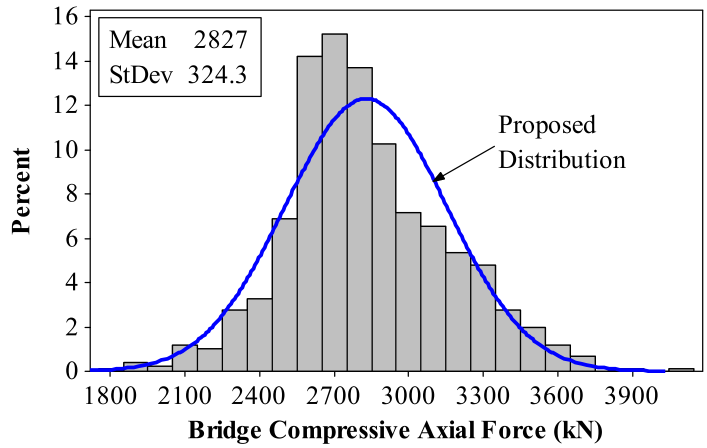

(a) L = 18.3 m (60 ft)

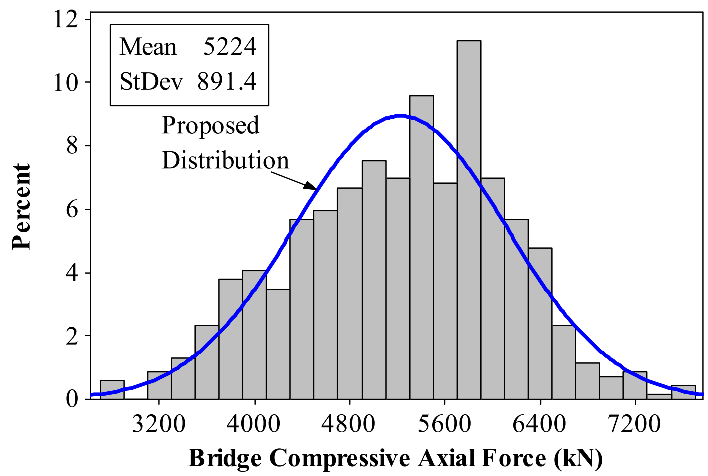

(b) L = 61.0 m (200 ft)

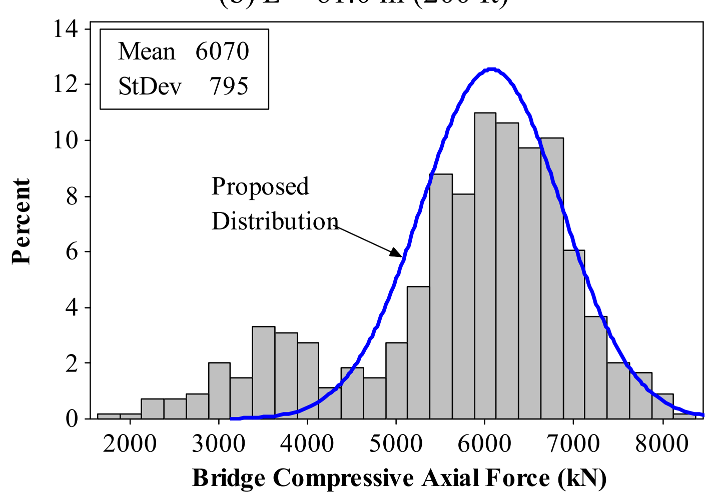

(c) L = 121.9 m (400 ft)

Figure 5.13: Histograms of Bridge Compressive Axial Force

Table 5.8 presents a summary of statistical characteristics of bridge compressive axial forces. The nominal responses do not consider the uncertainties, and therefore, the bias factors range from 1.231 to 1.788 and COVs range from 0.115 to 0.171. The bias factor decreases as the bridge length increases.

Table 5.8: Statistics for Bridge Compressive Axial Force

Bridge Length m (ft)	Distribution Type	Nominal kN (kip)	Mean kN (kip)	Bias Factor (λ)	Coefficient of Variation (COV)
18.3 (60)	Normal	1581 (355)	2827 (636)	1.788	0.115
61.0 (200)	Normal	3225 (725)	5224 (1174)	1.620	0.171
121.9 (400)	Normal	4932 (1109)	6070 (1365)	1.231	0.131

A best-fit statistical distribution for tensile (positive) bridge axial force was determined using a commercial program, and tensile bridge axial force is assumed to be normally distributed. Figures 5.14, 5.15 and 5.16 present probability distributions, CDFs and histograms for bridge tensile axial force with respect to L = 18.3, 61.0 and 121.9 m (60, 200 and 400 ft). However, bridges with L = 18.3 m (60 ft) did not produce bridge tensile axial forces (no positive axial forces), bridges with L = 61.0 m (200 ft) produced both tensile and compressive axial forces, and bridges with L = 121.9 m (400 ft) produced tensile axial forces. Therefore, maximum axial force in each bridge was investigated for tensile bridge axial force. The RGOVs of tensile axial forces encompass a wide range: for L = 18.3 m (60 ft), tensile axial force ranges between -1770 and 0.0 kN (-398 and 0.0 kips); for L = 61.0 m (200 ft), tensile axial force ranges between -670 and 1440 kN (-151 and 324 kips), and for L = 121.9 m (400 ft), tensile axial force ranges between -300 and 2190 kN (-67 and 492 kips).

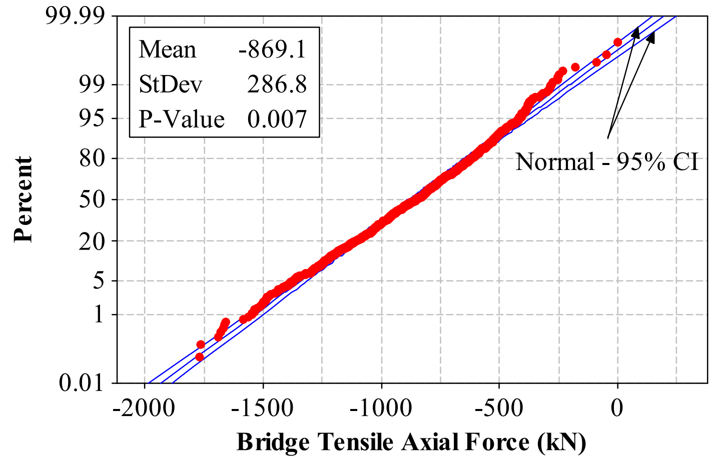

(a) L = 18.3 m (60 ft)

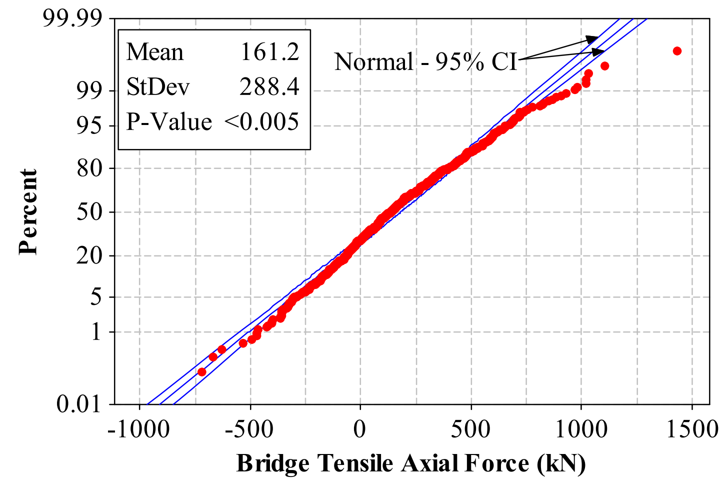

(b) L = 61.0 m (200 ft)

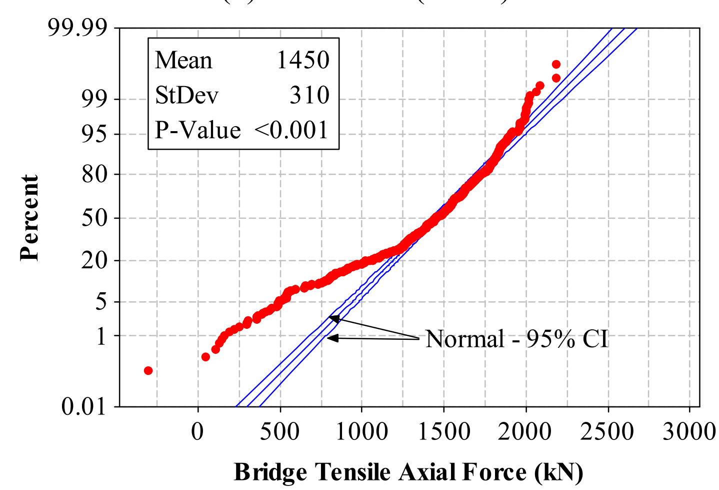

(c) L = 121.9 m (400 ft)

Figure 5.14: Probability Plots of Bridge Tensile Axial Force

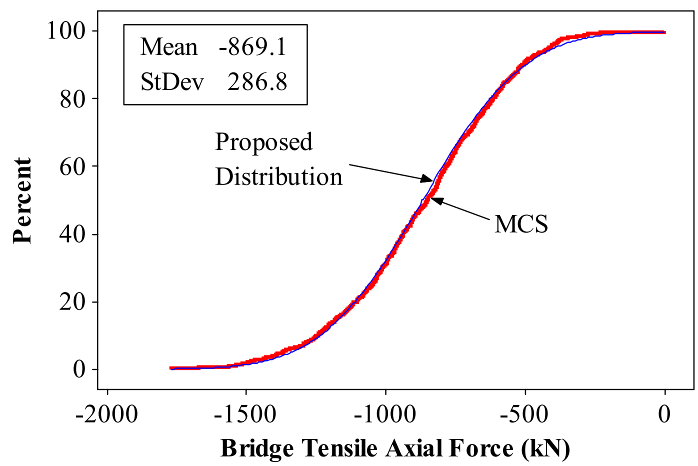

(a) L = 18.3 m (60 ft)

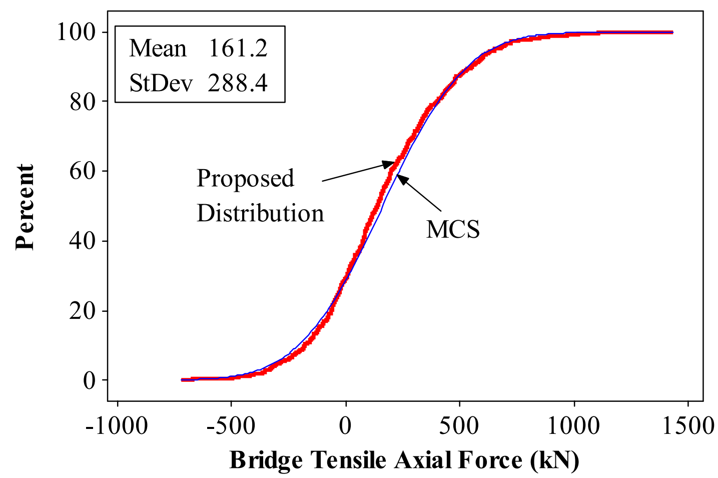

(b) L = 61.0 m (200 ft)

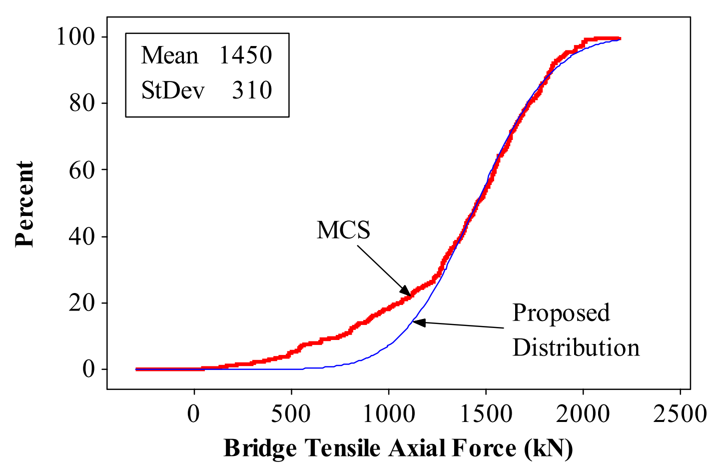

(c) L = 121.9 m (400 ft)

Figure 5.15: CDFs of Bridge Tensile Axial Force

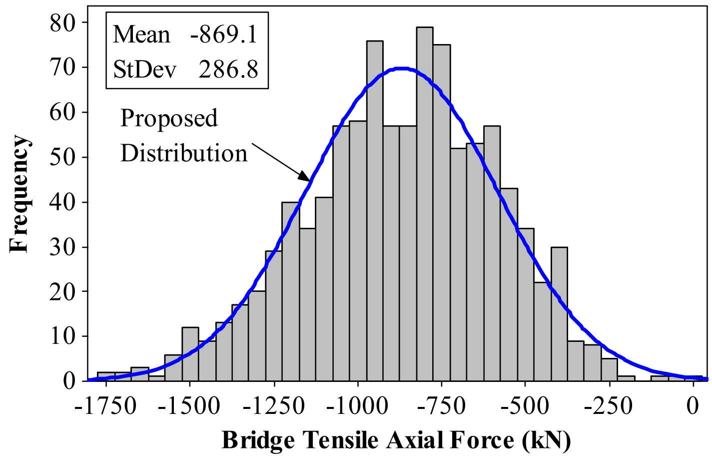

(a) L = 18.3 m (60 ft)

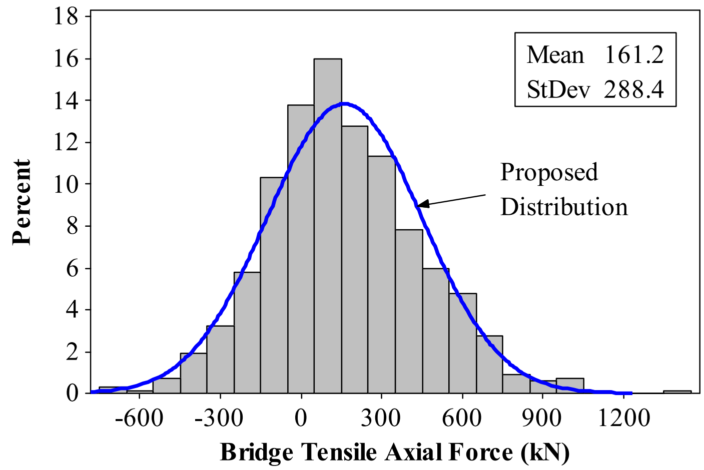

(b) L = 61.0 m (200 ft)

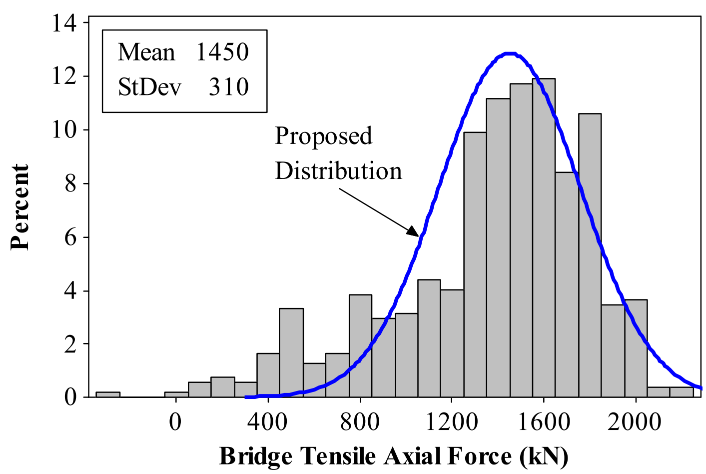

(c) L = 121.9 m (400 ft)

Figure 5.16: Histograms of Bridge Tensile Axial Force

A similar result to bridge compressive axial force was observed in bridge tensile axial force. From probability distributions, bridge tensile axial forces for L = 18.3 and 61.0 (60 and 200 ft) locate within 95% of CI, but bridge tensile axial forces for L = 121.9 m (400 ft) did not fully locate within 95% of CI. P-values are 0.7 % for L = 18.3 (60 ft) and less than 0.5% for L = 61.0 and 121.9 m (200 and 400 ft). CDFs of L = 18.3 and 61.0 (60 and 200 ft) match the proposed normal distribution CDFs very well. For L = 121.9 m (400 ft), a best-fit distribution determined by a commercial program, however, did not represent well maximum responses and peak frequency. Thus, a normal distribution was determined maximum responses to be located within 95% CI, be close to a proposed distribution CDF, and well-represent maximum peak frequency of MCS results.

Table 5.9 presents a summary of statistical characteristics of bridge tensile axial forces. The nominal responses do not consider the uncertainty, and therefore, the bias factors range from 1.175 to 1.591 and COVs range from 0.214 to 1.789. Bridge with L = 18.3 m (60 ft) did not produce tensile axial force. Because mean of L = 61.0 m (200 ft) is smaller than standard deviation of L = 61.0 m (200 ft), COV of L = 61.0 m (200 ft) is larger 1.0.

Table 5.9: Statistics for Bridge Tensile Axial Force

Bridge Length m (ft)	Distribution Type	Nominal kN (kip)	Mean kN (kip)	Bias Factor (λ)	Coefficient of Variation (COV)
18.3 (60)	Normal	-546 (-123)*	-869 (-195)*	1.591	0.330
61.0 (200)	Normal	137 (31)	161 (36)	1.175	1.789
121.9 (400)	Normal	1111 (250)	1450 (326)	1.305	0.214

* Compressive Stress

5.5.2 Bridge Bending Moment

MCS results established statistics of both positive and negative moments. A best-fit statistical distribution for maximum positive bridge moment was determined using a commercial program, and maximum positive bridge moment is assumed to be normally distributed. Figures 5.17, 5.18 and 5.19 present probability distributions, CDFs, and histograms for maximum positive bridge moments with respect to L = 18.3, 61.0 and 121.9 m (60, 200 and 400 ft). Maximum moments were investigated for positive moments, because bridge with L = 18.3 m (60 ft) produced only negative moments. The RGOVs of maximum positive bridge moments encompass in a wide range: for L = 18.3 m (60 ft), maximum positive moment ranges between -1158 and -56 kN-m (-854 and -41 ft-kips); for L = 61.0 m (200 ft), maximum positive moment ranges between -3548 and 988 kN-m (-2617 and 729 ft-kips); and for L = 121.9 m (400 ft), maximum positive moment ranges between -3381 and 411 kN-m (-2493 and 303 ft-kips).

From probability distributions, maximum positive bridge moments for L = 18.3, 61.0 and 121.9 m (60, 200 and 400 ft) locate within 95% CI. However, maximum positive bridge moments for L = 61.0 m (200 ft) did not fully locate within 95% CI because RGOVs are biased to the range between -2700 and -1500 kN-m (-1991 and -1106 ft-kips). P-values are less than 0.5% for L = 18.3 and 61.0 m (60 and 200 ft), and 0.01 for L = 121.9 m (400 ft). CDFs of L = 18.3 and 121.9 m (60 and 400 ft) match the proposed normal distribution CDFs very well, but CDFs of L = 61.0 m (200ft) has an offset from a proposed distribution.

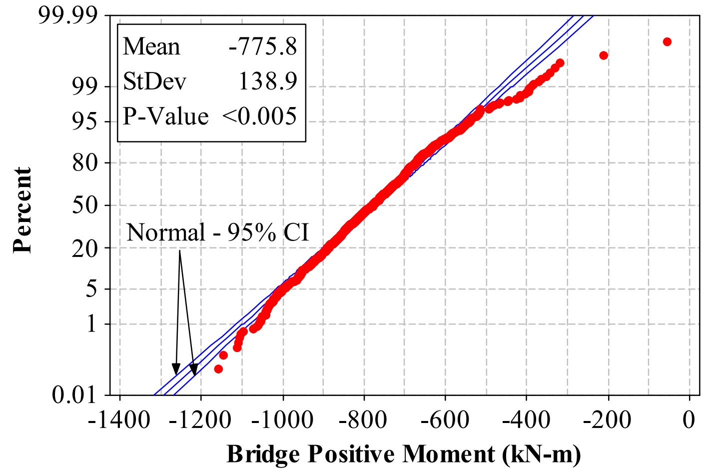

(a) L = 18.3 m (60 ft)

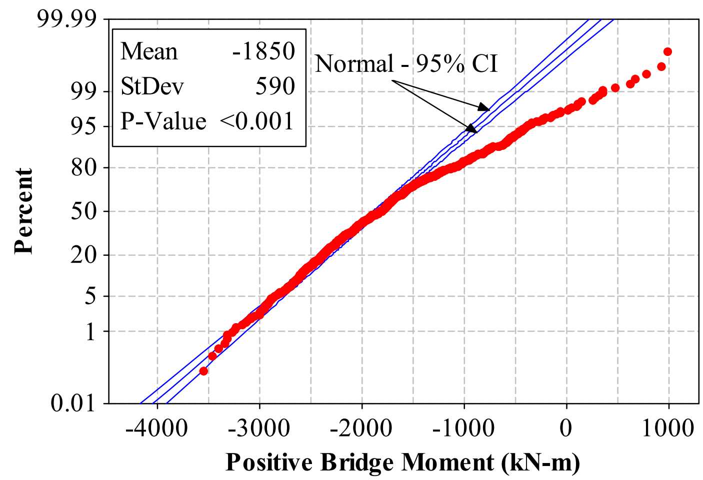

(b) L = 61.0 m (200 ft)

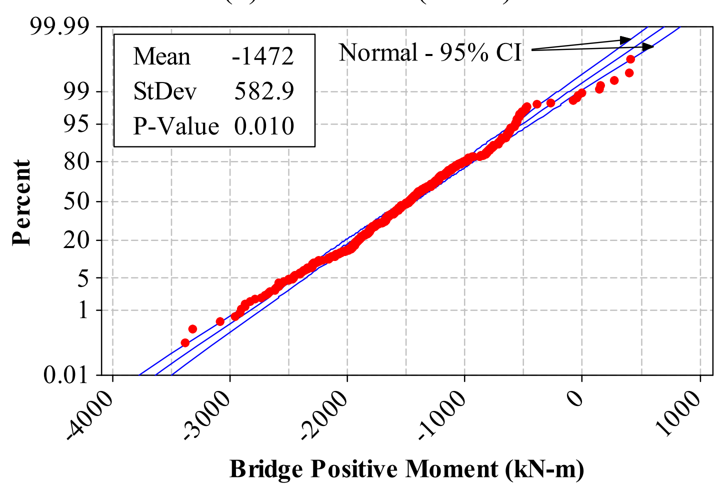

(c) L = 121.9 m (400 ft)

Figure 5.17: Probability Plots of Maximum Bridge Positive Moment

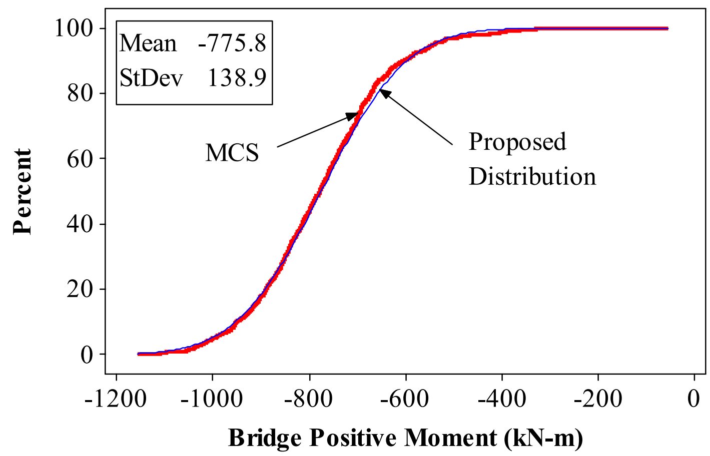

(a) L = 18.3 m (60 ft)

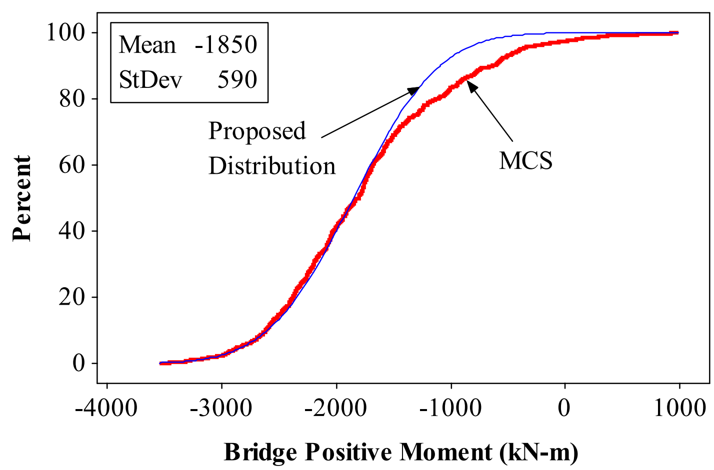

(b) L = 61.0 m (200 ft)

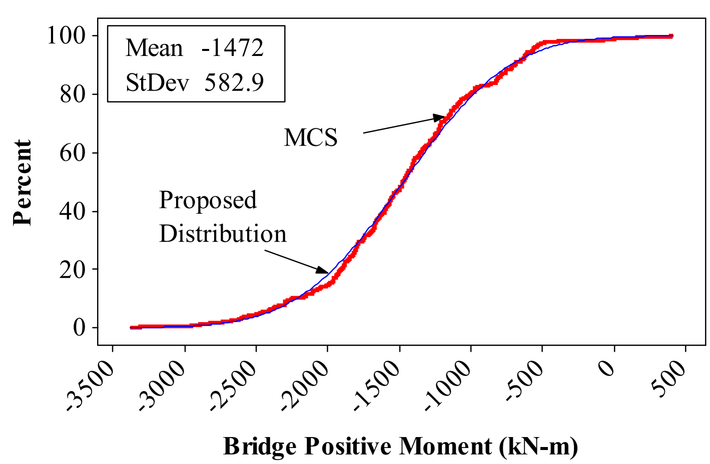

(c) L = 121.9 m (400 ft)

Figure 5.18: CDFs of Maximum Bridge Positive Moment

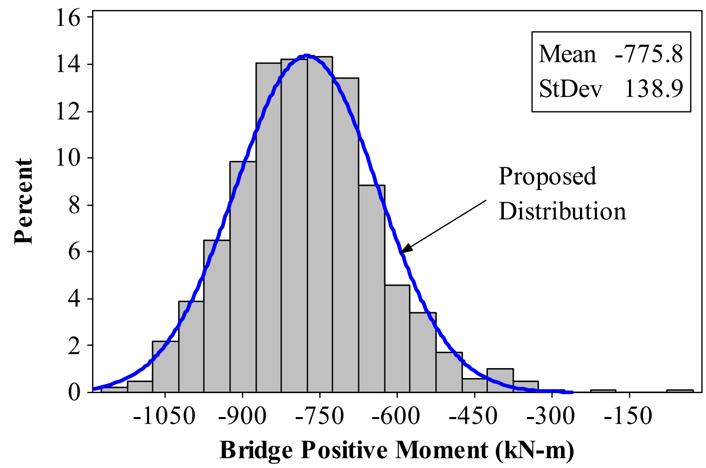

(a) L = 18.3 m (60 ft)

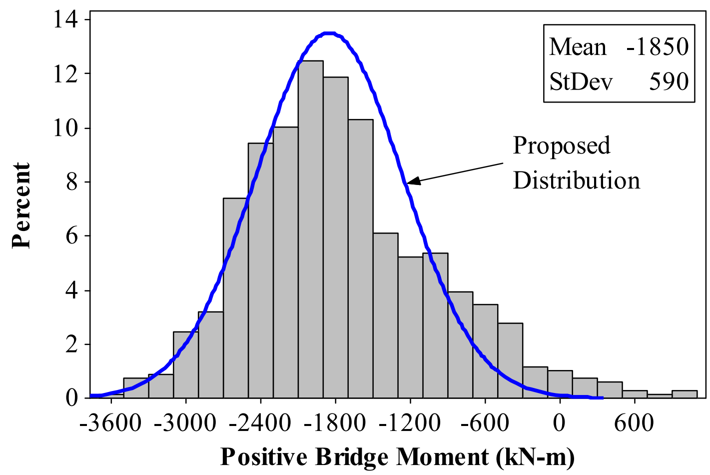

(b) L = 61.0 m (200 ft)

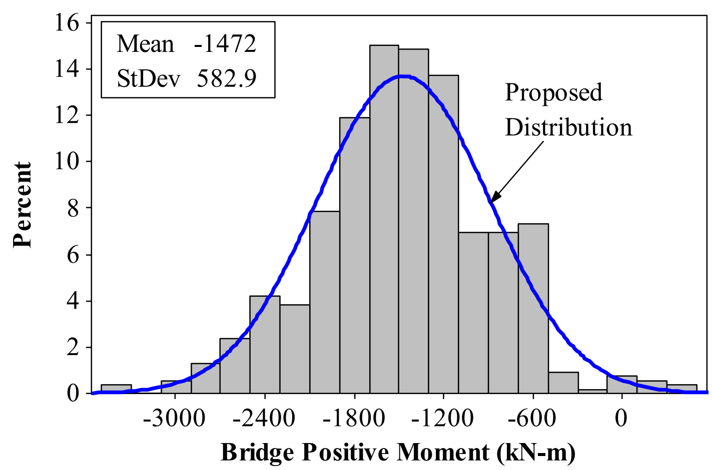

(c) L = 121.9 m (400 ft)

Figure 5.19: Histograms of Maximum Bridge Positive Moment

Both histograms of L = 18.3 and 121.9 m (60 and 400 ft) represent all frequency bars are within the proposed density function and evenly distributed. For L = 61.0 m (200 ft), the histogram presents that frequency bars are biased to the values between -2600 and -1800 kN-m (-1918 and -1328 ft-kips).

Table 5.10 presents a summary of statistical characteristics of maximum positive bridge moments. The nominal responses do not consider the uncertainties, and therefore, the bias factors range from 1.016 to 1.922 and COVs range from 0.179 to 0.396. As bridge length increases, bias factors increase.

Table 5.10: Statistics for Maximum Bridge Positive Moment

Bridge Length m (ft)	Distribution Type	Nominal kN-m (kip-ft)	Mean kN-m (kip-ft)	Bias Factor (λ)	Coefficient of Variation (COV)
18.3 (60)	Normal	-764 (-563)	-776 (-565)	1.016	0.179
61.0 (200)	Normal	-1005 (-741)	-1859 (-1371)	1.850	0.319
121.9 (400)	Normal	-766 (-565)	-1472 (-1086)	1.922	0.396

A best-fit statistical distribution for maximum negative bridge moment was determined using a commercial program, and maximum negative bridge moments are assumed to be Weibull distributions. Figures 5.20, 5.21 and 5.22 present probability distributions, CDFs, and histograms for maximum negative bridge moments with respect to L = 18.3, 61.0 and 121.9 m (60, 200 and 400 ft). RGOVs for L = 18.3 m (60 ft) are significantly biased to a range between 7900 and 8300 kN-m (5827 and 6122 ft-kips) and RGOVs for L = 121.9 m (400 ft) are significantly biased to a range between 13000 and 15000 kN-m (9588 and 11063 ft-kips).

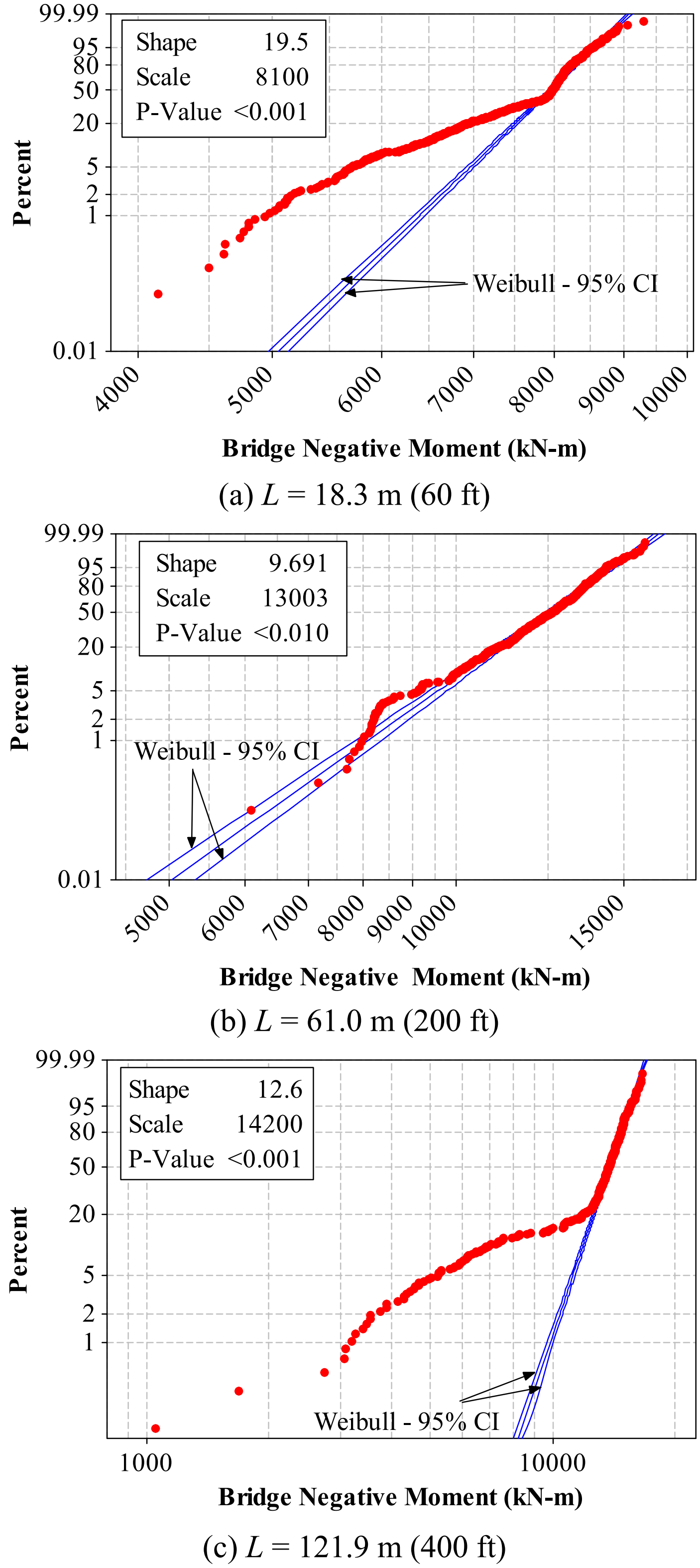

Figure 5.20: Probability Plots of Maximum Bridge Negative Moment

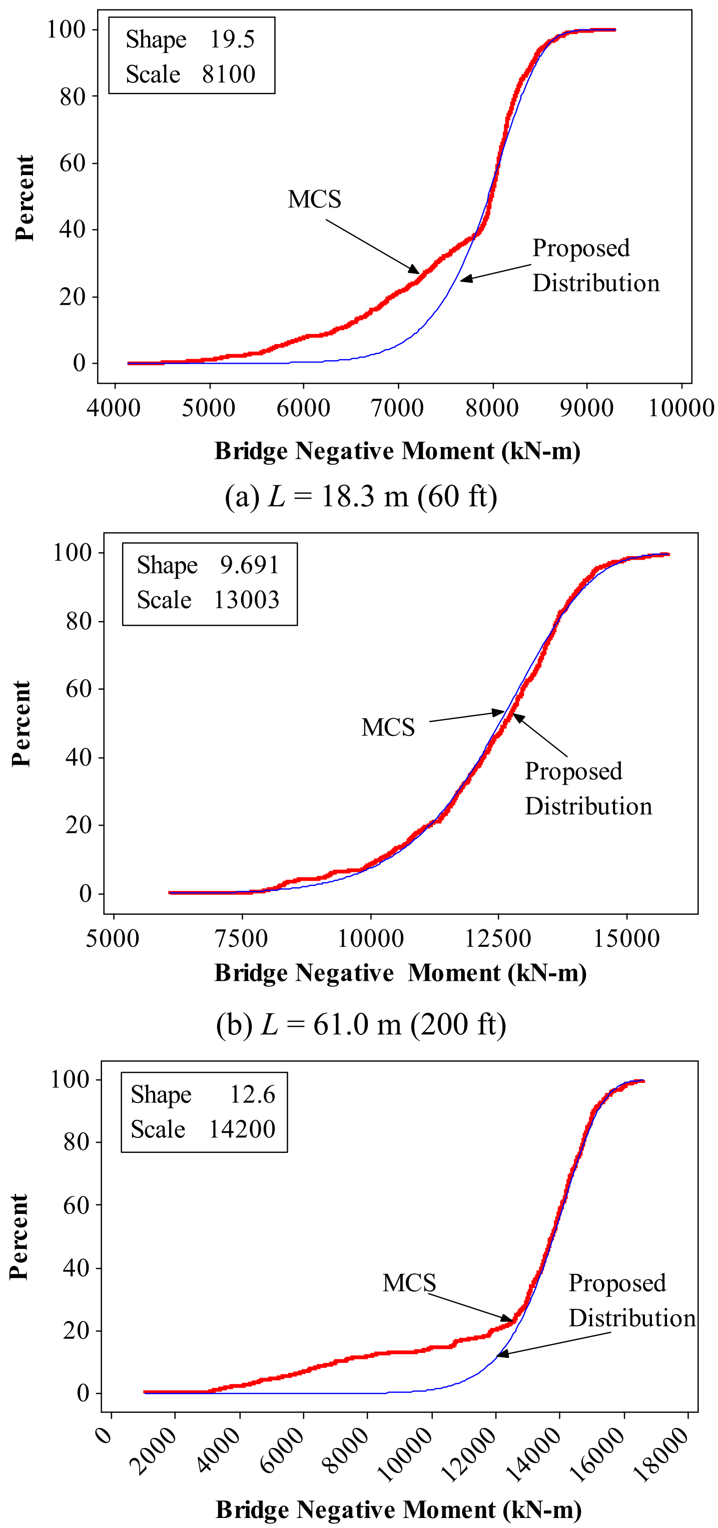

(a) L = 18.3 m (60 ft)

(b) L = 61.0 m (200 ft)

(c) L = 121.9 m (400 ft)

Figure 5.21: CDFs of Maximum Bridge Negative Moment

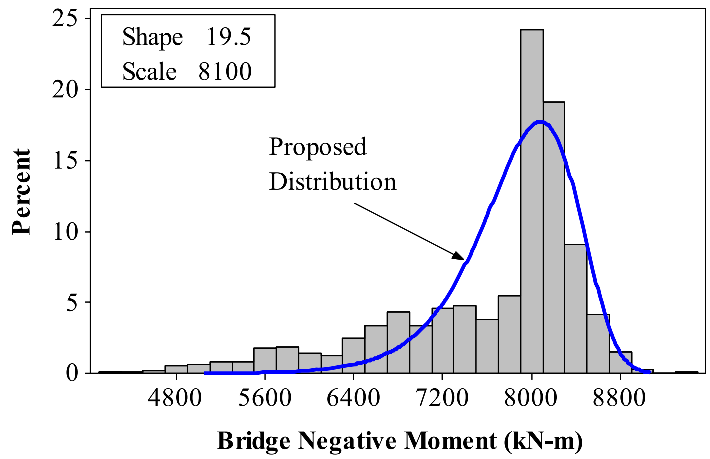

(a) L = 18.3 m (60 ft)

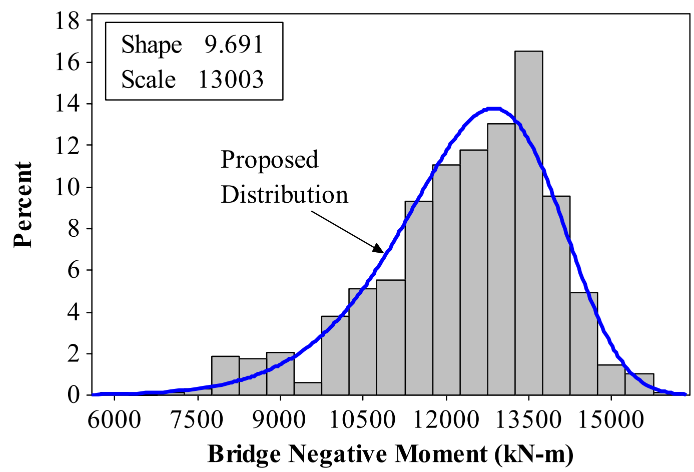

(b) L = 61.0 m (200 ft)

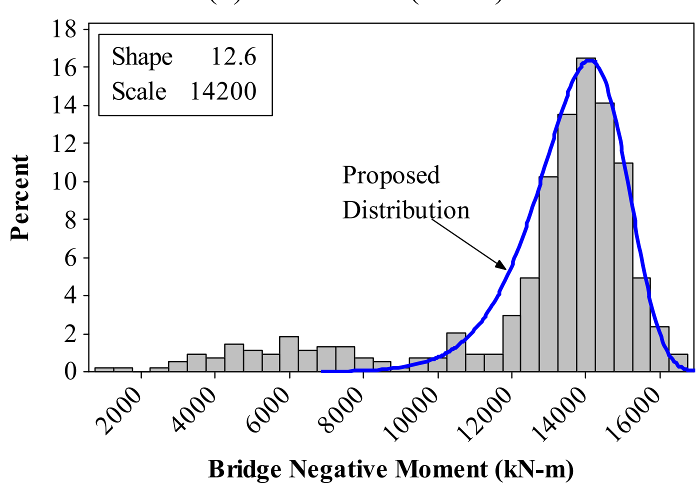

(c) L = 121.9 m (400 ft)

Figure 5.22: Histograms of Maximum Bridge Negative Moment

The RGOVs of maximum negative moments encompass in a wide range: for *L* = 18.3 m (60 ft), maximum negative moment ranges between 4130 and 9300 kN-m (3046 and 6859 ft-kips); for *L* = 61.0 m (200 ft), maximum negative moment ranges between 6100 and 15800 kN (4499 and 11653 ft-kips); and for *L* = 121.9 m (400 ft), maximum negative moment varies between 1680 and 16600 kN (1239 and 12244 ft-kips).

From probability distributions, maximum negative bridge moments for *L* = 61.0 m (200 ft) locate within 95% CI. However, maximum negative bridge moments for *L* = 18.3 and 121.9 m (60 and 400 ft) does not fully locate within 95% CI because RGOVs of *L* = 18.3 and 121.9 m (60 and 400 ft) are significantly biased to the range between 8000 and 8400 kN-m (5900 and 6196 ft-kips) and between 13000 and 15000 kN-m (9588 and 11063 ft-kips), respectively. CDFs of *L* = 61.0 m (200 ft) match the proposed normal distribution CDFs very well. For *L* = 18.3 and 121.9 m (60 and 400 ft), a best-fit distribution determined by a commercial program, however, did not represent well maximum responses and peak frequency. Thus, a Weibull distribution was determined maximum responses to be located within 95% CI, be close to a proposed distribution CDF, and well-represent maximum peak frequency of MCS results.

Table 5.11 presents a summary of statistical characteristics of maximum negative bridge moments. All responses were fit using Weibull distribution. The nominal responses do not consider the uncertainties, and therefore, the bias factors range from 1.276 to 2.530 and COVs range from 0.064 to 0.124. As bridge length increase, bias factors decrease and COVs increases.

Table 5.11: Statistics for Maximum Bridge Negative Moment

Bridge Length m (ft)	Distribution Type	Nominal kN-m (kip-ft)	Mean kN-m (kip-ft)	Bias Factor (λ)	Coefficient of Variation (COV)
18.3 (60)	Weibull	3115 (2297)	7880 (5812)	2.530	0.064
61.0 (200)	Weibull	6814 (5026)	12354 (9111)	1.813	0.124
121.9 (400)	Weibull	10686 (7882)	13632 (10054)	1.276	0.097

5.5.3 Pile Lateral Force

MCS results established statistics of maximum pile lateral forces. A best-fit statistical distribution for maximum pile lateral force was determined using a commercial program, and maximum pile lateral force for L = 18.3 and 61.0 m (60 and 200 ft) are assumed to be normally distributed and maximum pile lateral force for L = 121.9 m (400 ft) is assumed to be a Weibull distribution. Figures 5.23, 5.24 and 5.25 present probability distributions, CDFs, and histograms for maximum pile lateral force with respect to L = 18.3, 61.0 and 121.9 m (60, 200 and 400 ft). The RGOVs of pile lateral forces encompass in a wide range: for L = 18.3 m (60 ft), pile lateral force ranges between 460 and 1350 kN (103 and 330 kips); for L = 61.0 m (200 ft), pile lateral force ranges between 441 and 2060 kN (92 and 463 kips); and for L = 121.9 m (400 ft), pile lateral force ranges between 900 and 2920 kN (202 and 656 kips).

From probability distributions, maximum positive bridge moments for L = 18.3 and 61.0 m (60 and 200 ft) located within 95% of CI. For L = 18.3 and 61.0 m (60 and 200 ft), determined distributions by a commercial program represent well RGOVs.

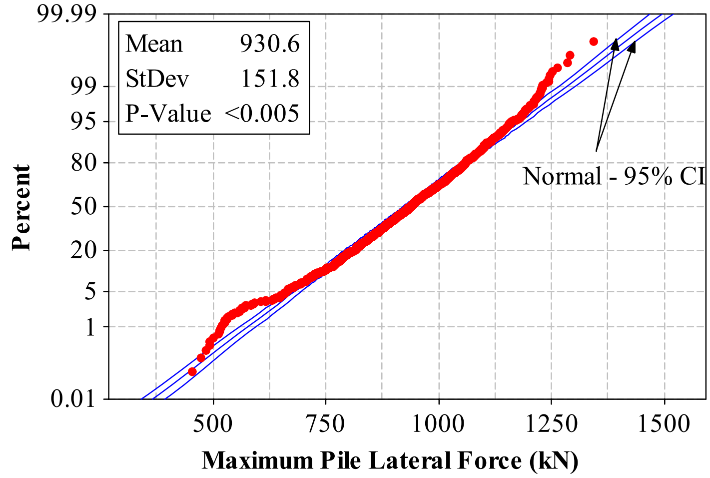

(a) L = 18.3 m (60 ft)

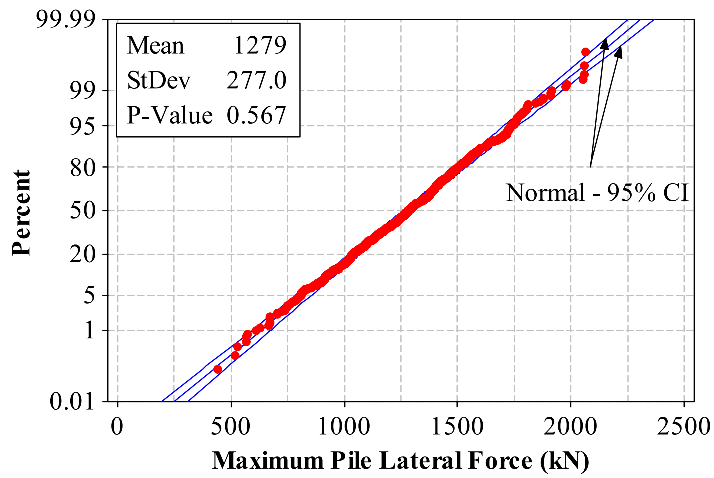

(b) L = 61.0 m (200 ft)

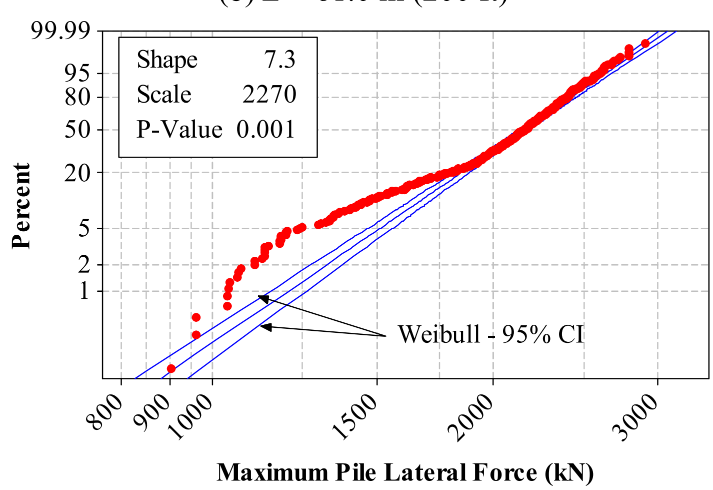

(c) L = 121.9 m (400 ft)

Figure 5.23: Probability Plots of Maximum Pile Lateral Force

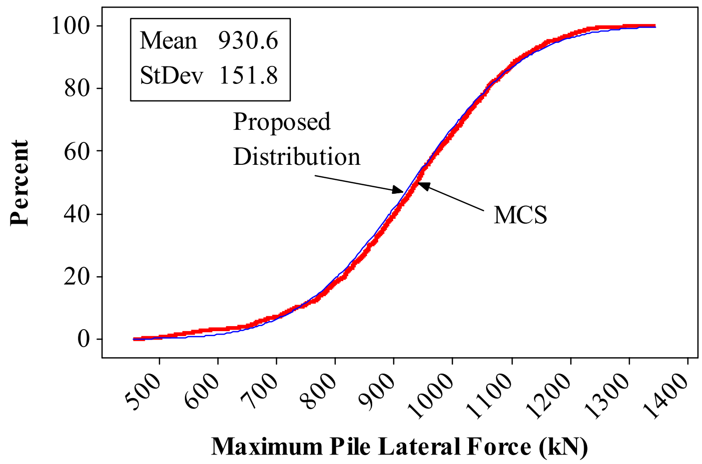

(a) L = 18.3 m (60 ft)

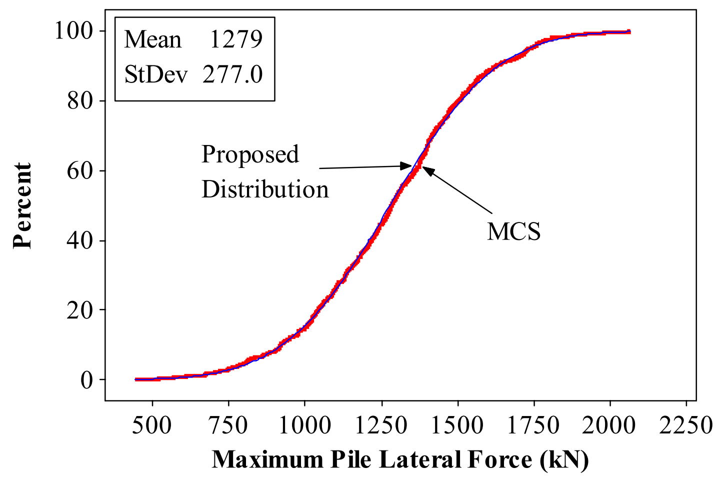

(b) L = 61.0 m (200 ft)

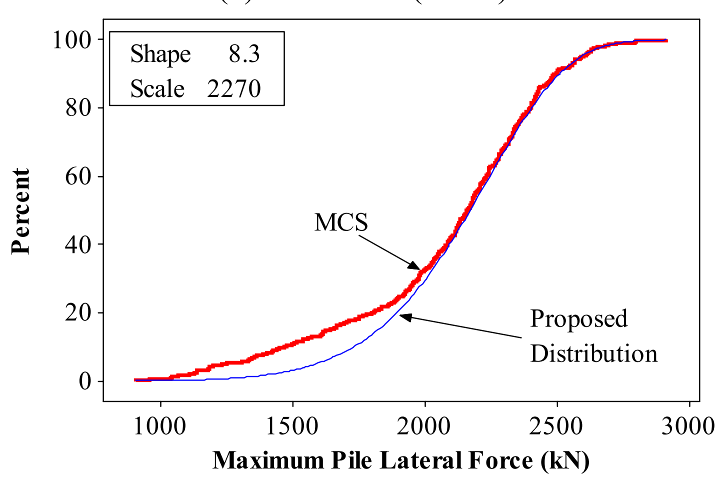

(c) L = 121.9 m (400 ft)

Figure 5.24: CDFs of Maximum Pile Lateral Force

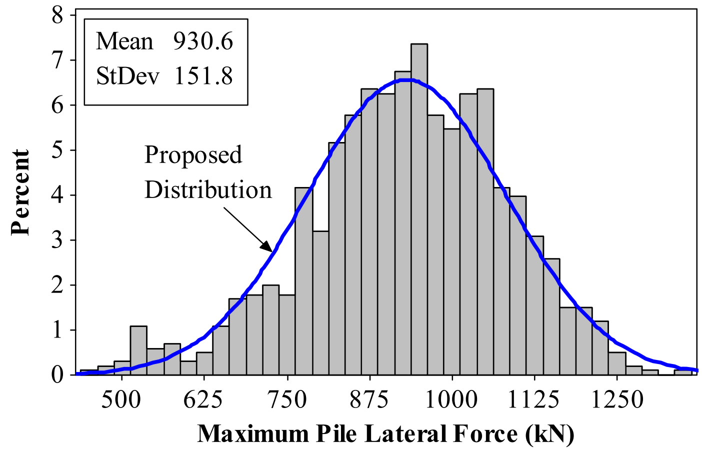

(a) L = 18.3 m (60 ft)

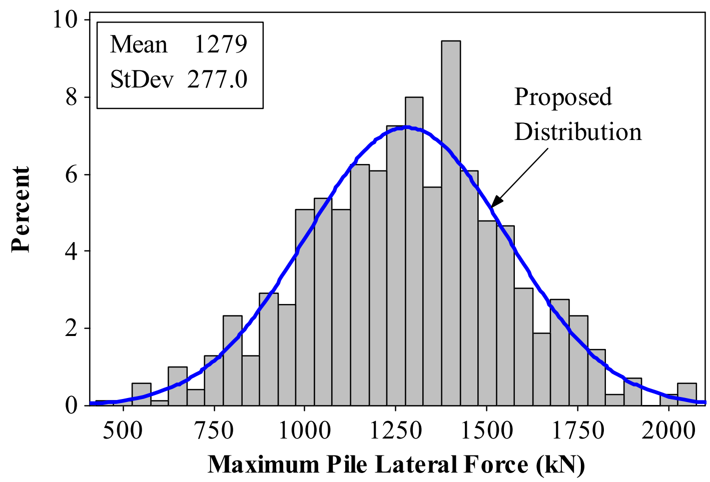

(b) L = 61.0 m (200 ft)

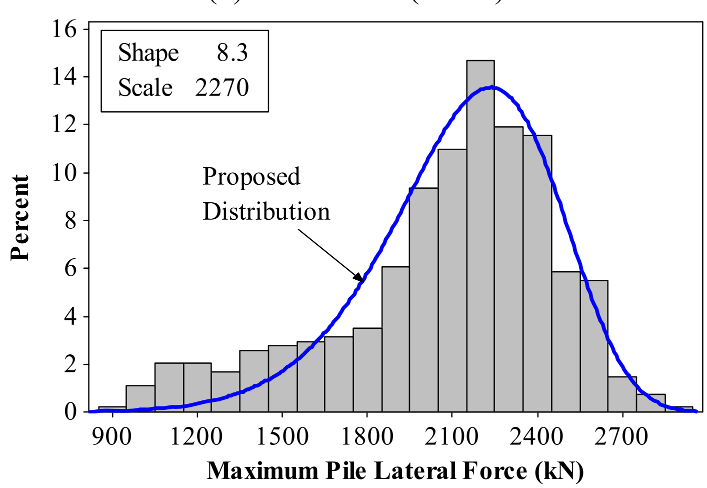

(c) L = 121.9 m (400 ft)

Figure 5.25: Histograms of Maximum Pile Lateral Force

For L = 121.9 m (400 ft), a best-fit distribution determined by a commercial program, however, did not represent well maximum responses and peak frequency. Thus, a Weibull distribution was determined maximum responses to be located within 95% CI, be close to a proposed distribution CDF, and well-represent maximum peak frequency of MCS results.

Table 5.12 presents a summary of statistical characteristics of maximum pile lateral forces. The bias factors ranges between 0.707 and 0.962 and COVs ranges between 0.143 and 0.216.

Table 5.12: Statistics for Maximum Pile Lateral Force

Bridge Length m (ft)	Distribution Type	Nominal kN (kip)	Mean kN (kip)	Bias Factor (λ)	Coefficient of Variation (COV)
18.3 (60)	Normal	1260 (283)	931 (209)	0.739	0.163
61.0 (200)	Normal	1809 (407)	1279 (288)	0.707	0.216
121.9 (400)	Weibull	2226 (500)	2142 (482)	0.962	0.143

5.5.4 Pile Moment

MCS results established statistics of maximum pile moments at the pile head. A best-fit statistical distribution for maximum pile moment was determined using a commercial program, and maximum pile moments are assumed to be normally distributed (Figures 5.26, 5.27 and 5.28). The RGOVs of maximum pile moments encompass in a wide range: for L = 18.3 m (60 ft), maximum pile moment ranges between 140 and 1250 kN-m (103 and 922 ft-kips); for L = 61.0 m (200 ft),

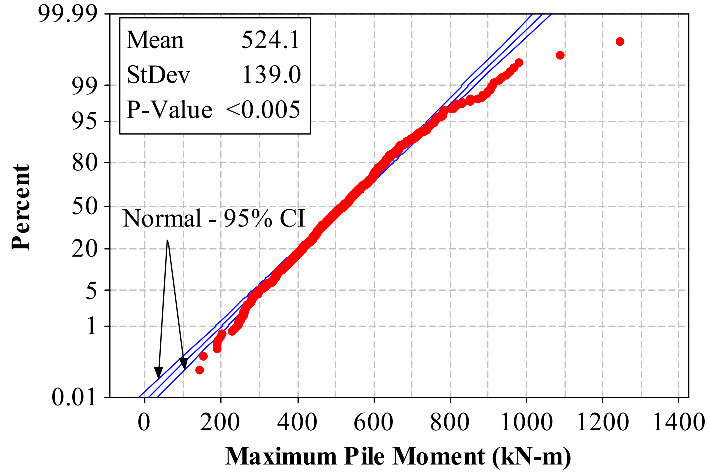

(a) L = 18.3 m (60 ft)

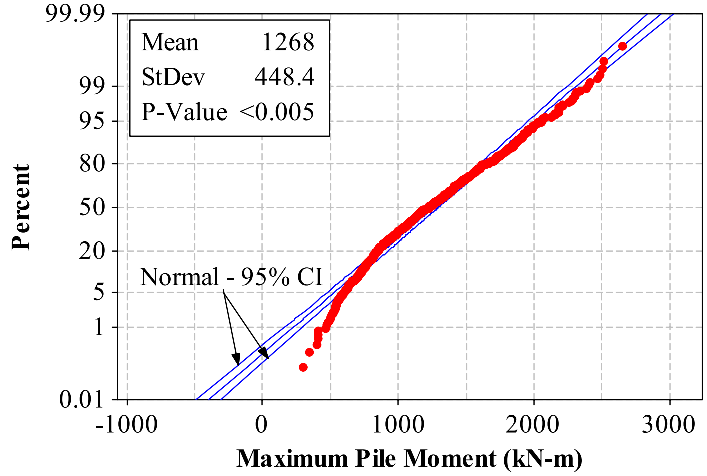

(b) L = 61.0 m (200 ft)

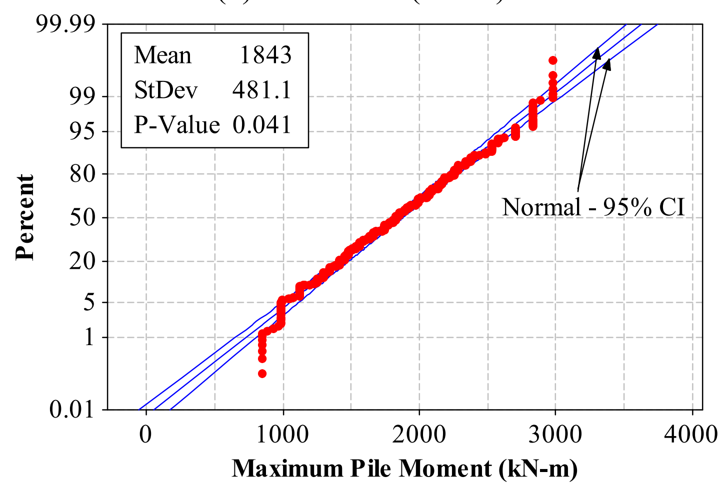

(c) L = 121.9 m (400 ft)

Figure 5.26: Probability Plots of Maximum Pile Moment

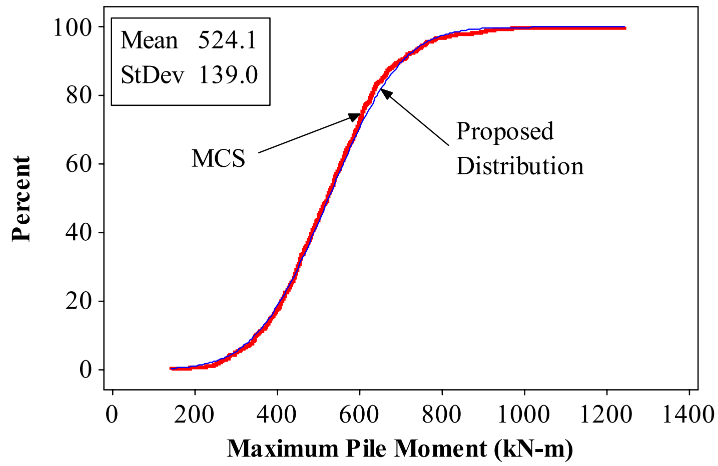

(a) L = 18.3 m (60 ft)

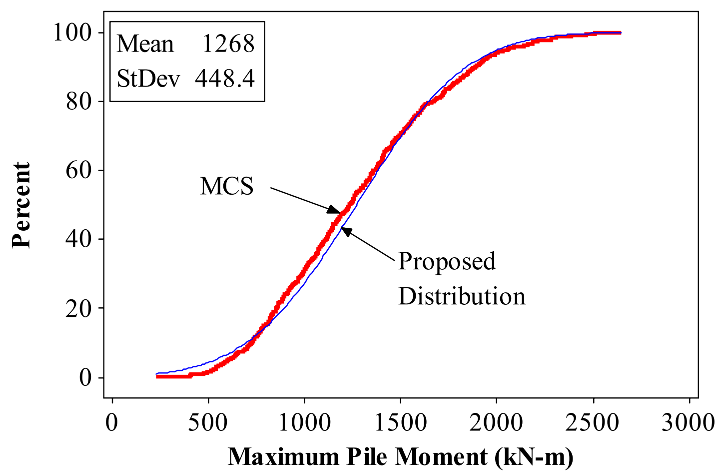

(b) L = 61.0 m (200 ft)

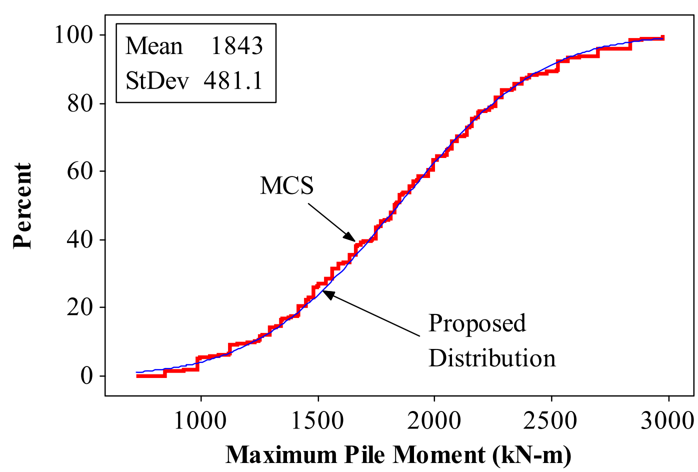

(c) L = 121.9 m (400 ft)

Figure 5.27: CDFs of Maximum Pile Moment

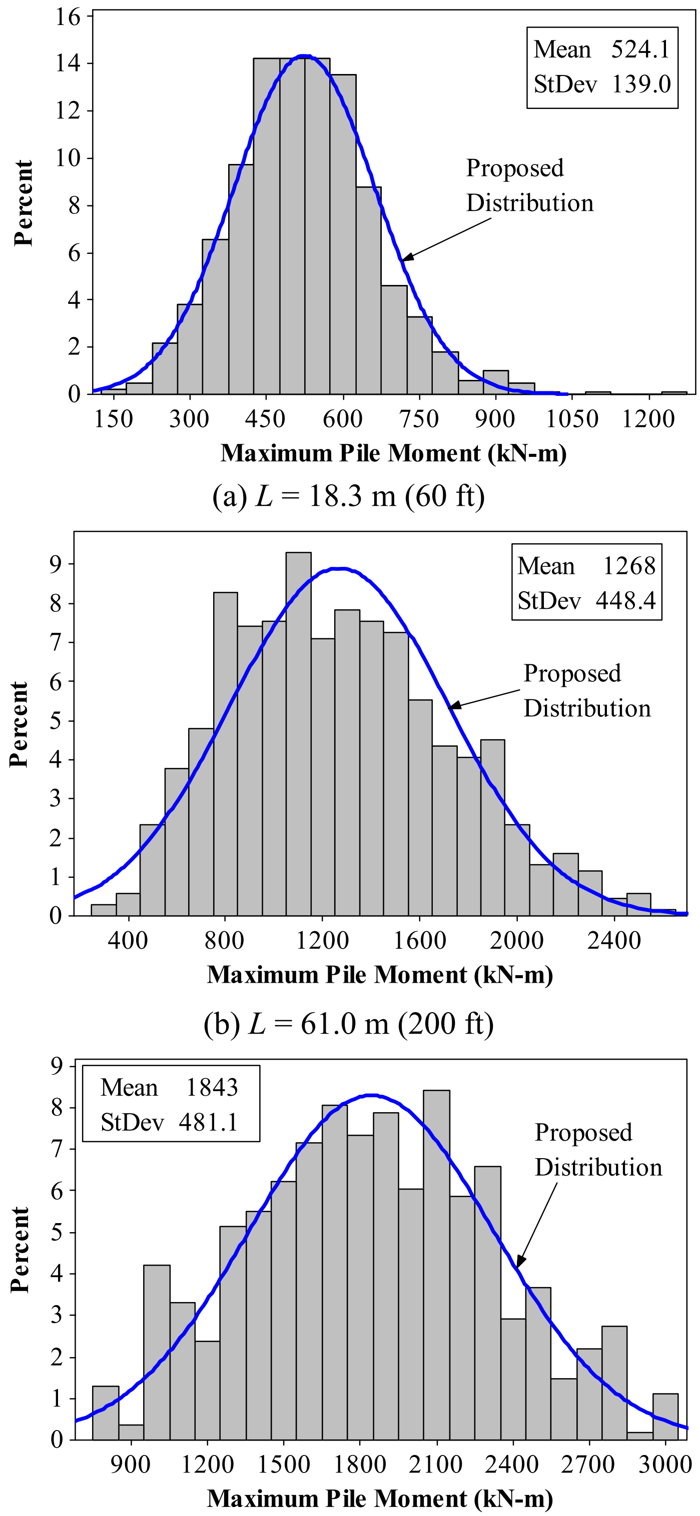

(a) L = 18.3 m (60 ft)

(b) L = 61.0 m (200 ft)

(c) L = 121.9 m (400 ft)

Figure 5.28: Histograms of Maximum Pile Moment

maximum pile moment ranges between 300 and 2650 kN-m (221 and 1954 ft- kips); and for L = 121.9 m (400 ft), maximum pile moment ranges between 850 and 2900 kN-m (627 and 2139 ft-kips).

From probability distributions, maximum pile moments for L = 18.3 and 61.0 m (60 and 200 ft) located within 95% of CI. However, maximum pile moments for L = 121.9 m (400 ft) did not fully located within 95% of CI because RGOVs were slightly biased to the range between 1900 and 2400 kN-m (1401 and 1770 ft-kips). P-values are less than 0.5% for L = 18.3, 61.0 m (60 and 200 ft) and 3.8% for L = 121.9 (400 ft), respectively. CDFs of L = 18.3, 61.0 and 121.9 m (60, 200 and 400 ft) match the proposed normal distribution CDFs very well. However, CDF of L = 121.9 m (400 ft) represents a plastic behavior due to randomly selected pile capacity. Histograms of L = 18.3, 61.0 and 121.9 m (60, 200 and 400 ft) represent that frequency bars of RGOVs reasonably match the proposed distributions.

Table 5.13 presents a summary of statistical characteristics of maximum pile moments. The nominal responses do not consider the uncertainty, and therefore, the bias factors range from 0.867 to 1.167 and COVs range from 0.265 to 0.354. As bridge length increases, bias factor increases.

Table 5.13: Statistics for Maximum Pile Moment

Bridge Length m (ft)	Distribution Type	Nominal kN-m (kip-ft)	Mean kN-m (kip-ft)	Bias Factor (λ)	Coefficient of Variation (COV)
18.3 (60)	Normal	604 (445)	524 (386)	0.867	0.265
61.0 (200)	Normal	1103 (814)	1268 (935)	1.150	0.354
121.9 (400)	Normal	1559 (1150)	1843 (1359)	1.182	0.261

5.5.5 Pile Head/Abutment Displacement

MCS results established statistics of maximum pile head/abutment displacements at the pile head. A best-fit statistical distribution for maximum pile head/abutment displacement was determined using a commercial program, and maximum pile head/abutment displacements for L = 18.3 (60 ft) are assumed to be lognormally distributed and maximum pile head/abutment displacements for L = 61.0 and 121.9 m (200 and 400 ft) are assumed to be normally distributed. Figures 5.29, 5.30 and 5.31 present probability distributions, CDFs, and histograms for maximum positive bridge moments with respect to L = 18.3, 61.0 and 121.9 m (60, 200 and 400 ft). The RGOVs of maximum pile displacements encompass in a wide range: for L = 18.3 m (60 ft), maximum pile displacement ranges between 2.27 and 10.05 mm (0.09 and 0.40 in); for L = 61.0 m (200 ft), maximum pile displacement ranges between 3.60 and 27.27 mm (0.14 and 1.07 in); and for L = 121.9 m (400 ft), maximum pile displacement ranges between 8.08 and 69.84 mm (0.32 and 2.75 in). The ratios of maximum to minimum displacements are 4.4, 7.6 and 8.6 for L = 18.3, 61.0 and 121.9 m (60, 200 and 400 ft), respectively.

From probability distributions, maximum pile moments for L = 18.3, 61.0 and 121.9 m (60, 200 and 400 ft) locate within 95% of CI. P-values are 4.2, 3.1 and less than 0.5 % for L = 18.3, 61.0 and 121.9 m (60, 200 and 400 ft), respectively. CDFs of L = 18.3, 61.0 and 121.9 m (60, 200 and 400 ft) match the proposed distribution CDFs very well. However, CDF of L = 121.9 m (400 ft) has a little offset from the proposed empirical CDF.

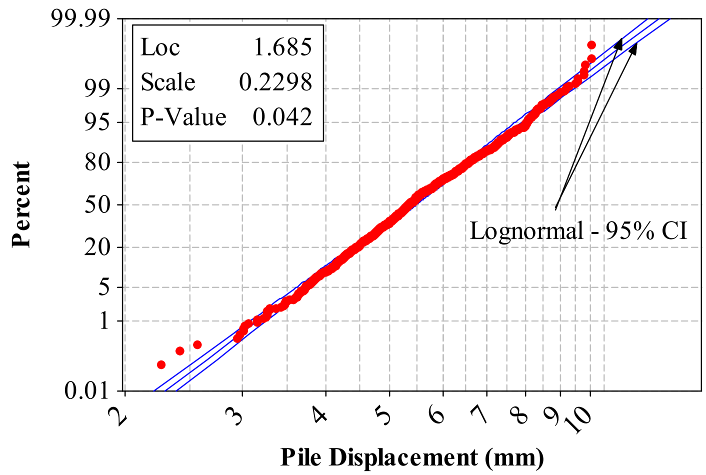

(a) L = 18.3 m (60 ft)

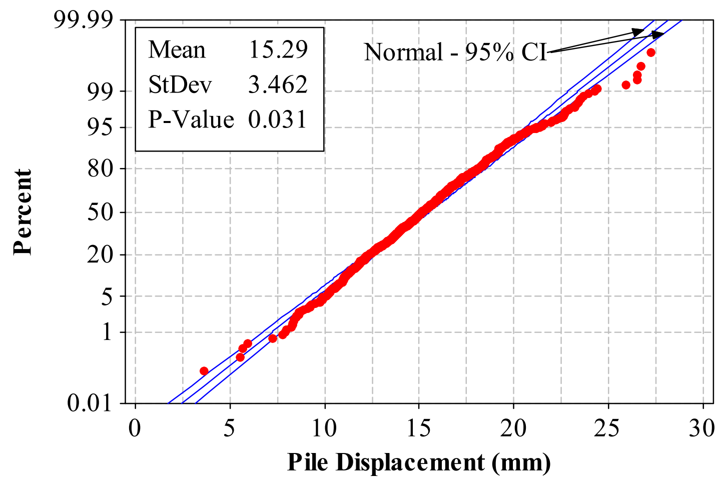

(b) L = 61.0 m (200 ft)

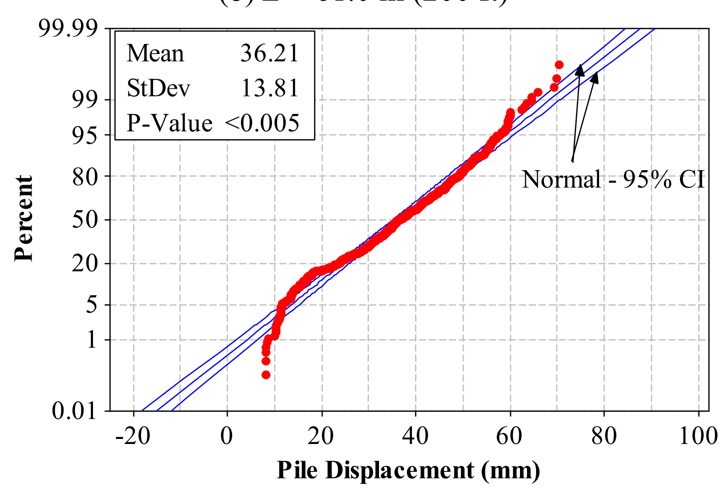

(c) L = 121.9 m (400 ft)

Figure 5.29: Probability Plots of Maximum Pile Head Displacement

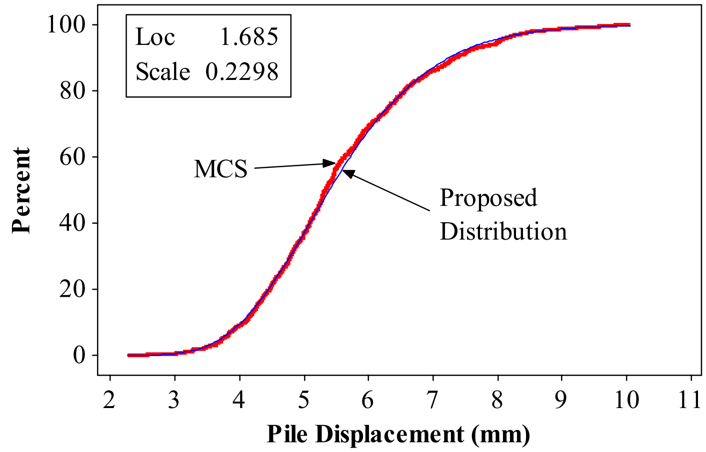

(a) L = 18.3 m (60 ft)

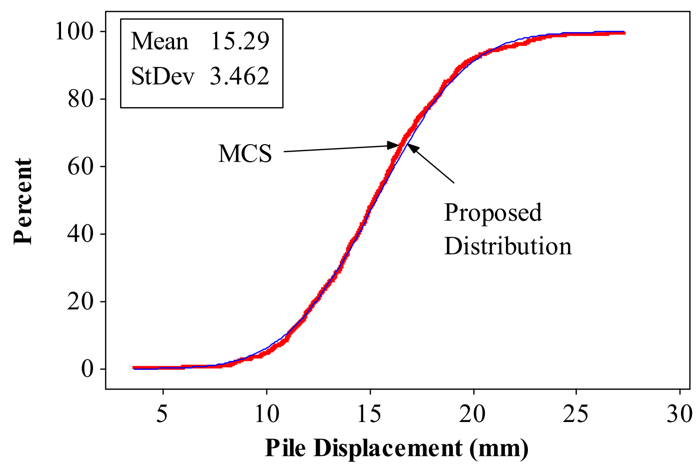

(b) L = 61.0 m (200 ft)

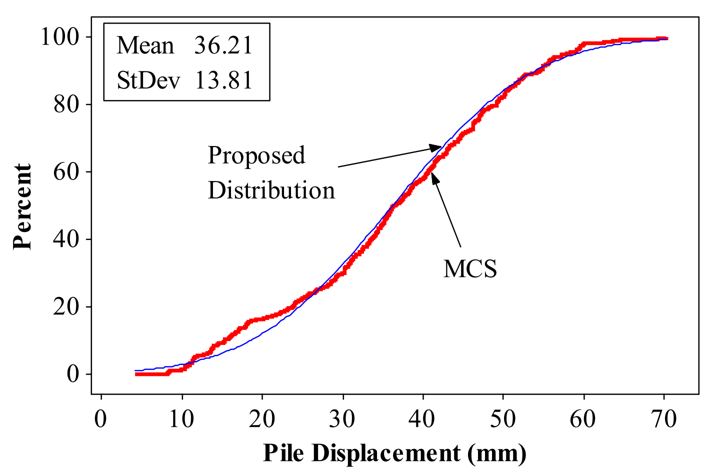

(c) L = 121.9 m (400 ft)

Figure 5.30: CDFs of Maximum Pile Head Displacement

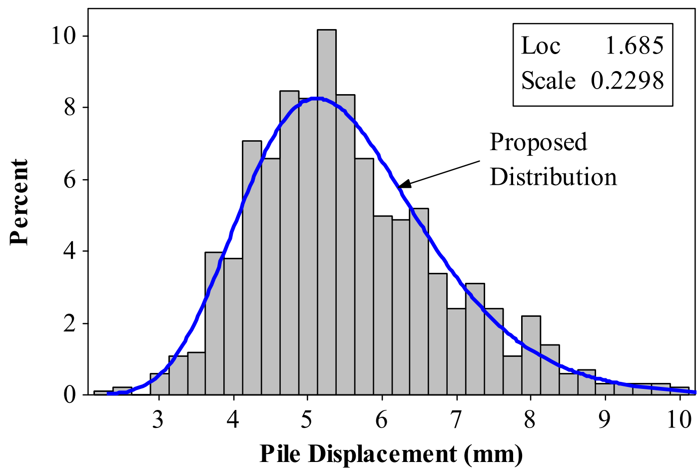

(a) L = 18.3 m (60 ft)

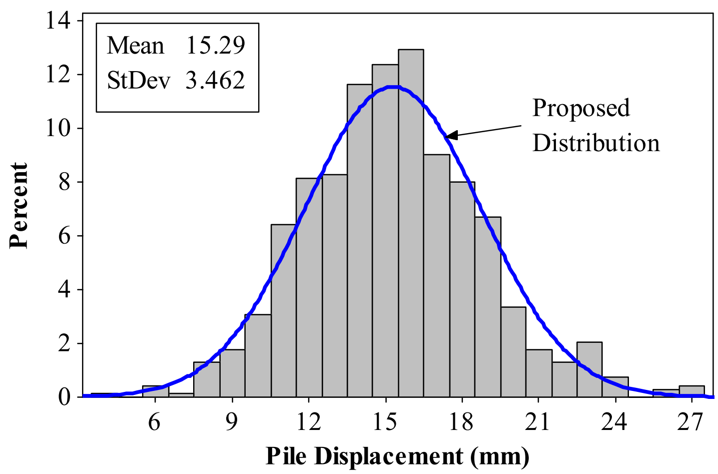

(b) L = 61.0 m (200 ft)

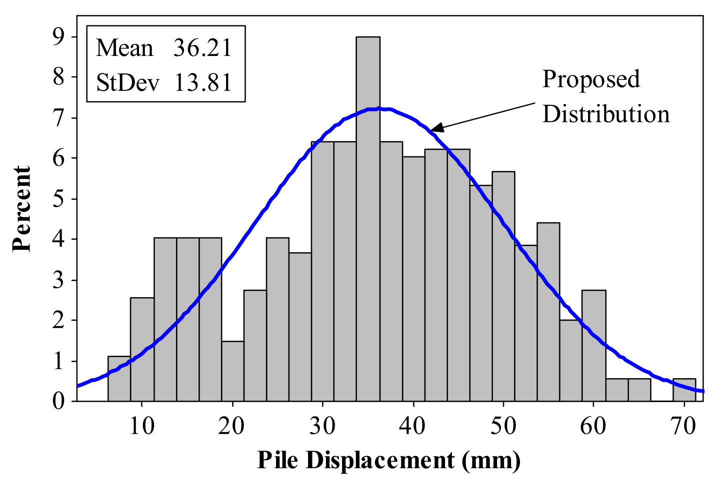

(c) L = 121.9 m (400 ft)

Figure 5.31: Histograms of Maximum Pile Head Displacement

Histograms for L = 18.3 and 61.0 m (60 and 200 ft) represent all frequency bars within the proposed density function and are evenly distributed. However, two peak values of 15 and 35 mm (0.59 and 1.38 in) are observed in the histogram for L = 121.9 m (400 ft). This is also originated from the pile yielding. If pile soil stiffness is stronger and thermal movement is small, the pile head displacement is small. If pile soil stiffness is not strong, the pile may yield due to long bridge length and larger thermal movements.

Table 5.14 presents a summary of statistical characteristics of maximum pile head displacements. The bias factors range between 1.472 and 2.131 and COVs range between 0.233 and 0.381. Bias factors decrease as bridge length increases while COVs increase as bridge length increases.

Table 5.14: Statistics for Maximum Pile Head Displacement

Bridge Length m (ft)	Distribution Type	Nominal mm (in)	Mean mm (in)	Bias Factor (λ)	Coefficient of Variation (COV)
18.3 (60)	Lognormal	2.6 (0.10)	5.5 (0.218)	2.131	0.233
61.0 (200)	Normal	8.7 (0.34)	15.3 (0.602)	1.757	0.226
121.9 (400)	Normal	17.4 (0.69)	36.2 (1.425)	2.080	0.381

5.5.6 Compressive Stress at the Top Fiber of the Mid-span of the Exterior Span

MCS results established statistics of compressive stresses (negative) at the top fiber of the mid-span of the exterior span. A best-fit statistical distribution for maximum compressive stresses at the top fiber was determined using a commercial program, and compressive stresses at the top fiber are assumed to be normal distributions (Figures 5.32, 5.33 and 5.34).

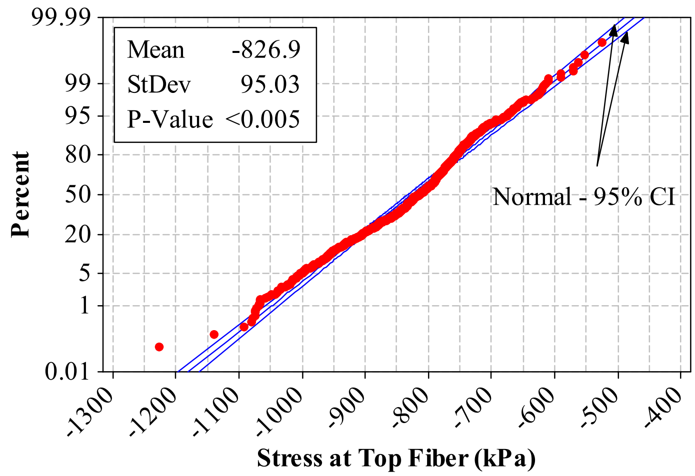

(a) L = 18.3 m (60 ft)

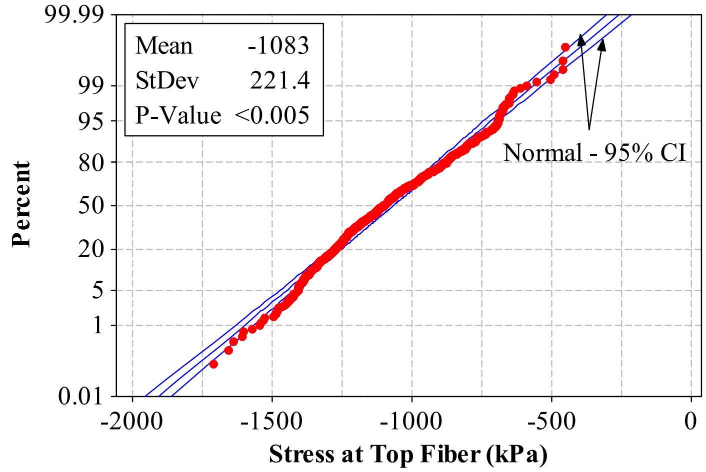

(b) L = 61.0 m (200 ft)

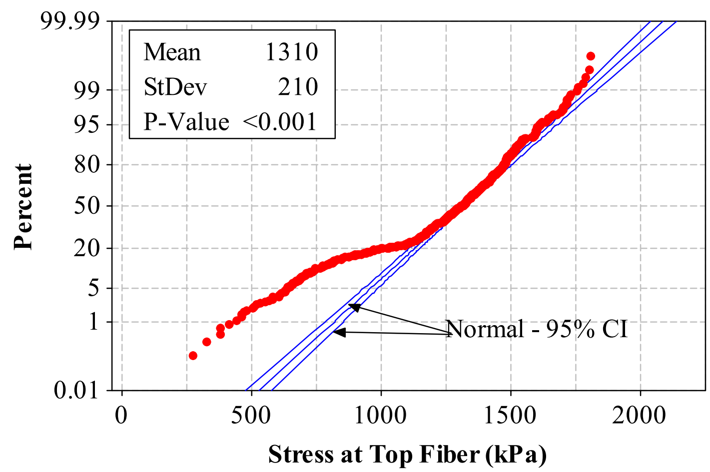

(c) L = 121.9 m (400 ft)

Figure 5.32: Probability Plots of Maximum Compressive Stress at the Top Fiber

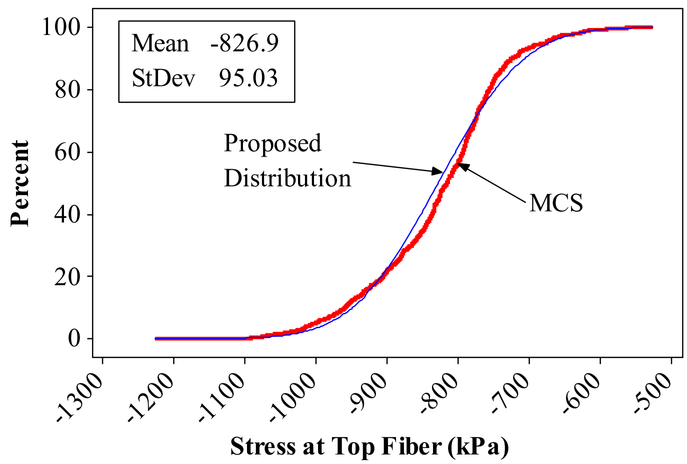

(a) L = 18.3 m (60 ft)

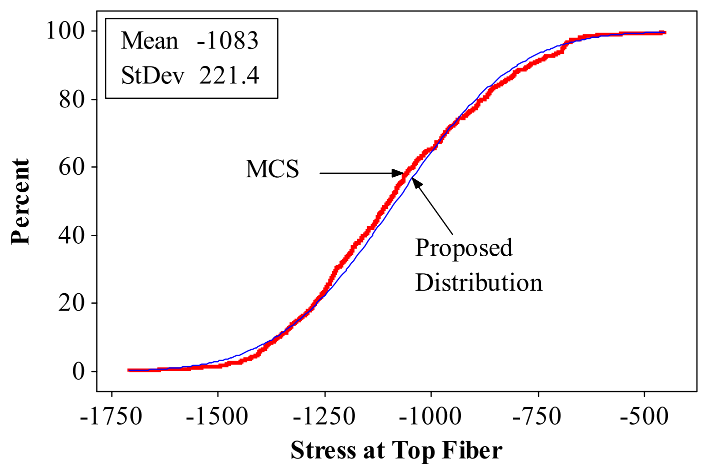

(b) L = 61.0 m (200 ft)

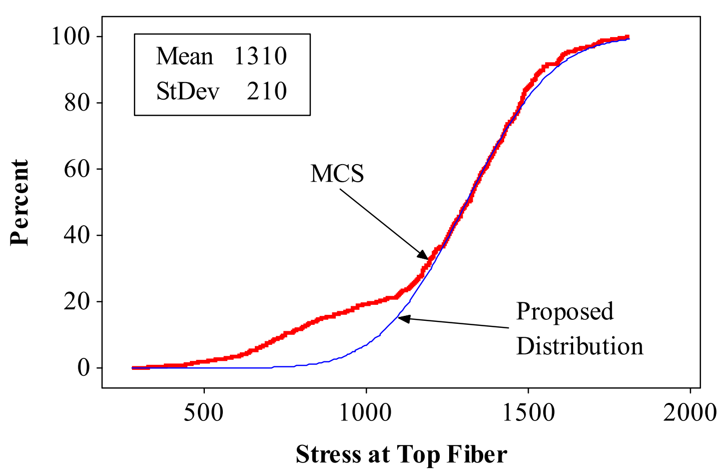

(c) L = 121.9 m (400 ft)

Figure 5.33: CDFs of Maximum Compressive Stress at the Top Fiber

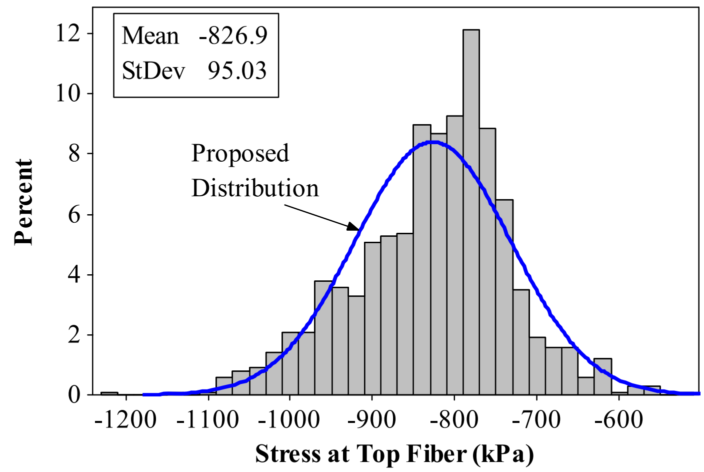

(a) L = 18.3 m (60 ft)

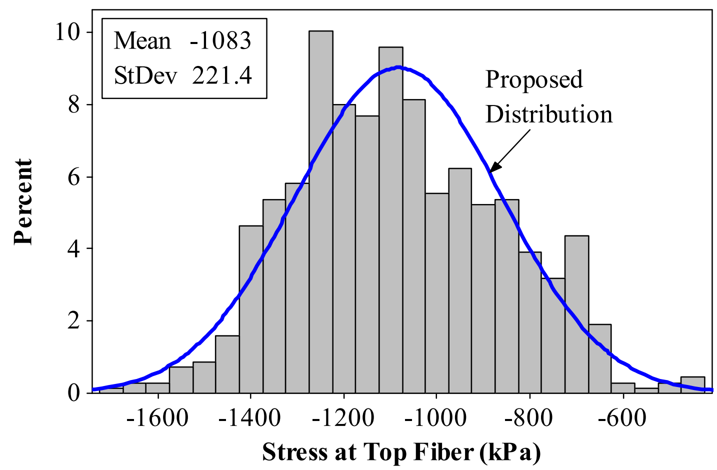

(b) L = 61.0 m (200 ft)

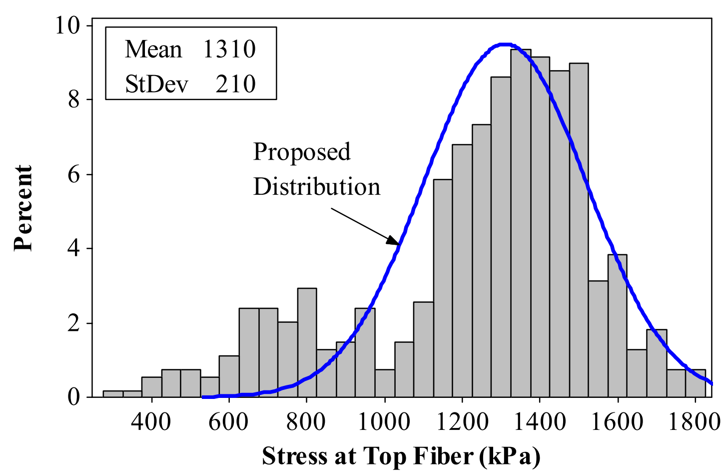

(c) L = 121.9 m (400 ft)

Figure 5.34: Histograms of Maximum Compressive Stress at the Top Fiber

The RGOVs of compressive stresses at the top fiber encompass in a wide range: for *L* = 18.3 m (60 ft), compressive stress ranges between -1230 and -40 kPa (-0.178 and -0.006 ksi); *L* = 61.0 m (200 ft), compressive stress ranges between -1710 and 330 kPa (-0.248 and 0.048 ksi); and for *L* = 121.9 m (400 ft), compressive stress ranges between -1790 and 500 kPa (-0.260 and 0.073 ksi).

From probability distributions, compressive stresses at the top fiber for *L* = 18.3 and 61.0 m (60 and 200 ft) located within 95% of CI. CDFs of *L* = 18.3 and 61.0 m (60 and 200 ft) match the proposed normal distribution CDFs. For *L* = 121.9 m (400 ft), a best-fit distribution determined by a commercial program, however, did not represent well maximum responses and peak frequency. Thus, a normal distribution was determined maximum responses to be located within 95% CI, be close to a proposed distribution CDF, and well-represent maximum peak frequency of MCS results.

Table 5.15 presents a summary of statistical characteristics of maximum compressive stresses at the top fiber of the mid-span of the exterior span. The bias factors range between 1.020 and 1.756 and COVs range between 0.115 and 0.239.

Table 5.15: Statistics for Maximum Compressive Stress at the Mid-span of the exterior span at the Top Fiber

Bridge Length m (ft)	Distribution Type	Nominal kPa (ksi)	Mean kPa (ksi)	Bias Factor (λ)	Coefficient of Variation (COV)
18.3 (60)	Normal	471 (0.068)	827 (0.120)	1.756	0.115
61.0 (200)	Normal	860 (0.125)	1083 (0.157)	1.259	0.204
121.9 (400)	Normal	1216 (0.176)	1310 (0.190)	1.077	0.160

5.5.7 Tensile Stress at the Bottom Fiber of the Mid-span of the Exterior Span

MCS result established maximum tensile stresses (positive) at the bottom fiber of the mid-span of the exterior span. A best-fit statistical distribution for maximum tensile stresses at the bottom fiber was determined using a commercial program, and tensile stresses at the bottom fiber are assumed to be normally distributed. Figures 5.35, 5.36 and 5.37 present probability distributions, CDFs, and histograms for tensile stresses at the bottom fiber of the girder with respect to L = 18.3, 61.0 and 121.9 m (60, 200 and 400 ft). The RGOVs of tensile stresses at the top fiber encompass in a wide range: for L = 18.3 m (60 ft), tensile stress ranges between -500 and 23 kPa (-0.073 and 0.003 ksi); for L = 61.0 m (200 ft), tensile stress ranges between -200 and 380 kPa (-0.029 and 0.055 ksi); and for L = 121.9 m (400 ft), tensile stress ranges between -95 and 610 kPa (-0.014 and 0.088 ksi). Bridges with L = 18.3 m (60 ft) produced no tensile stresses at the bottom fiber—only two samples produced positive stresses. Bridges with L = 61.0 m (200 ft) produced both positive and negative stresses at the bottom fiber at the mid-span of the exterior span. Bridges with L = 121.9 m (400 ft) produced no compressive stresses at the bottom fiber—only one sample produced a negative stress.

From probability distributions, tensile stresses at the bottom fiber for L = 18.3 and 61.0 m (60 and 200 ft) locate within 95% CI, but tensile stresses at the bottom fiber for L = 121.9 m (400 ft) does not fully locate within 95% CI. CDFs of L = 18.3 and 61.0 m (60 and 200 ft) match the proposed normal distribution CDFs. Histograms provide a similar result. Histograms of L = 18.3 and 61.0 m (60 and 200 ft) represent all frequency bars within the proposed density function.

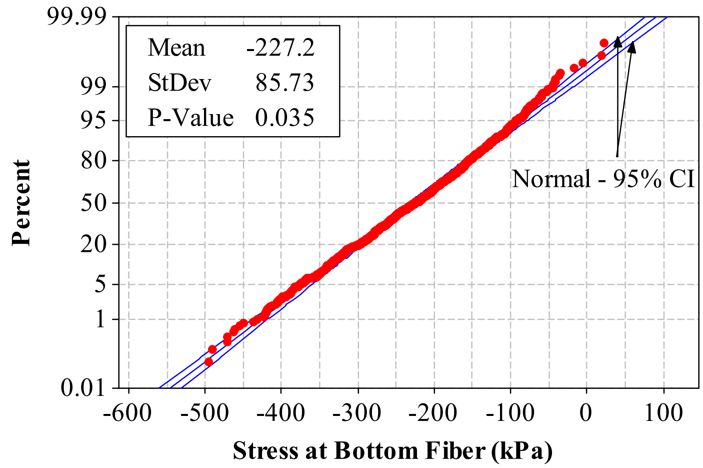

(a) L = 18.3 m (60 ft)

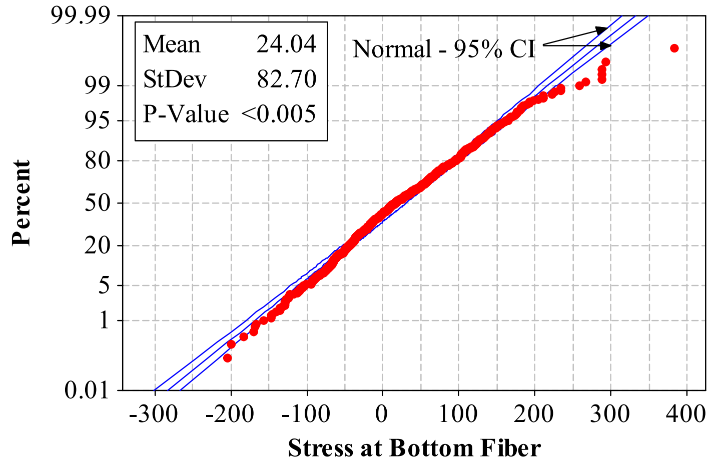

(b) L = 61.0 m (200 ft)

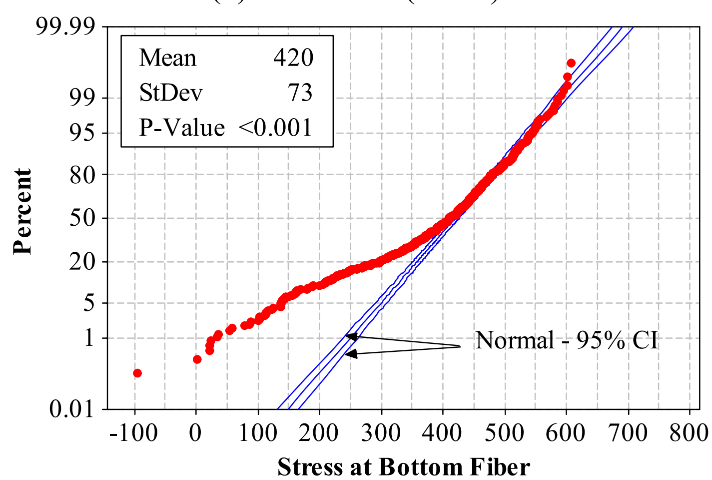

(c) L = 121.9 m (400 ft)

Figure 5.35: Probability Plots of Maximum Tensile Stress at Girder Bottom Fiber

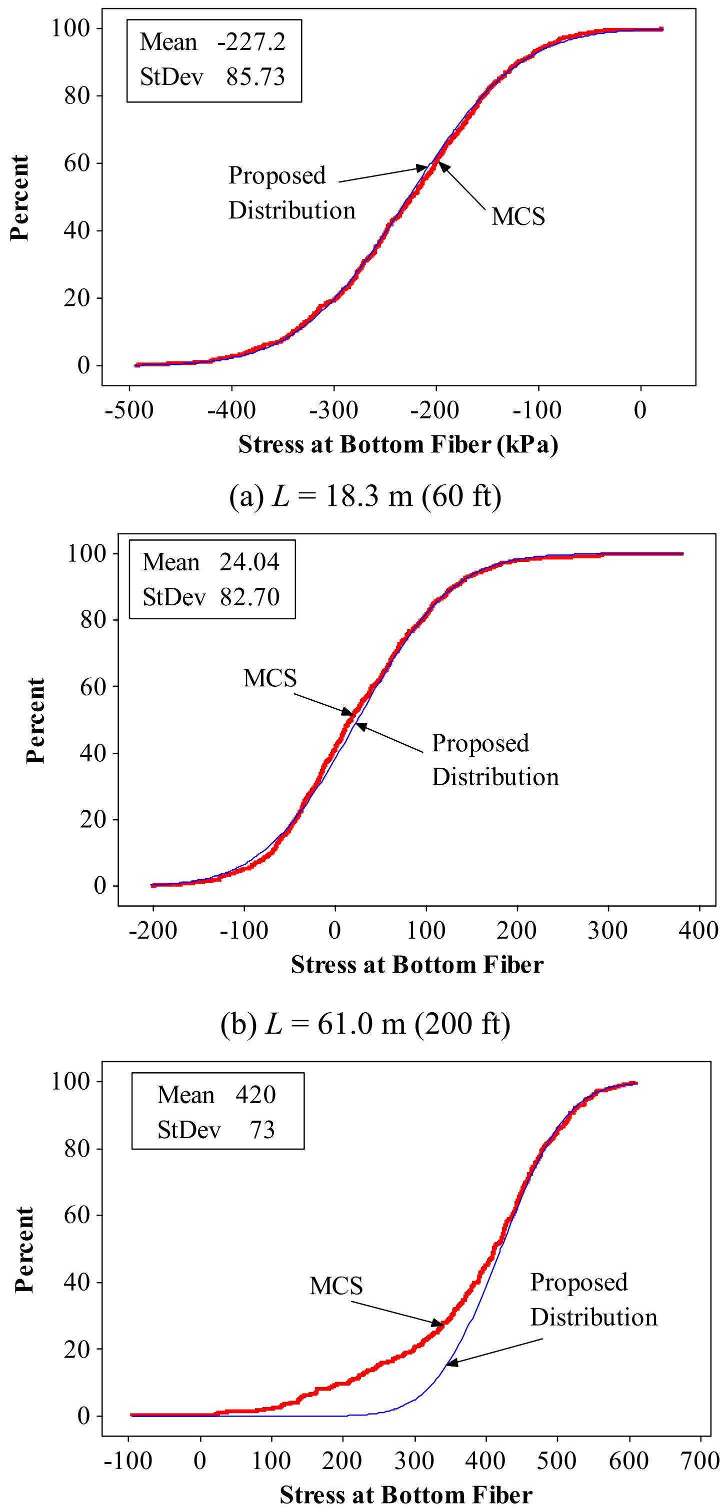

(a) L = 18.3 m (60 ft)

(b) L = 61.0 m (200 ft)

(c) L = 121.9 m (400 ft)

Figure 5.36: CDFs of Maximum Tensile Stress at Girder Bottom Fiber

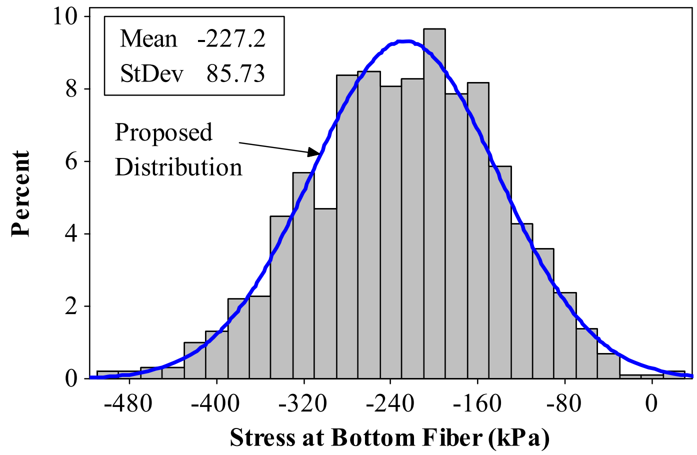

(a) L = 18.3 m (60 ft)

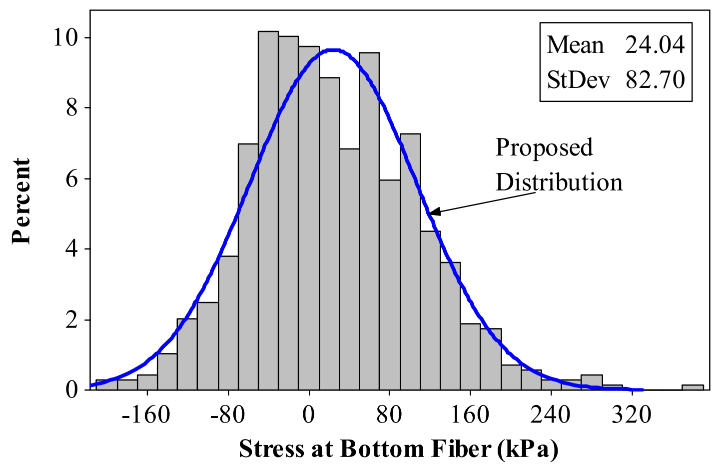

(b) L = 61.0 m (200 ft)

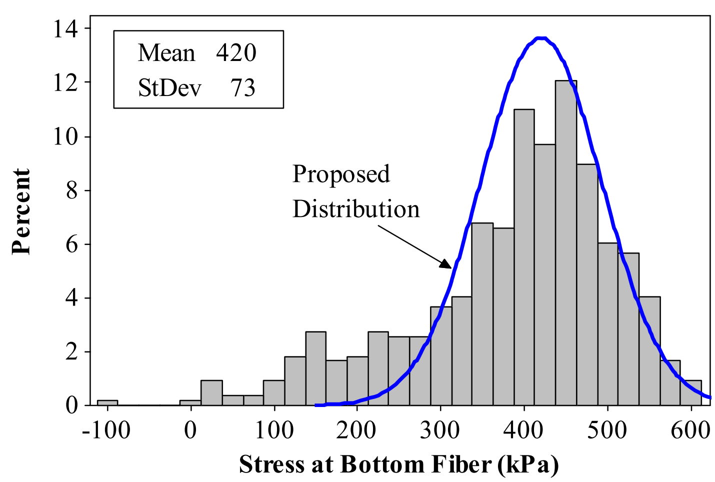

(c) L = 121.9 m (400 ft)

Figure 5.37: Histograms of Maximum Tensile Stress at Girder Bottom Fiber

For L = 121.9 m (400 ft), a best-fit distribution determined by a commercial program, however, did not represent well maximum responses and peak frequency. Thus, a normal distribution was determined maximum responses to be located within 95% CI, be close to a proposed distribution CDF, and well-represent maximum peak frequency of MCS results.

Table 5.16 presents a summary of statistical characteristics of maximum tensile stresses at the bottom fiber of the mid-span of the exterior span. Bridges (99.6%) with L = 18.3 m (60 ft) produce only compressive stresses at the bottom fiber of the mid-span of the exterior span. Bridges with L = 61.0 m (200 ft) produce both tensile and compressive stresses, and standard deviation is larger than mean value. Thus, COV of L = 61.0 m (200 ft) is larger than 1.0. Bridges (99.8%) with L = 121.9 m (400 ft) produce only tensile stresses at the location. The bias factors range between 0.387 and 1.867 and COVs range between 0.174 and 3.440.

Table 5.16: Statistics for Maximum Tensile Stress at the Mid-span of the exterior span at the Bottom Fiber

Bridge Length m (ft)	Distribution Type	Nominal kPa (psi)	Mean kPa (psi)	Bias Factor (λ)	Coefficient of Variation (COV)
18.3 (60)	Normal	-221 (-32.1)*	-227 (-32.9)*	1.027	0.377
61.0 (200)	Normal	62 (8.99)	24 (3.5)	0.387	3.440
121.9 (400)	Normal	225 (32.6)	420 (60.9)	1.867	0.174

* Compressive stress

5.6 Summary

MCS evaluated the uncertainties in nominal IAB response prediction and the results established response statistics. Based on the established IAB load and resistance variable statistics, MCS determined the distribution and statistics of the IAB responses, utilizing the previously developed nominal numerical model with the LHS method.

RGIVs to deal with uncertainties in IABs are resistance and load variables. Resistance variables are: (1) concrete elastic modulus; (2) backfill stiffness; and (3) lateral pile soil stiffness. Load variables are: (1) superstructure temperature variation; (2) superstructure concrete thermal expansion coefficient; (3) superstructure temperature gradient; (4) concrete creep and shrinkage; (5) prestressing steel relaxation; (6) bridge construction sequence/timeline; and (7) backfill pressure on backwall and abutment. The probabilistic simulation considered three deterministic bridge lengths: 18.3 m (60 ft), 61.0 m (200 ft) and 122.0 m (400 ft). MCS results established IAB response statistics: (1) bridge axial force; (2) bridge bending moment; (3) pile lateral force; (4) pile moment; (5) pile head/abutment displacement; (6) compressive stress at the top fiber at the mid-span of the exterior span; and (7) tensile stress at the bottom fiber at the mid-span of the exterior span.

Utilizing a commercial program, a best-ft distribution for each IAB response was determined and was modeled using normal, lognormal and Weibull distributions. For long bridges, bridge compressive axial force, bridge negative bending moment, pile displacement and compressive stress at the top fiber produced two peak frequencies that represent elastic and plastic pile supports. For these responses, a best-fit distribution determined by a commercial program, however, did not represent well maximum responses and peak frequency. A best-fit distribution was, therefore, determined maximum responses to be located within 95% CI, be close to a proposed distribution CDF, and well-represent maximum peak frequency of MCS results.

IAB response statistics provide the basis for a reliability-based design format, allowing the determination of appropriate load factors. Based on the determined IAB response statistics, a reliability analysis of IABs is performed to develop new load and resistance factors for IABs.

Chapter 6

DETERMINATION OF PARTIAL SAFETY FACTORS

6.1 Introduction

Development of reliability-based IAB design load combinations with partial safety factors provides a consistent level of design safety. The current AASHTO LRFD specifications [4] was developed using structural reliability analyses, however, load and resistance factors for the situation encountered by IABs does not exist. In practice, bridge specifications for conventional jointed bridges are used in IAB designs. However, IABs have different boundary conditions and additional loads with inherent uncertainties: temperature variation, temperature gradient, time-dependent effects and backfill pressure. Figure 6.1 presents a stress change in a prestressed concrete girder due to thermal loads that must be considered in the design process. Considering uncertainties in thermal loads, the present study determines partial safety factors for IAB designs.

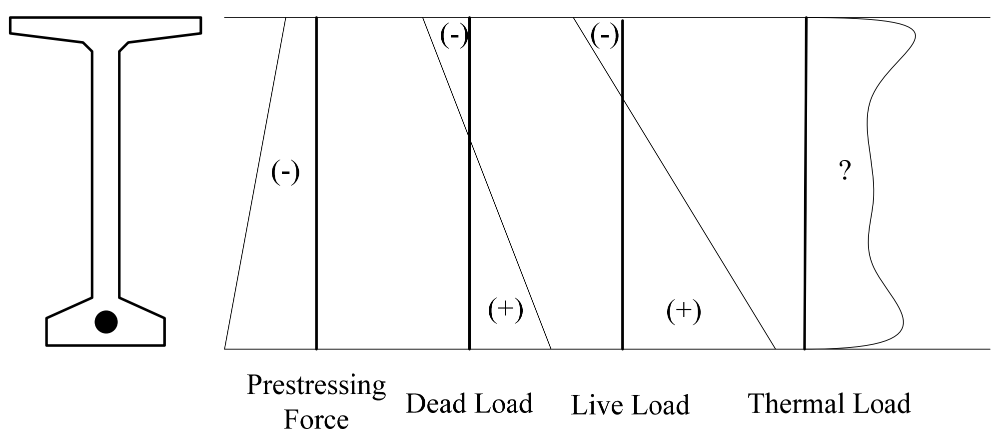

Figure 6.1: Stress in an IAB with Prestressed Concrete Girders

Load combinations for IABs are developed in accordance with the procedure in Figure 6.2. The developed partial safety factors and load combinations use the same format as current the AASHTO LRFD specification covering prestressed concrete girder highway IABs with short to medium lengths: 18.3 to 121.9 m (60 to 400 ft). The proposed load combinations consider prestressing force, dead load of bridge component (*DC*), dead load of wearing surface (*DW*), traffic live load (*LL*), vehicular impact load (*IM*) and thermal load (*IAB*). Distribution types and statistics for all loads and resistances are determined based on published literature [101, 103] and as established in Chapter 5 for thermal load. For the nominal design methods, the nominal IAB response prediction models developed in Chapter 4 are utilized. The limit states are based on established load combinations of Service I, Service III and Strength in AASHTO LRFD.

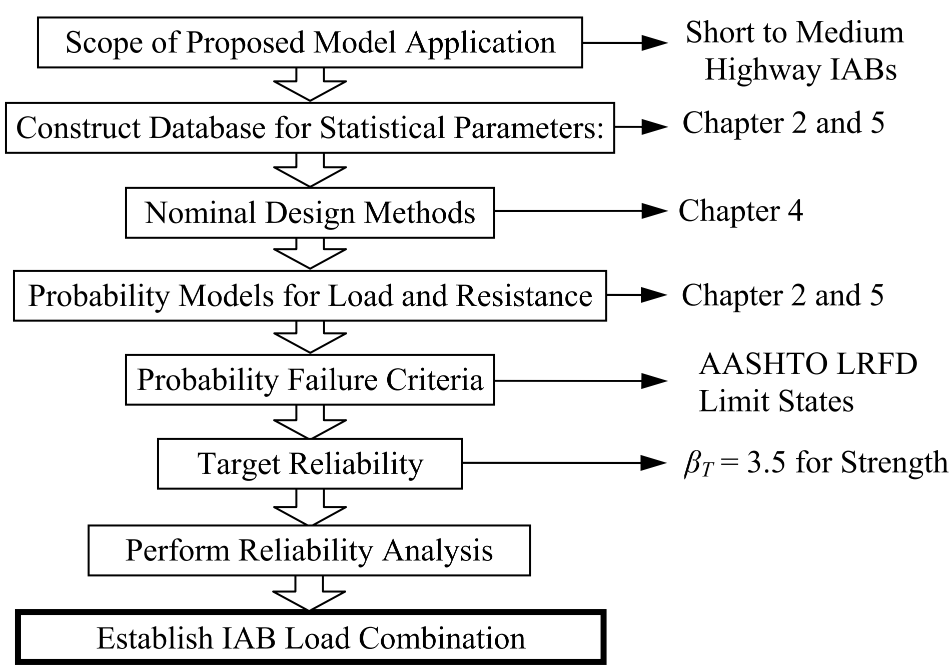

Figure 6.2: Load Combination Development Procedure

The present study establishes load combinations in the same format as the current AASHTO LRFD. The design limit state requires the factored nominal resistance to be equal to or greater than the total factored nominal loads. As presented in Figure 6.3, nominal resistance is reduced by a resistance factor and nominal load is amplified by a load factor. The load factor is determined such that the area that exceeds the resistance is the same for all load situations. The resistance factor is determined by calibration to obtain a target reliability index.

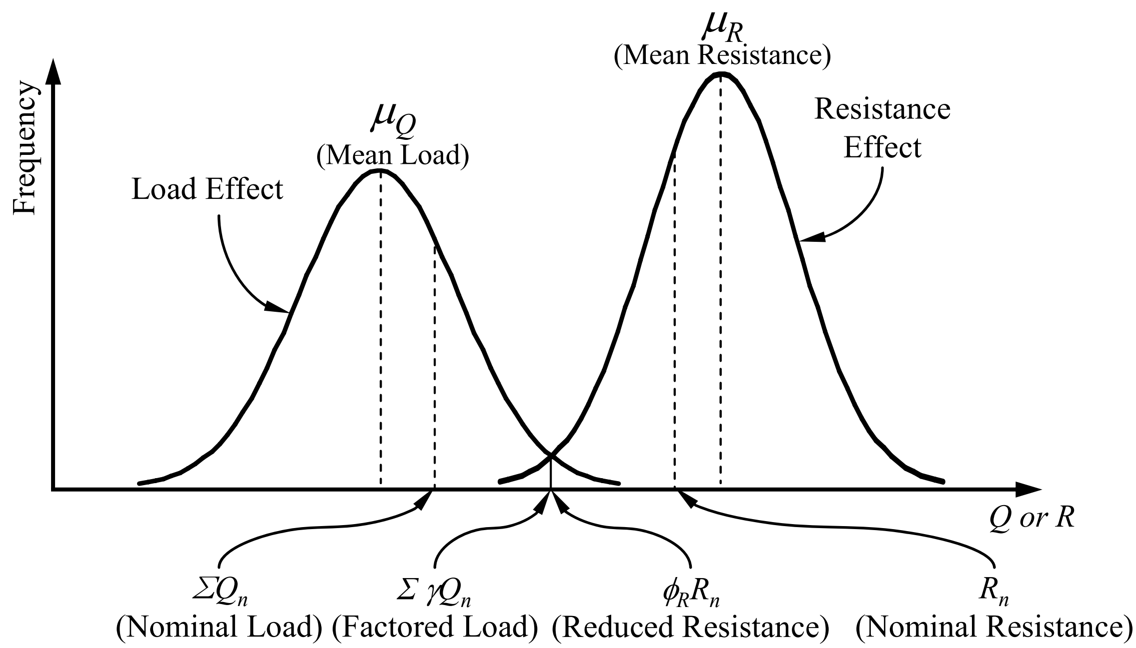

Figure 6.3: Relationship among Mean, Design and Factored Resistance or Load

Based on Figure 6.3, the basic format of LRFD code is:

$$\phi_R R_n \geq \sum_i \gamma_i Q_i \tag{6.1}$$

where, ϕ_R = resistance factor;
Rn = nominal resistance;
γ_i = load factor for load i, and
Q_i = load i.

Considering loads of interest for this study, the basic limit state equation is expanded as:

$$\phi_R R_n \geq \gamma_{DC}DC + \gamma_{DW}DW + \gamma_{LL}LL + \gamma_{IM}IM + \gamma_{IAB}IAB \qquad (6.2)$$

where, DC = dead load of component;
DW = dead load of wearing surface;
LL = vehicular live load;
IM = vehicular dynamic load allowance, and
IAB = thermal load due to backfill pressure, temperature variation, temperature gradient; and time-dependent effects.

Each load and resistance has inherent uncertainties. Partial safety factors (load factors) are, therefore, used to ensure the specified safety level. Reliability analysis determines the partial safety factors for each limit state based on the statistics of load and resistance variables.

6.2 Statistics of Loads and Resistances

The load components of interest include dead load, live load and thermal load. Dead load is sustained and consists of bridge component self-weight (*DC*)—girders, deck slab, diaphragms and parapets—and wearing surface self-weight (*DW*). Other dead loads due to signs and utilities are not considered in this study. Bridge components are divided into cast-in-place components and factory-made components because of different uncertainties and statistical characteristics. Bridge girders are assumed to be factory-made components and all other dead loads are cast-in-place components. Dead loads exhibit less variability and randomness, therefore, less uncertainty compared to other loads. IAB and conventional bridge dead load statistics are similar, therefore, the statistics from published literature [102] are utilized and presented in Table 6.1. In the analysis, dead load is assumed to be equally distributed to individual girders.

Table 6.1: Dead Load Statistics [102]

Load	Distribution	Bias Factor	COV
Dead Load (Factory-made)	Normal	1.03	0.08
Dead Load (Cast-in-place)	Normal	1.05	0.10
Dead Load (Asphalt Wearing Surface)	Normal	1.00	0.25
Prestressing Force (f_{ps})	Normal	1.04	0.025

Live load statistics, which include traffic loads with vehicular impact for a 75-year bridge life, are obtained from published literature [29, 102] and are presented in Table 6.2. Other live loads of wind load, snow load, etc. are not considered in this study.

Table 6.2: Live Load Statistics [29, 102]

Load	Distribution	Bias Factor	COV
Live Load and Dynamic Load (HL-93)	Normal	1.10	0.18

This study considers two live load models: (1) HL-93; and (2) HS-25 truck load + lane load. HL- 93 load refers to the AASHTO LRFD design live load and is based on AASHTO HS-20 truck load + 9.3 kN/m (0.64 kip/ft) lane load. The current AASHTO LRFD utilizes this HL-93 load for a partial safety factor calibration. Figure 6.4(a) presents HL-93 load and HS-25 truck load + lane load, 125% of HL-93 load. This vehicle load, HS-25 truck load + lane load, is also used to consider future growth in vehicular live loads, but the bias factor for this load was derived as 1.10/1.25 = 0.88 based on the bias factor for the HL-93 load (bias factor = 1.10). Truck impact load is taken as 33% [4] increase in only truck live loads. To distribute live loads to individual girders, the AASHTO LRFD live load girder distribution factors are used.

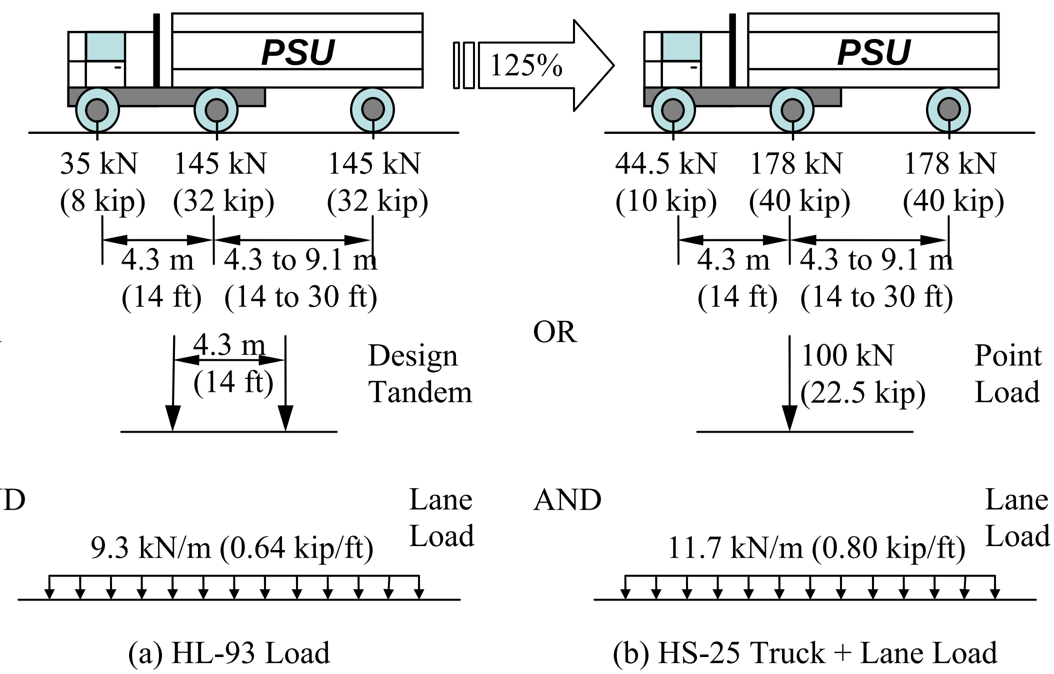

Figure 6.4: Vehicle Live Load [3, 4]

The limit state requires accounting for superstructure temperature variation (*TU*), superstructure thermal gradient (*TG*), time-dependent effects (*CR*+*SH*) and backfill pressure (*EH*). The thermal load statistics, established in Chapter 5, are summarized in Table 6.3.

Table 6.3: Thermal load Statistics

Load Component	Notation	L m (ft)	Distribution	Bias Factor	COV
Tensile Stress	$f_{IAB\text{-}T}$	18.3 (60) 61.0 (200) 121.9 (400)	Normal	1.027 0.387 1.867	0.377 3.440 0.174
Compressive Stress	$f_{IAB\text{-}C}$	18.3 (60) 61.0 (200) 121.9 (400)	Normal	1.756 1.259 1.077	0.115 0.204 0.160
Bending Moment*	M_{IAB}	18.3 (60) 61.0 (200) 121.9 (400)	Normal	1.016 1.850 1.922	0.179 0.319 0.396

* Negative moments at the mid-span.

To describe uncertainties in bridge structure resistance, statistics from published literature [101, 102, 103, 120, 136] that are the basis of the current AASHTO LRFD are utilized and described in Table 6.4.

Table 6.4: Statistics for Resistance

Material	Distribution	Bias Factor	COV
Prestressed Concrete (Bending) [101, 102, 120]	Lognormal	1.05	0.075
f_c' = 55.2 MPa (8.0 ksi) [103]	Lognormal	1.09	0.090
Modulus of Rupture (f_r) (for f_c' = 55.2 MPa (8.0 ksi)) [136]	Lognormal	1.54	0.095

6.3 Reliability Analysis of AASHTO LRFD Limit State

Reliability analyses of AASHTO LRFD [4] limit states are performed to determine whether additional thermal load reduce structure safety. A reliability analysis determines the safety level of a structure in terms of a reliability index (β) and is computed here for two loading cases: (1) a bridge without thermal load; and (2) a bridge with thermal load. In the reliability analysis of this study, correlations between load variables are assumed equal to zero.

AASHTO LRFD [4] limit states, with the same objectives and definitions, are considered in the reliability analysis. A thermal loading is added to the limit state function. Considered AASHTO LRFD limit states include Service I, Service III and Strength I limit states. The service limit states intend to provide a serviceability limit for deflection, cracking, vibration and gradual deterioration based on user's comfort, aesthetics or cost. Thus, a serviceability limit state does not directly preclude reinforcement and prestressing steel deterioration or structural failure. The strength limit state provides a minimum level of safety based on strength capacity. The objective of the Service I limit state is to provide for the normal operation of a bridge without compressive failure. The Service III limit state limits tension crack of prestressed concrete superstructures under normal operation. As discussed in AASHTO LRFD commentary (C3.4.1) [4], Service III limit state event occurs about once per day for single traffic lane bridges, once per year for two traffic lane bridges and less often for bridges with more than two traffic lanes.

The Rackwitz-Fiessler procedure [114, 115] is utilized to compute reliability indices. This method produces an accurate result while requiring basic statistics and distribution types of all related variables in a limit state function. The basic principal of this method is to establish equivalent normal statistics for non-normal variables. This approximation is achieved by the assumption that the CDF and PDF of the actual function of random variable, X are equal to the normal CDF and PDF at the design point, x^* [114, 115]:

$$F_X(x^*) = \Phi\left(\frac{x^* - \mu_X^e}{\sigma_X^e}\right) \text{ and } f_X(x^*) = \frac{1}{\sigma_X^e}\phi\left(\frac{x^* - \mu_X^e}{\sigma_X^e}\right) \tag{6.3}$$

where, F_X = CDF of random variable X;
f_X = PDF of random variable X;
Φ = standard normal CDF;
ϕ = standard normal PDF;
μ^e_X = equivalent normal mean of random variable X, and
σ^e_X = equivalent normal standard deviation of random variable X.

From Eq. 6.3, the equivalent normal mean and the standard deviation of random variable, X is derived as [114, 115]:

$$\begin{aligned} \mu_X^e &= x^* - \sigma_X^e[\Phi^{-1}(F_X(x^*))] \\ \sigma_X^e &= \frac{1}{f_X(x^*)}\phi\left(\frac{x^* - \mu_X^e}{\sigma_X^e}\right) = \frac{1}{f_X(x^*)}\phi\left[\Phi^{-1}(F_X(x^*))\right] \end{aligned} \tag{6.4}$$

The limit states of interest include a non-normal variable of the lognormal distribution for a resistance variable. Using Eq. 6.4, the equivalent statistics for lognormal variables can be computed [102]:

$$\mu_X^e = x^*[1 - \ln(x^*) + \mu_{\ln x}] \text{ and } \sigma_X^e = x^*\sigma_{\ln X} \tag{6.5}$$

where, $\mu_{\ln X} = \ln(\mu_X) - \frac{\sigma_X^2}{2}$, and $\sigma_{\ln X} = \ln\left(1 + \frac{\sigma_X^2}{\mu_X^2}\right)$.

Based on Eq. 6.5, a reliability analysis for AASHTO LRFD limit states is performed in accordance with Figure 6.5.

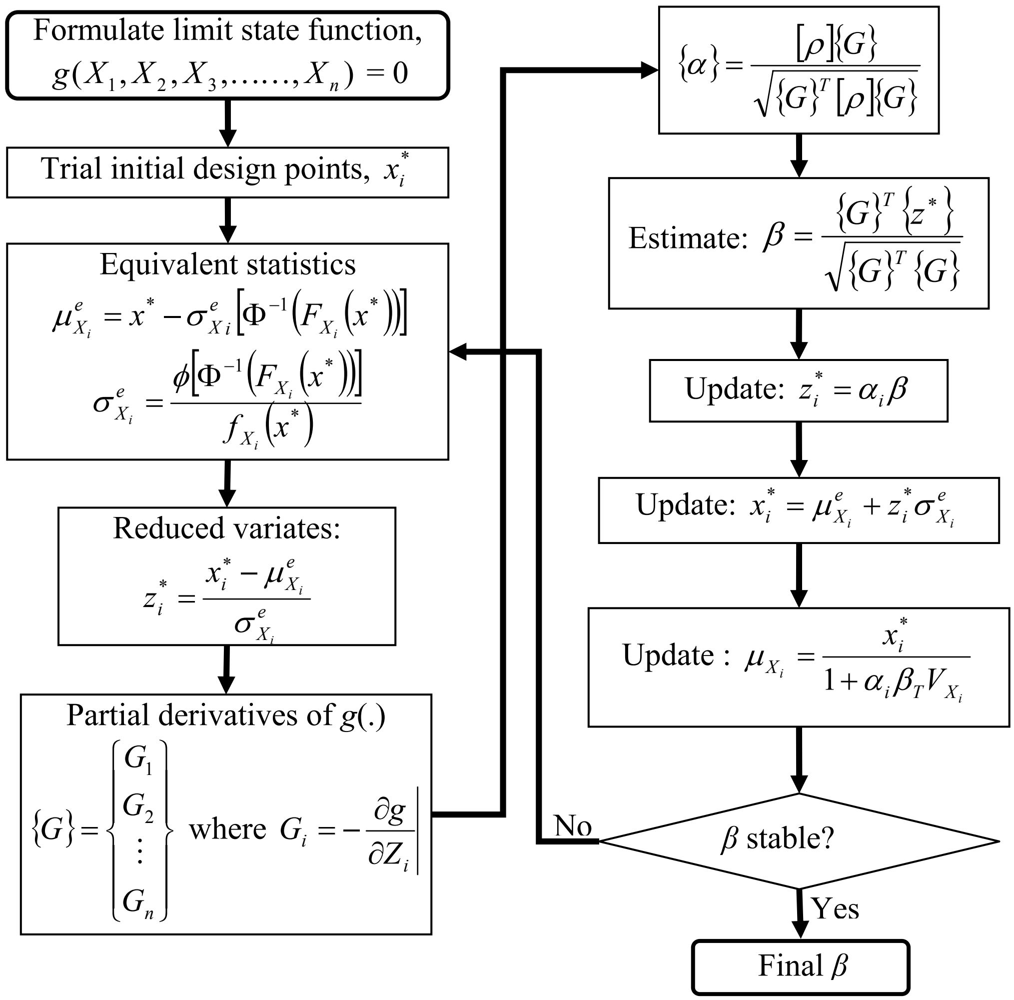

Figure 6.5: Reliability Analysis Procedure

In the iterative reliability analysis, a limit state function, $g(.) = 0$, is first established, including all loads and resistance components of interest in this limit state. The initial design point (x_i*) is assumed to start the analysis, based on $g(.) = 0$. Then, equivalent normal variables are computed using Eq. 6.4 and 6.5, and these variables are transferred to the reduced variates (z_i*) corresponding to the design point (x_i*). Partial derivatives of $g(.) = 0$ and the directional cosine vector are determined at the design point. Then the reliability index is computed and the design point in reduced variates and original coordinates is updated based on this computed reliability index. This procedure is iterated until the reliability index become stable.

6.3.1 Service I Limit State

The AASHTO LRFD Service I limit state (AASHTO LRFD 5.9.4.2.1) [4] is a load combination relating to the normal operational use of a bridge. This load limit state intends to limit compressive stress at nominal values. Therefore, all load factors are taken as 1.0. The load combination for the Service I limit state at the top fiber of the prestressed concrete girder is:

$$\phi_R f_n \geq \sum_i \gamma_i f_i = 1.0\, f_{DC1} + 1.0\, f_{DC2} + 1.0\, f_{DW} + 1.0\, f_{LL+IM} \tag{6.6}$$

where, ϕ_R = resistance factor, f_n = nominal compressive stress, f_{DC1} = compressive stress due to factory-made DC, f_{DC2} = compressive stress due to cast-in-place DC, f_{DW} = compressive stress due to DW, and f_{LL+IM} = compressive stress due to LL+IM. AASHTO specifies two compressive stress limits: (1) $0.45\, f_c'$ for the sum of effective prestress and permanent loads; and (2) $0.6\, f_c'$ for the sum of effective prestress, permanent loads, and transient loads. The required resistance can be obtained from the summation of all load effects. Therefore, the stress limit specified by AASHTO LRFD is adopted as the nominal resistance (f_n) of the structure. Considering the additional compressive stress due to thermal load (f_{IAB}), the Service I load combination for permanent loads is:

$$\phi_R f_n = 0.45\, f_c' \geq 1.0\, f_{DC1} + 1.0\, f_{DC2} + 1.0\, f_{DW} + 1.0\, f_{IAB} \tag{6.7}$$

For all dead loads and live loads, the Service I load combination is:

$$\phi_R f_n = 0.6\, f_c' \geq 1.0\, f_{DC1} + 1.0\, f_{DC2} + 1.0\, f_{DW} + 1.0\, f_{LL+IM} + 1.0\, f_{IAB} \tag{6.8}$$

Therefore, the limit state function, $g(.)$ for permanent loads is:

$$g(.) = 0.45\, f_c' - (f_{DC1} + 1.0\, f_{DC2} + f_{DW} + f_{IAB}) = 0 \tag{6.9}$$

For all dead loads and live loads, $g(.)$ is:

$$g(.) = 0.6\, f_c' - (f_{DC1} + 1.0\, f_{DC2} + f_{DW} + f_{LL+IM} + f_{IAB}) = 0 \tag{6.10}$$

Reliability indices (β) are computed for both Service I limit states and are presented in Figures 6.6 and 6.7. Based on Eq. 6.9 and 6.10, βs for the Service I limit state with thermal load ('IA bridge' in Figure 6.6 and 6.7) are computed. For comparison purposes, β for the Service I limit state without thermal load (without f_{IAB} in Eq. 6.9 and 6.10) are also computed. In addition, two live load models in Figure 6.4 are considered for all loading cases (Figure 6.7). The transition of design live load from HL-93 load to HS-25+lane load (bias factor decreases 25% and live load increases 25%) causes β decrease approximately 29%.

For Service I permanent loads (Figure 6.6), f_{IAB} significantly influences bridge reliability. For permanent loads, β for IABs range between 7.0 and 8.1 and β for jointed bridges range between 7.8 and 8.5. The f_{IAB} reduced by approximately 8.1% of β for Service I permanent load limit state.

For Service I all loads (Figure 6.7), f_{IAB} influence is relatively much less on bridge reliability. For HL-93 load, β for IABs range between 8.5 and 9.0 and β for jointed bridges range between 8.8 and 9.4. The f_{IAB} reduced by approximately 3.5% of β for

Service I with HL-93 load. For HS-25 truck + lane load, β for IABs range between 6.3 and 6.9 and βs for jointed bridges range between 5.8 and 6.5. The f_{IAB} reduced by approximately 5.1% of β for Service I with HS-25 truck + lane load. The computed reliability indices represent very low probabilities of failures; less than 4.8E-13 for HL-93 load and 7.4E-10 for HS-25 truck + lane load. Therefore, f_{IAB} must be considered in the Service I limit state because f_{IAB} has an influence on bridge reliability.

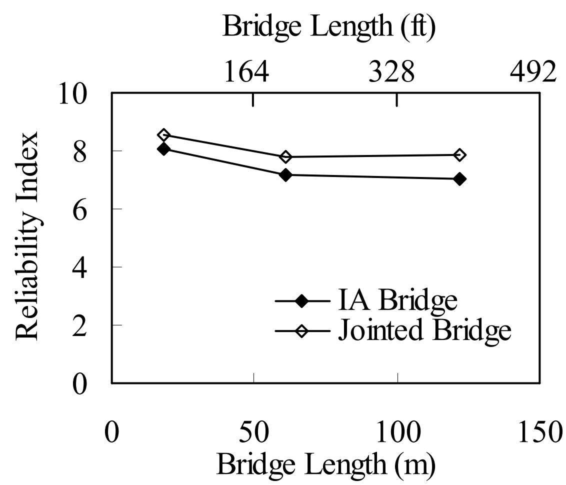

Figure 6.6: Service I Limit State Reliability Indices for Permanent Loads

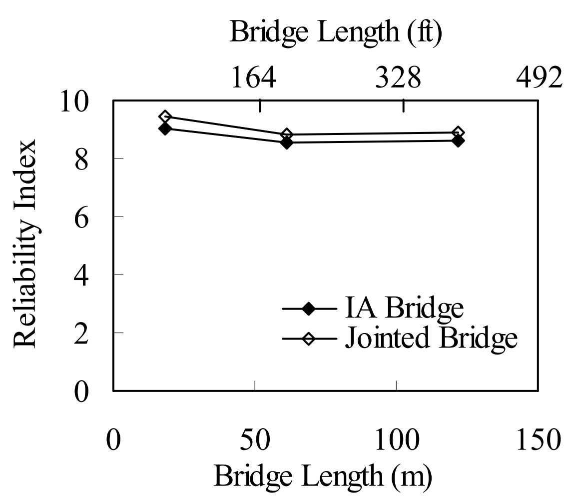

(a) HL-93 Load

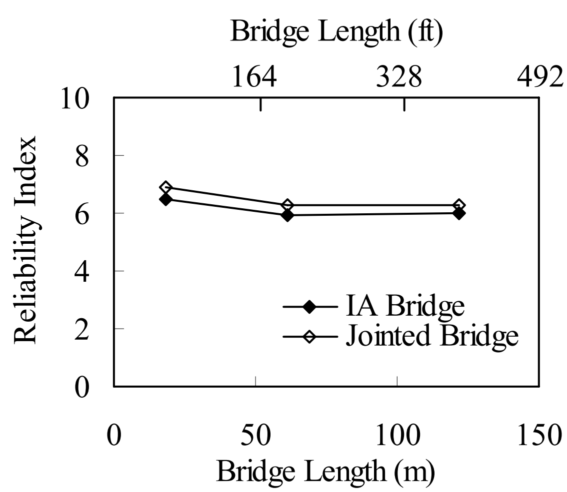

(b) HS-25 Truck + Lane Load

Figure 6.7: Service I Limit State Reliability Indices for All Loads

6.3.2 Service III Limit State

The AASHTO LRFD Service III limit state (AASHTO LRFD 5.9.4.2.2) [4] addresses tension in prestressed concrete girder bridges for crack control. The load combination for Service III limit state at the bottom fiber of the prestressed concrete girder is:

$$\phi_R f_n \geq \sum_i \gamma_i f_i = 1.0\, f_{DC1} + 1.0\, f_{DC2} + 1.0\, f_{DW} + 0.8\, f_{LL+IM} \tag{6.11}$$

where, ϕ_R = resistance factor, f_n = nominal tensile stress, f_{DC1} = tensile stress due to factory-made DC, f_{DC2} = tensile stress due to cast-in-place DC, f_{DW} = tensile stress due to DW, and f_{LL+IM} = tensile stress due to $LL+IM$. This limit state adopts load factors equal to 1.0 for all loads except vehicular live loads. As discussed in AASHTO [4], the live load load factor (γ_{LL+IM} = 0.8) in the Service III load combination has been selected to represent an occurrence of prestressed concrete girder crack opening once per day for single traffic lane bridges, once per year for two traffic lane bridges, and less often for bridges with more than two traffic lanes.

AASHTO LRFD specifies a tensile stress limit of $0.5\sqrt{f_c'}$ (MPa) ($0.19\sqrt{f_c'}$ (ksi)), which is a lower-bound value for the tensile strength [136]. Thus, the bias factor for the modulus of rupture (1.54) from published literature [136] is greatly larger than 1.0 as presented in Table 6.4. The required stress for the Service III limit state can be obtained by a resultant stress due to expected loads. However, this resultant stress is limited by the tensile stress limit of $0.5\sqrt{f_c'}$ (MPa) ($0.19\sqrt{f_c'}$ (ksi)). The tensile stress limit by AASHTO, therefore, is the nominal resistance (f_n) in a reliability analysis. Considering the additional tensile stress due to thermal loads (f_{IAB}), the load combination of Service III is:

$$\begin{aligned}\phi_R f_n &= 0.5\sqrt{f'_c} \geq 1.0\, f_{DC} + 1.0\, f_{DW} + 0.8\, f_{LL+IM} + 1.0\, f_{IAB} \text{ (MPa)} \\ \phi_R f_n &= 0.19\sqrt{f'_c} \geq 1.0\, f_{DC} + 1.0\, f_{DW} + 0.8\, f_{LL+IM} + 1.0\, f_{IAB} \text{ (ksi)}\end{aligned} \tag{6.12}$$

Therefore, the limit state function, $g(.)$ for Service III is:

$$\begin{aligned}g(.) &= 0.5\sqrt{f'_c} - (f_{DC} + f_{DW} + 0.8\, f_{LL+IM} + f_{IAB}) \text{ (MPa)} \\ g(.) &= 0.19\sqrt{f'_c} - (f_{DC} + f_{DW} + 0.8\, f_{LL+IM} + f_{IAB}) \text{ (MPa)}\end{aligned} \tag{6.13}$$

Reliability indices (β) are computed for the Service III limit state and are presented in Figures 6.8. Based on Eq. 6.13, β for the Service III limit state with thermal load (‘IA bridge’ in Figure 6.8) are computed. For a comparison purpose, β for the Service III limit state without thermal load (without f_{IAB} in Eq. 6.13) are also computed. In addition, live load models of HL-93 and HS25 truck + lane load in Figure 6.4 are considered.

The β for HL-93 load is a constant value of approximately 2.0. Similarly, β for HS-25+lane load produce a constant value of approximately 1.0. The transition of design live load from HL-93 load to HS-25+lane load (bias factor decreases 25% and live load increases 25%) causes β to decrease by approximately 43%.

For the Service III limit state, the f_{IAB} influence is relatively less on bridge reliability of considered bridge lengths. For HL-93 load, β for IABs range between 1.9 and 2.1 and β for jointed bridges range between 1.9 and 2.3. The f_{IAB} reduced β by approximately 5.4% for Service III limit state for L = 60.9 and 121.9 m (200 and 400 ft). However, βs for L = 18.3 m (60 ft) increased 6.2% because bridges with L = 18.3 m (60 ft) experience no tensile stress due to f_{IAB} but always compression. In addition, it is expected that the f_{IAB} influence will be much worse for longer spans because the influence continuously increases (Figure 6.8).

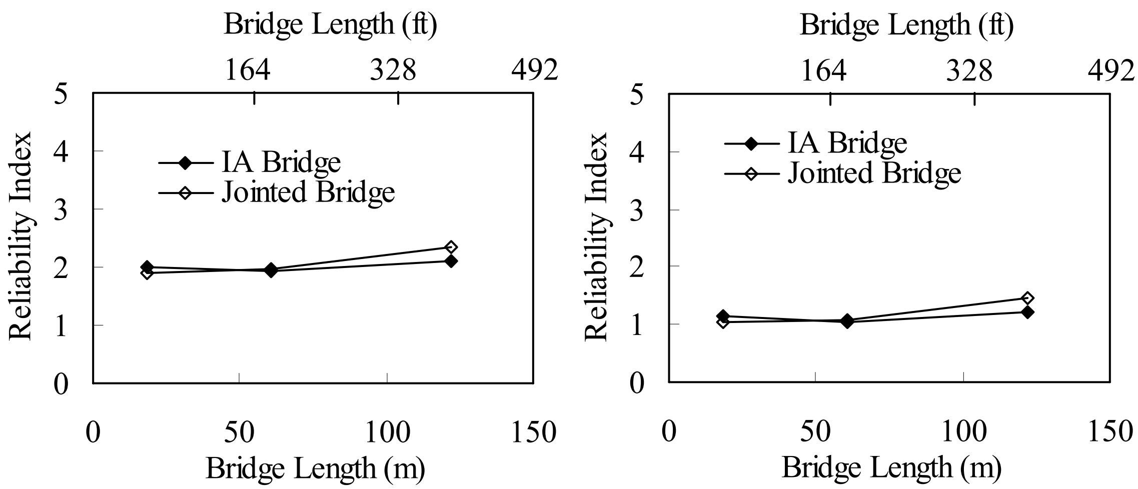

(a) HL-93 Load (b) HS-25 Truck + Lane Load

Figure 6.8: Load Factors for Service III Limit State

6.3.3 Strength I Limit State

AASHTO LRFD Strength I limit state is a load combination for investigating strength demand. A general form of strength limit state is formulated as Eq. 6.1. Relative to bending moment, the load combination for Strength I limit state is:

$$\phi_R M_n \geq 1.25M_{DC1} + 1.25M_{DC2} + 1.5M_{DW} + 1.75M_{LL+IM} \tag{6.14}$$

where, M_{DC1} = moment due to factory-made DC, M_{DC2} = moment due to cast-in-place DC, M_{DW} = moment due to DW, and M_{LL+IM} = moment due to $LL+IM$. The load factor for thermal loading (γ_{IAB}) is determined as:

$$\gamma_{IAB} = \lambda_{IAB}(1+\eta COV_{IAB}) \tag{6.15}$$

where, λ_{IAB} = bias factor for thermal loading, η = constant determined by the target reliability exceedance probability (η = 2.0 for current AASHTO [101]), and COV_{IAB} = coefficient of variation of thermal loading.

In a strength load combination considered here, resistance is measured in terms of flexural strength. The nominal flexural strength (M_n) is derived from the design load combination as:

$$M_n = \frac{1}{\phi_R}[1.25M_{DC1} + 1.25M_{DC2} + 1.5M_{DW} + 1.75M_{LL+IM}] \tag{6.16}$$

where, ϕ_R = resistance factor (= 1.0 for bending in accordance with AASHTO [4]). Considering the additional bending moment due to thermal load (M_{IAB}), a limit state function for Strength I limit state is:

$$g = M_n - (M_{DC1} + M_{DC2} + M_{DW} + M_{LL+IM} + M_{IAB}) = 0 \tag{6.17}$$

A target reliability of 3.5 was adopted for the Strength I limit state for consistency with current AASHTO LRFD [4].

Reliability indices (β) are computed for Strength I limit state and are presented in Figures 6.9. Based on Eq. 6.17, β for the Strength I limit state with thermal load ('IA bridge' in Figure 6.9) are computed. For comparison purposes, β for the Strength I limit state without thermal load (without M_{IAB} in Eq. 6.17) are also computed. In addition, β for current practice ('Current Practice' in Figure 6.9) are computed to represent a design condition that IABs are designed without considering thermal load (M_n(Eq. 6.16) without M_{IAB})while thermal load are present in IABs (g(.)(Eq 6.17) with M_{IAB}). Both live load models of HL-93 and HS25 truck + lane load in Figure 6.4 are considered.

Considering thermal load in Strength I limit state tends to decrease by approximately 5.9% and 0.6% for HL-93 loads and HS-25 truck + lane loads, respectively. For IABs, an average of β for Strength I limit state with thermal load is 3.2 for HL-93 loads and 4.4 for HS-25 truck + lane load. The average of β for current practices is 3.9 for HL-93 loads and 5.0 for HS-25 truck + lane load, and may result in a significant overdesign. Therefore, the load factors for thermal load are re-computed to obtain a constant reliability index over L and to be consistent with the current AASHTO LRFD.

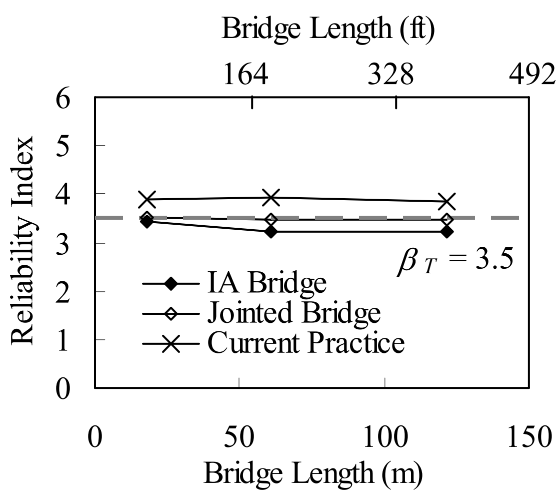

(a) HL-93 Load

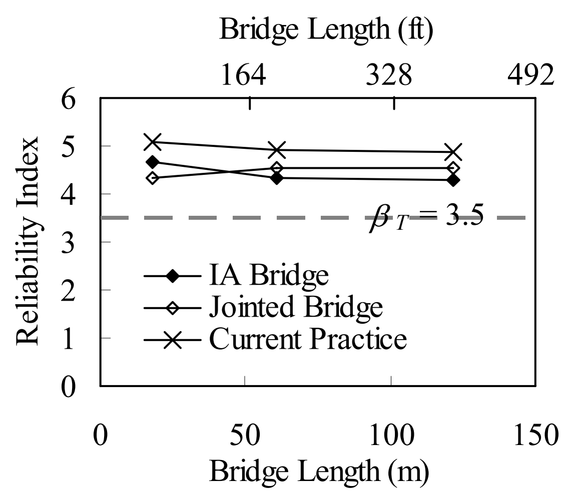

(b) HS-25 Truck + Lane Load

Figure 6.9: Strength I Limit State Reliability Indices

6.4 Calibration of Load and Resistance Factors

Load and resistance factors are determined for Strength I limit state. This study performs reliability analyses to determine the partial safety factors for AASHTO load combinations.

Using the partial safety factor calibration procedure [101] presented in Figure 6.10, partial safety factors to achieve the target reliability index ($\beta_T = 3.5$) are computed. The calibration procedure is an iterative computational procedure that is similar to that presented in Figure 6.5.

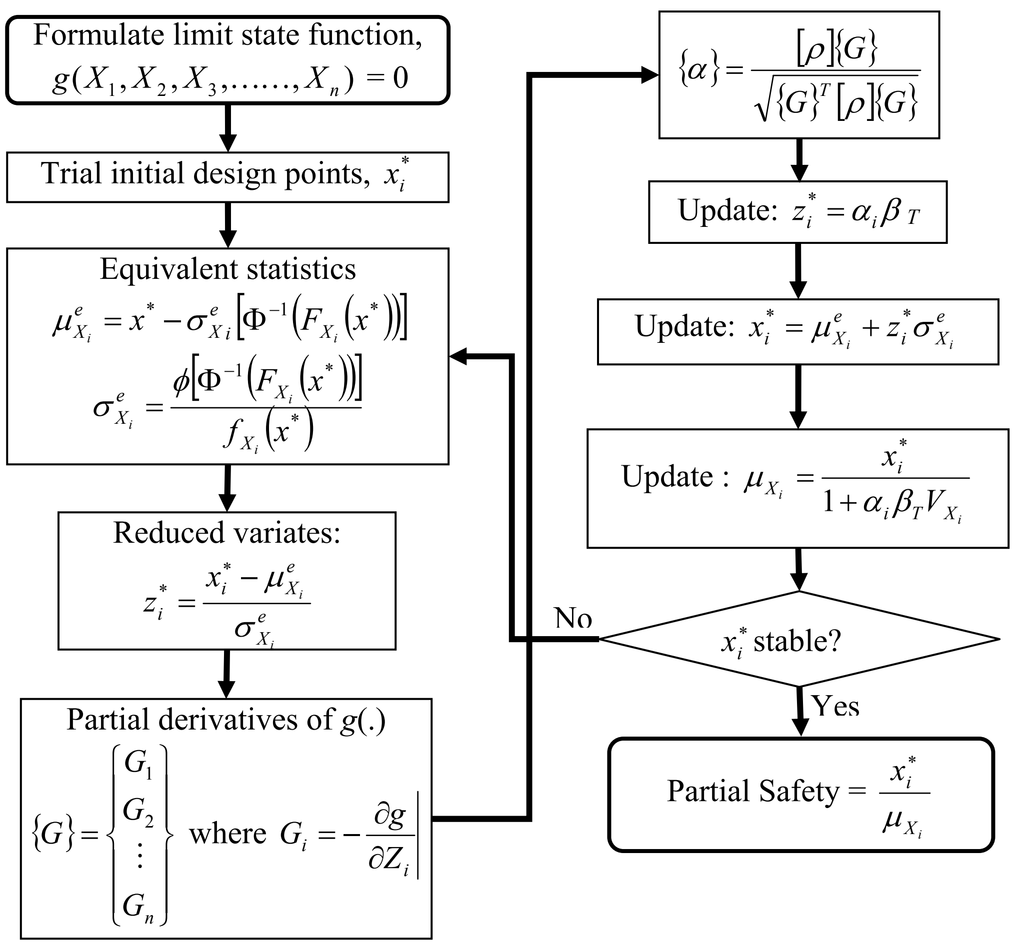

Figure 6.10: Partial Safety Factor Calibration Procedure

First a limit state function, $g(.) = 0$, is established, including all loads and resistance components of interest in this limit state. The initial design point (x_i*) is assumed to start the analysis, based on $g(.) = 0$. Then, equivalent normal variables are computed using Eq. 6.4 and 6.5, and these variables are transferred to the reduced variates (z_i*) corresponding to the design point (x_i*). Partial derivatives of $g(.) = 0$ and the directional cosine vector are determined at the design point. Using the target reliability index, an updated design point is computed in reduced variates. The design point in the original coordinates is updated based on this updated design point in reduced variates. This procedure is iterated until the design point become stable. Using the procedure presented in Figure 6.10, partial safety factors to achieve the target reliability index ($\beta_T = 3.5$) are presented in Tables 6.5 and 6.6. The computed load and resistance factors ensure the prescribed safety level of $\beta_T = 3.5$.

Table 6.5: Partial Safety Factors for $\beta_T = 3.5$ (HL-93 Load)

Limit State	Length m (ft)	ϕ_R	γ_{DC1}	γ_{DC2}	γ_{DW}	γ_{LL+IM}	γ_{IAB}
Strength I	18.3 (60)	0.85	1.10	1.05	1.20	1.60	1.00
	61.0 (200)	0.85	1.15	1.05	1.20	1.50	1.50
	121.9 (400)	0.85	1.15	1.05	1.20	1.50	1.50

Table 6.6: Partial Safety Factors for $\beta_T = 3.5$ (HS-25 Truck + Lane Load)

Limit State	Length m (ft)	ϕ_R	γ_{DC1}	γ_{DC2}	γ_{DW}	γ_{LL+IM}	γ_{IAB}
Strength I	18.3 (60)	0.85	1.10	1.05	1.20	1.60	1.00
	61.0 (200)	0.85	1.15	1.05	1.15	1.55	1.30
	121.9 (400)	0.85	1.15	1.05	1.15	1.55	1.55

As presented in Tables 6.5 and 6.6, a different set of load and resistance factors result in each design case for loads and bridge lengths. However, establishing load and resistance factors for every single bridge is not practical and unfeasible. Therefore, this study investigated thermal load factors with respect to different resistance factors to achieve the target reliability index.

A resistance factor, ϕ_R, equal to 1.0 is recommended by AASHTO LRFD [4] for prestressed concrete girders subjected to bending moment. For a compression-controlled section, ϕ_R equal to 0.75 is recommended to prevent brittle failure. For those sections subjected to axial force with flexure, ϕ_R is calculated as 0.75 (compression-controlled) × 1.0 (prestressed girder bending) = 0.75 (AASHTO LRFD C5.5.4.2.1) [4]. However, prestressed concrete girders in IABs are not compression controlled sections and still are tension-controlled section because compressive stress is relatively small compared to bending as investigated in the Service I limit state. Because the current AASHTO LRFD does not provide a resistance factor for bending moment + compressive stress, the present study, therefore, investigates γ_{IAB} with respect to ϕ_R = 0.85 to 1.0.

For comparison purposes, boundary conditions of IABs are considered in the reliability analysis. An IAB has integral abutments that have a rotational stiffness between a simple support and a fixed end support. The girders and deck slabs are integrally cast to the abutments. However, the construction joint and weak-axis oriented supporting piles may allow structure rotation. The rotational stiffness of an abutment is difficult to estimate because it is related to the superstructure and substructure dimensions and shapes, pile rotational capacity and load history. Therefore, the present study analyzes the bridge reliability based on both simple support and fixed end support. Figure 6.11 illustrates the boundary conditions. For the fixed end support condition, the superstructure end, which is an integral part, is assumed to be fixed.

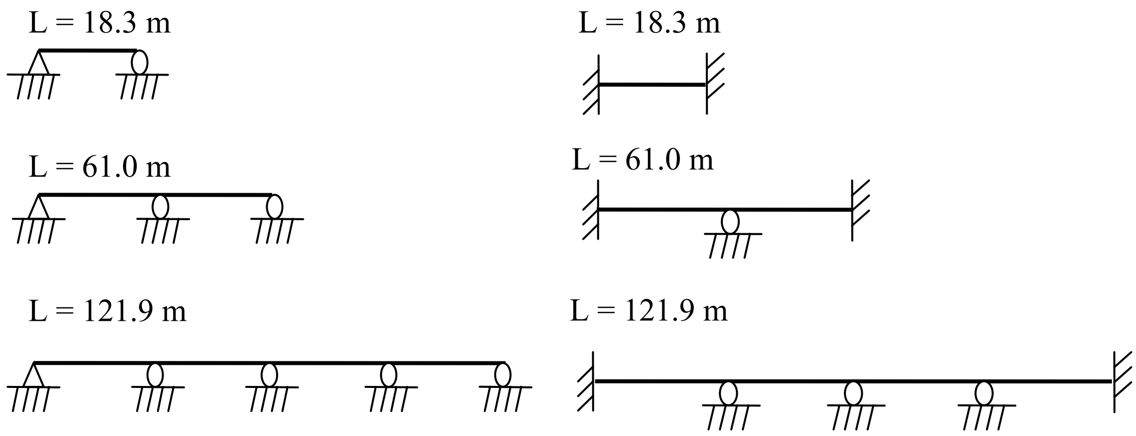

(a) Simple Support (b) Fixed End Support

Figure 6.11: Analysis Boundary Conditions

6.4.1 Simple Support Condition

Based on the simple support condition, a reliability analysis was performed to determine load factors for thermal load (γ_{IAB}) with respect to ϕ_R = 0.9 to 1.0. Both HL-93 and HS-25 truck + lane loads were applied to establish appropriate load factors for each

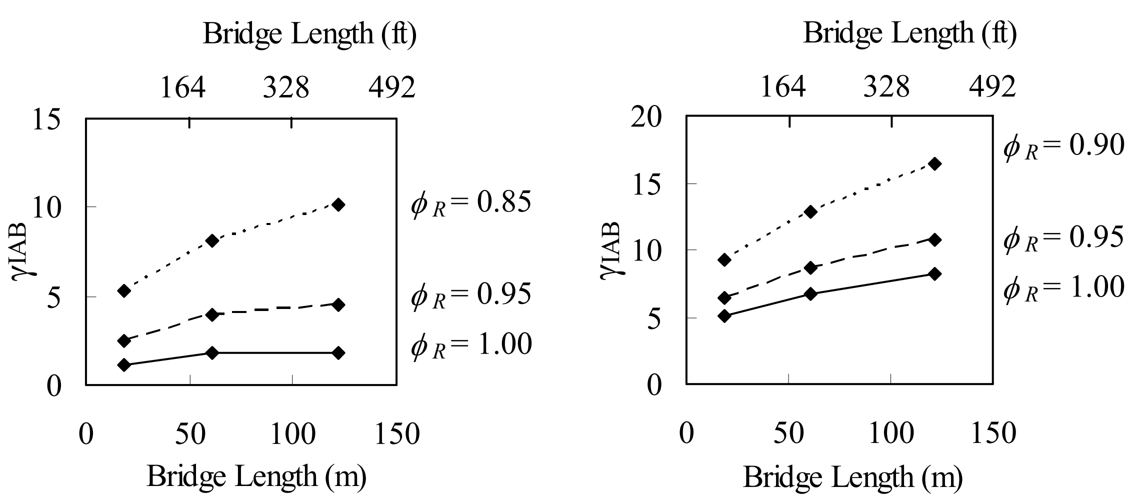

(a) HL-93 Load (b) HS-25 truck + Lane Load

Note: γ_{DC} = 1.25, γ_{Dw} = 1.5, γ_{LL+IM} = 1.75

Figure 6.12: Load Factors for Thermal Loads (Simple Support)

live load model. To be consistent with AASHTO LRFD, load factors for *DC*, *DW* and *LL* + *IM* are taken from AASHTO LRFD Strength I limit state. The γ_{IAB} with respect to ϕ_R = 0.85 to 1.0, to achieve the target reliability, were determined for each bridge length as presented in Figure 6.12. The γ_{IAB} for HS-25 truck load + lane load change significantly as bridge lengths increase. Based on the reliability analysis results, ϕ_R = 1.00 and γ_{IAB} = 1.15 for HL-93 loads provides a constant level of safety. Figure 6.13 presents reliability indices of various combinations of ϕ_R and γ_{IAB}.

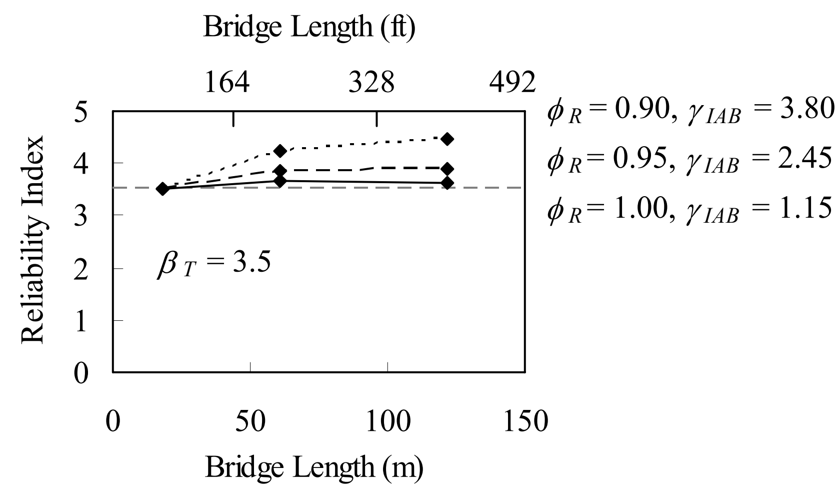

(a) HL-93 Load

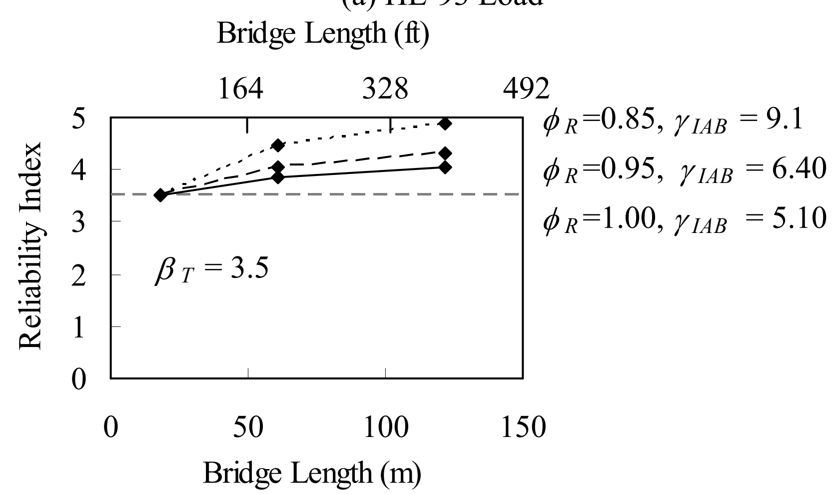

(b) HS-25 Truck + Lane Load

Figure 6.13: Proposed Load and Resistance Factors (Simple Support)

Based on the determined load and resistance factors (γ_{IAB} = 1.15 and ϕ_R = 1.00), a reliability analysis was performed for a full range of dead load over total load (*DC*/(*DC*+*LL*)), varying from 0.0 to 1.0. In addition, thermal load varies with respect to bridge length and boundary conditions. The ratio of thermal to dead load (*IAB*/*DC*) was varied between 0.05 to 0.15. The ratio of thermal load to dead load = 0.05 and 0.15, Figure 6.14 presents β variations with respect to the load ratios. In the analysis, *DW*/*DC* = 12.5% was assumed. For the practical load ratio ranges between 0.3 and 0.9 [103], β varies from 2.9 to 3.8.

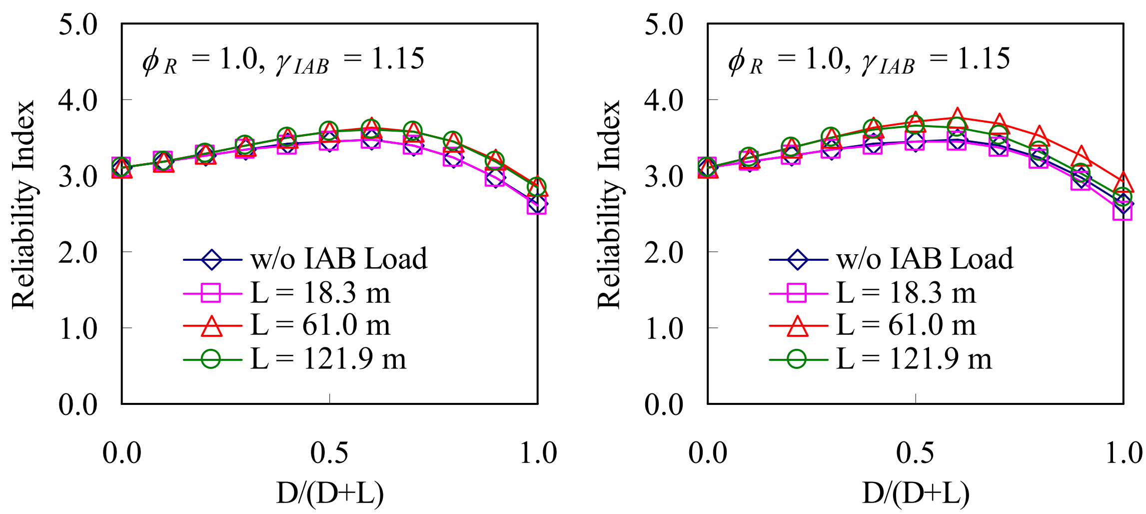

(a) *IAB*/*DC* = 0.05 (b) *IAB*/*DC* = 0.15

Figure 6.14: Reliability Indices for Ratios of *IAB* to *DC*

6.4.2 Fixed End Support

Based on the fixed end support condition, a reliability analysis was performed to determine load factors for thermal loads (γ_{IAB}) with respect to ϕ_R = 0.85 to 1.0. Both HL-

93 and HS-25 truck + lane loads were applied to establish appropriate load factors for each live load model. For consistency with AASHTO, load factors for *DC*, *DW* and *LL* + *IM* are taken from AASHTO LRFD Strength I limit state.

Current IAB design practice considers an IAB as a simple support condition, although integral abutments have rotational stiffness. Figure 6.14 presents the reliability indices for when an IAB is designed as a simple support, but the actual boundary condition is a fixed end condition (DSBF) and when an IAB is designed as a simple support and the actual boundary condition is a simple support condition (DSBS). The actual boundary may vary between fixed end condition and simple support condition. As in Figure 6.15, reliability indices of DSBF are much greater than Strength I limit state target reliability, 3.5. Especially, reliability indices for short bridges range between 10 and 12. While the actual rotational stiffness is not fixed, results in Figure 6.15 indicate that the current IAB design is significantly conservative.

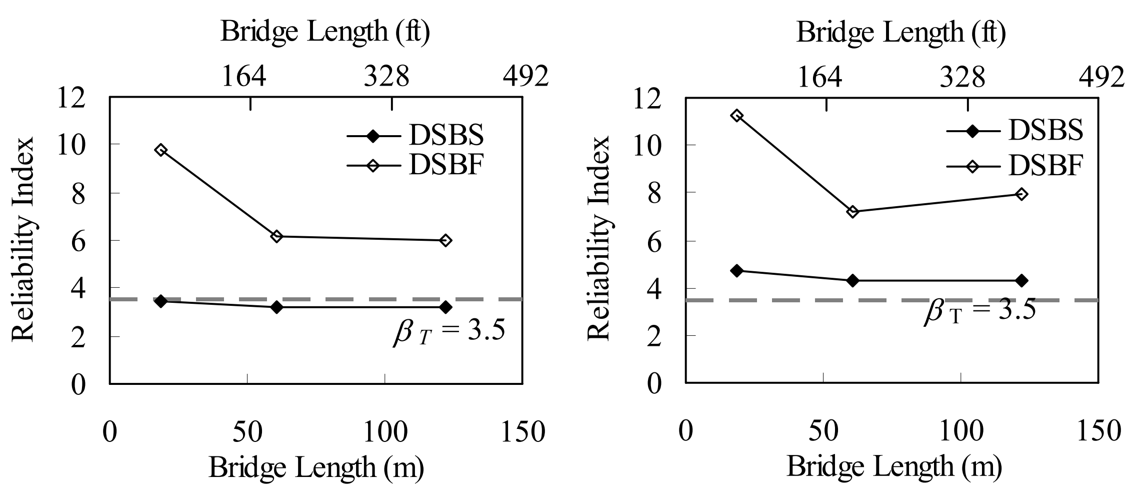

(a) HL-93 Load (b) HS-25 Truck + Lane Load

Figure 6.15: Reliability Indices for IABs with respect to Boundary Condition

Determined load factors with respect to ϕ_R = 0.85 to 1.0 to achieve the target reliability for each bridge are presented in Figure 6.16. For IABs with fixed end support design and fixed end boundary, load and resistance factors that can provide β > 3.5 for all bridges were investigated. The present study determined that ϕ_R = 1.00 and γ_{IAB} = 1.15 for HL-93 loads provide a constant level of safety. Figure 6.17 presents reliability indices based on the proposed load and resistance factors and comparison to different ϕs and γ_{IAB}s.

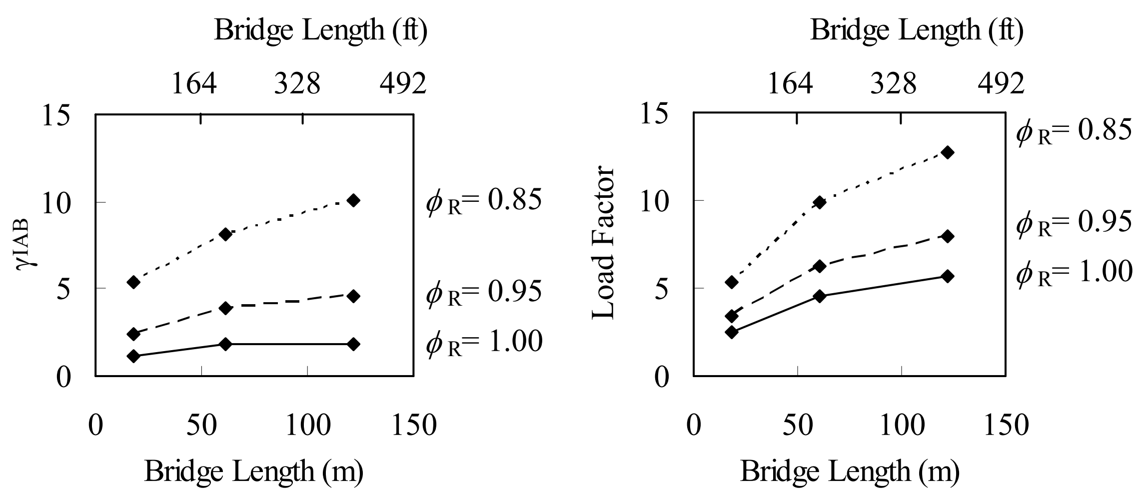

(a) HL-93 Load

(b) HS-25 truck + Lane Load

Note: γ_{DC} = 1.25, γ_{Dw} = 1.5, γ_{LL+IM} = 1.75

Figure 6.16: Load Factors for Thermal Loads (Fix End Support)

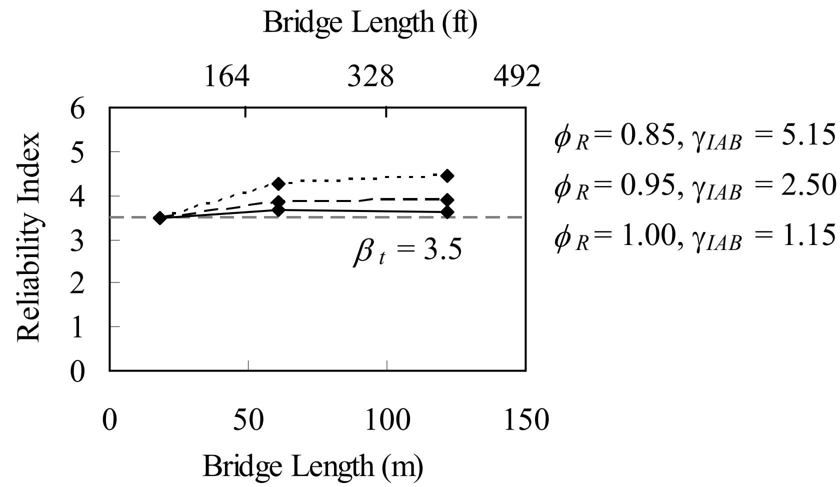

(a) HL-93 Load

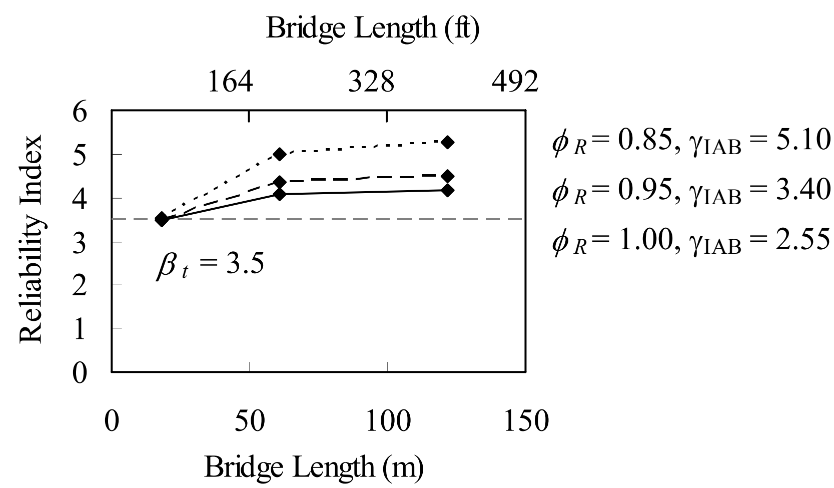

(b) HS-25 Truck + Lane Load

Figure 6.17: Proposed Load and Resistance Factors (Fixed End Support)

6.5 Summary

Based on the previously established thermal load response statistics, reliability analyses were performed to determine the load and resistance factors for IABs. The AASHTO LRFD Service I, Service III and Strength I limit state were selected as limit state function. For live loads, both live load models of HL-93 loads and HS-25 truck +

lane loads were considered in the reliability analyses. Simple support and fixed end support conditions were also considered in the reliability analysis for Strength I limit state.

Established load combinations for IABs are:

(1) Service I (permanent loads only):

$$1.0\, f_{DC} + 1.0\, f_{DW} + 1.0\, f_{IAB} \leq 0.45\, f_c' \tag{6.18}$$

(2) Service I (all dead loads and live loads):

$$1.0\, f_{DC} + 1.0\, f_{DW} + 1.0\, f_{LL+IM} + 1.0\, f_{IAB} \leq 0.6\, f_c' \tag{6.19}$$

(3) Service III:

$$\begin{aligned} &1.0\, f_{DC} + 1.0\, f_{DW} + 0.8\, f_{LL+IM} + 1.0\, f_{IAB} \leq 0.5\sqrt{f_c'} \text{ (MPa)} \\ &1.0\, f_{DC} + 1.0\, f_{DW} + 0.8\, f_{LL+IM} + 1.0\, f_{IAB} \leq 0.19\sqrt{f_c'} \text{ (ksi)} \end{aligned} \tag{6.20}$$

(4) Strength I:

$$\phi_R M_n = 1.25 M_{DC} + 1.50 M_{DW} + 1.75 M_{LL+IM} + 1.15 M_{IAB} \; (\phi_R = 1.0) \tag{6.21}$$

Chapter 7

SUMMARY AND CONCLUSIONS

7.1 Summary

Numerical Model Development

The present study developed numerical modeling methodologies to accommodate long-term simulations and probabilistic simulations. To validate the numerical modeling methodology, four numerical models of field tested IABs have been created and compared to field monitored responses. The key components of the numerical model include abutment-backfill interaction, soil-pile interaction and construction joints. Thermal loads include backfill pressure, time-dependent effects, temperature change and temperature gradient. The developed numerical model requires very low resources and computing times. Also, the numerical model effectively simulated the actual IAB behavior and provides accurate predictions.

Parametric Study and IAB Response Prediction Models

Based on the developed numerical method, a 243 set parametric study with five parameters was performed. The considered key parameters are: (1) thermal expansion coefficient; (2) bridge length; (3) backfill height; (4) backfill stiffness; and (5) soil stiffness around pile. Based on the results, regression analysis has been performed for

IAB response predictions for (1) girder axial force; (2) girder bending moment; (3) pile lateral force; (4) pile moment; and (5) pile head/abutment displacement.

Probabilistic Analysis

Statistical models of IAB critical responses were established using probabilistic numerical simulations. The Monte Carlo simulation results provided basic statistics and distribution types for (1) tensile and bridge compressive axial force; (2) positive and negative bridge bending moment; (3) pile lateral force; (4) pile moment; (5) pile head/abutment displacement; (6) compressive stress at the mid-span of the exterior span at the top fiber; and (7) tensile stress at the mid-span of the exterior span at the bottom fiber. The established statistics are the basis for reliability analysis and development of load and resistance factors for IABs.

Determination of Partial Safety Factors

The present study performed reliability analysis to identify the structural safety, considering 75-year thermal loads in short to medium-long length prestressed concrete bridges. The reliability analysis process performed is based on developed nominal response prediction models and established statistical parameters. In order to provide AASHTO LRFD format load combinations, Service I and III, and Strength I limit state were considered and investigated. For the AASHTO limit states, the present study developed new load combinations considering thermal loads.

7.2 Conclusions

Due to the excellent performance of IABs for the past decades, more than 10,000 IABs have been built over U.S. IABs will be a more preferable bridge type and the number of IABs will rapidly increase. The proposed field data calibrated numerical model for IABs is very versatile so that many researchers and bridge designers can use the model for short- and long-term bridge simulations. In preliminary analysis and plan, the IAB response prediction models developed in this study can be used as approximate methods. In addition, the statistics established here for IAB responses will be a basis to develop LRFD format bridge design code. Therefore, the established load and resistance factors provide a more economic and efficient IAB design process.

Nonlinear condensed numerical model development led to the following conclusions:

1. Measured and predicted responses indicate the abutment displacements are cyclic and irreversible along temperature variation. Based on the 75 year numerical simulation, this “ratcheting” behavior continues to increase for approximately 30 years.
2. The maximum abutment displacement is significantly less than the free expansion of superstructure used for the current design estimation.
3. Measured and predicted girder axial force and moment due to temperature, superstructure temperature gradient, and time-dependent loads is significant and must be considered in an IAB design process.

The parametric study considering superstructure thermal movement, soil-structure interaction, temperature gradient and time-dependent effects during a 75-year bridge life revealed following conclusions and recommendations:

1. Thermal expansion coefficient significantly influences girder axial force, girder bending moment, pile lateral force, pile moment and pile head/abutment displacement.
2. Bridge length significantly influences girder axial force, pile lateral force, pile moment and pile head displacement. The influence of bridge length on girder bending moment is relatively weak.
3. Backfill height and backfill stiffness are relatively less influential on IAB responses, but the influence of these parameters is affected by soil stiffness around piles. When soil stiffness around piles is high, backfill height inversely influences pile lateral force and pile moment.
4. Increase of soil stiffness around piles increases bridge bending moment, pile lateral force, pile moment and reduces pile head displacement. While pile lateral force, even in an extreme case, consumes only 15% of pile shear capacity, the restraints from stiffer soils cause piles to reach a yield moment due to large abutment rotation.
5. Both lower thermal expansion coefficient and shorter bridge length are main parameters to abate IAB responses. Bridges with higher thermal expansion coefficients, shorter span lengths and stiffer piles produce positive bending moments that may reduce girder capacity. Because bridge designers have

difficulty controlling thermal expansion coefficient, as a practical point of view, flexible piles and compacted backfills help relieve IAB responses.

6. During a 75-year bridge life, girder axial forces due to thermal load can reach 23.3% and 8.6% of the AASHTO LRFD tensile and compressive service stress limits, respectively. In addition, bending moment translates to 6.5% and 1.2% tensile stress at top and bottom fibers, and 0.14% and 1.4% compressive stress at top and bottom fibers.
7. The developed IAB response prediction models are accurate and easily provide expected critical bridge responses. Therefore, the prediction models can be utilized in a preliminary IAB designs within the scope of this study.

Using MCS, critical IAB responses have been investigated for (1) bridge axial force; (2) bridge bending moment; (3) pile lateral force; (4) pile moment; (5) pile head/abutment displacement; (6) compressive stress at the top fiber at the mid-span of the exterior span; and (7) tensile stress at the bottom fiber at the mid-span of the exterior span. The MCS for IAB responses during a 75-year bridge life led to the following conclusions:

1. Most of IAB responses could be fitted using normal distribution, but some of the responses followed lognormal distribution or Weibull distribution due to nonlinear behavior of IABs.
2. For long bridges, bridge compressive axial force, bridge negative bending moment, pile displacement and compressive stress at the top fiber produced two peak frequencies that represent elastic and plastic pile behavior.

3. The determined distributions for IAB responses represent maximum responses and frequencies. Using probability plots with CI and CDFs, a distribution was determined maximum responses to be located within 95% CI, be close to a proposed distribution CDF, and well-represent maximum peak frequency of MCS results.
4. The established statistical parameters provide the basis to design and analyze IABs.

Based on the previously determined nominal response prediction model and IAB response statistics, reliability analyses were performed and revealed the following conclusions:

1. Thermal load must be considered in IAB design process. Reliability analysis revealed that thermal load influences reliability of AASHTO LRFD limit state: Service I and III and Strength I.
2. The influence of thermal load on Strength I may result in an economic design because of negative moments at the mid-span.
3. Based on the reliability analysis results and target reliability ($\beta_T = 3.5$), $\phi_R = 1.00$ and $\gamma_{IAB} = 1.15$ is appropriate for IABs. Load factors for all other loads are the same as AASHTO LRFD so the developed load combination can be consistently used with the current practice.

7.3 Recommendations for Future Research

The present study focused on two traffic lanes, and short to medium length IABs. A study including various bridge dimensions, configurations and longer bridges would be valuable. Because a steel girder IAB has a different response from a prestressed concrete girder IAB due to time-dependent effects and thermal expansion coefficients, a study considering various superstructure materials is also valuable. In addition, it is worthy of studying live load distributions in IABs to better load estimations. Finally, a study to establish a rotational stiffness in an integral abutment will improve accuracy in design of IABs.

Bibliography

1. Abendroth, R. E. and Greimann, L. F. (2005). *Field Testing of Integral Abutments*. Final Report No. HR-399. Iowa Department of Transportation, Ames, IA.

2. Alaska Department of Transportation and Public Facilities (AKDOT). (2004). *Standard Specifications for Highway Construction*, Alaska Department of Transportation and Public Facilities, Juneau, Alaska.

3. American Association of State Highway and Transportation Officials (AASHTO). (2002). *AASHTO Standard Specifications*, 17th Ed., Washington, D.C.

4. American Association of State Highway and Transportation Officials (AASHTO LRFD). (2008). *AASHTO LRFD Bridge Design Specifications*, Washington, D.C.

5. American Association of State Highway and Transportation Officials (AASHTO Guide). *AASHTO Guide Specifications Thermal Effects in Concrete Bridge Superstructures.* (1989). Washington, D.C.

6. American Concrete Institute Committee 209 (ACI 209). (2004). "Prediction of Creep, Shrinkage, and Temperature Effects in Concrete Structures," *ACI Manual of Concrete Practice Part I*, American Concrete Institute, Farmington Hills, MI.

7. America Concrete Institute Committee 363 (ACI 363). (1998). *Guide to Quality Control and Testing of High-Strength Concrete*, American Concrete Institute, Farmington Hills, MI.

8. Ang, A.-S., and Tang, W. (1975). *Probability Concepts in Engineering Planning and Design. Volume I: Basic Principles*. John Wiley & Sons, Inc., New York, N.Y.

9. ANSYS Release 11.0, ANSYS University Advanced, ANSYS Inc.

10 American Petroleum Institute (API) (1993). *Recommended Practice for Planning, Designing, and Constructing Fixed Offshore Platforms—Working Stress Desgin*. 20th Ed., API RP2A-WSD, Washingtond, D.C.

11. Arockiasamy, M., Butrieng, N. and Sivakumar, M. (2004). "State-of-the-Art of Integral Abutment Bridges: Design and Practice," *Journal of Bridge Engineering*, ASCE, Vol. 9, No. 5.

12. Arockiasamy, M. and Sivakumar, M. (2005). “Time-Dependent Behavior of Continuous Composite Integral Abutment Bridges,” *Practice Periodical on Structural Design and Construction*, ASCE, Vol. 10, No. 3.

13. Arsoy, S., and R. M. Barker, and J. M. Duncan, and C. E. Via (1999). “Behavior of Integral Abutment Bridges,” *Final Report FHWA/VTRC-00/CR3*, Virginia Transportation Research Council, Charlottesville.

14. Ashour, M. and Norris, G. (2000). “Modeling Lateral Soil-Pile Response Based on Soil-Pile Interaction,” *Journal of Geotechnical and Geoenvironmental Engineering*, ASCE, Vol. 126, No. 5.

15. American Society of Heating, Refrigeration, and Air-Conditioning Engineers (ASHRAE). (1993). *Fundamentals Handbook*, American Society of Heating, Refrigeration, and Air-Conditioning Engineers, New York, NY.

16. Ayyub, B. M., and McCuen, R. H. (2003). Probability, statistics, and reliability for engineers and scientists, Chapman and Hall/CRC Press, Boca Raton, FL.

17. Ayyub, B. M., and Popescu, C. (2003). “Risk-based Expenditure Allocation for Infrastructure Improvement,” *Journal of Bridge Engineering*, ASCE, Vol.8, No. 6.

18. Barker, R. M., Duncan, J. M., Rojiani, K. B., Ooi, P. S. K., Tan, C. K., and Kim., S. G. (1991). “Manuals for the Design of Bridge Foundations,” NHCRP Report 343, Transportation Research Board.

19. Bakeer, R. M., Mattei, N. J., Almalik, B. K., Carr, S. P., and Homes, D. (2005). “Evaluation of DOTD Semi-Integral Bridge and Abutment System,” Report No. FHWA/LA.05/397, Louisiana Transportation Research Center, Baton Rouge, LA.

20. Barr, P. J., Stanton, J. F. and Eberhard, M. O. (2005). “Effects of Temperature Variation on Precast, Prestressed Concrete Bridge Girders,” *Journal of Bridge Engineering*, ASCE, Vol. 10, No. 2.

21. Bartlett, F. M, and MacGregor, J. G. (1996). “Statistical Analysis of the Compressive Strength of Concrete in Structures,” *ACI Materials Journal*, Vol. 93, No. 2, pp. 158-168.

22. Bazănt, Z. P., and Baweja, S. (1995). “Justification and Refinement of Model B3 for concrete creep and shrinkage models—1. Statistics and sensitivity,” *Materials and Structures*, Vol. 28, No. 181, pp. 415-430.

23. Bazănt, Z. P., and Baweja, S. (2000). “Creep and Shrinkage Prediction Model for Analysis and Design of Concrete Structures: Model B3—Short Form,” *Adam*

Neville Symposium: Creep and Shrinkage: Structural Design Effects, American Concrete Institute, pp. 85-100.

24. Baecher, G. B., and Christian, J. T. (2003). *Reliability and Statistics in Geotechnical Engineering*, John Wiley & Sons. ISBN: 0-471-49833-5.

25. Boulanger, R. W., Curras, C. J., Kutter, B. L., Wilson, D. W., and Abghari, A. (1999). "Seismic Soil-Pile-Structure Interaction Experiments and Analysis," *Journal of Geotechnical and Geoenvironmental Engineering*, ASCE, V.125, No.9, pp750-759.

26. Breña, S. F., Bonczar, C. H., Civjan, S. A., DeJong, J. T., and Crovo, D. S. (2007). "Evaluation of Seasonal and Yearly Behavior of an Integral Abutment Bridge," *Journal of Bridge Engineering*, ASCE, Vol. 12, No. 3, pp. 296-305.

27. Burke Jr., M. P. (1990). "Integral bridge design is on the rise," *Modern Steel Construction*, 30(4), 9-11.

28. California Department of Transportation (CALTRAN). (2006). *Bridge Design Specifications*, California Department of Transportation, Sacramento, CA.

29. Cheung, M. S., and Li, W. C. (2002). "Reliability Assessment in Highway Bridge Design," *Canadian Journal of Civil Engineering*, NRC Research Press. Vol. 29. pp.799-805.

30. Civjan, S. A., Bonczar, C., Breña, S. F., DeJong, J., and Crovo, D. (2007). "Integral Abutment Bridge Behavior: Parametric Analysis of Massachusetts Bridge," *Journal of Bridge Engineering*, ASCE,Vol.12, No.1, pp.64-71.

31. Clough, G. W., and Duncan, J. M. (1991). *Foundation Engineering Manual*, 2nd Ed., H. Y. Fang, ed., Van Nostrand Reinhold, New York.

32. Colorado Department of Transportation (CODOT). (2002). *Bridge Design Manual*, Colorado Department of Transportation, Denver.

33 Comite Euro-Internationale du Beton (CEB) (1990). *CEB-FIP Model Code for Concrete Structures*, *Buletin D'Information* No. 213/214, Lausanne, Switzerland.

34. Darley, P., Carder, D. R. and Alderman, G. H. (1996). "Seasonal Thermal Effects on the Shallow Abutment of an Integral Bridge in Glasgow," TRL Report 178, E465A/BG,Transport Research Laboratory, ISSN 0968-4107.

35. Das, B. M. (1999). *Principles of Foundation Engineering*, Brooks/Cole Publishing Company, 4th Ed. ISBN: 0-534-95403-0

36. Das, B. M. (2002). *Soil Mechanics Laboratory Manual*, 6th Ed., Oxford University Press.

37. DeJong, J. T., Howey, D. S., Civjan, S. A., Brena, S. F., Butler, D. S., Crovo, D. S., Hourani, N. and Connors, P. (2004). “Influence of Daily and Annual Thermal Variations on Integral Abutment Bridge Performance,” *Proceedings of Geotechnical Engineering for Transportation Projects*, GeoTrans 2004, ASCE, pp.496-505.

38. Dicleli, M. (2000). “Simplified Model for Computer-Aided Analysis of Integral Bridges,” *Journal of Bridge Engineering*, Vol. 5, No. 3, pp. 240-248.

39. Dicleli, M and Albhaisi, S. M. (2003). “Estimation of Length Limits for Integral Bridges Built on Clay,” *Journal of Bridge Engineering*, ASCE, Vol. 9, No. 6.

40. Dicleli, M and Albhaisi, S. M. (2004). “Effect of Cyclic Thermal Loading on the Performance of Steel H-Piles in Integral Bridges with Stub-Abutments,” *Journal of Construction Steel Research*, 60, pp. 161-182.

41. Dicleli, M. and Albhaisi, S. M. (2004). “Performance of abutment-backfill system under thermal variations in integral bridges built on clay,” *Engineering Structures*, Elsevier, No. 26, pp. 949-962.

42. Dicleli, M. (2005). “Integral Abutment-Backfill Behavior on Sand Soil—Pushover Analysis Approach,” *Journal of Bridge Engineering*, ASCE, Vol. 10, No. 3.

43. Delattre, L. (2001). “A Century of Design Methods for Retaining Walls – The French Point of View: I. Calculation – Based Approaches – Conventional and Subgrade Reaction Methods,” BLPC-2001/234, Laboratoire Central des Ponts et Chaussées.

44. Duncan, J. M (2000). “Factors of Safety and Reliability in Geotechnical Engineering”, *Journal of Geotechnical and Geoenvironmental Engineering*, ASCE, Vol. 126, No. 4.

45. Duncan, J. M. and Mokwa, R. L. (2001). “Passive Earth Pressure: Theories and Tests”, *Journal of Geotechnical and Geoenvironmental Engineering*, ASCE, Vol. 127, No. 3.

46. Dunker, K. F., and Liu, D. (2007). “Foundations for Integral Abutments,” *Practical Periodical on Structural Design and Construction*, ASCE, Vol. 12, No.1, pp. 22-30.

47. Elbadry, M. M. and Ghali, A. (2001). “Analysis of Time-Dependent Effects in Concrete Structures Using Conventional Linear Computer Programs,” *Canadian Journal of Civil Engineering*, CNRC Canada, Vol. 28, pp.190-200.

48. Ellingwood, B., MacGregor, J. G., Galambos, T. V., and Cornell, C. A. (1982). "Probability Based Load Criteria: Load Factors and Load Combinations," *Journal of Structural Engineering*, ASCE, Vol. 108, No. ST5, pp. 978-997.

49. Eloseily, K. H., Ayyub, B. M., and Patev, R. (2002). "Reliability Assessment of Pile Groups in Sands," *Journal of Structural Engineering*, ASCE, Vol. 128, No. 10, pp. 1346-1353.

50. Emanuel, J. H. and Hulsey, J. L. (1977). Prediction of the Thermal Coefficient of Expansion of Concrete. *Journal of American Concrete Institute*, Vol. 74, No. 4, pp, 149-155, April.

51. Faraji, S., Ting, J. M., Crovo, D. S. and Ernst, H. (2001). "Nonlinear Analysis of Integral Bridges: Finite-Element Model", *Journal of Geotechnical and Geoenvironmental Engineering*, ASCE, Vol. 127, No. 5.

52. Fennema, J. L., Laman, J. A., and Linzell, D. G. (2005). "Predicted and Measured Response of an Integral Abutment Bridge," *Journal of Bridge Engineering*, ASCE, Vol. 10, No. 6, pp. 666-677.

53. Florida Department of Transportation (FDOT) (2007). *Structures Design Guidelines*, Florida Department of Transportation, Talahassee, FL.

54. Folse, M. D. (1989). "Reliability Analysis for Laterally Loaded Piling," *Journal of Structural Engineering*, ASCE, Vol. 114, No. 5, pp. 1001-1020.

55. Fu, K. and Lu, F. (2003). "Nonlinear Finite-Element Analysis for Highway Bridge Superstructures," *Journal of Bridge Engineering*, ASCE, Vol. 8, No. 3.

56. Galambos, T. V., Ellingwood, B., MacGreger, J. G., and Cornell, C. A. (1982). " Probability Based Load Criteria: Assessment of Current Design Practice," *Journal of Structural Engineering*, ASCE, Vol. 108, No. ST5,pp.959-977.

57. Geyskens, P., Der Kiureghian, A., and Monteiro, P. (1998). "Bayesian Prediction of Elastic Modulus of Concrete," *Journal of Structural Engineering*, ASCE, Vol. 124, No. 1, pp. 89-95.

58. Ghali, A., Favre, R., and Elbadry, M. (2002). *Concrete Structures: Stresses and Deformation*, 3th Ed., Spon Press, London.

59. Girton, D. D., and T. R. Hawkinson, and L. F. Greimann (1991). "Validation of Design Recommendations for Integral-Abutment Piles," *Journal of Structural Engineering*, ASCE, Vol. 117, No. 7, pp. 2117-2134.

60. Greimann, L. F., Yang, P., and Wolde-Tinsae, A. M. (1986). “Nonlinear Analysis of Integral Abutment Bridges,” *Journal of Structural Engineering*, ASCE, Vol. 112, No. 10, pp.2263-2280.

61. Harr, M. E. (1987). *Reliability-based design in civil engineering.* Mc-Graw-Hill, New York.

62. Horvath, J. S. (2004). “Integral-Abutment Bridges: A Complex Soil-Structure Interaction Challenge,” *Proceedings Geotechnical Engineering for Transportation Projects,* GeoTrans 2004, ASCE.

63. Huang, J., Shield, C. K., and French, C. (2005). “Time-dependent Behavior of a Concrete Integral Abutment Bridges,” *Transportation Research Record: Journal of the Transportation Research Board*, CD 11-S, Transportation Research Board of the National Academies, Washington D.C., pp 299-309.

64. Hwang, E-S., and Nowak, A. S. (1991). “Simulation of dynamic load for bridges.” *Journal of Structural Engineering*, ASCE, 117(5), 1413-1434.

65. Illinois Department of Transportation (ILDOT). (2003). *Bridge Manual*, Illinois Department of Transportation, Springfield, Illinois.

66. Iowa Department of Transportation (IADOT). (2006). *Bridge Design Manual*, Iowa Department of Transportation, Ames, Iowa.

67. Imbsen, R. A., Vandershaf, D. E., Shamber, R. A., and Nutt, R. V. (1985). *Thermal Effects in Concrete Superstructures*. NCHRP Report No. 276, Transportation Research Boarc, Washington, D.C.

68. Ingram, E. E., Burdette, E. G., Goodpasture, D. W., Deatherage, J.H., and Bennett , R. M. (2004). “Behavior of Steel H-piles Supporting Integral Abutments,” *Proceedings* Structure 2004, ASCE, pp. 1-7.

69. Jaky, J. (1944). “The Coefficient of Earth Pressure at Rest,” *J. Soc. Hung. Eng. Arch.*, 355-358.

70. Jirásek, M. and Bažant, Z. P. (2002). “Inelastic Analysis of Structures,” John Wiley & Sons, New York.

71. Julian, O. G. (1966). “Discussion of strength variations in ready-mixed concrete by A. E. Cummings.” ACI Journal, 51(9), 772-2-772-8.

72. Kada, H., Lachemi, M., Petrov, N., Bonneau, O., and Aïtcin, P.-C. (2002). “Determination of the coefficient of thermal expansion of high performance concrete from initial setting,” *Materials and Structures*, Vol. 35, pp. 35-41.

73. Kim, W. (2008). “Simplified Nonlinear Numerical Analysis Method for Integral Abutment Bridges,” *Proceedings of the 2008 International Bridge Conference*, Pittsburgh, PA, IBC-08-43, June 2-4.

74. Knickerbocker, D., and Basu, P. K. (2004). “Analysis of Prestressed Concrete Jointless Bridges with Integral Abutments,” *Proceedings*: Structure 2004, ASCE, pp. 1-10.

75. Koskinen, M. *Soil-Structure-Interaction of Jointless Bridges on Piles*. Geotechnical Laboratory, Tampere University of Technology, Finland, pp. 1091-1096.

76. Kulhawy, F. H. (1992). “On the evaluation of soil properties,” ASCE Geotech. Special Publication, No. 31, pp.95–115.

77. Kunin, J., and S. Alampalli (2000). “Integral Abutment Bridges: Current Practice in United States and Canada,” *Journal of Performance of Constructed Facilities*, ASCE, Vol. 14, No. 3, pp. 104-111.

78. Lacasse, S., and Nadim, F. (1997). ‘‘Uncertainties in characterizing soil properties,’’ *Publication No. 201*, Norwegian Geotechnical Institute, Oslo, Norway, 49–75.

79. Laman, J. A., Linzell, D. G., Leighty, C. A., and Fennema, J. L. (2003). “Methodology to Predict Movement and Stresses in Integral Abutment Bridges,” *Report No. FHWA-PA-2002-039-97-04(80)*, Pennsylvania Transportation Research Council.

80. Laman, J. A., Pugasp, K., and Kim, W. (2006). “Field Monitoring of Integral Abutment Bridges,” *Report No. FHWA-PA-2006-006-510401-01*, Pennsylvania Transportation Research Council.

81. Lpile Plus Version 4.0, ENSOFT Inc.

82. Ministry of Transportation. (1991). *Ontario highway bridge design code*, 3rd Ed., Quality and Standards Division, Downsview, Ont. Canada.

83. Maine Department of Transportation. (2003). *Maine DOT Bridge Design Guide*, Maine Department of Transportation, Augusta, Maine.

84. Massachusetts Highway Department. (2005). *Bridge Manual*. Commonwealth of Massachusetts, Massachusetts Highway Department, Boston, MA.

85. Mirza, S. A., Hatzinikolas, M., and MacGregor, J. G. (1979). “Statistical descriptions of the strength of concrete.” *Journal of Structural Division*, ASCE, 105(6), 1021-1037.

86. Moorty, S., and Roeder, C. W. (1992). “Temperature Dependent Bridge Movements,” *Journal of Structural Engineering*, ASCE, Vol. 118, No. 4, pp. 1090-1105.

87. Moulton, L. K., GangaRao, H. V. S., and Halverson, G. T. (1985) *Tolerable Movement Criteria for Highway Bridges*, FHWA/RD-85/107, FHWA, U.S. Department of Transportation, Washington, D.C., 118 pp.

88. Mourad, S., and S. W. Tabsh (1999). “Deck Slab Stresses in Integral Abutment Bridges,” *Journal of Bridge Engineering*, ASCE, Vol. 4, No. 2, pp. 125-130.

89. National Climate Data Center (NCDC). (2006). *Comparative Climate Data for the United States through 2006.* National Oceanic and Atmospheric Administration. (http://www.noaa.gov/).

90. National Cooperative Highway Research Program (NCHRP). (1991). *Manuals for the Design of Bridge Foundations*, R. M. Baker, J. M. Duncan, K. B. Rojiani, P. S. D. Ooi, C. K. Tan, and S. G. Kim, eds. Rep 343, Transportation Research Board, Washington, D. C.

91. National Cooperative Highway Research Program (NCHRP 18-07). (1999). *Prestress Losses in Pretensioned High-Strength Concrete Bridge Girders*, M. K. Tadros, N. Al-Omaishi, S. J. Seguirant, J. G. Gallt. Rep 496, Transportation Research Board, Washington, D. C.

92. New Jersey Department of Transportation. (2004). *Bridges and Structures Design Manual*, New Jersey Department of Transportation, Trenton, N.J.

93. Nielsen, R. J., and Schmeckpeper, E. R. (2002). “Single-Span Prestressed Girder Bridge: LRFD Design and Comparison,” *Journal of Bridge Engineering*, ASCE, Vol. 7, No. 1, pp. 22-30.

94. Nilson, A.H. (1991). *Design of Concrete Structures, Eleventh Edition*, McGraw-Hill Inc., New York.

95. North Dakota Department of Transportation. (2002). *Standard Specifications for Road and Bridge Construction,* North Dakota Department of Transportation, Bismarck, ND.

96. Ndon, U. J., and K. L. Bergeson (1995). “Thermal Expansion of Concretes: Case Study in Iowa. *Journal of Materials in Civil Engineering*, ASCE, Vol. 7, No. 4, pp. 246-251.

97. New York Department of Transportation. (2006). *Bridge Manual*, New York Department of Transportation, Albany, N.Y.

98. Noorzaei, J., Viladkar, M. N. and Godbole, P. N. (1995). “Elasto-Plastic Analysis for Soil-Structure Interaction in Framed Structures”, *Computers & Structures*, Vol. 55, No. 5, 797-807.

99. Nowak, A. S., and Hong, Y-K. (1991). “Bridge live load models.” *Journal of Structural Engineering*, ASCE, 117(9), 2757-2767.

100. Nowak, A. S., Yamani, A. S., and Tabsh, S. W. (1994). “Probabilistic models for resistance of concrete bridge girders.” *ACI Structural Journal*, 91(3), 269-276.

101. Nowak, A. S. (1995). “Calibration of LRFD Bridge Code,” *Journal of Structural Engineering*, ASCE, Vol. 121, No. 8.

102. Nowak, A. S., Collins, K. R. (2000). *Reliability of Structures*. McGraw-Hill, ISBN 0-07-048163-6.

103. Nowak, A. S., and Szerszen, M. M. (2003). “Calibration of Design Code for Buildings (ACI 318): Part 1—Statistical Models for Resistance,” *ACI Structureal Journal*, Vol. 100, No. 3, pp. 377-382.

104. Ott, R. L., and Longnecker, M. (2001). *An Introduction to Statistical Methods and Data Analysis*, 5th edition, Duxbury, Thomson Learning, Inc., Pacific Grove, CA.

105. Oesterle, R. G, Refai, T. M., Volz, J. S., Scanlon, A., and Weiss, W. J. (1998). “Jointless and Integral Abutment Bridges Analytical Research and Proposed Design Procedures”, Construction Technology Laboratories, Inc., Draft Final Report to Federal Highway Administration, Washington, D.C.

106. Paul, M. D. (2003). “Thermally Induced Superstructure Stress in Prestressed Girder Integral Abutment Bridges,” *M.S. Thesis*, The Pennsylvania State University.

107. Paul, M. D., Laman, J. A., and Linzell, D. G. (2005). “Thermally Induced Superstructure Stresses in Prestressed Girder Integral Abutment Bridges,” Transportation Research Record: *Journal of the Transportation Research Board*, Transportation Research Board of the National Academies, Washington D.C., 287-297.

108. PCI (2001). “The State of the Art of Precast/Prestressed Integral Bridges,” ISBN 0-937040-66-5, Precast/Prestressed Concrete Institute, Chicago, IL.

109. PCI (2005). *PCI Bridge Manual*, Precast/Prestressed Concrete Institute, Chicago, IL.

110. Pennsylvania Department of Transportation (PennDOT). (2000). *Design Manual Part 4,* “Structures: Procedures-Design-Plans Presentation,” *PennDOT Design*

Manual Part 4, Commonwealth of Pennsylvania, Department of Transportation, Harrisburg, PA.

111. The Pennsylvania State Climatologist (PSC), http://pasc.met.psu.edu/PA_Climatologist.

112. Pugasap, K. (2006). "Hysteresis Model Based Prediction of Integral Abutment Bridge Behavior," Ph.D. Dissertation, The Pennsylvania State University, University Park, PA.

113. Pugasap, K., Kim, W., and Laman, J. A. "Long-term Response Prediction of Integral Abutment Bridges," *Journal of Bridge Engineering*, ASCE, (*accepted*).

114. Rackwitz, R. (1976). "Practical Probabilistic Approach to Design," *Bull. 112*, Comité European Du Beton, Paris, France.

115. Rackwitz, R., and Fiessler, B. (1978). "Structural Reliability under Combined Random Load Sequences," *Computers and Structures*, Elsvier, Vol. 9, pp. 489-494.

116 Russell, H. G., Miller, R. A., Ozyildirim, H. C., Tadros, M. K. (2006). *Compilation and Evaluation of Results from High-Performance Concrete Bridge Porjects, Volume I: Final Report*. FHWA-HRT-05-056. U.S. Department of Transportation, Federal Highway Adminstration, McLean, VA.

117. Shoukry, S. N., William, G. W., and Riad, M. Y. (2006). "Structural Behaviour of an Integral Abutment Bridge under Environmental Conditions," *Proceedings of Structures 2006*, ASCE.

118. South Dakota Department of Transportation (SDDOT). *Structures Construction Manual*, South Dakota Department of Transportation, Pierre, SD.

119. Stewart, M. G. (1997). "Time-dependent Reliability of Existing RC Structures," *Journal of Structural Engineering*, ASCE, Vol. 123, No. 7, pp. 896-902.

120. Tabsh, S. W., and Nowak, A. S. (1991). "Reliability of highway girder bridges," *Journal of Structural Engineering*, ASCE, 117(8), 2373-2388.

121. Tabsh, S. W., and Aswad, A. (1995). "Statistics of Steam-Cured Plant-Produced High Strength Concrete," *Engineering Mechanics: Proceedings of the 10th conference*, University of Colorado at Boulder, Boulder, Colorado, Vol. 2, pp. 1155-1158.

122. Tanesi, J., Kutay, M. E., Abbas, A., and Meininger, R. (2007). "Effect of CTE Variability on Concrete Pavement Performance as Predicted Using the

Mechanistic-Empirical Pavement Design Guide," *Proceedings: TRB 86th Annual Meeting*, Jan.25-27, 2007. Transportation Research Board, Washington D.C.

123. Terzaghi, K. E., and Peck, R. B. (1948). *Soil Mechanics in Engineering Practice*, John Wiley and Sons, Inc.

124. Theodoer A. Thomson, Jr. and Lutenegger, A. J. (1998). "Passive Earth Pressure Tests On An Integral Bridge Abutment", *Proceedings: Fourth International Conference on Case Histories in Geotechnical Engineering*, St. Louis, Missouri.

125. Thippeswamy, H. K., GangaRao, H. V. S. and Franco, J. M. (2002). "Performance Evaluation of Jointless Bridges," *Journal of Bridge Engineering*, ASCE, Vol. 7, No. 5.

126. Thomas, M. E. (1999). "Field Study of Integral Abutment Bridges," M.S. Thesis, Iowa State University, Ames, Iowa.

127. Turkstra, C. J. (1970). "Theory of Structural Design Decisions," *Solid Mechanics Study* No.2, University of Waterloo, Waterloo, Canada.

128. Turkstra, C. J., and Madsen, H. O. (1980). "Load Combination in Codified Structural Design," *Journal of the Structural Division*, ASCE, Vol. 106, No. ST12, Dec., pp. 2527-2543.

129. Vintzēleou, E. N., and Tassios, T. P. (1987). "Behavior of Dowels under Cyclic Deformations," *ACI Structural Journal*, ACI, pp. 18-30.

130. Virginia Department of Transportation (2007). *Design Aids and Typical Details*, Volume V, Part 2. Commonwealth of Virginia, Department of Transportation, Richmond, VA.

131. Wang, S. and Reese, L. C. (1993). "COM624P—Laterally Loaded Pile Analysis Program for the Microcomputer," *Report No. FHWA-SA-91-048*, U.S. Department of Transportation.

132. West Virginia Department of Transportation. (2004). *Bridge Design Manual*, West Virginia Department of Transportation, Charleston, W.Va.

133. Wu, T. H. (1974). "Uncertainty, Safety, and Decision in Soil Engineering," *Journal of Geotechnical Engineering*, ASCE, Vol. 100, No. GT3, 329-348.

134. Yang, I. (2005). "Uncertainty and Updating of Long-term Prediction of Prestress Forces in PSC Box Girder Bridges," *Computers and Structures*, Elsevier, No. 83, pp. 2137-2149.

135. Yazdani, N., Eddy, S. and Cai, C. S. (2000). “Effect of Bearing Pads on Precast Prestressed Concrete Bridges”, *Journal of Bridge Engineering*, ASCE, Vol. 5, No. 3, pp. 224-231.

136. Hueste, M. B. D., Chompreda, P., Trejo, D., Cline, D. B. H., and Keating, P. B. (2004). “Mechanical Properties of High-Strength Concrete for Prestressed Members,” *ACI Structural Journal*, ACI, No. 101-S45, pp. 457-465.

VITA

Woo Seok Kim

Education:

The Pennsylvania State University, University Park, PA
Doctor of Philosophy in Civil Engineering

The Pennsylvania State University, University Park, PA
Master of Science, Civil Engineering (December 2004)

Hanyang University, Seoul, Korea
Bachelor of Science, Civil Engineering (February 2002)

Selected Publications:

Pugasap, K., Kim, W., and Laman, J. A. (2009) "Long-Term Response Prediction of Integral Abutment Bridges," *Journal of Bridge Engineering*, ASCE, March.

Laman, J. A., and Kim, W. (2008) "Development of Integral Abutment Bridge Design Specifications," *Draft Report*, Pennsylvania Transportation Research Council.

Kim, W. (2008) "Simplified Nonlinear Numerical Method for Integral Abutment Bridges," IBC 08-43, *Proceedings of 2008 International Bridge Conference*, Pittsburgh, PA.

Kim, W., Laman, J. A., and Linzell, D. A (2007) "Live Load Radial Moment Distribution for Horizontally Curved Bridges," *Journal of Bridge Engineering*, ASCE, Vol. 12, No. 6, Nov./Dec. pp.727-736.

Laman, J. A., Pugasap, K., and Kim, W. (2006) "Field Monitoring of Integral Abutment Bridges," *Final Report No. FHWA-PA-2006-006-510401-01*, Pennsylvania Transportation Research Council.